

**COMSAT**  
Technical Review

Volume 9 Number 2B, Fall 1979

# COMSAT TECHNICAL REVIEW

Volume 9 Number 2, Fall 1979

<i>Advisory Board</i>	Joseph V. Charyk William W. Hagerty John V. Harrington B. I. Edelson Sidney Metzger
<i>Editorial Board</i>	Pier L. Bargellini, Chairman S. J. Campanella William L. Cook C. Dorian H. W. Fliieger Jorge C. Fuenzalida William J. Getsinger R. W. Kreutel Akos G. Revesz George R. Welti

<i>Editorial Staff</i>	Daniel N. Crampton MANAGING EDITOR Margaret B. Jacocks Elizabeth Christie Pearl Coleman TECHNICAL EDITORS Edgar Bolen PRODUCTION Vicki A. Araujo CIRCULATION
------------------------	---

COMSAT TECHNICAL REVIEW is published twice a year by Communications Satellite Corporation (COMSAT). Subscriptions, which include the two issues published within a calendar year, are: one year, \$7 U.S.; two years, \$12; three years, \$15; single copies, \$5; article reprints, \$1. Make checks payable to COMSAT and address to Treasurer's Office, Communications Satellite Corporation, 950 L'Enfant Plaza, S.W., Washington, D.C. 20024, U.S.A.

© COMMUNICATIONS SATELLITE CORPORATION 1980

## PART A (TDMA)

v	FOREWORD	P. L. Bargellini
293	THE INTELSAT TDMA FIELD TRIAL	S. J. Campanella, R. J. Colby, B. A. Pontano, H. Suyderhoud, AND M. Onufry
341	OPEN-LOOP TDMA FRAME ACQUISITION AND SYNCHRONIZATION	S. J. Campanella AND K. Hodson
387	TECHNIQUES FOR TDMA SYSTEM MONITORING	D. J. Schaefer
413	TDMA MODEM DESIGN CRITERIA	C. J. Wolejsza AND D. Chakraborty
465	OPTIMUM FILTERING FOR QPSK IN BANDWIDTH-LIMITED NON-LINEAR SATELLITE CHANNELS	M. E. Jones AND M. R. Wachs
509	TRANSLATIONS OF ABSTRACTS	FRENCH 509 SPANISH 513

## PART B

517	FSK BURST RECEIVER FOR DATA COLLECTION SYSTEMS	K. H. Greene AND R. F. Hefele
549	SMALL EARTH TERMINALS AT 12/14 GHz	J. Kaiser, I. Veenstra, E. Ackermann, AND F. Seidel
604	PERIODIC BANDPASS CHARACTERISTIC OF MICROSTRIP MEANDER LINE	Y. S. Lee AND R. C. Trushel
617	12-GHz 10-W AMPLIFIER USING GaAs IMPATT DIODES	S. Chou
629	RAIN DEPOLARIZATION MEASUREMENTS AT 4 GHz	D. J. Kennedy
669	A MODEL FOR PACKET SWITCHING NODE INCLUDING PACKET RETRANSMISSION EFFECTS	A. Kaul
689	CTR NOTES	THE EFFECT OF BUFFER ACCESS TIME ON HDLC PERFORMANCE A. Kaul 689
	INTELLIGIBLE CROSSTALK BETWEEN LARGE FDM-FM CARRIERS AMPLIFIED BY KLYSTRONS	C. B. Cotner AND A. J. Barnes 705
	NOTE ON CRYPTOSYSTEMS	L. N. Lee 717
	FREQUENCY REUSE LIMITS FOR THE GEOSTATIONARY ORBIT	G. R. Welti 723
731	TRANSLATIONS OF ABSTRACTS	FRENCH 731 SPANISH 735

# **FSK burst receiver for data collection systems**

K. H. GREENE AND R. F. HEFELE

(Manuscript received June 1, 1979)

## **Abstract**

A burst receiver designed for FSK modulated carrier burst reception in a data collection system is described. The significant feature of this receiver is that it must acquire short information bursts (244 bits) whose frequency uncertainty ( $\pm 10$  kHz) is an order of magnitude greater than the signal bandwidth (2 kHz).

Demodulator and acquisition circuit performances are investigated and experimental results presented. Emphasis is given to techniques for analyzing the loss of lock resulting from the switching of the acquisition loop bandwidth. An analytical method is presented for determining the number of bits required to achieve a given missed acquisition rate as a function of  $E_b/N_o$  and acquisition loop bandwidth.

## **Introduction**

Data collection systems are a recent application of communications satellite technology to the gathering of small amounts of information transmitted over the same channel by a large number of transmitter platforms scattered over a wide geographical area. These systems typically gather information on the environment, production, transportation, inventory, and other related data; the information rate is

usually much smaller than that of a voice channel. Since platforms are often accessible only at prohibitive costs, satellite links offer an economically expedient means of obtaining data. However, the characteristics of these platforms (*i.e.*, remoteness, poor accessibility, and widely varying climatic conditions) also pose difficult implementation problems. Large diurnal and long-term frequency variations as well as large variations from platform to platform must be expected. Because of the 6-GHz up-link frequency used in satellite links, the platform's transmit frequency variations are expected to be much greater than the signal bandwidth.

The data collection system is characterized by a channel bandwidth which is determined by frequency uncertainties rather than by the information rate. Frequency uncertainty is typically an order of magnitude greater than the signal bandwidth; therefore, the signal-to-noise ratio in the input bandwidth is usually at least 10 dB below that required to obtain an acceptable bit-error rate (BER).

### Prototype environmental data collection system

This paper describes the design, development, and performance of a burst receiver built by COMSAT Laboratories to operate in a prototype data collection system. This system was planned and implemented by COMSAT GENERAL in conjunction with TELESAT Canada to serve the U.S. Geological Survey (Department of the Interior). It consists of a network of 13 remote unattended platforms which transmit short bursts of environmental data via TELESAT's ANIK satellite to COMSAT GENERAL's central receive station at Southbury, Connecticut. The bursts are transmitted at random intervals and without synchronization among the platforms. At the central receive station, the bursts are demodulated and the recovered data are processed and distributed to various offices of the U.S. Geological Survey. The system immediately distributes information gathered over widely scattered areas, a function which in the past typically required many weeks. Figure 1 is a diagram of the prototype data collection system. The pilot link is necessary to remove satellite and down-converter frequency errors.

Data processing by the communications processing unit (CPU) at the central receive station involves time tagging and data storage in a disc subsystem for later retrieval. Stored data can be forwarded to user computers via 4,800 bits/s autocall telephone lines. Individual users also have access to 110-baud dial-up lines to obtain data at their

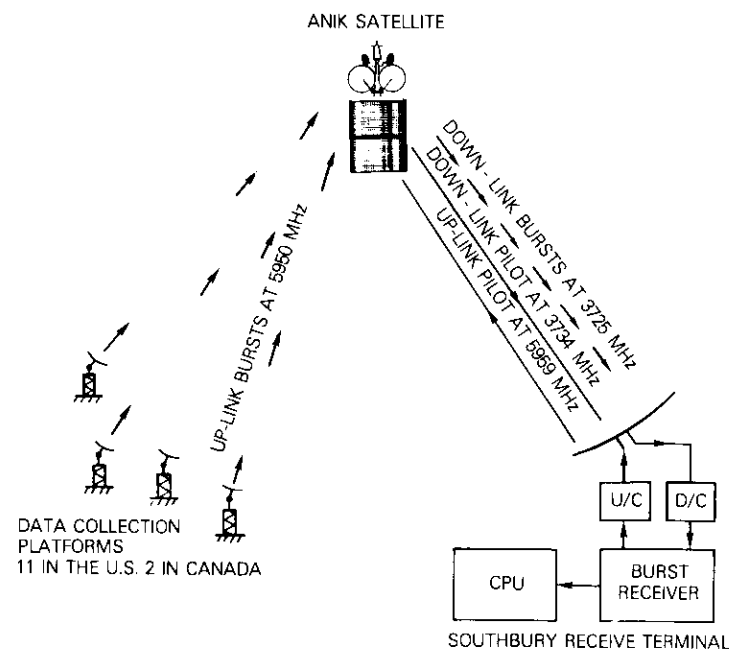


Figure 1. *Prototype Environmental Data Collection System*

discretion. The operating software also monitors the performance of each data collection platform (DCP) in the network and alerts the station operator if a particular unit fails.

Thirteen remote unattended platforms (11 in the United States, 2 in Canada) transmit carrier bursts, FSK modulated at a 1-kbit/s rate, to the Southbury central receive station and to a backup station operated by TELESAT at Ottawa, Ontario. Each platform is battery powered and transmits 244-ms duration bursts on a 5950-MHz carrier frequency using a 1.4-m-diameter paraboloid dish antenna with a 34.5-dB gain and a nominal output power of 1.25 W to obtain an e.i.r.p. of 35.5 dBW.

The burst preamble consists of 100 identical bits for carrier acquisition, 30 alternating bits for clock acquisition, and 15 bits for the unique word (UW). This is followed by 83 bits of data and 16 bits of parity check code. Figure 2 is a diagram of the burst format.

Each platform is programmed at site activation to transmit bursts during 2-min apertures centered on fixed intervals of 15, 30, or 60 min.

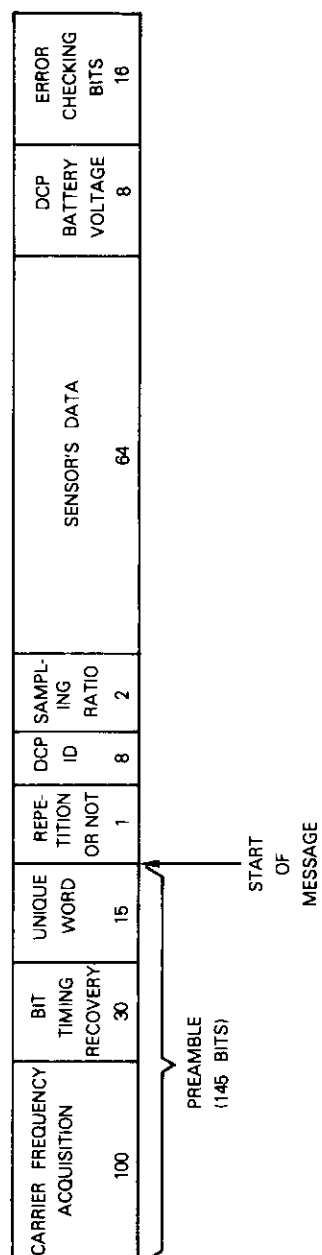


Figure 2. Burst Format

One burst is transmitted per aperture, and the actual transmission time within the aperture is determined by a random number generator to reduce the probability of the overlapping of bursts from different platforms since there is no synchronization among the platforms. For each transmitted burst, a redundant burst is transmitted  $5 \text{ min} \pm 10 \text{ s}$  later. The actual transmission time within the 20-s aperture is determined by a random number generator so that, in the event that a burst is lost by overlap, it is highly unlikely that the redundant burst will also be overlapped.

The transmitted burst is modulated by deviating the center frequency of a 6.20-MHz voltage-controlled oscillator a total of 1.56 Hz and then frequency multiplying the output by 960 to achieve the desired 5,950-MHz carrier frequency with a 1,500-Hz frequency deviation. The burst, after multiplication to 1,500 MHz, is amplified to a power level of 10 W. It is then fed to a passive X4 multiplier, yielding the required power of 1.25 W. Bursting is obtained by switching DC power to the 10-W amplifier, a method which greatly reduces power consumption from the platform's batteries. The output frequency is specified to be within  $\pm 6 \text{ kHz}$  of the nominal value of 5,950 MHz. A complete description of the prototype data collection system is presented in Reference 1.

#### Receiver characteristics

The receiver must acquire and demodulate randomly arriving bursts with large frequency offsets. Frequency offset is caused by the variation from the individual platform oscillators as a result of the conditions described above and the frequency shift resulting from the satellite translator. Since the latter source of error has a common magnitude for all platforms, it can be removed by a pilot signal generated and received by the central receive terminal. The frequency difference between the transmitted and received pilot signals is then used to correct the bursts before they are applied to the demodulator acquisition circuit.

The acquisition circuit must derive a reference frequency during the unmodulated portion of the burst preamble, which can be used for data demodulation during the subsequent portion of the burst. The demodulator is a noncoherent FSK type consisting of two parallel filters, each followed by an amplitude detector and separated in center frequency by approximately the amount of the carrier frequency deviation due to modulation. The reference frequency derived by the

acquisition circuit must position the burst during the preamble in the center of one of the two filters as shown in Figure 3. If this reference is maintained throughout the burst, the alternating MARK and SPACE frequencies will appear at the outputs of the appropriate filters, and the amplitude detectors will provide the corresponding baseband data signal.

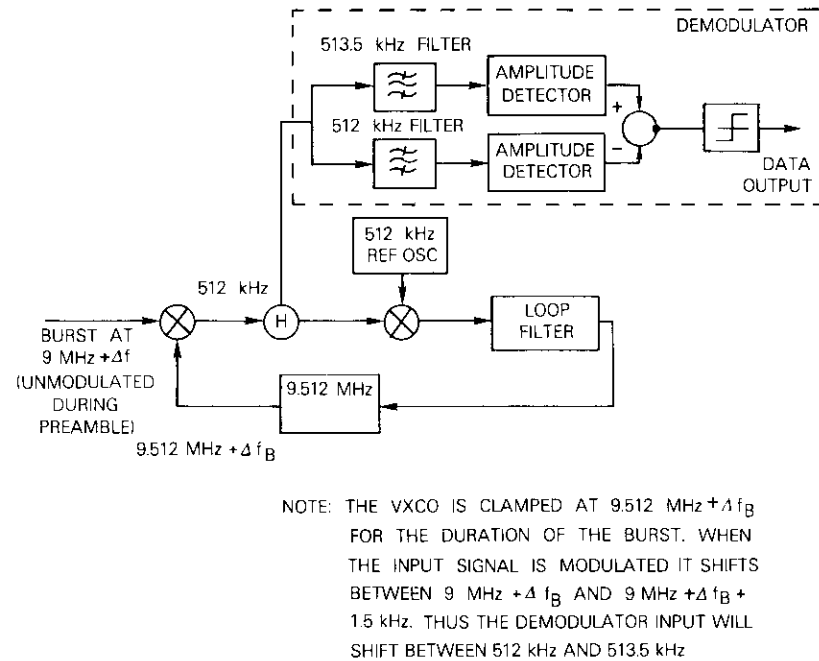


Figure 3. Burst Mode FSK Demodulator

The reference frequency is acquired and maintained as follows. The received burst at a nominal frequency of 9 MHz with an offset of  $\Delta f_p$  is phase locked to a 512-kHz reference oscillator when it is mixed with the output of a 9.512-MHz voltage-controlled crystal oscillator. Thus, during the unmodulated preamble, the difference frequency at the mixer output is 512 kHz, and the frequency error,  $\Delta f_p$ , has been eliminated.

Frequency coherence only, rather than phase coherence, is required for FSK demodulation; therefore, the voltage-controlled crystal oscil-

lator is clamped shortly after acquisition at the acquired frequency and remains clamped for the duration of the burst. This design approach assumes that the variation in burst frequency for the duration of the burst will be negligible; this assumption has been verified during system operation. Clamping the voltage-controlled crystal oscillator eliminates the problems associated with maintaining loop lock and with loop-induced jitter on the reference carrier. It should also be noted that this type of demodulator can be applied to either continuous-phase FSK modulation or discontinuous-phase (two-oscillator) modulation; whereas a phase-locked loop (PLL) demodulator, besides having problems with cycle slipping, cannot be used for discontinuous-phase modulation.

#### Logic and control circuitry

The logic and control circuitry derives symbol timing, detects the UW, generates a start of message (SOM) pulse to the CPU in response to UW detection, actuates the clamping mechanism on the 9.512-MHz voltage-controlled crystal oscillator, and releases the clamp after the last data bit of the burst.

It also provides the conditional function that, if a carrier acquisition signal is received from the acquisition circuit causing the voltage-controlled crystal oscillator to be clamped, but the UW is not detected, then the voltage-controlled crystal oscillator will be released 153 bits after carrier acquisition has been indicated. This eliminates the possibility of the loop locking onto a burst and then remaining permanently clamped because no UW had been detected.

After the carrier has been acquired, the voltage-controlled crystal oscillator's input voltage must be maintained precisely. This was accomplished with a high time constant RC network and a relay at the voltage-controlled crystal oscillator input voltage, controlled by the carrier acquisition signal. When a carrier acquisition is received, the relay contacts are held open for the duration of the burst.

The carrier acquisition signal enables the UW detector. The data are shifted into a 15-bit shift register, and after each shift, the contents of the register are checked to determine if the UW is present. The appropriate outputs of the register are inverted to produce 15 ones when the register contains the correct UW. A UW that contains up to two errors can be detected.

If no UW is detected within the allocated time (up to 153 ms after carrier acquisition), the clamp on the voltage-controlled crystal oscil-

lator is released, allowing the acquisition circuit to search for another carrier. When a UW is detected, an SOM pulse is generated, and the detector is disabled to ensure that no false UWs appear in the information data. The reclocked and recovered data are then gated out to the CPU, and an end of message (EOM) pulse is generated after the last data bit. The EOM pulse releases the clamp on the voltage-controlled crystal oscillator in the acquisition circuit.

### FSK modulation and detection

The selection of a modulation scheme for the data collection system was influenced primarily by the low data rate and the requirements imposed on the platform design: low cost, low power consumption, unattended operation, and operation over a large temperature range. Therefore, large values of phase jitter should be expected in the transmitted carrier burst. Studies performed at COMSAT Laboratories concluded that the short-term frequency stability of an oscillator which meets platform design requirements necessitates an FSK modulation scheme.

FSK modulation is attractive in this application because of its relative insensitivity to phase jitter at low data rates, the ease of implementing both the modulator and demodulator, and its low cost. FSK modulation may be either continuous or discontinuous in phase. A continuous-phase FSK modulator is implemented by a single voltage-controlled oscillator which is deviated between the two transmitted frequencies; consequently, there is no phase discontinuity in the transmitted carrier. In discontinuous-phase FSK modulation, two oscillators (one at frequency  $f_1$  and the other at frequency  $f_2$ ) are alternately gated on and off by the data. As a result, a frequency deviation ( $f_2 - f_1$ ) is achieved; however, no phase coherence is maintained. Reference 2 discusses the spectral characteristics of both types of FSK modulation. It also presents the computer and hardware simulations which provided design information for choosing modulation indexes and receiver filter bandwidths, and determined the effects of frequency offsets and jitter.

A simple approach to the demodulation of either continuous or discontinuous FSK modulation is noncoherent detection which compares the envelopes of the signals appearing in small bands about  $f_1$  and  $f_2$ . Its theoretical performance is about 1.2 dB worse than that of coherent FSK at a BER of  $10^{-3}$ ; the difference becomes progressively smaller as the BER decreases. This was considered an acceptable loss

in the data collection system because of the simplification and reliability achieved.

The FSK demodulator is shown in Figure 4. It consists of two crystal filters, each with a noise bandwidth of 1 kHz and center frequencies at 512 and 513.5 kHz. For a bit rate of 1 kbit/s, this separation corresponds to a modulation index of 1.5.

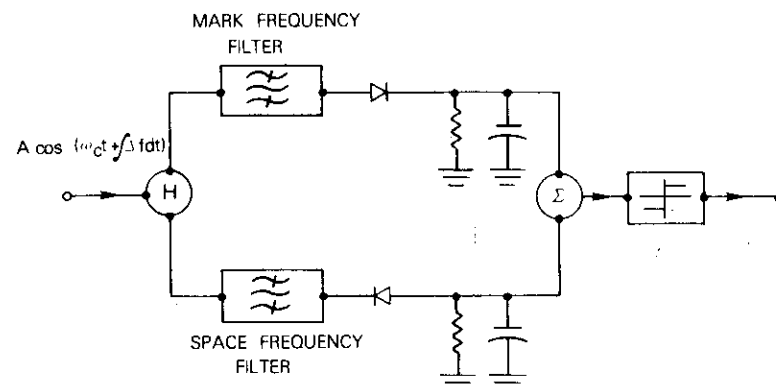


Figure 4. Noncoherent FSK Demodulator

Measured BERs for continuous mode operation are plotted in Figure 5 against  $E_b/N_o$  for no frequency offset and for 20- and 40-percent frequency offset (ratio of frequency offset to bit rate). A 20-percent offset had a negligible effect on BER while a 40-percent offset produced a loss of 1 dB. This relative insensitivity to frequency offset can be attributed to the wide noise bandwidth of the crystal filters.

### Burst acquisition

The acquisition circuit of the burst receiver employs a PLL to frequency center a carrier burst. The distinctive characteristic of this application is that the frequency uncertainty of the input burst is an order of magnitude larger than the signal bandwidth.

The voltage-controlled crystal oscillator in the PLL must be swept through the frequency range to acquire the signal. The maximum sweep rate that can be tolerated while still obtaining reliable acquisition performance is a function of the loop noise bandwidth; generally the sweep rate increases with bandwidth until the loop signal-to-noise ratio

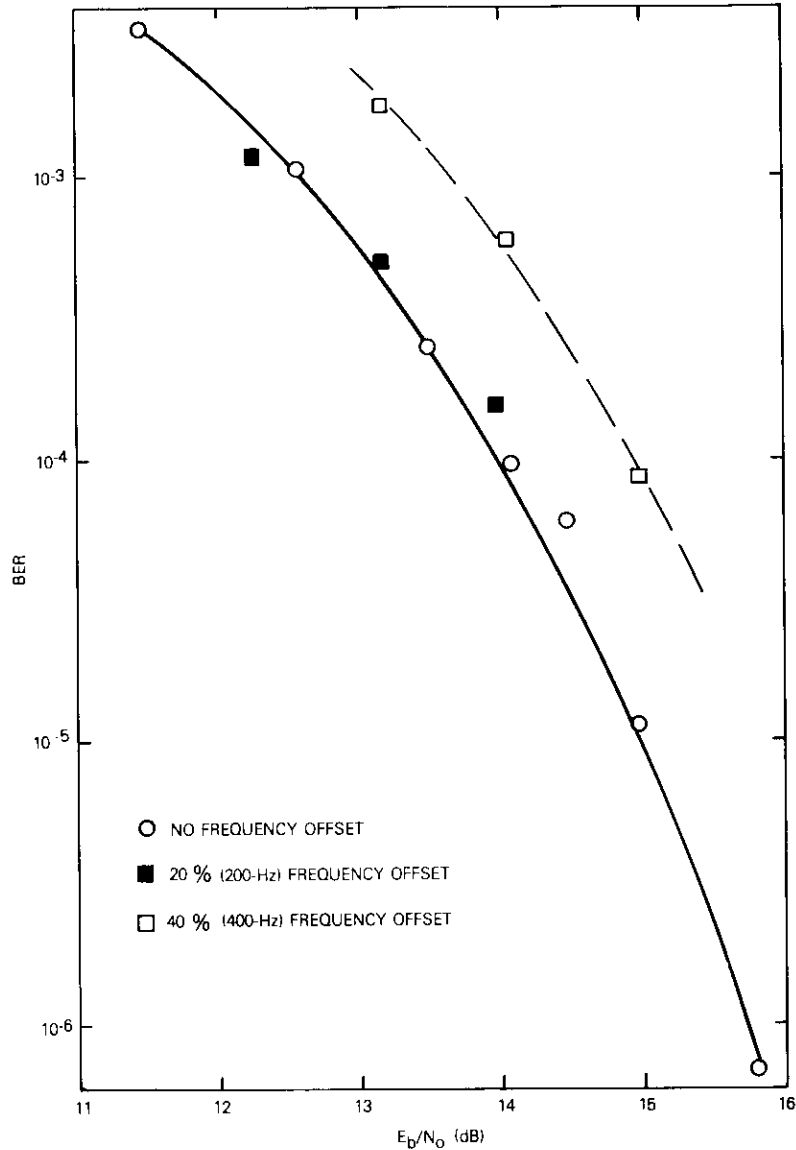


Figure 5. FSK Demodulator BER vs  $E_b/N_0$ , Continuous Mode

becomes seriously degraded. The requirement for rapid acquisition, and consequently wide-loop bandwidth, conflicts with the requirement for narrow bandwidth dictated by the need for accurate frequency centering. To circumvent this problem, a switched bandwidth technique is employed in which the loop parameters are adjusted for a wide bandwidth mode during the acquisition phase, but are switched to a narrow bandwidth mode in response to a signal from the acquisition detector. After a time interval required for the settling of transients, the voltage-controlled crystal oscillator is clamped at the acquired frequency for the duration of the burst; it serves as a reference oscillator for FSK demodulation at this clamped frequency.

The normal operation of the loop is shown in Figure 6, which is a time plot of typical voltage-controlled crystal oscillator output frequency variation,  $f_0$ , due to the sweep voltage and the input noise. The

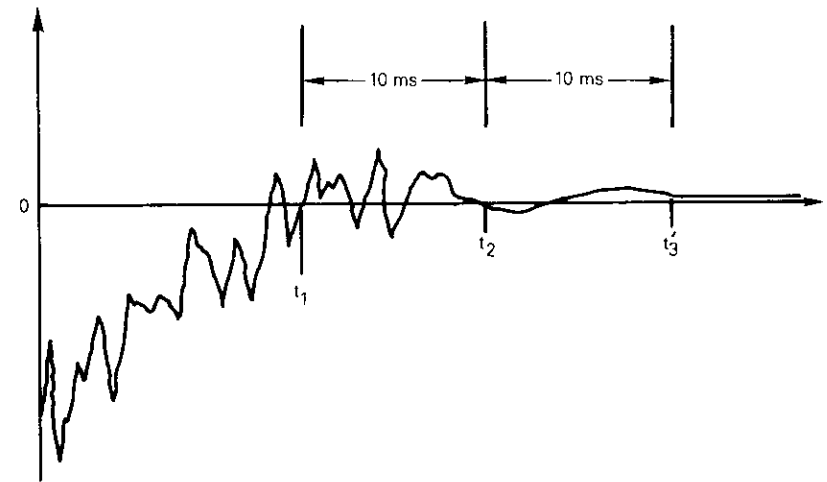


Figure 6. Normal Acquisition Process

ramp frequency variation superimposed with jitter due to noise in the wideband mode is shown from  $t = 0$  to  $t = t_1$ , where  $t_1$  is the instant of acquisition. Sweep is inhibited by the acquisition so that from  $t_1$  to  $t_2$  the mean value of frequency variation is zero; however, the jitter due to wideband noise remains. At  $t_2$  the loop bandwidth is step reduced to its narrowband value, and the frequency jitter is charac-

terized by much smaller variations. Finally at  $t_3$ , the voltage-controlled crystal oscillator is clamped at the current value of frequency jitter.

In contrast to the normal operation is the acquisition process shown in Figure 7, in which the frequency offset due to noise at the switching instant is much larger than the lock-in range of the narrowband loop. The input frequency is pulled in to phase lock if the time interval  $t_3 - t_2$  is sufficiently long. Otherwise, the residual frequency offset of the voltage-controlled crystal oscillator will consist of both noise jitter and the remainder due to incomplete pull-in.

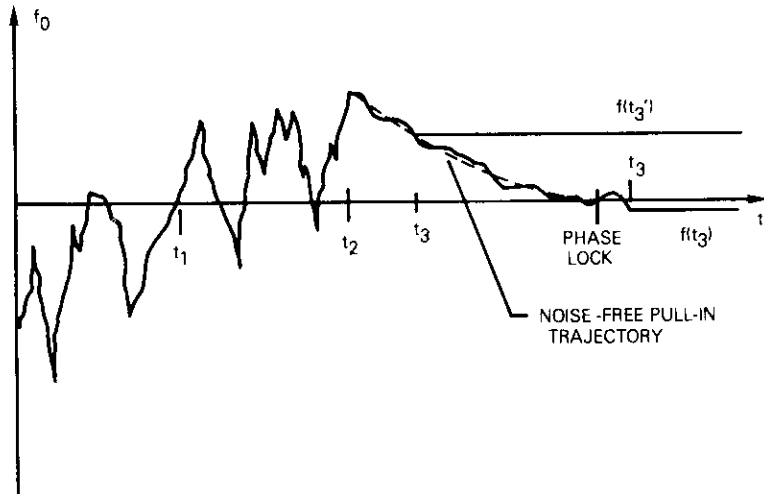


Figure 7. Loss of Lock During Bandwidth Switching

The operation of the above described circuit will now be analyzed. The approximate number of bits for acquisition is determined in terms of the ratio of frequency uncertainty to bit rate. It will also be shown that there is a large probability of loss of lock due to the switching transient response. The result is that the total acquisition time is significantly increased by the time required for the narrowband loop to pull in from the frequency offset value at the switching instant.

Figure 8 shows a typical PLL. The loop filter,  $H(s)$ , is usually an integrator with a lead term for compensation resulting in an unconditionally stable second-order loop that has a zero steady-state phase error. However, in this application an additional pole is required in the

loop filter to avoid large values of frequency jitter on the recovered carrier as a result of the wide noise bandwidth (26 kHz) at the loop input.

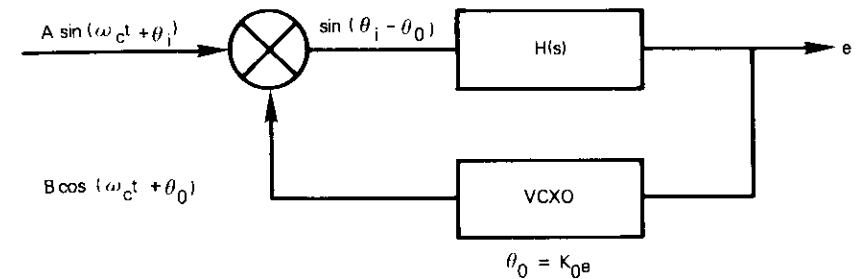


Figure 8. Phase Lock Loop

The resulting closed loop is a third-order loop which is not unconditionally stable. The break angular frequency,  $\omega_B$ , of the noise limiting pole must therefore be large enough to provide sufficient phase margin. In the burst receiver, 0.05 was selected as the ratio of loop natural angular frequency ( $\omega_n$ ) to break angular frequency ( $\omega_B$ ), although subsequent analysis indicates that a ratio as high as 0.3 will provide a phase margin of better than  $45^\circ$  when  $\zeta = 1/\sqrt{2}$ . In this case,  $\omega_n$  and  $\zeta$  are the natural angular frequency and damping coefficients of the second-order loop which result when  $\omega_B \rightarrow \infty$ .

The closed-loop transfer function is given by

$$\frac{\theta_o}{\theta_i} = \frac{1 + 2\zeta(s/\omega_n)}{(\omega_n/\omega_B)(s/\omega_n)^3 + (s/\omega_n)^2 + 2\zeta(s/\omega_n) + 1} \quad (1)$$

The loop IF noise bandwidth can be shown to be given by

$$2B_L = \frac{\omega_n}{2} \left( \frac{1 + 4\zeta^2}{2\zeta - \omega_n/\omega_B} \right) \quad (2)$$

and the rms frequency jitter, normalized with respect to the bit rate,  $R$ , is

$$\frac{\sigma_i}{R} = K_i \sqrt{\frac{(2B_L/R)_i^2 (2B_L/R)_1}{E_b/N_o}} \quad (3)$$

where  $\sigma_i = \sqrt{f_0}$

$R$  = bit rate

$i = 1, 2$  (1 indicates wideband mode and 2 narrowband mode)

$$K_i = \sqrt{\frac{2[2\zeta(\omega_B/\omega_{n_i}) - 1](2\zeta - \omega_{n_i}/\omega_B)(8\zeta^3 + \omega_{n_i}/\omega_B)}{(2\pi)^2(1 + 4\zeta^2)^3}}$$

In this application,  $\omega_B$  was not switched when  $\omega_n$  changed from the wideband to the narrowband mode, and loop component values were chosen so that  $\zeta$  was approximately the same before and after switching. For  $\omega_{n_i}/\omega_B = 0.05$  and  $\zeta = 1/\sqrt{2}$ , the values of  $K_i$  become

$$K_1 \approx K_2 \approx 0.45$$

Equations (2) and (3) will be used subsequently to describe the performance of the acquisition circuit. It is now necessary to consider the sweep rate that can be used to attain a given missed acquisition rate.

### Wideband mode operation

The voltage-controlled crystal oscillator in the acquisition PLL must be swept over the range of frequency uncertainty at a rate of at least one sweep in 90 ms. A carrier recovery preamble of 100 ms ensures that at some time during the preamble the voltage-controlled crystal oscillator will pass through the frequency of a randomly arriving burst, and that 10 ms will be available for bandwidth switching and narrowband mode phase lock. Whether acquisition is achieved during the sweep is a probabilistic function of the instantaneous phase and frequency difference between the burst frequency and the voltage-controlled crystal oscillator frequency, and depends heavily on the loop bandwidth and signal-to-noise ratio.

Frazier and Page [3] present useful data on missed acquisition rates. These data, interpreted by Gardner [4], provide the following empirical formula for the maximum sweep rate, which yields a missed acquisition rate of 0.1 in a second-order loop:

$$\frac{\Delta f}{\Delta T} = \frac{1}{2\pi} \frac{[1 - \sqrt{(2B_L/R)_1/(E_b/N_o)}]}{1 + d} (\omega_{n_i})^2 \quad (4)$$

where  $\Delta f$  = frequency range over which the voltage-controlled crystal oscillator is swept (equal to frequency uncertainty range)

$\Delta T$  = time in which one sweep is made

$$d = e^{-\zeta\pi/\sqrt{1-\zeta^2}}$$

The present application considers a third-order loop because of a noise limiting pole which is normally at least three times the frequency of any other poles or zero. Hence, it seems that for sweep rate estimation the loop can be viewed as second-order.

Equation (4) is limited to determining the maximum sweep rate for a missed acquisition of 0.1. An approach involving multiple sweeps will be used to determine bandwidth requirements at lower miss rates. That is, the number of bits required to achieve a missed acquisition rate of  $10^{-3}$  will be obtained by determining the time required to sweep the frequency uncertainty range three times at the rate prescribed by equation (4).

Experimental results suggest that the missed acquisition rate will decrease by an order of magnitude for each dB increase in  $E_b/N_o$ . Thus, if the loop is operated with three sweeps during the burst preamble to obtain a missed acquisition rate of  $10^{-3}$  at  $E_b/N_o = 12$  dB, the same circuit should achieve the design goal of  $10^{-5}$  at an  $E_b/N_o$  of 14 dB.

Substituting  $\omega_{n_i}$  from equation (2) into equation (4), normalizing on  $R$ , and noting that  $\Delta N = R\Delta T$  yield the following expression for the number of bits required to achieve the missed acquisition rate of  $10^{-3}$ :

$$N(10^{-3}) = 3\Delta N = \frac{3C_1(\omega_{n_i}/\omega_B, \zeta) \Delta f/R}{[1 - \sqrt{(2B_L/R)_1/(E_b/N_o)}](2B_L/R)^2_1} \quad (5)$$

where  $\Delta N$  = number of bits in one sweep and

$$C_1\left(\frac{\omega_{n_i}}{\omega_B}, \zeta\right) = \frac{(1 + 4\zeta^2)^2(1 + d)\pi}{2(2\zeta - \omega_{n_i}/\omega_B)} \quad (6)$$

In the special case of  $\omega_{n_i}/\omega_B = 0.05$  and  $\zeta = 1/\sqrt{2}$

$$C_1\left(0.05, \frac{1}{\sqrt{2}}\right) = 10.81$$

In the prototype data collection system, the frequency uncertainty is 20 kHz and the bit rate is 1 kbit. At  $E_b/N_0 = 12$  dB with  $\zeta = 1/\sqrt{2}$  and  $\omega_{n_1}/\omega_B = 0.05$ , the required number of bits will then be

$$N(10^{-3}) = \frac{648.6}{[1 - \sqrt{(2B_i/R)_1/15.849}](2B_i/R)_1^2} \quad (7)$$

This is plotted against  $(2B_i/R)_1$  in Figure 9, which shows that to obtain an acquisition rate substantially less than 90 bits at an  $E_b/N_0$  of 12 dB, the bandwidth to bit ratio in the wideband mode must be of the order of 5 or greater. Increasing the ratio to 10 results in a theoretically more rapid acquisition; however, the loop signal-to-noise ratio is only 2 dB. Consequently, the lock condition is rather precarious, and the as-

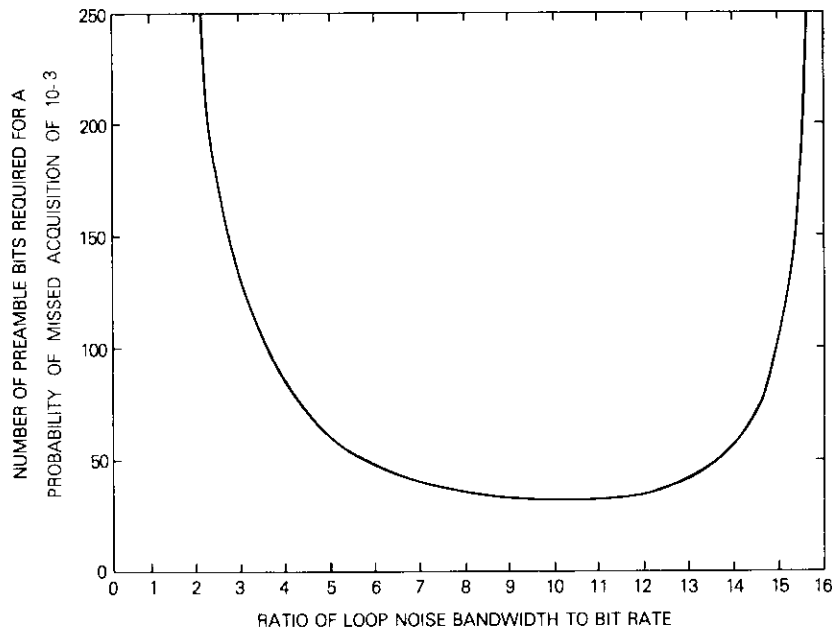


Figure 9. Required Preamble Bits vs Bandwidth Ratio

sumption of linearity in describing noise perturbations becomes questionable. The curve rises again at the wider bandwidths because the faster response time of the larger bandwidth is offset by the increasing amount of noise in the loop.

### Bandwidth switching

Following acquisition in the wideband mode, resistive components in the loop filter are switched to cause a step reduction in loop bandwidth, thereby reducing the magnitude of frequency jitter at the instant of clamping. The necessary reduction will depend on the bandwidths of the detector filters: the wider the filter bandwidth the less sensitive the detector to frequency offset, as indicated in Reference 2. On the other hand, increasing the detector filter bandwidth increases the minimum achievable BER. No attempt has been made to solve the extremely complex problem of finding an optimum combination of loop bandwidth ratio and detector filter bandwidth to achieve a minimum BER and a minimum missed acquisition rate.

This section investigates a representative range of narrowband bandwidths and calculates the resulting rms frequency jitter. The rms frequency jitter in the narrowband mode is obtained from equation (3). Figure 10 plots the result for  $E_b/N_0 = 12$  dB and for a loop with  $\zeta = 1/\sqrt{2}$  and  $\omega_{n_1}/\omega_B = 0.05$  against a narrowband bandwidth for various wideband bandwidths. Also shown for each value of wideband bandwidth is the number of bits required to achieve a missed acquisition rate of  $10^{-3}$  as calculated from equation (7) and plotted in Figure 9.

Bandwidth switching is accomplished by switching resistive elements in the input and feedback paths of the loop filter operational amplifier as shown in Figure 11a. Opening switch S1 removes R1 from the input circuit so that the loop gain is decreased. Switch S2 is required to change the feedback resistance so that the loop damping coefficient remains the same.

The question of whether the loop remains in lock when bandwidth switching occurs must be considered. An approximation to loop behavior at bandwidth switching can be derived by considering the forward loop as composed of two parallel branches between the noise limiting filter and the voltage-controlled crystal oscillator output as shown in Figure 11b; one branch is switched out at the instant of bandwidth switching. That is, prior to the switching instant the forward loop transfer function is

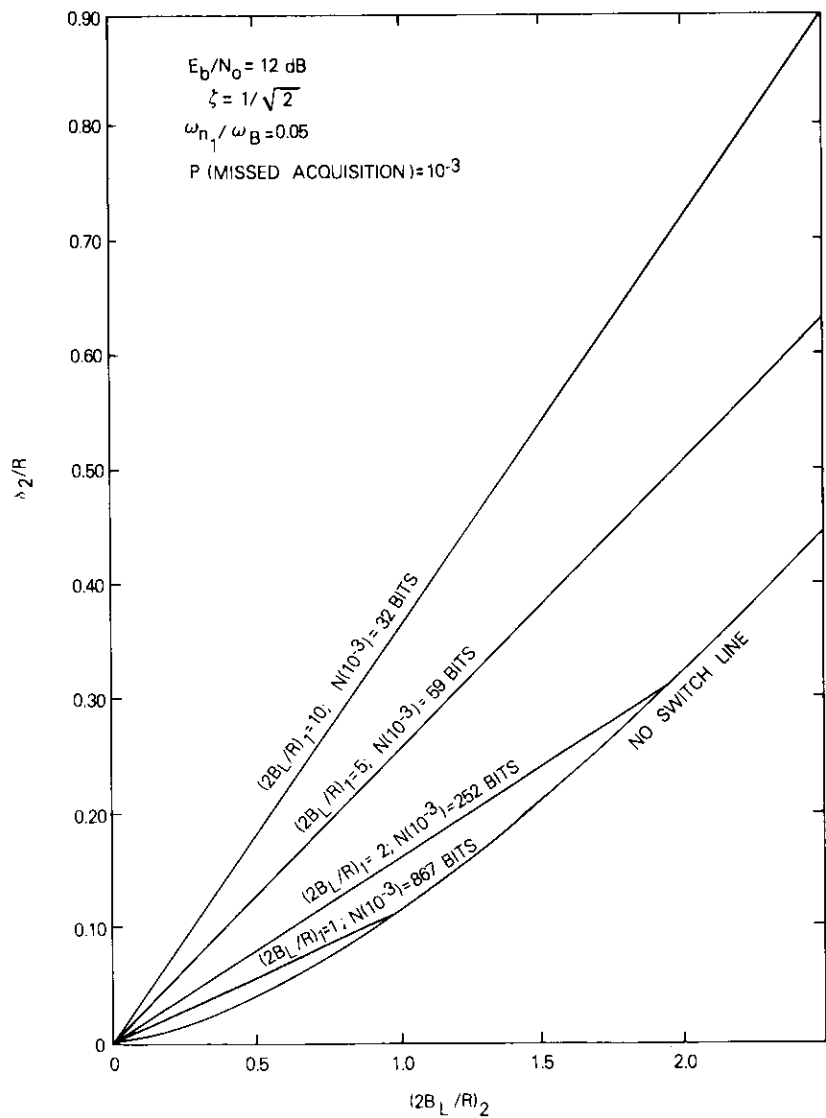


Figure 10. rms Frequency Jitter vs Narrowband Bandwidth

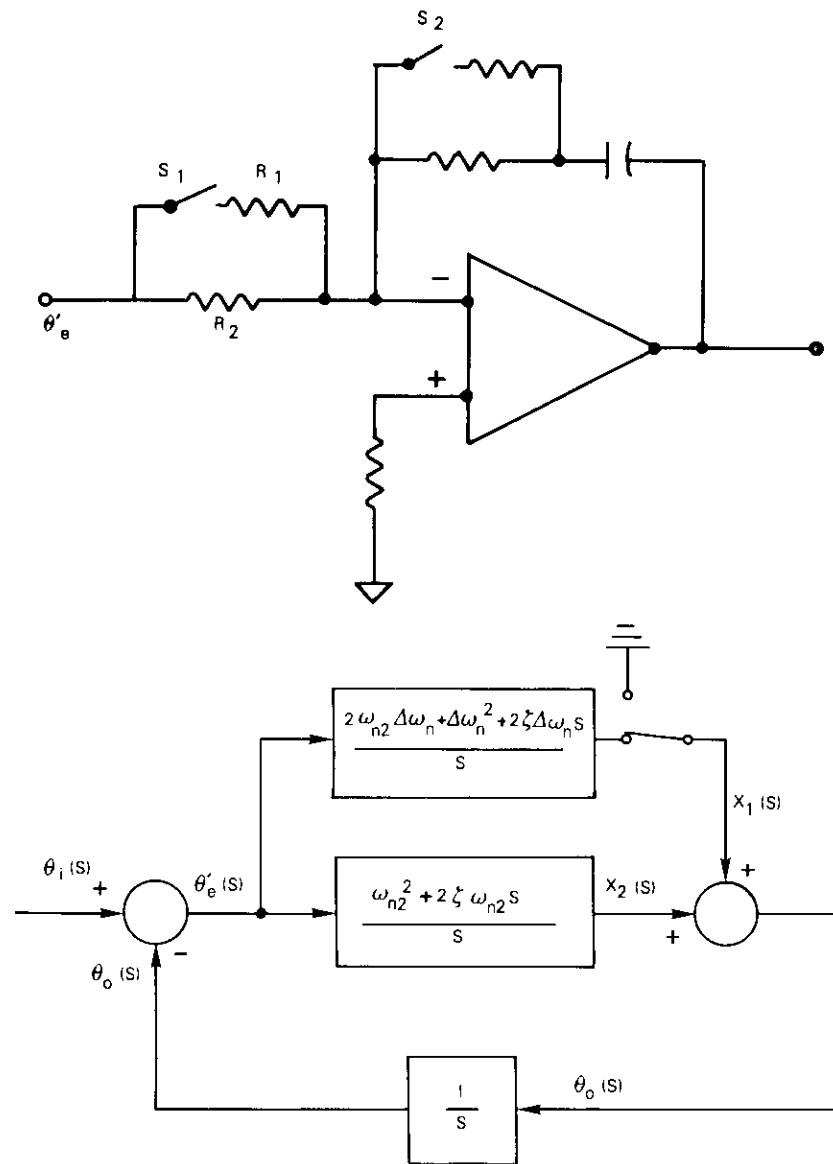


Figure 11. Acquisition Circuit PLL

$$\frac{x_0(s)}{\theta'_c} = \left[ \frac{(\omega_{n_2})^2 + 2\zeta\omega_{n_2}s}{s} + \frac{2\omega_{n_2}\Delta\omega_n + \Delta(\omega_n)^2 + 2\zeta\Delta\omega_n s}{s} \right] \quad (8)$$

where  $\omega_{n_1} = \omega_{n_2} + \Delta\omega_n$ .

At the switching instant, as a result of switching out the resistors shown in Figure 11, the second term in equation (8) vanishes. If the phase output of the voltage-controlled crystal oscillator exceeds  $\pi/2$ , due to transients resulting from switching, the loop has lost lock. The length of time that it remains out of lock depends on the frequency offset of the voltage-controlled crystal oscillator when lock is lost. If  $\dot{\theta}_0$  is within the lock-in frequency, the loop will reacquire immediately with an acquisition time of the order of  $1/\omega_{n_1}$ . If  $\dot{\theta}_0$  is greater than this value, pull-in by the narrowband loop commences. As indicated by equation (8), the loop transfer function following bandwidth switching is given by

$$\frac{\theta_0(s)}{\theta_i(s)} = \frac{(\omega_{n_2})^2 + 2\zeta\omega_{n_2}s}{s^2 + 2\zeta\omega_{n_2}s + (\omega_{n_2})^2} \quad (9)$$

Since a new loop configuration is involved, the initial conditions must be considered so that the complete response including transients is

$$\theta_0(s) = \frac{(\omega_{n_2})^2 + 2\zeta\omega_{n_2}s}{s^2 + 2\zeta\omega_{n_2}s + (\omega_{n_2})^2} \theta_i(s) + \frac{s + 2\zeta\omega_{n_2}}{s^2 + 2\zeta\omega_{n_2}s + (\omega_{n_2})^2} \theta_0(0+) + \frac{\dot{\theta}_0(0+)}{s^2 + 2\zeta\omega_{n_2}s + (\omega_{n_2})^2} \quad (10)$$

where time  $t = 0+$  indicates the instant immediately after switching.

Figure 11 shows that  $\theta_0(0+) = \theta_0(0-)$  and that

$$\dot{\theta}_0(0-) = x_1(0-) + x_2(0-)$$

while

$$\dot{\theta}_0(0+) = x_2(0-) \quad .$$

Therefore, equation (10) becomes

$$\theta_0(s) = \frac{(\omega_{n_2})^2 + 2\zeta\omega_{n_2}s}{s^2 + 2\zeta\omega_{n_2}s + (\omega_{n_2})^2} \theta_i(s) + \frac{x_2(0-) + 2\zeta\omega_{n_2}\theta_0(0)}{s^2 + 2\zeta\omega_{n_2}s + (\omega_{n_2})^2} + \frac{s}{s^2 + 2\zeta\omega_{n_2}s + (\omega_{n_2})^2} \dot{\theta}_0(0) \quad (11)$$

Subsequent to switching, the loop output consists of the loop response to the noisy input,  $\theta_i(s)$ , and the transient response to the initial conditions as indicated by the second two terms in equation (11). The transient response will be given by

$$\theta_{0t} = \frac{e^{-\zeta\omega_{n_2}t}}{\sqrt{1-\zeta^2}} \left[ \frac{x_2(0)}{\omega_{n_2}} \sin \sqrt{1-\zeta^2} \omega_{n_2}t + \theta_0(0) \sin \left( \sqrt{1-\zeta^2} \omega_{n_2}t + \tan^{-1} \frac{\sqrt{1-\zeta^2}}{\zeta} \right) \right] \quad (12)$$

In this equation,  $x_2(0)/\omega_{n_2}$  and  $\theta_0(0)$  are zero-mean Gaussian random variables with the following rms values:

$$\sigma_{x_2} \triangleq \sqrt{\frac{x_2(0)}{\omega_{n_2}^2}} = \sqrt{\frac{(2\zeta)^3}{(1+4\zeta^2)(2\omega_{n_1}/\omega_B)}} \sqrt{\frac{(2B_L/R)_1}{E_b/N_0}}$$

and

$$\sigma_{\theta_0} = \frac{1}{\sqrt{2}} \sqrt{\frac{(2B_L/R)_1}{E_b/N_0}} \quad (13)$$

For  $\zeta = 1/\sqrt{2}$  and  $\omega_{n_1}/\omega_B = 0.05$ ,  $\sigma_{x_2}$  is much larger than  $\sigma_{\theta_0}$ . To simplify the analysis, the transient response due to  $\theta_0(0)$  will not be included. The resulting peak value of  $\dot{\theta}_0$  will be

$$\dot{\theta}_0|_{\text{peak}} = \frac{x_2(0)}{\omega_{n_2}} \omega_{n_2} e^{-\pi/2} \quad (14)$$

and the output phase at the peak frequency will be

$$\theta_{0t} = \sqrt{2} \frac{\dot{\theta}_0|_{\text{peak}}}{\omega_{n_2}} \quad (15)$$

If  $\theta_{0,peak} > \omega_L$ , the lock-in frequency, the output phase transient will be

$$\theta_{0_t} \geq \sqrt{2} \frac{\omega_L}{\omega_{n_2}} \quad (16)$$

Gardner [4] provides the following expression for lock-in frequency:

$$\omega_L = 2\zeta\omega_{n_2} \quad (17)$$

which when substituted into equation (16) with  $\zeta = 1/\sqrt{2}$  yields:

$$\theta_{0_t} \geq 2 \quad (18)$$

Thus, whenever the transient response of the output frequency exceeds the loop lock-in frequency, the output phase will be greater than  $\pi/2$  and the loop must pull-in to phase lock. The probability that pull-in occurs is then

$$P(\text{pull-in}) = P(\theta_{0,peak} \geq \omega_L) = P\left(\left|\frac{x_2(0)}{\omega_{n_2}}\right| \geq e^{\pi/2} \frac{\omega_L}{\omega_{n_2}}\right) \quad (19)$$

From equation (17) with  $\zeta = 1/\sqrt{2}$  this becomes

$$P(\text{pull-in}) = P\left(\left|\frac{x_2(0)}{\omega_{n_2}}\right| \geq 6.803\right) = 2\left[1 - F\left(\frac{6.803}{\sigma_{x_2}}\right)\right] \quad (20)$$

where  $F(x) = \frac{1}{\sqrt{2\pi}} \int_{-\infty}^x e^{-t^2/2} dt$  is tabulated in Reference 5. Substituting equation (13) into equation (20) yields

$$P(\text{pull-in}) = 2\left\{1 - F\left[2.216\sqrt{\frac{E_b/N_o}{(2B_L/R)_1}}\right]\right\} \quad (21)$$

Evaluation of equation (21) indicates that the probability of loss of lock and pull-in caused by the bandwidth switching transient is very small.

Loss of lock may also be caused by noise in the loop when the transient phase response reaches  $\pi/2$ . The contribution of the transient response to phase is much greater than that due to noise in the narrowband loop; at the peak of the phase excursion, the transient response of output frequency is zero and frequency offset will be due

entirely to narrowband noise. The peak phase excursion is obtained from equation (12):

$$\theta_{0,peak} = e^{-\pi/4} \frac{x_2(0)}{\omega_{n_2}} \quad (22)$$

so that the probability of the peak phase exceeding  $\pi/2$  is given by

$$\begin{aligned} P\left(|\theta_{0,peak}| > \frac{\pi}{2}\right) &= P\left(\left|\frac{x_2(0)}{\omega_{n_2}}\right| \geq e^{\pi/4} \frac{\pi}{2}\right) \\ &= 2\left[1 - F\left(\frac{e^{\pi/4} \pi/2}{\sigma_{x_2}}\right)\right] \quad (23) \end{aligned}$$

The frequency offset is due to random-noise-induced frequency jitter which has an rms value given by equation (3). The probability that the frequency offset exceeds the lock range is given by

$$P(|\dot{\theta}_0| \geq \omega_L) = 2\left[1 - F\left(\frac{\omega_L}{2\pi\sigma_2}\right)\right] \quad (24)$$

which, based on equations (17) and (3) with  $\zeta = 1/\sqrt{2}$ , becomes

$$P(|\dot{\theta}_0| \geq \omega_L) = 2\left[1 - F\left(0.472\sqrt{\frac{E_b/N_o}{(2B_L/R)_1}}\right)\right] \quad (25)$$

Multiplying equation (23) by equation (24) after substituting  $\sigma_{x_2}$  from equation (13) yields a minimum probability that loss of lock and pull-in will occur as a result of bandwidth switching:

$$\begin{aligned} P(\text{pull-in})_{\min} &= 4\left[1 - F\left(1.122\sqrt{\frac{E_b/N_o}{(2B_L/R)_1}}\right)\right] \\ &\cdot \left[1 - F\left(0.972\sqrt{\frac{E_b/N_o}{(2B_L/R)_1}}\right)\right] \quad (26) \end{aligned}$$

Equation (26) is plotted against  $E_b/N_o$  in Figure 12 for several bandwidth ratios. It can be seen that there is a substantial probability that loss of lock and pull-in will occur over the entire range of  $E_b/N_o$  values.

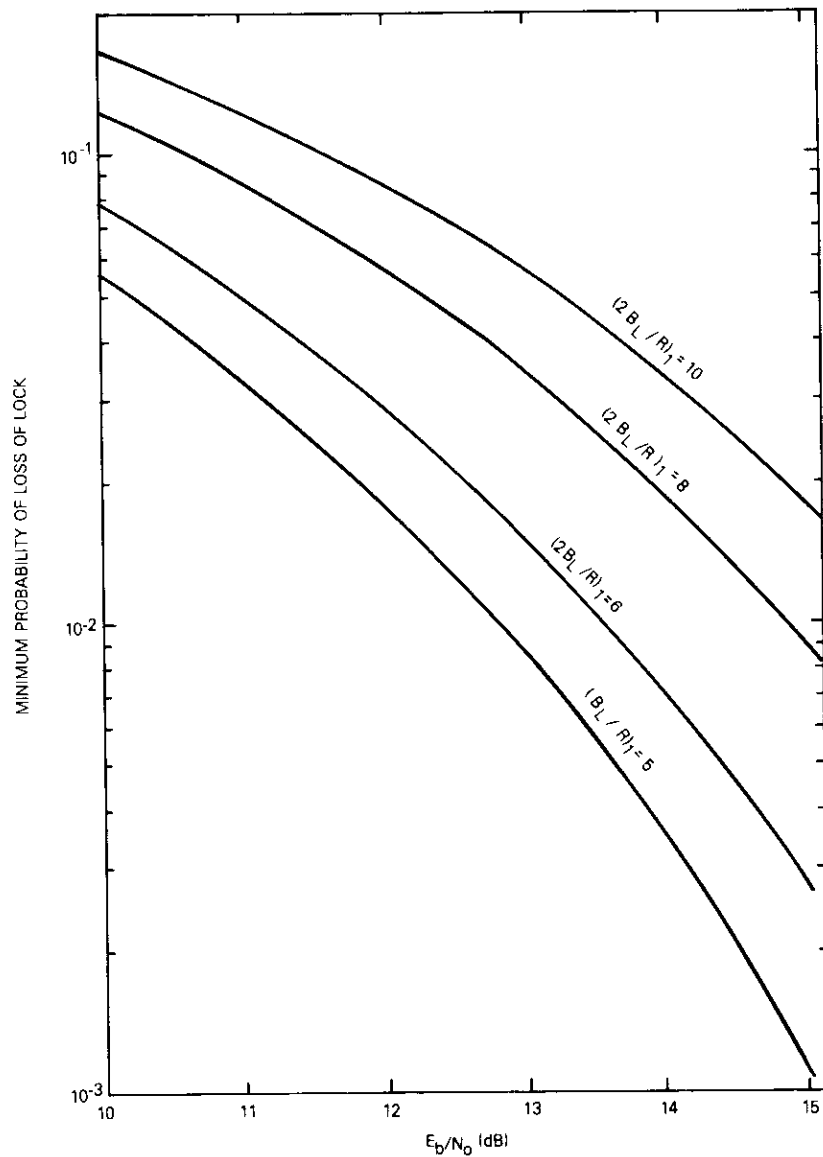


Figure 12. Minimum Probability of Loss of Lock due to Bandwidth Switching

Loss of lock means that the voltage-controlled crystal oscillator must be pulled in to lock from the frequency offset that exists when lock is lost. The time required to pull-in to phase lock is proportional to the square of the initial offset. In the described receiver, a fixed number of bits were allowed for pull in because of the limited number of bits in the preamble, mostly allotted to sweep acquisition. The effect of a fixed number of bits for pull-in is that there is a finite probability that the voltage-controlled crystal oscillator will be clamped prematurely, that is, before phase lock is achieved. This will result in a residual frequency offset of the voltage-controlled crystal oscillator, which is a combination of the offset due to incomplete pull-in and that caused by frequency jitter in the narrowband mode.

The residual frequency offset will result in deteriorated BER performance, and if it is large enough, will lead to a missed UW detection. A complete derivation of the residual frequency offset would involve the solution of the probability density distribution of  $\theta_0(t)$  as described by equations (11) and (12), a complete solution to the problem of lock loss probability, and finally the effect on the frequency density distribution of the pull-in phenomenon. The resulting analysis is extremely complicated and beyond the scope of this paper. The foregoing limited analysis is presented to describe the various mechanisms and magnitudes of loop parameters involved in causing loss of lock when a step change in loop bandwidth occurs. It provides certain conclusions and directions for future designs:

a. If the predominant cause of loss of lock is the switching transient, then the probability of loss of lock is independent of the narrowband loop bandwidth. Decreasing the narrowband bandwidth reduces the transient phase excursion, but at the same time decreases the lock-in range which is linearly proportional to the loop bandwidth.

b. The noise limiting filter with break frequency  $\omega_B$  should be reduced as much as possible without excessively decreasing the loop phase margin. In the present design, it was found that the ratio of  $\omega_n/\omega_B$  could have been increased to 0.3 from the existing 0.05 and the phase margin still would have been better than  $45^\circ$ . Consequently,  $\sigma_{r_2}$  would have been reduced by a factor of 2.4.

c. Switching the bandwidth,  $\omega_B$ , at the same time that the loop bandwidth is switched will enhance the burst receiver performance because of the reduced narrowband frequency jitter.

d. A variable time delay between initial acquisition and voltage-

controlled crystal oscillator clamping to allow complete pull-in will reduce the residual frequency offset. The variable delay could be activated only when loss of lock is detected subsequent to bandwidth switching.

### Experimental results

The following is a description of missed acquisition, missed UW, and BERS obtained during acceptance tests of the burst receiver.

#### Missed acquisition and missed UW rates

Measurements of the missed acquisition and missed UW rates were accomplished using the test setup shown in Figure 13. The HP8016A word generator, which can generate TTL level data sequences up to 256 bits, is used to simulate the preamble and data portions of DCP bursts. The preamble consists of 100 identical bits (0's) for carrier acquisition, 30 alternating bits for clock acquisition, and the 15-bit uw: 100010011010111.

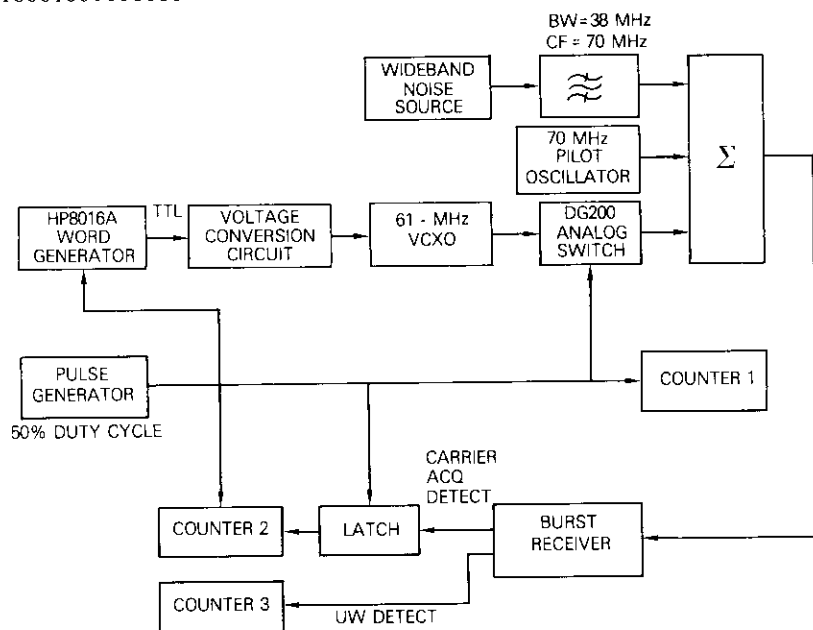


Figure 13. Test Configuration for Missed Carrier Acquisition Rate and Missed UW Rate

The FSK modulator is a voltage-controlled crystal oscillator with an input circuit designed to convert the TTL output of the word generator to a 1.5-kHz carrier deviation. Bursting is achieved by gating the DG200 analog switch by the pulse generator which also serves as a start pulse for the word generator. Counter 1 counts the number of bursts that have been generated.

On the receive side, separate counters calculate the number of carrier acquisition and uw pulses. The difference between the reading on counters 2 and 3 and that on counter 1 yields the miss rate. The latch circuit is incorporated such that after an acquisition pulse has been received, the counter cannot resume counting until it has been activated by the transmit gate pulse. This eliminates the possibility of multiple counts for one burst, which results from loss of lock at bandwidth switching and reacquisition.

Tests were conducted for  $E_b/N_o$  values from 10.5 to 14.5 dB. Higher signal-to-noise ratios require inordinately longer times to complete tests at the low burst rate of two bursts per second.

Missed acquisition and missed uw rates obtained during these acceptance tests are plotted in Figure 14. The acquisition sweep time in the receiver under test is approximately 70 bits. The wideband loop bandwidth to bit ratio is 5. A missed acquisition rate of  $10^{-3}$  was obtained at an  $E_b/N_o$  of 12.2 dB, which agrees closely with the theoretical result of Figure 9. It should be noted that the missed acquisition rate decreases by approximately an order of magnitude for each 1-dB increase in  $E_b/N_o$ .

The missed uw detection rate presented in Figure 14 is the rate measured during acceptance tests using the configuration shown in Figure 13. It is obvious that every missed carrier acquisition must cause a missed uw detection. Therefore, the true uw miss rate, *i.e.*, the number of uws not detected relative to the actual number of bursts acquired, is obtained by subtracting the measured missed carrier acquisition rate from the missed uw detection rate. This difference is also plotted in Figure 14. The true uw miss rate is much higher than that expected for the BERS shown in Figure 15. Presumably a large number of bursts have residual frequency offsets at the instant of clamping substantial enough to cause a much larger BER than that apparent in the measurements. These bursts with high BER do not show in the burst mode BER because no data are transferred to the CPU if no UW is detected.

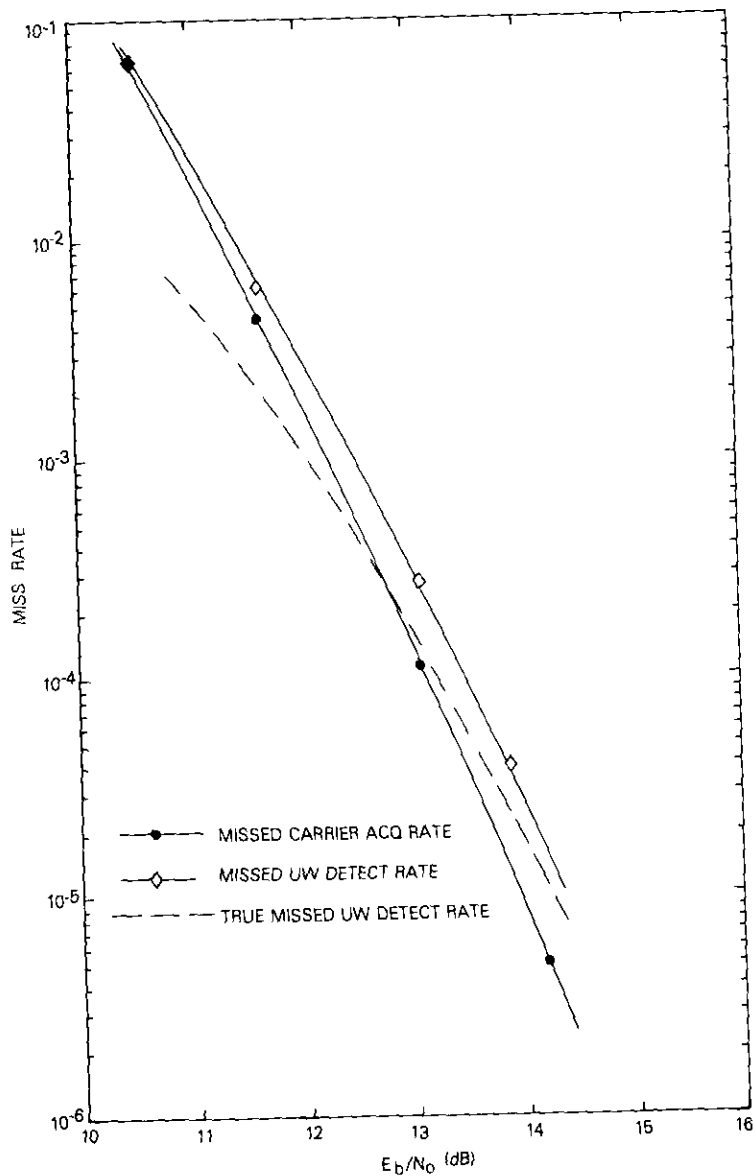


Figure 14. Burst Receiver Measured Missed Carrier Acquisition and Missed UW Detection Rates

### BER performance

A continuous FSK modulated carrier was generated and the control voltage of the burst receiver grounded to obtain continuous mode BER performance. Results are plotted in Figure 15. For the burst mode BER tests, the same data sequence modulated every burst and the printout of the receiver was scanned for errors to obtain the BER. Figure 15 shows that burst mode performance is between 0.5 and 1.0 dB worse than the continuous mode due to the frequency offsets resulting from bandwidth switching transients and narrowband noise. When this result is compared with those of the frequency offset tests of Figure 5, it appears that an average residual frequency offset of approximately 40 percent occurs in the burst mode.

### Conclusions

A burst mode receiver has been designed, built, and operated in a satellite data collection link. The receiver can rapidly acquire short-duration bursts whose frequency uncertainty is an order of magnitude larger than the signal bandwidth. Sources of performance degradation have been identified, and suggestions for significantly reducing the magnitude of these sources described. The receiver performed successfully in an operational system over a period of approximately six months.

### Acknowledgments

The authors would like to thank G. Forcina and S. Rhodes for many helpful discussions and S. Lebowitz for his frequent assistance in applying the CHAMP program to the simulation program which proved essential in the receiver design. V. Uzunoglu and G. House provided valuable suggestions for circuit designs.

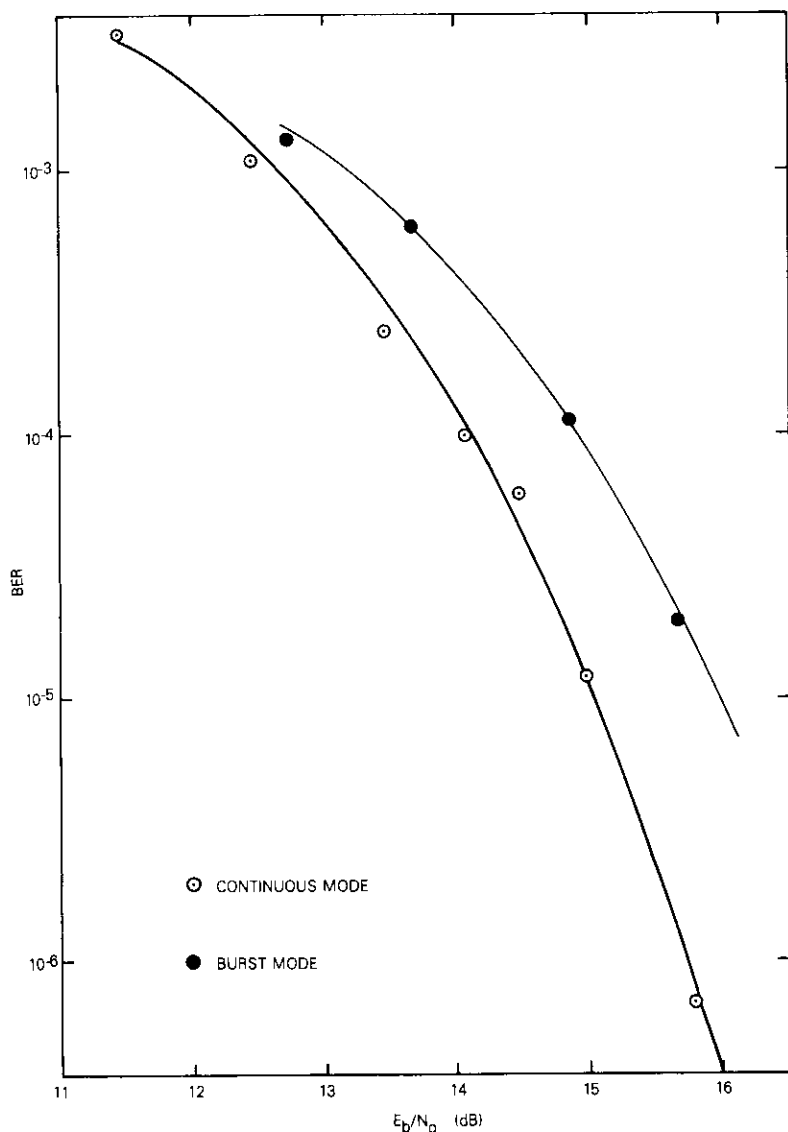
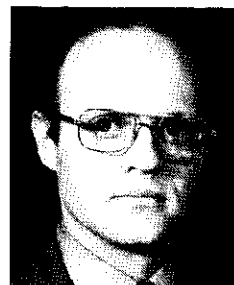
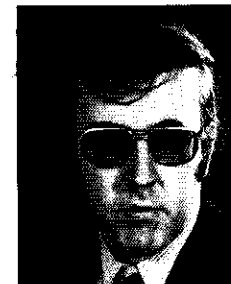


Figure 15. Burst Receiver BER

### References

- [1] G. P. Forcina, K. F. Manning, and K. J. Singh, "A Developmental Program of Satellite Data Collection," *COMSAT Technical Review*, Vol. 8, No. 2, Fall 1978, pp. 421-454.
- [2] K. H. Greene, "FSK Receiver for Data Bursts in Data Collection Systems," 4th International Conference on Digital Satellite Communications, 1978.
- [3] J. P. Frazier and J. Page, "Phase-Lock Loop Frequency Acquisition Study," *Transactions of the IRE*, SET-8, September 1962, pp. 210-227.
- [4] Floyd M. Gardner, *Phase Lock Techniques*, New York: John Wiley, 1966.
- [5] R. C. Weast and S. M. Selby, *Handbook of Tables for Mathematics*, Cleveland: The Chemical Rubber Co., 1967.

Kenneth H. Greene received a B.S. from Polytechnic Institute of Brooklyn in 1959 and an M.S. and Ph.D. from the University of Connecticut in 1964 and 1969, respectively. He joined COMSAT in 1969 as a member of the Systems Simulation Laboratory participating in the simulation of the INTELSAT IV satellite system and supervising simulation of the domestic satellite system. In 1972, he joined the Modulation Techniques Department, where he supervised the field trials and operation of the shipboard terminal for the MARAD Experiment. His principal activities have involved modem development for data collection systems. Dr. Greene is presently a Staff Scientist in the Optical Communications Laboratory.



Robert F. Hefe is a Technical Specialist in the Communications Processing Laboratory. Prior to joining COMSAT Laboratories in 1969, he served in the Navy where he was responsible for the success of an experimental shipboard passive satellite communications systems for which he was awarded the Navy Achievement Medal. He was involved in the design and development of the single channel per carrier system, the MARISAT system, the data collection receive terminals for the U.S. Geological Survey, and the seismic data transmission earth station terminals for SANDIA Laboratories. He has attended Montgomery College, Rockville, Maryland, and Newark College of Engineering, Newark, New Jersey.

## ***Small earth terminals at 12/14 GHz***

J. KAISER, L. VEENSTRA,  
E. ACKERMANN, AND F. SEIDEL

(Manuscript received July 11, 1979)

### ***Abstract***

Four earth terminals were designed for a wide variety of experiments with the Communications Technology Satellite (CTS), which is also called HERMES. These terminals have antenna diameters of 1.2, 2.0, 2.4, and 4.6 m. Unique designs for the transmitter and receiver, antenna feeds, filters, and power monitoring within the feed waveguide structure were adopted. The 1.2- and 2.0-m terminals were used in simulated and real disaster communications; the others were used for experiments involving high-speed facsimile, slow-scan video, computer-to-computer communications, and digital full color TV with 60 voice channels, and for an experiment in remote interpretation between a United Nations conference in Buenos Aires and the United Nations Headquarters in New York. In this experiment, a unique combination of two different multiplex systems allowed the transmission of broadcast quality video, high- and low-speed data, and seven 2-way voice circuits on a single carrier. Another experiment explored the feasibility of synchronizing two precision master clocks via satellite.

### ***Introduction***

COMSAT has participated in experiments with the CTS for over three years. The CTS (called HERMES in Canada), an experimental commu-

nications satellite jointly sponsored by the U.S. (NASA) and Canada (CRC) [1], [2], was placed in geostationary orbit at 116° W longitude in January 1976. It is a body-stabilized spacecraft with two transponders of 85-MHz bandwidth each. Figure 1 shows the frequency plan in the 14/12-GHz bands. Each transponder is connected to a separate antenna. The transponder with the lower frequencies, designated TB-2, is connected to a nominal 20-W TWT. The other, TB-1, is connected to a 200-W TWT; however, its signals also pass through the 20-W TWT about 20 dB below the level of signals that saturate TB-2. Both antennas and transponders are required for a 2-way link. The antennas have 38-dB gain on receive and 37-dB gain on transmit with a half-power beamwidth of 2.5°; they are steerable on command from the control center. In general, the antennas have been pointed directly toward the locations of the earth stations used in the specific experiments which were underway at any given time.

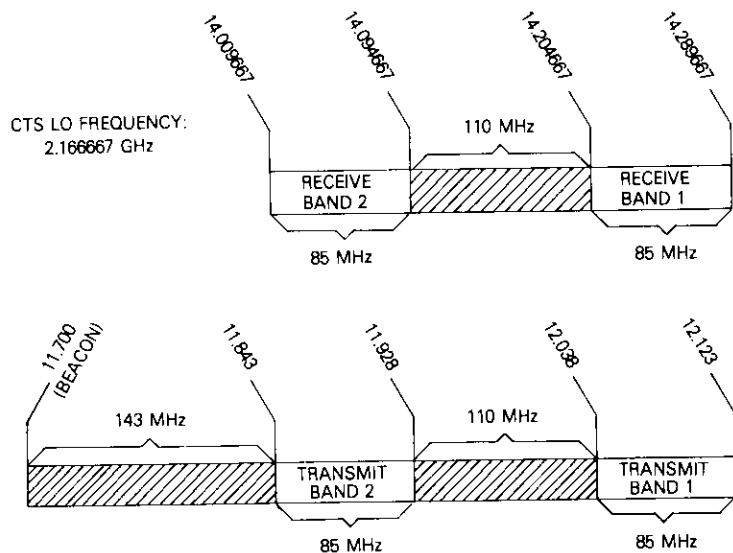


Figure 1. CTS Frequency Plan

It is possible, on ground command, to insert attenuators into the receive bands of the transponders. TB-1 can have 0- or 5-dB attenuation, and TB-2 can have 0- or 4-dB attenuation. These attenuators have

been used for some of the experiments to balance the up-link and down-link power budgets.

The front end of the CTS is a paramp with a system noise temperature of 1,280 K, resulting in an on-axis G/T of +6.4 dB/K. The nominal small signal gains through each transponder are 131 dB for TB-1 and 116 dB for TB-2, without the attenuators in the link. Figure 2 is a simplified block diagram of the CTS communications transponders.

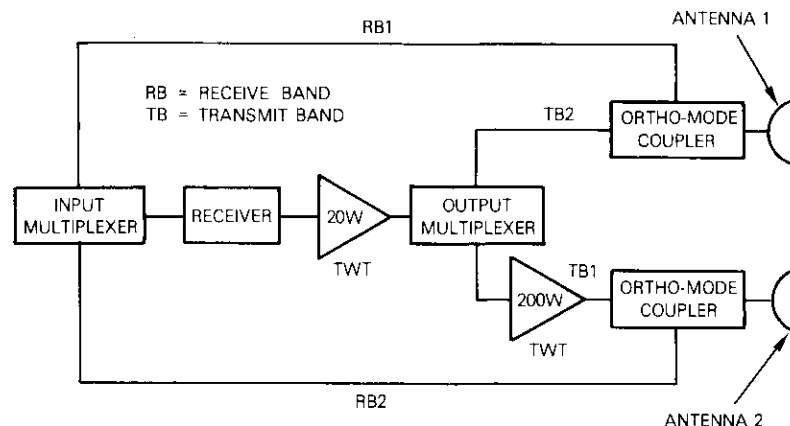


Figure 2. CTS 12/14-GHz Communications Transponder Schematic

Schedules for the access of U.S. experimenters to CTS were established six months in advance. Amended and updated schedules were published two weeks prior to spacecraft use by the experiment controllers at NASA Lewis Research Center in Cleveland, Ohio. Each experimenter was required to subscribe to a computer conference system (an electronic mailbox) known as PLANET, supplied by Infomedia Inc., for scheduling and other information regarding the spacecraft status. Generally, the U.S. had access to the spacecraft on alternate days. Each quarter this schedule changed from Monday, Wednesday, and Friday to Tuesday, Thursday, and Saturday, with Canada and the U.S. obtaining access on alternate Sundays. Exceptions were made when the spacecraft was required for certain important experiments. COMSAT's experiment had spacecraft preemption rights in case of a national emergency. These rights were exercised twice during the experiment.

The earth terminals constructed by COMSAT Laboratories and

described in detail in the following sections were licensed by the Federal Communications Commission (FCC) to be deployed virtually without restrictions anywhere within the continental U.S. A 2.0-m terminal was taken to Buenos Aires, Argentina, for a remote interpretation experiment via CTS between Buenos Aires and New York City.

COMSAT's experiment on CTS was entitled "Small, Highly Transportable Earth Terminals." Its purpose was to develop a number of small earth terminals and to work with disaster relief agencies, such as the American National Red Cross, to reestablish communications via satellite if a national disaster caused a loss of normal communications. During the experiment period from January 1976 to June 1979, several other uses for small earth terminals were found to be of interest; these will also be described.

The earth terminals developed for these experiments consisted of a tripod-mounted 1.2-m antenna terminal, a trailer-mounted 2.0-m terminal, two trailer-mounted 2.4-m terminals, and a fixed 4.6-m terminal which was mounted on the roof of COMSAT Laboratories in Clarksburg, Maryland. A small horn antenna with an aperture of 17 cm  $\times$  20 cm was constructed for a receive-only FM audio broadcast experiment.

### **1.2-m transportable earth terminal**

The design goals for this terminal were portability, simple field deployment, and flexibility, *i.e.*, the ability to use any part of the 85-MHz bandwidth of either CTS transponder and to accommodate any modulation and multiple-access scheme [*e.g.*, FDM/FM, PSK, and single channel per carrier (SCPC)/FM]. Implementation of the terminal to satisfy these goals resulted in oversized equipment for any specific mission (*e.g.*, to provide three full-duplex voice grade channels in a disaster relief application); however, this equipment later proved to be well suited for handling more sophisticated experiments in broadband digital TV transmissions.

#### **Antenna**

Figure 3 shows the 1.2-m transportable earth terminal. The antenna is a fiberglass parabola with an  $f/d$  ratio of 0.375 and a Cassegrain feed system using a corrugated horn. An orthomode transducer (OMT) separates the orthogonal linear polarizations of the transmit and receive signals with an isolation of 30 dB. Changes of polarization orientation resulting from changes in the geographical position of the earth terminal

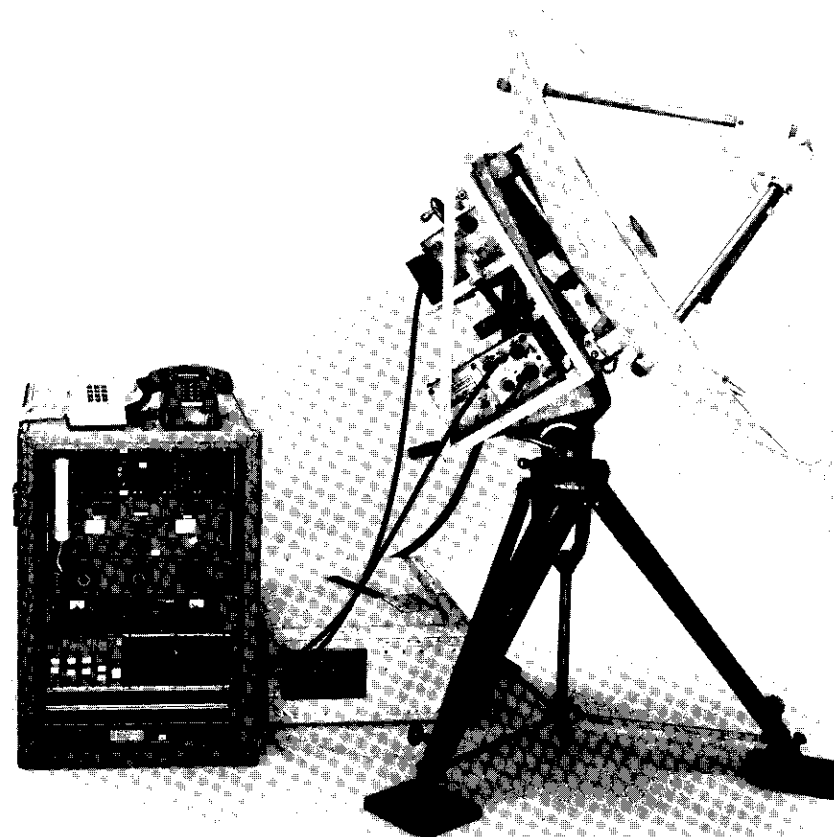


Figure 3. 1.2-m Transportable Earth Terminal

are accommodated by rotating the feed horn to the required angle. The antenna efficiency is 50 percent, yielding a gain of 40.5 dB at 12 GHz and 42 dB at 14 GHz.

The antenna is mechanically rugged and can be transported with the subreflector mounted or dismounted. The feed is easily removable from the back of the antenna. The feed horn is covered by a flat mylar window, and no pressurization is used. The antenna has been successfully shipped by truck, car, and aircraft, packed and unpacked, assembled and disassembled.

### Antenna mount

The antenna mount is a standard commercially available TV camera tripod modified with additional foot pads for stability. The azimuth bearing was found to have excessive mechanical play and was reworked to achieve stability. Azimuth pointing is accomplished by rotating the tripod head. Elevation has a coarse control via the tilt head of the tripod and a fine control built into the antenna backup structure. This structure also holds the traveling wave tube amplifier (TWTA) and low-noise receiver.

### Transmitter

The transmitter is based on a TWTA built by Varian, with a nominal power output of 20 W and a 59-dB small signal gain. The relatively high TWT gain allows it to be driven directly from a mixer without requiring a driver amplifier. The TWTA was integrated with a mixer and oscillator that convert the nominal 1.5-GHz second IF to 14 GHz. A waveguide bandpass filter prevents the image spectrum generated in the mixing process from entering the TWT; another waveguide bandpass filter with a passband of 14.0 to 14.3 GHz following the TWT serves as the transmit filter. The combined loss of the flexible waveguide and transmit filter is 0.3 dB.

The TWT, mixer, and local oscillator operating at 12.578167 GHz are contained in a waterproof housing. The TWT is mounted on a copper heat sink that is cooled by two weather-resistant fans mounted outside of the housing. A 6-m cable separates the TWT from its high-voltage power supply unit, which is enclosed in a weather-resistant container also used for shipping.

### Receiver paramp

A paramp development was initiated with LNR Corporation for the receiver. This paramp is a single-stage paramp-plus-transistor amplifier and mixer preamp operating at a nominal first IF of 1.5 GHz. The receiver has a noise temperature of 260 K at center band and exhibits a 63-dB overall gain from RF to IF. The paramp is contained in a waterproof housing complete with power supply, heater, mixer, and local oscillator operating at 10.4115 GHz. Power input to the receiver is 110 VAC at 300 W. The terminal system noise temperature is about 300 K yielding a G/T ratio of 15.5 dB/K.

### Up/down-converter

The antenna and its RF components are connected to an indoor unit via RG 214/U cables up to 30 m long. The indoor unit contains a COMSAT-designed and built up/down-converter that translates the frequency from 70 MHz to 1.5 GHz and vice versa, and provides gain at 70 MHz. It also has a beacon receiver that is used for initial spacecraft acquisition and antenna pointing. Figure 4 is a block diagram of the up/down-converter and Figure 5 is a photograph of the unit.

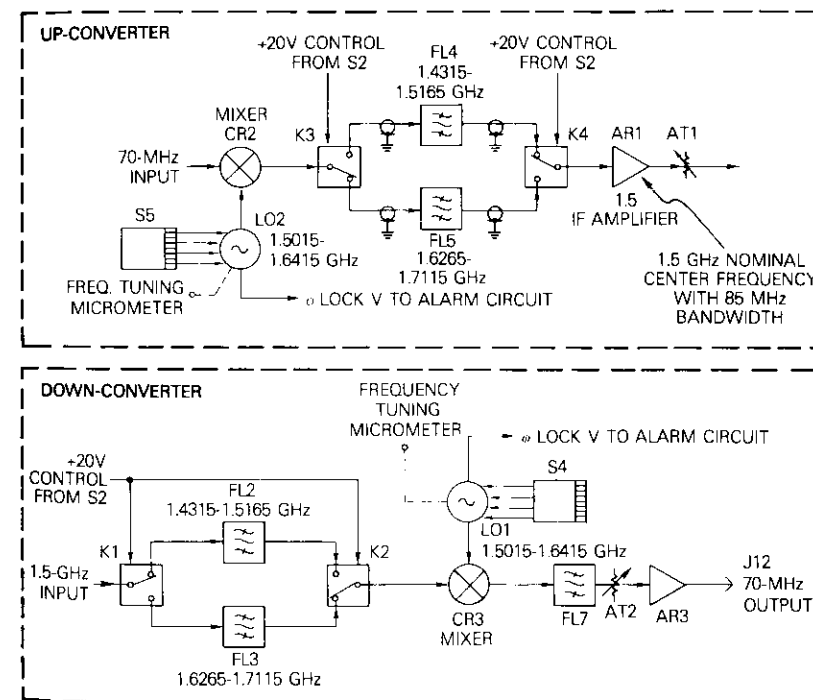


Figure 4. Up/Down-Converter Schematic

The receive signal chain feeds the input signal through one of two filters centered at 1.669 GHz for receiving band No. 1 and 1.474 GHz for receiving band No. 2. Each filter is 85 MHz wide, which corresponds to the transponder bandwidth of the cts. The received signal is then

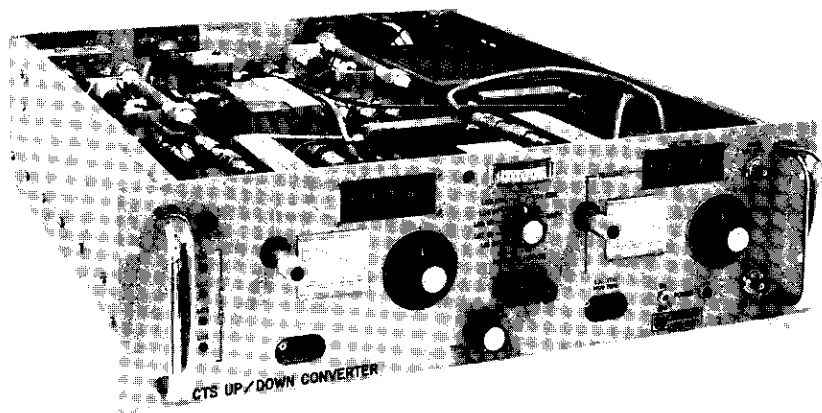


Figure 5. *Up/Down-Converter*

mixed with a local oscillator signal derived by a synthesizer-controlled tunable cavity oscillator to produce a nominal 70-MHz IF output. The beacon signal received at 11.7 GHz is translated to 1.2885 GHz by the first mixer at the receiver; it is then translated to 70 MHz in the down-converter, passed through a 30-kHz-wide crystal filter, and amplified to drive a meter on the front panel.

The spacecraft beacon signal, which is always available, is circularly polarized and is transmitted by an earth coverage antenna at an e.i.r.p. of 8 dBW. The beacon receiver can therefore be used to locate the spacecraft when the earth terminal is first set up in the field. At that time, there is usually no other communications signal available to assist in pointing the antenna. The beacon receiver has also proved to be an invaluable tool for verifying the performance of the receiving systems of all of the terminals.

The transmit chain mixes the first 70-MHz IF input from the baseband equipment up to a nominal 1.5 GHz. The signal is then passed through the appropriate 85-MHz-wide bandpass filter corresponding to transmit bands TB-1 and TB-2. The resulting nominal 1.5-GHz signal is then passed to the transmitter.

A front panel switch permits the selection of four transmit/receive combinations: T1/R1, T1/R2, T2/R2, and T2/R1. This arrangement enables the terminal to operate in either of the two transponders and also permits the transmitted signal, after being relayed by the satellite, to be received back at the transmitting terminal, if the two CTS antennas

are pointed such that they provide sufficient gain in the direction of the transmitting earth station.

The flexibility in selecting the transmit bands proved valuable during the experiments, since the two links are not symmetric. (TB-1 is always connected to the spacecraft 200-W TWT, and TB-2 is connected to the 20-W TWT.) The design of the up/down-converter allows frequency selection with 0.25-MHz steps within each transponder as well as the selection of the particular transponder to be used.

To conserve the range of frequencies required by the synthesizers for frequency selection within the 85-MHz bands, the upper sideband of the mixing process is used for transmitting in TB-1 (higher frequencies) and the lower sideband is used for transmitting in TB-2. Using the lower sideband for TB-2 presented no problems when the COMSAT terminals were operating with each other; however, the other experimenters in the CTS project always used the upper sideband, which required video and phase-shift-keyed signals to be reversed in sense. Table 1 summarizes the up/down-converter technical characteristics.

#### **Baseband equipment**

The baseband equipment consists of an FM modulator and baseband multiplex equipment on the transmit side, and a tunable FM receiver and baseband demultiplex equipment. In a standard configuration, the field terminal contains three multiplexed 2.4-kHz voice-grade channels. Two of these are connected to 4-wire Touch-Tone\* telephones; the third is used as an engineering order wire for the earth station operators. The Touch-Tone telephones permit the user in the field to access the public switched telephone network via CTS using specially designed equipment at the fixed earth terminal in Clarksburg, Maryland. Other equipment such as facsimile machines and high-speed 300-wpm teleprinter machines can be connected via standard acoustic couplers to the Touch-Tone telephones.

The 1.2-m emergency communications earth terminal, when set up in the field location, consists of three pieces:

- a. the antenna on its pedestal with the receiver and transmitter,
- b. the TWT power supply unit,
- c. the indoor unit containing the up/down-converter and the IF and baseband interface.

The indoor unit and the power supply boxes are also used as shipping containers for their respective subsystems. For transportation, the

\* Registered trademark of AT&T.

TABLE I. TECHNICAL DATA ON COMSAT'S UP/DOWN-CONVERTER

Physical	
Dimensions	52 cm (20.5 in.) long, 48.3 cm (19 in.) wide, 13 cm (5.25 in.) deep
Weight	27 kg (60 lb)
Power Required	115 VAC, 60 Hz, 300 W
Signal Input/Output Connectors	Type N
Up-Converter	
Input	70 MHz, $-5 \text{ dBm} \pm 5 \text{ dB}$
Gain from 70 MHz to 1.5 GHz	10 dB
Maximum Output Power at 1.5 GHz	10 dBm
Frequency	Selectable in 0.25-MHz steps; Output band TB-1, TB-2-switch selection
Local Oscillator Tuning	Synthesizer setting and local oscillator cavity tuning by micrometer
Stability	0.0005 percent, long-term
First Local Oscillator Frequency	1.5 GHz, nominal (synthesizer controlled)
Down-Converter	
Input	1.5 GHz, nominal
Input Dynamic Range	$-60 \text{ dBm}$ to $-30 \text{ dBm}$
Maximum Signal Input	$-30 \text{ dBm}$
Gain from 1.5 GHz to 70 MHz	32 dB
Maximum Output at 70 MHz	0 dBm
Beacon Signal Processor	
Local Oscillator Frequency	1.2185 GHz, fixed
Crystal Filter ( $F_c$ )	70 MHz, 3-dB bandwidth = 30 kHz

antenna reflector is disconnected from the backup structure by removing three pins, the backup structure is separated from the tripod, and the feed is removed from the reflector and packed into a separate box with the cables and miscellaneous equipment. The tripod is transportable without additional packing, whereas the antenna reflector can be packed into a box or protected by a cardboard cover. The backup structure containing the transmitter and receiver is packed in a special box.

Preparation of the small terminal for transmission after arrival on site requires less than one-half hour. The required 110 VAC is supplied either from mains available on site or from a generator with about 2-kW capacity.

### Design of the 2.4-m terminals

Satellite Business Systems (SBS) and COMSAT Laboratories cooperated in an experiment using CTS to demonstrate business communications via satellite directly to customer premises. For this experiment, COMSAT Laboratories designed two transportable earth terminals with 2.4-m antennas. Figure 6 is a photograph of one of the terminals. The design goals for these terminals were as follows:

- a. a self-contained road transportable terminal;
- b. operation in all types of weather and climate;
- c. the capability of transmitting and receiving via CTS full motion color TV with three audio channels or alternately using a 1.5-Mbit/s digital bit stream and three FM analog voice channels.

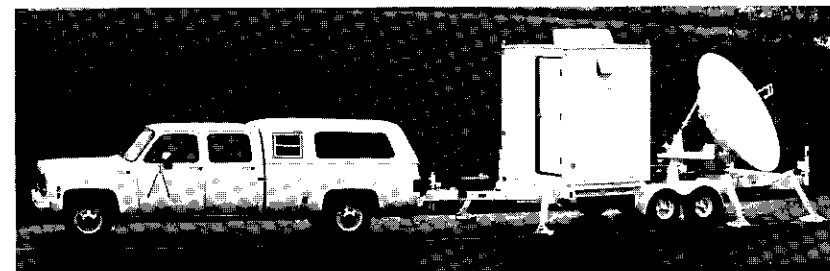


Figure 6. 2.4-m Transportable Terminal

#### Antenna

A 2.4-m fiberglass antenna was a special design by Prodelin that required an exact diameter of 2.4 m (8 ft) to keep the system within the allowable width for road travel. The antenna is on an elevation over azimuth mount and is stowed in a horizontal position during travel. It is provided with a front feed designed by COMSAT. Table 2 summarizes the technical data on the antenna.

#### Feed system

The feed system designed by COMSAT is a dual linearly polarized front feed with a matched radome over the waveguide and concentric ring feed horn. Both the transmit and receive bandpass filters and a calibrated power pickoff for transmit power monitoring are built into the waveguide structure. Figure 7 gives the design details. The feed is

TABLE 2. 2.4-M ANTENNA TECHNICAL DATA

Antenna	
Reflector	2.4 m
Feed	Prime focus
Gain	
Transmit	48.5 dB
Receive	47.2 dB
Beamwidth (3 dB)	
Transmit	0.6°
Receive	0.7°
First Sidelobes	1.2°
Voltage Standing Wave Ratio	
Transmit	1.33:1
Receive	1.22:1
Mount	
Azimuth Limits	±75° reference trailer axis
Elevation Limits	5° to 75°
Speed of Movement Under Power Drive	0.06°/s

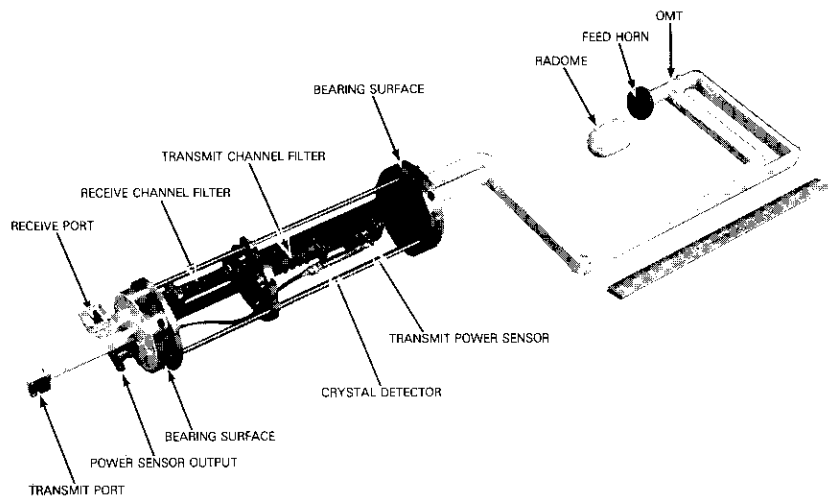


Figure 7. RF Feed for 2.4-m Terminal Antenna

mounted in a tube at the center of the antenna which permits rotation for polarization alignment. It is secured to a tray in the back of the

reflector. This tray holds the TWT transmitter and the FET low-noise receiver and rotates with the feed as one unit. This permits the transmitter and receiver to be mounted without a flexible waveguide. The feed system is kept dry by periodic purging with dry air obtained via a hand pump and desiccant combination.

**Receiver**

The 12-GHz receiver designed and integrated by COMSAT consists of a low-noise FET amplifier (Amplifica Corp) followed by a mixer and IF preamplifier (RHG Corp). Figure 8 is a block schematic. The

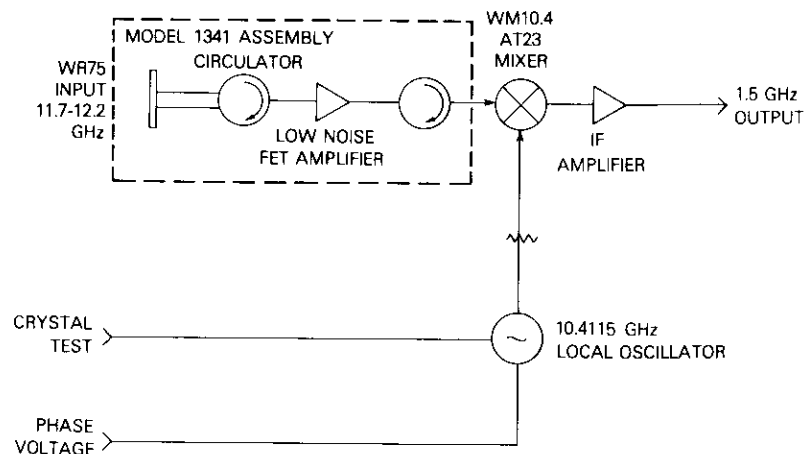


Figure 8. Receiver Schematic

waterproof housing contains the first local oscillator (Frequency West Co.). The FET, mixer, and IF preamplifier are constructed as one unit with waveguide input and intermediate connectors all matched carefully to the FET and mixer characteristics. The resulting noise temperature for the entire receiving system is 340 K at the center of the 11.7- to 12.2-GHz frequency band ±10 K at the band edges. The figure of merit, G/T, of the terminal is 21.2 dB/K at antenna elevation angles greater than 20°. Table 3 summarizes the receiver characteristics, and Figure 9 shows a top view.

TABLE 3. RECEIVER CHARACTERISTICS

Dimensions	20 cm (8 in.) long, 15 cm (6 in.) wide, 13 cm (5 in.) deep
Weight	1.4 kg (3 lb)
Power Required	20 VDC, 1.25 A
Signal Input Connector (12 GHz)	WR75 waveguide flange
Signal Output Connector (1.5 GHz)	Type N
Input Frequency	11.7 to 12.2 GHz
Instantaneous Bandwidth	500 MHz
System Noise Temperature	340 K
Gain	>54 dB
Local Oscillator Frequency	10.411500 GHz, fixed
Local Oscillator Stability	$\pm 5$ parts in $10^8/24$ hr, 5 parts in $10^7/30$ days
Output Frequency	1.50 GHz $\pm$ 150 MHz

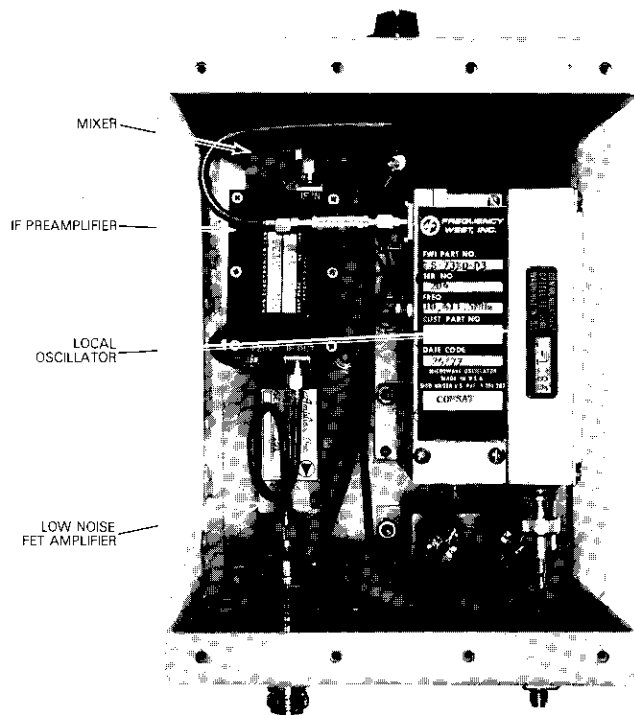


Figure 9. Receiver (top view)

**Transmitter**

The transmitter is a 20-W TWTA based on a Varian TWT. The TWT, mixer, and local oscillator are built into a waterproof housing with conduction cooling via a finned heat sink and external cooling fan. Figure 10 shows a block schematic of the transmitter and Figure 11 is a photograph of the unit. The compact design of this unit made it possible to mount it directly behind the antenna on a tray in a fixed

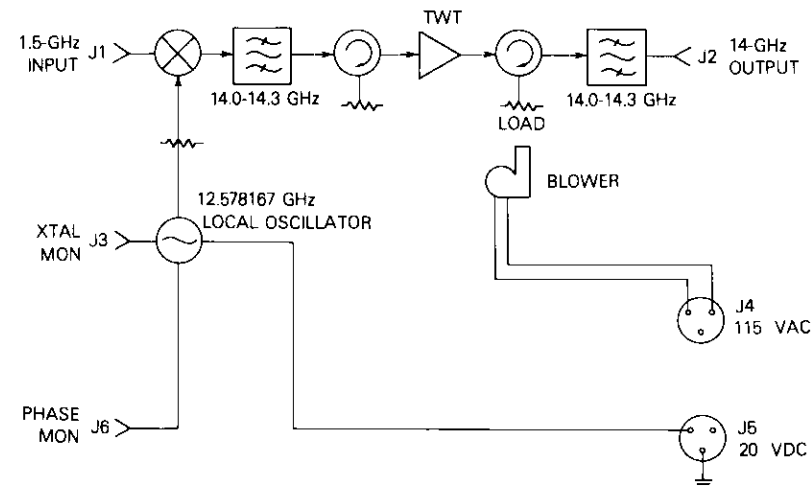


Figure 10. Transmitter Schematic

position relative to the feed. This mounting allows the rotation of the feed, receiver, and transmitter as one unit for polarization adjustment.

The high-voltage power supply unit for the TWT is contained in the electronics shelter. A 7-m high-voltage cable runs through the hub of the antenna mount and under the trailer in a plastic pipe to connect the power supply with the TWT. The separation of the power supply and TWT has proved reliable and avoided long waveguide connections between the TWT and the feed system.

The TWT (Varian, Type VTU 6191-HB) has a nominal saturated power output of 20 W and a small signal gain of 59 dB at 14.25 GHz. This high gain makes it possible to drive the tube to saturation from the mixer output of the up/down-converter without a driver amplifier, thus simplifying the transmitter chain. A built-in circulator and load at

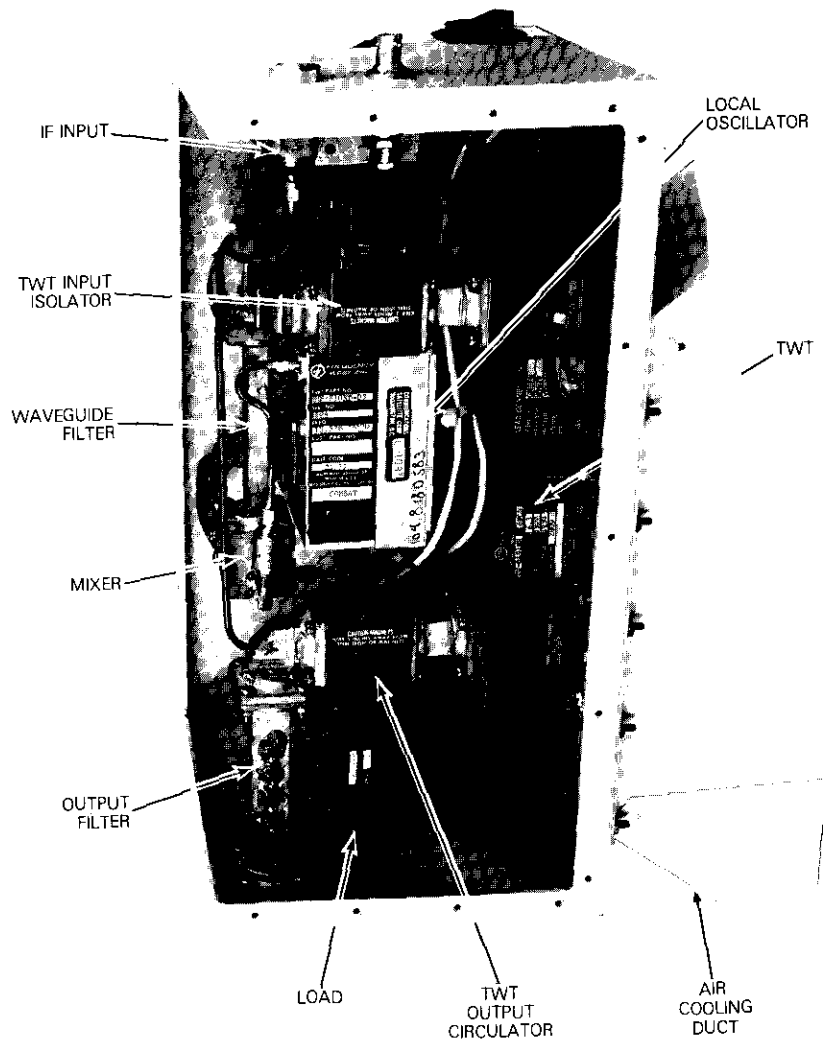


Figure 11. *Transmitter*

the output of the TWT protects it against accidental shorts or a power mismatch at the feed. Thermal overload protection is also a part of the control logic for the TWT.

### Trailer

The trailer, a flat bed platform with a tandem axle, weighs 4,100 kg (9,000 lb) fully loaded and can be towed easily at highway speeds with a light-duty truck or other towing vehicle. It has self-contained stabilizers that can be operated by two persons. The trailer forms a very stable base for the antenna with deflections less than  $0.05^\circ$  from any cause while operating. The antenna mount is secured to the trailer and consists of an azimuth-elevation mount with the azimuth axis supported by a large flat ball bearing and the elevation axis using ball bearing pillow block supports. Azimuth and elevation angles are controlled from the electronics shelter, and 12 VDC is used to drive a screw jack mechanism.

Elevation angles can be set from  $5^\circ$  to  $75^\circ$  by a coarse/fine arrangement, with the fine drive covering  $15^\circ$ . The coarse settings are made by inserting various lengths of push rods. The azimuth axis also has a coarse/fine drive arrangement with the coarse setting obtained by mounting the push rod assembly at different locations on the azimuth bearing ring. Azimuth has a range of  $\pm 75^\circ$  from the rear direction of the trailer with about  $15^\circ$  fine-drive movement. Fine-drive speed is  $0.06^\circ/\text{s}$ . The wide azimuth range makes it easy to deploy the trailer in virtually any situation.

The trailer also contains the electronics shelter and a 5-kVA (Onan) gasoline-driven generator and the battery that drives the antenna axes and the associated control relays. The antenna is stowed facing the zenith during road travel after the feed system and receiver/transmitter tray have been removed. These are carried in separate, specially designed, wooden transport boxes that can either be placed in the shelter or in the towing vehicle. The trailer is shown in Figure 6. Its specifications are given in Table 4.

### Electrical system

The electrical power system for the terminal operates either from 115-V or 220-V power mains, or from the trailer contained generator. The antenna drives are powered by a 12-V battery that is charged from the 115-V supply. Figure 12 is a schematic of the electrical system.

### Shelter

The electronics shelter is climate controlled with an air conditioner and heater. It contains two racks for the baseband and IF equipment

TABLE 4. TRAILER SPECIFICATIONS

Length	8.2 m (27 ft)
Width	2.44 m (8 ft)
Height	3.66 m (12 ft)
Weight	4,100 kg (9,000 lb)
Brakes	Electric, activated from tow vehicle with battery operated safety brake system on trailer.
Components	Antenna, AC generator, and electronics shelter; all components are weather resistant.
Generator	Onan AC with 5-kW capacity; two 110-V windings that can be combined to yield 220 V; nominally 60 Hz; running time between refills is 8 hr under normal load, using gas tank internal to generator; self-contained electric battery starter.
Electronics Shelter	Designed for towing speeds up to 55 mph; contains electric heater and air conditioner and fan ventilator; houses the IF and baseband equipment and test equipment; shelter door equipped for padlock securing.
Towing Vehicle	Chevrolet pickup truck with 4 doors and camper body; special rear axle for heavy load pulling; automatic transmission, air conditioning, two gas tanks; electric proportional break system for the trailer; special trailer hitch for heavy loads; weight, 2,700 kg (6,000 lb).

and a small desk for the operator (see Figure 13). Cables to the antenna are permanently routed through a 10-cm (4-in.) diameter pipe under the trailer between the shelter and the center of the antenna hub. In addition to the signal cables at 1.5 GHz, there are provisions for monitoring the transmitted power and the frequencies of the local oscillator in the transmitter and receiver, respectively. The up/down-converter for these terminals is similar to that for the 1.2-m terminal.

**IF configurator**

For business communications experiments, it was required to transmit and receive full motion color video with three audio channels, or alternatively a digital bit stream with data rates up to 1.5 Mbit/s and three audio channels. It was also required to switch from one configuration to the other in about 30 s. To satisfy these requirements, an IF configurator was designed that uses the subcarrier modulators from

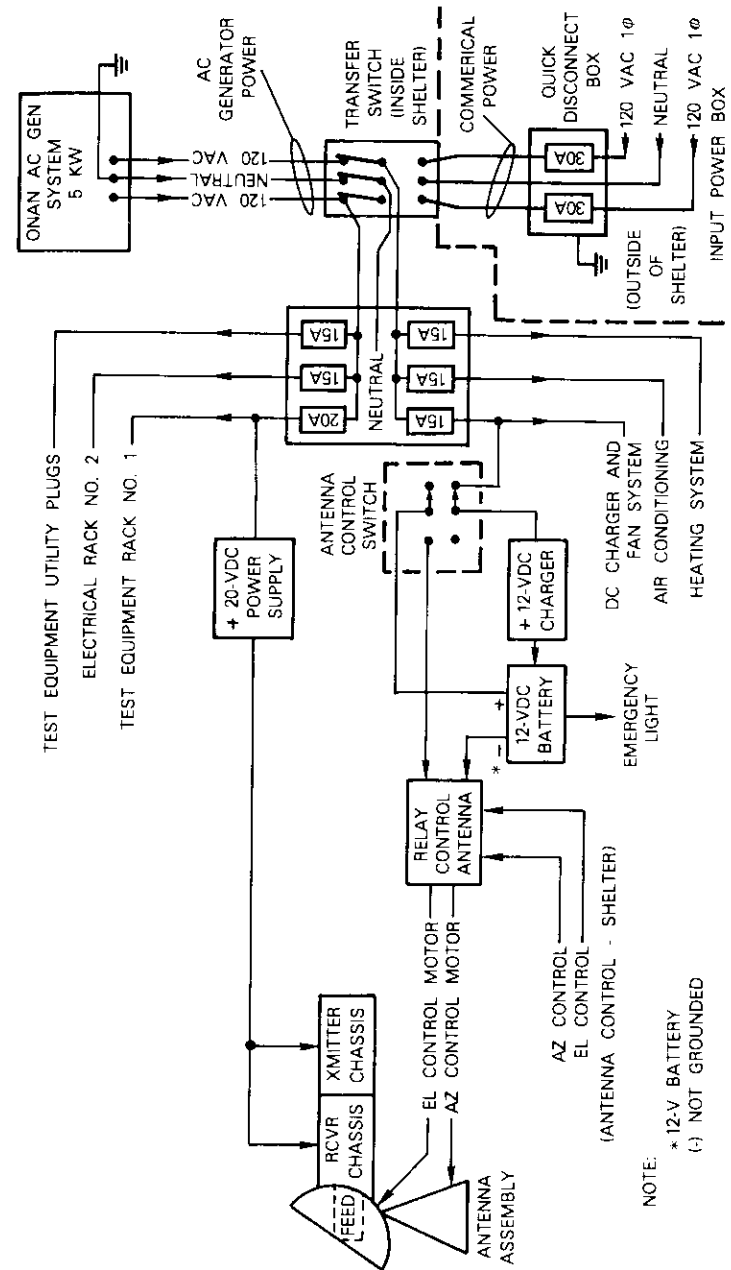


Figure 12. Trailer, Electrical Schematic

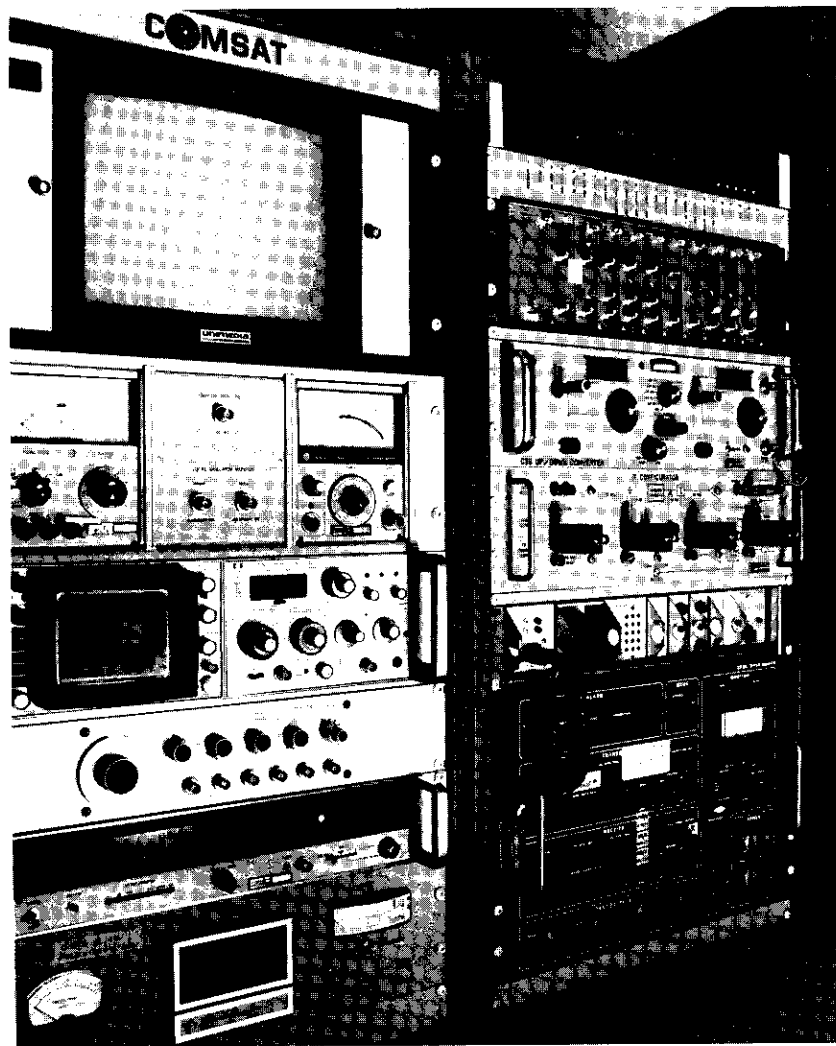


Figure 13. *Electronics Shelter, Interior*

the Farion video system as SCPC/FM signals for the voice channels and substitutes the digital signal from a PSK modem for the video carrier. The changeover between the two modes is accomplished by changing four plugs in the front panel of the IF configurator. There are

also provisions for monitoring the received and transmitted signals. Figure 14 is a block schematic of the IF configurator. A front panel view showing the patching for the data carrier and single-channel voice carrier is shown in Figure 15. The IF spectra for each of the transmission modes are shown in the schematic in Figure 16.

#### **Modem**

The modem used with this terminal for the digital transmissions is a variable rate modem (MD-1002A, Harris Corp.) with data rates selectable between 10 kbit/s and 10 Mbit/s. The data input and output for the modem are obtained from the peripheral equipment via balanced twin-axial cables of up to 300 m (1,000 ft) in length. A master control unit for switching between the analog and digital modes of transmission and containing cable driver amplifiers and video signal conditioners is located at the far end of the cables. The master control unit contains signal conditioners for the digital signals generated by the peripheral equipment to make these signals compatible with the modem input requirements.

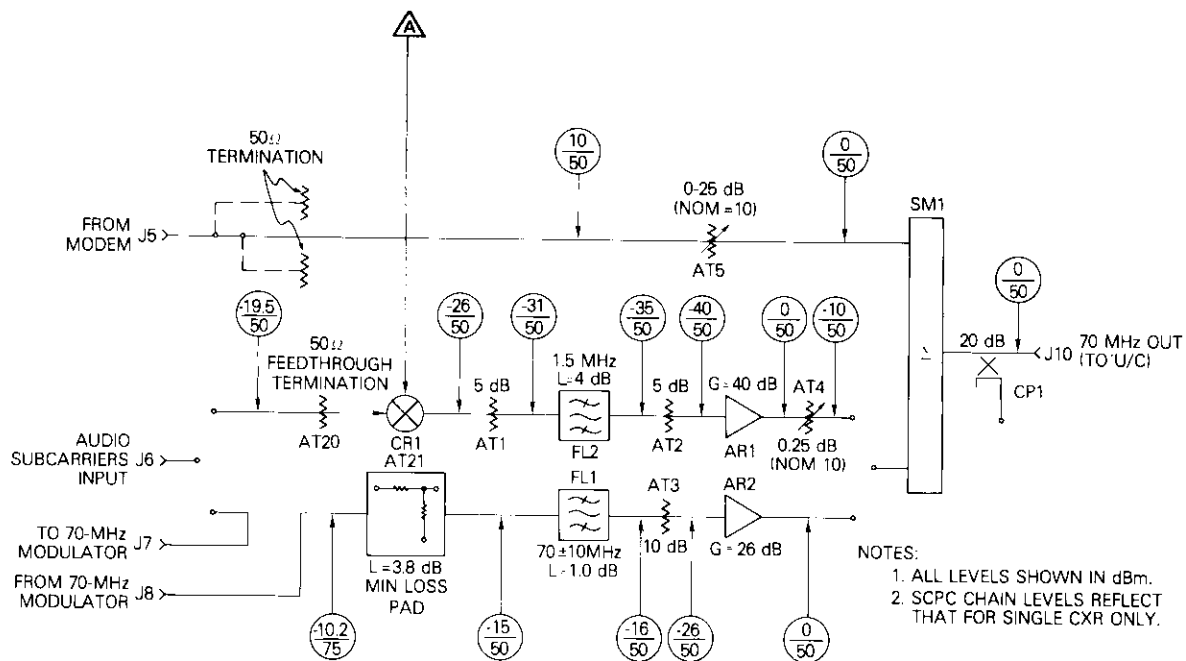
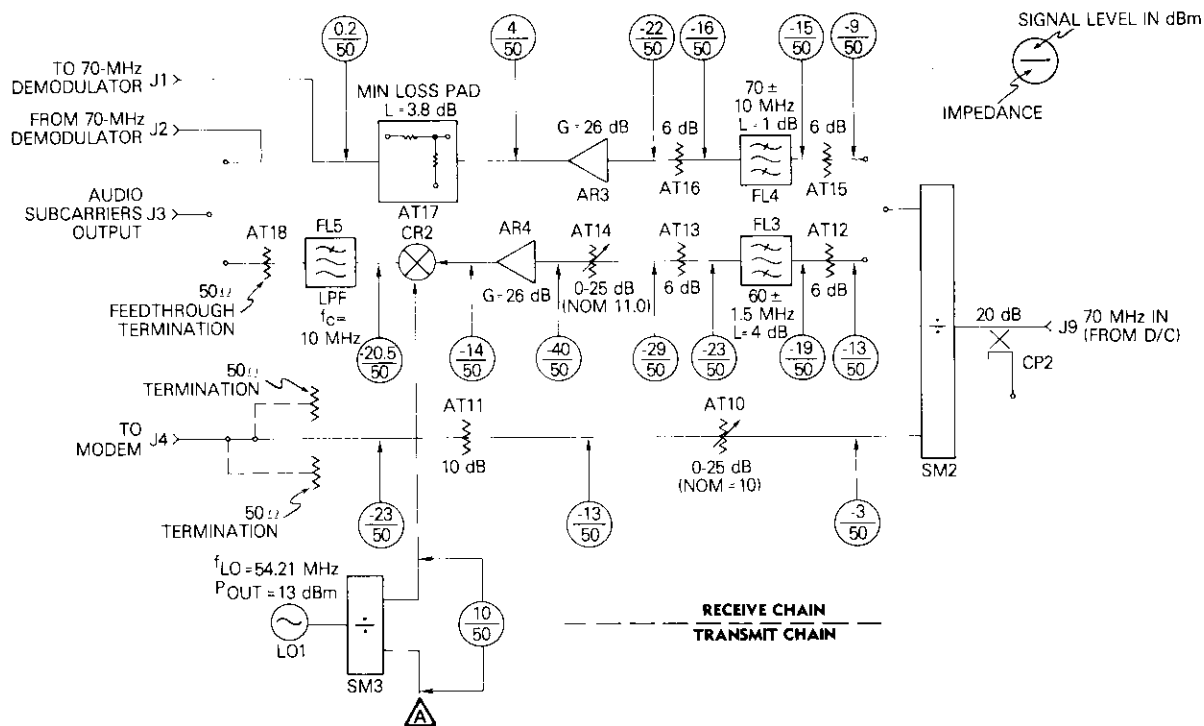
#### **Design of the 4.6-m terminal**

##### **Terminal RF/IF equipment**

In addition to the transportable terminals, a fixed terminal was designed for operation at COMSAT Laboratories (see Figure 17). This terminal uses a fiberglass antenna consisting of a central hub and six petals. It is a Cassegrain configuration with a corrugated feed horn designed by COMSAT Laboratories.

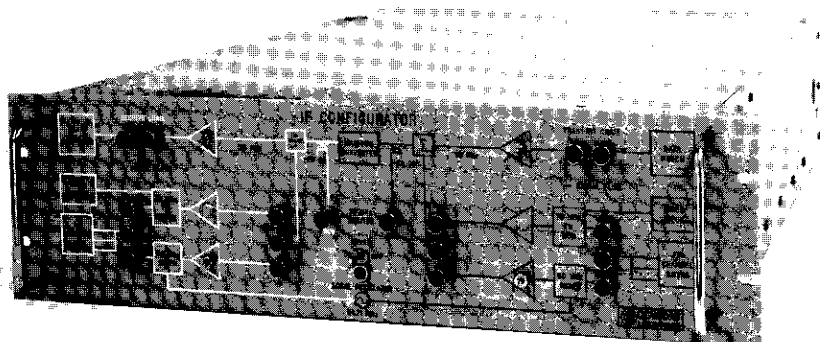
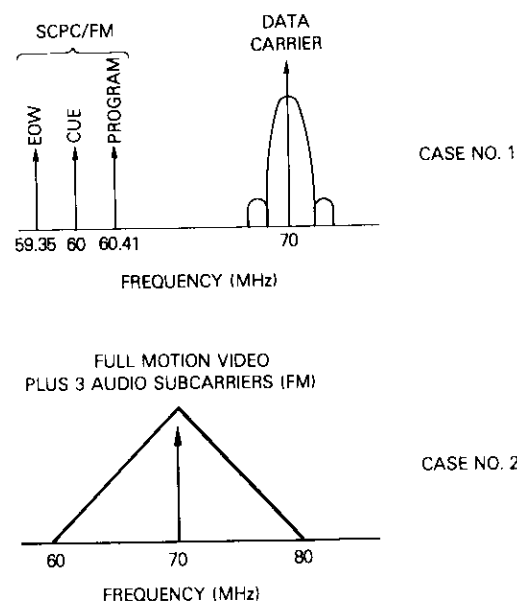
The antenna gain is 53 dB at 12 GHz and 54 dB at 14 GHz. The waveguide and filter losses between the TWT and the feed horn flange total 0.4 dB. The RF equipment consists of a TWT transmitter based on a Varian TWTA (type VZU-6993D1) integrated with a local oscillator, filters, a mixer, and isolators; the transmitter has a saturated output of 200 W. The receiver is similar to that described for the 2.4-m terminals. The up/down-converter is located in the Laboratories building and is connected to the antenna unit by two 50-m long low-loss "Spiroflex" cables.

The 200-W TWT transmitter (Figure 18) is mounted integrally with the antenna reflector. Its schematic is similar to that of the 20-W units shown in Figure 10. The 200-W unit has a convection cooling system and is protected from the elements by a rain-resistant cover.

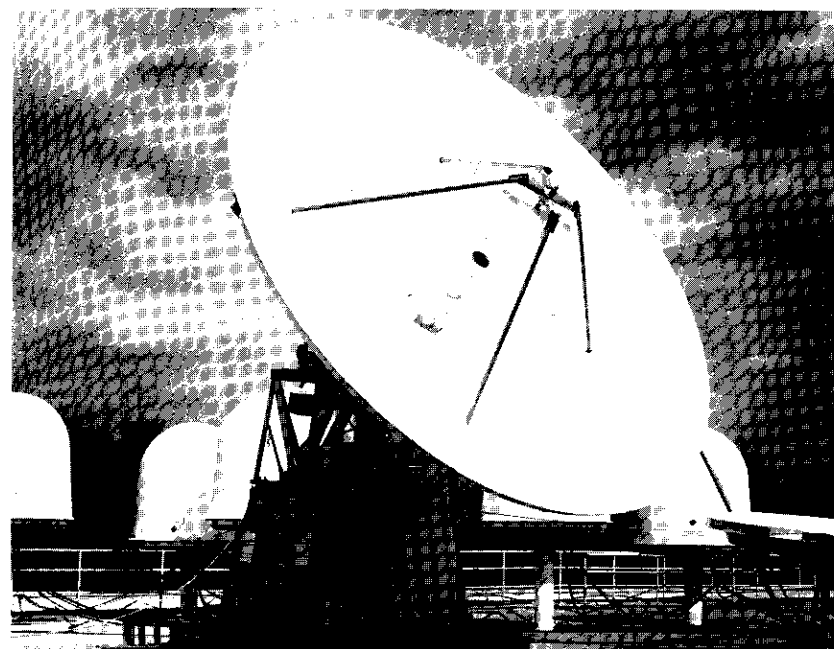


- NOTES:  
 1. ALL LEVELS SHOWN IN dBm.  
 2. SCPC CHAIN LEVELS REFLECT THAT FOR SINGLE CXR ONLY.

Figure 14. IF Configurator Schematic

Figure 15. *IF Configurator (front view)*Figure 16. *IF Spectra for Two Transmission Modes*

The TWT power supply unit is mounted in the enclosure under the antenna pedestal, with automatic cooling providing ambient air in the

Figure 17. *4.6-m Fixed Earth Terminal*

summer and heating in the winter. The feed system is pressurized with dry air obtained from a motor-driven air drier located inside the Laboratories building.

The elevation over azimuth mount is pointed using screw jack actuators controlled remotely from the operating position. A minicomputer pointing system has been implemented for open-loop command pointing of the antenna. The baseband equipment for the fixed earth terminal consists of FM video and SCPC audio equipment, and various voice and data multiplex equipment. The 70-MHz interface allows a variety of baseband equipment to be used as required for the experiments.

For the emergency communications experiments, echo control equipment was designed and an interface was provided with the public switched-telephone network; this interface permits a field telephone at the transportable terminal to dial any number from the remote location.

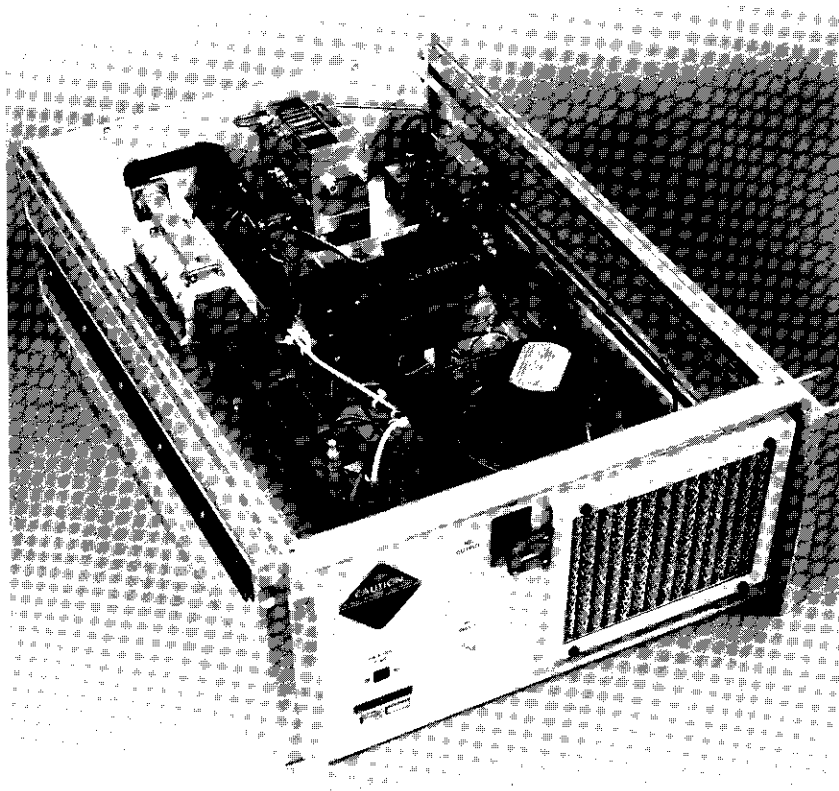


Figure 18. 200-W TWT Transmitter (top view)

#### Interfacing with the public switched telephone network

The primary purpose of the COMSAT experiment with the CTS spacecraft was to demonstrate the usefulness of emergency communications via satellite. Therefore, it was necessary to interface the emergency terminal in the field with the public switched telephone network. This interface was installed in the fixed earth terminal, which was always used as one end of the emergency communications link. The field terminal has two 4-wire telephone instruments that have been found sufficient for most emergency applications. The field terminal is not connected to any other existing telephone system since such facilities are not available in the disaster area. However, the usefulness

of the emergency communications link is directly related to the ability to contact a variety of relief agencies rapidly and reliably from the field location. The interface is compatible with any dial access lines (e.g., DDD, Centrex, FTS, Autovon, WATS, and TWX) that might be available to the fixed terminal.

The telephone interface provides 2-wire to 4-wire conversion and level control, as well as signaling and supervision via the satellite circuit. It also provides echo control at the fixed earth terminal, which is not required at the field terminal, since it operates entirely in a 4-wire mode. At the field terminal, the telephones supplied to the user appear identical to standard 2500 type Touch-Tone instruments. However, they are 4-wire units modified to use multifrequency (Touch-Tone) dials and an internal battery supply. Inside these instruments, the transmit and receive lines are appropriately attenuated and bandpass filtered so that they can be directly connected to the transmission facility at a 0-dBm point.

Figure 19 shows the telephone system interface schematic at the fixed 4.6-m terminal. Incoming calls from the public network intended for the field terminal are answered manually at the fixed terminal location, and then announced to the field terminal operators via the order wire circuit. The connection is then made manually between the 2-wire incoming call and the interface system via a network protective device (CBT 1001A data coupler) to isolate the satellite system from the switched network. The 2-wire to 4-wire conversion is made using a standard hybrid network. Provisions are included to balance this hybrid for optimum isolation between the receive and transmit ports. It was found that the best results were obtained in balancing the network when a source of flat noise band limited to 300–3,000 Hz was used instead of a test tone. Inside the interface noise, test tone levels were set at the standard +7-, -16-dBm levels for transmit and receive, respectively, to allow the use of a standard single channel COMSAT digital echo canceller [3].

During operation, the user at the field site can control the telephone line with Touch-Tone signals. The dual-tone multifrequency (DTMF) decoder recognizes the "\*" signal from the user and grounds the on-off hook control (OH) and the "request data transmission path cut-through" (DA) leads of the coupler. The field user out-pulses the actual called number with touch tones, and at the conclusion of a call, releases the line by using the "#" key.

This system has performed well during the simulated and real disaster

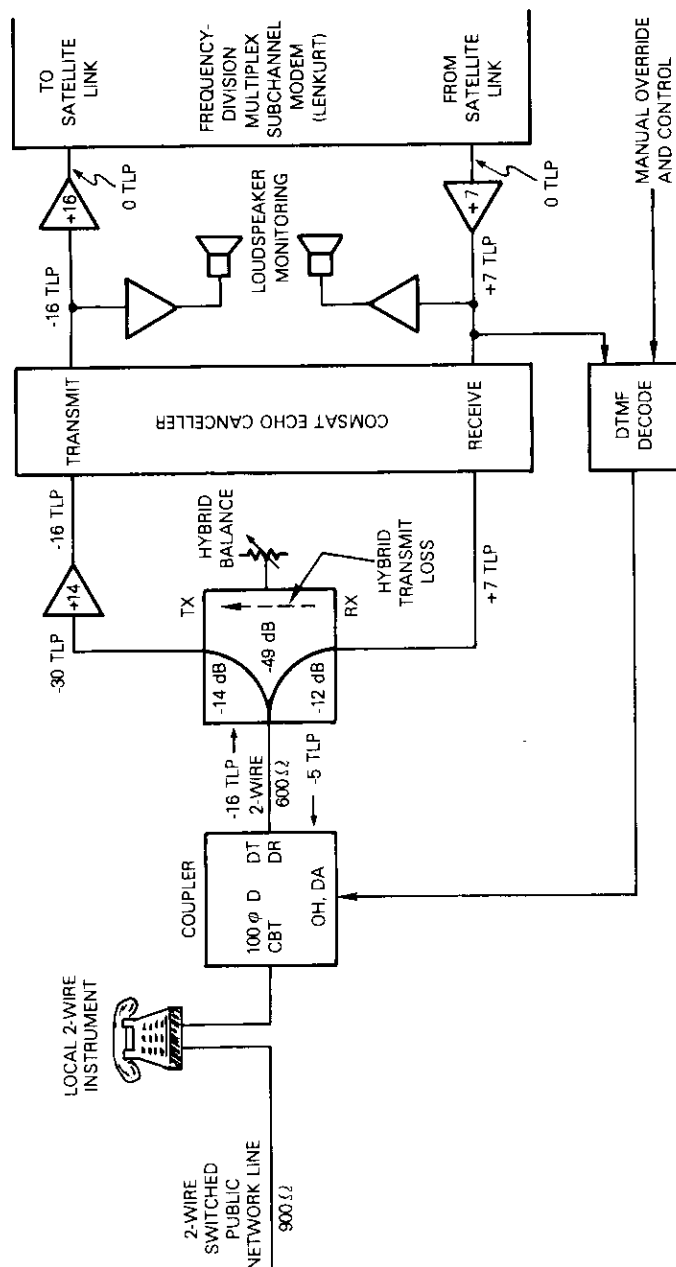


Figure 19. Telephone Interface Schematic

communications situations involving the use of the 1.2-m terminal in the field with a satellite link established via CTS to the 4.6-m terminal at COMSAT Laboratories.

### Descriptions of the experiments

#### Experiments using the 1.2-m terminal

For experiments using the 1.2-m terminal in the field, a communications link was established with the 4.6-m terminal at COMSAT Laboratories.

#### FOREST FIRE EXERCISE

A test of the use of satellites for emergency communications simulating a forest fire was conducted at the George Washington National Forest in Virginia in June 1976. Participants in this experiment were the National Red Cross and the U.S. Forest Service. The small terminal and 5-kW AC generator were transported in a van to a field accessible only by a gravel road, and prepared for transmission about 1 hr after arrival at the site. Communications included telephone, facsimile, and 300-wpm teletype. Three 2-way voice channels were established via CTS to the fixed terminal at Clarksburg, and thence to the American Red Cross Headquarters in Washington, D.C., via the telephone network. Calls were also placed to the U.S. Forest Service Headquarters in California. For this test, the RF power to the antennas at each terminal was about 10 W. The link budgets for the transmission are presented in Table A-1 of the appendix. The experiment proved that a small transportable earth terminal can be deployed in an unprepared site to furnish emergency communications.

#### FLOOD WATCH

In a similar exercise in Cincinnati, Ohio, the small terminal was transported in a U-Haul trailer towed by a station wagon. The exercise was conducted with the American National Red Cross to simulate a flood disaster along the Ohio River. Emergency messages were channeled to the terminal location in Cincinnati via local radio links and telephones, sent to the 4.6-m fixed station in Clarksburg via CTS, and then into the telephone network to the Red Cross Disaster Coordination Center in Alexandria, Virginia, and other points. The information exchanged included status reports and requests for aid. The use of teletypewriters was emphasized since hard copy for files and records could be produced.

## EARTHQUAKE EXERCISE

Another exercise was conducted at San Francisco using the 1.2-m terminal, which was transported to the city by commercial aircraft and to the downtown area by truck for a simulated earthquake emergency. Three voice channels were established via CTS to the 4.6-m terminal in Clarksburg, and telephone communications were made to the Red Cross Headquarters in Washington, D.C.

## HURRICANE WATCH

A fourth exercise was held for a hurricane watch in Houston and Corpus Christi, Texas. A 2.4-m terminal and the 1.2-m terminal were carried to Texas in a Red Cross van with a small boat trailer as the base for the 2.4-m terminal. Houston and Corpus Christi were linked with Austin, Texas, by first accessing the 4.6-m terminal in Maryland via CTS and then by telephone to Austin, the coordinating disaster headquarters location.

## JOHNSTOWN FLOOD DISASTER

While the exercise was being conducted in Texas, a real flood emergency occurred in Johnstown, Pennsylvania. The 1.2-m terminal was transported to Pittsburgh by commercial airplane, then taken to Johnstown by van and installed at the disaster site. Two voice-grade circuits were established for communications with the Red Cross Headquarters via CTS and the 4.6-m terminal at COMSAT Laboratories. Figure 20 shows the 1.2-m terminal on site at Johnstown. At one time, the satellite link was the only means of communications to and from the flood-stricken area. Messages included casualty reports, requests for equipment and personnel, and sketches of major damage areas transmitted by facsimile. For this real emergency, the CTS was preempted from use by other experimenters and was used exclusively for emergency communications for about two days.

During this emergency, a rainstorm occurred, which degraded the transmitted signal from Johnstown. (The signal was in transponder No. 2, the 20-W TWT.) This problem was overcome by switching the transmission into transponder No. 1 at a different frequency offset from that used for the transmission from Clarksburg, thus utilizing the higher power of the 200-W TWT. Both spacecraft antennas were pointed toward Clarksburg, making it possible for both terminals to transmit in the same transponder. Since Johnstown and Clarksburg are sufficiently close together, both are well within the beam of the spacecraft

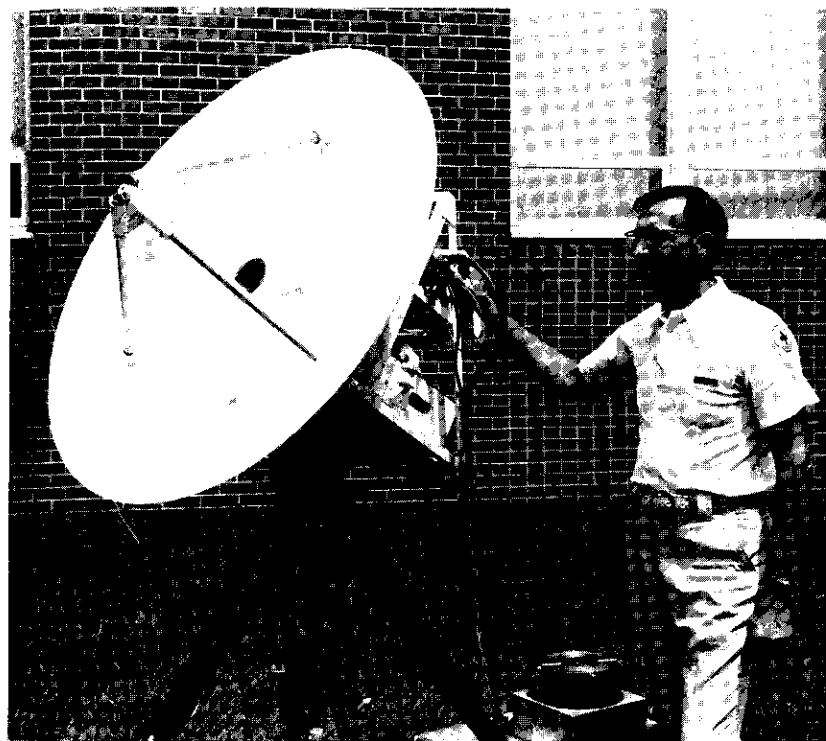


Figure 20. 1.2-m Terminal at Flood Disaster Site

antennas. The 3-dB contour of the CTS antenna footprints covers the eastern third of the U.S. as shown in Figure A-1 in the appendix. The emergency communications were terminated in about two days when normal telephone communications were restored.

## TORNADO DISASTER

The 1.2-m terminal was deployed for a tornado emergency at Wichita Falls, Texas, in May 1979. However, normal communications were restored rapidly and the continued need for CTS emergency communications was eliminated.

**Experiments using the 2.0-m terminal**

## YELLOWSTONE TV

The 2.0-m terminal was used for a number of special transmissions.

Color TV programs were transmitted from Yellowstone National Park via CTS to Cleveland, and then into the national TV network for the bicentennial special TV broadcast sponsored by NBC on July 4, 1976. For this purpose, a 2.0-m reflector was positioned on a transportable azimuth/elevation mount and transported to Yellowstone National Park, Wyoming. Earth station transmitted power in TB-1 was 20 W, resulting in an up-link e.i.r.p. of 59 dBW from the earth terminal. This produced a weighted signal-to-noise ratio for the video signal of about 44 dB. The receiving station was the 4.8-m terminal at NASA Lewis Research Center in Cleveland, Ohio. The transmission included three audio subcarriers, one for program audio and two for order wire. A return video link was also used in TB-2. The level of the return link carrier was deliberately kept low to avoid suppression of the forward link in TB-1 by the return signal in TB-2. This resulted in a relatively poor quality return link, which provided voice order-wire service and made it possible to view the composite program transmitted over the terrestrial TV network. It was returned by CTS to Yellowstone from the earth terminal at Cleveland, Ohio. A link power budget for this experiment is shown in Table A-2 of the appendix.

#### GRANDFATHER MOUNTAIN TV

A similar transmission was made of the Scottish Games from Grandfather Mountain in North Carolina. The color TV was transmitted from the 2.0-m terminal to the 1.2-m terminal located in Columbia, South Carolina; the 1.2-m terminal operated in a receive only mode. The received video signal was about 43 dB weighted signal to noise, which was minimally acceptable for use in the public TV network. Table A-3 contains the link power budgets.

#### Simultaneous interpretation via satellite

An experiment was conducted to determine the feasibility of simultaneous language interpretation via satellite for a multilingual meeting (teleinterpretation). The United Nations (U.N.), the U.S. National Aeronautics and Space Administration (NASA), and COMSAT Laboratories tested simultaneous language interpretation and translation of documents via satellite communications links in connection with a U.N. meeting on the technical cooperation among developing countries held in Buenos Aires, Argentina, in August 1978. For this experiment, NASA furnished a 2.4-m transportable earth terminal contained in a bus and placed near the U.N. building in New York City.

COMSAT's transportable 2.0-m earth terminal used for the teleinterpretation experiment was a combination of the COMSAT earth terminal designs previously described. The antenna was a standard Prodelin 2-m fiberglass reflector. The mount consisted of a platform 30 cm high with an integrally mounted large ring bearing and antenna support structures that held the antenna in its operating position with its lower edge 30 cm off the ground. Elevation adjustment was accomplished with an electrically driven jack screw and the azimuth adjustment using a modified antenna rotor. Both axes were controlled from a remote location. The entire antenna support structure was packed as a self-contained unit on its own pallet for air shipment.

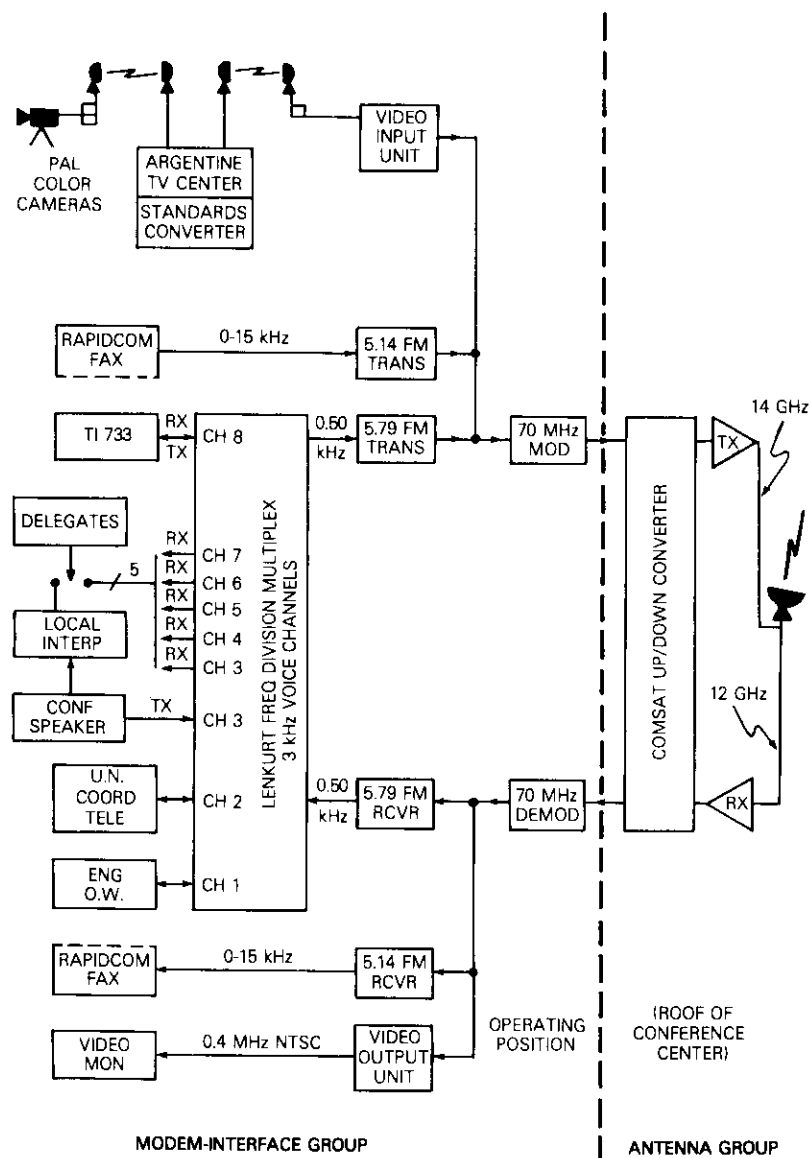
The antenna feed was adapted from the 2.4-m terminal feed by mounting it such that the focal length corresponded to the 2-m reflector. The 200-W TWT transmitter from the fixed terminal was used and adjusted for 220-V, 50-Hz operation. The box containing the TWT, mixer, and local oscillator was also used as the shipping container for these items. Similarly, the TWT power supply was operated from its shipping container. An FET low-noise receiver and up/down-converter described previously completed the RF and IF complement of the terminal.

The baseband equipment, constructed specifically for this experiment, consisted of an 8-channel Lenkurt multiplex system and a Farinon TV modulator and demodulator. Figure 21 is a block schematic of the system. A similar baseband unit was furnished to the NASA terminal in New York.

The transmission system provided full color TV (NTSC) with one 15-kHz audio channel, an engineering order wire for use by the earth station operators, a coordination circuit for the U.N. experiment coordinators, five channels of voice-grade audio for the interpretation, and one channel for a high-speed teletype machine operating at 300 bauds. The TV audio circuit was also used for a high-speed facsimile transmission (Rapicom). The 70-MHz IF interface was separated from the up/down-converter by about 300 m of RG 58 cable. The antenna unit was placed on top of the 14-story conference building (see Figure 22).

The TV signal originating at Buenos Aires was in the PAL format. It was first transmitted to a conversion center in midtown Buenos Aires and returned in the NTSC format via microwave link; then it was transmitted via CTS to New York.

The results of the experiment showed that remote interpretation is

Figure 21. *Teleinterpretation System Schematic*Figure 22. *2.0-m Terminal on Site in Buenos Aires, Argentina*

technically feasible. A teleconference held at the conclusion of the experiment between the interpreters in New York and Buenos Aires concluded that voice circuit quality is important in the interpretation process, whereas the delay introduced by the satellite link presents no problem. Documents were transmitted using the Rapicom facsimile machines modified for 4-wire operation. Documents prepared by a Chinese language typewriter in Buenos Aires were transmitted at the medium speed of the Rapicom machine (approximately 50 s per page) and were considered of adequate quality for translation.

#### Experiments using the 2.4-m terminals

##### VIDEO TRANSMISSIONS FOR AN AIRCRAFT DISASTER EXERCISE

One of the 2.4-m terminals was used to demonstrate emergency communications in a disaster involving a medical crisis. It was taken to the Baltimore-Washington International Airport to establish a television link in a simulated disaster involving the collision of a passenger aircraft and a gasoline tank truck. The 1-way tv and audio return link was used to connect the medical and paramedical teams at the disaster

site with medical experts at a burn center in San Antonio, Texas. The experts were shown color TV pictures of casualties and were asked to assess the severity of injuries and render advice on the type and relative urgency of treatment. This experiment successfully illustrated the possibility of using a transportable earth terminal and satellite communications in disasters requiring medical assistance from a remote location. Figure 23 is a composite picture of the disaster.

#### BUSINESS COMMUNICATIONS, PROJECT PRELUDE

The 2.4-m transportable terminals were primarily developed to demonstrate business communications via satellite directly between user premises. Satellite Business Systems and COMSAT initiated project PRELUDE to advance the state of the art in intra-company communications services, equipment, and techniques to be available commercially in the 1980's. The 2.4-m terminals were successively installed at the premises of the user organizations in three pairs of locations in the U.S. during November 1977 to March 1978. Table 5 lists the participants and locations.

TABLE 5. PROJECT PRELUDE PARTICIPANTS

Host Company	Terminal Locations
Rockwell International Co.	Pittsburgh, Pa., and Los Angeles, Ca.
Texaco	Harrison, N.Y., and Houston, Texas
Montgomery Ward & Co. Inc.	Chicago, Ill., and Baltimore, Md.
Equipment	Manufacturer
Large Screen Color TV	Advent Corporation
TV Freeze-Frame Storage	Arvin/Echo
High-Speed, High-Resolution Facsimile Terminal	Dacom/Rapidfax
High-Speed "Any Datarate" Modem	Harris Corporation
Computer System Data Processing Network	Hewlett-Packard Co.
Color TV Cameras	Ikegami Electronics (U.S.A.) Inc.
Color Freeze-Picture Transmission System	NEC America Inc.

The transmissions consisted of high-speed data up to 1.544 Mbit/s, high-speed facsimile, and voice and video communications. Equipment from the manufacturers listed in Table 5 was connected to the earth terminal using a master control unit which enabled rapid switchover

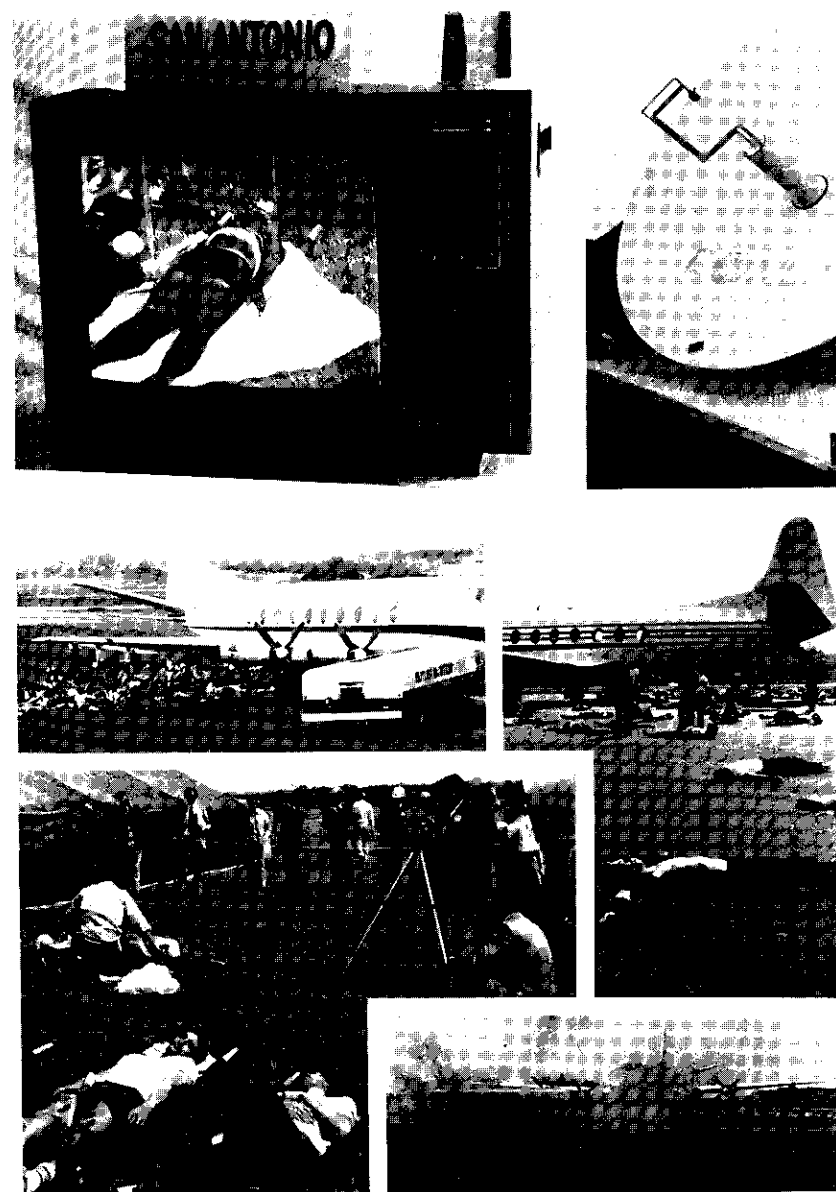


Figure 23. Composite of Disaster Communications Aspects

between sets of equipment and transmission modes. The link used either an analog video with audio subcarrier mode, or a digital bit stream plus SCPC voice mode illustrated in Figure 16. Link power budgets for the PRELUDE experiments are shown in Table A-4.

#### CLOCK SYNCHRONIZATION

The 2.4-m transportable earth terminals were used for an experiment in clock synchronization between the primary time standards at the U.S. National Bureau of Standards in Boulder, Colorado, and the U.S. Naval Observatory Time Service in Washington, D.C., and the 7.0-m terminal at the Canadian National Research Council (NRC) in Ottawa, Canada.

Prior to COMSAT's participation, this experiment had used earth stations located away from the primary time standards, with attendant problems in logistics and accuracy in transporting cesium beam clocks from one location to another [4]. The 2.4-m terminals were set up at Boulder and Washington, sufficiently close to the primary time standards to permit a direct short cable connection to these facilities.

The clocks are synchronized by transmitting time pulses in both directions via CTS from two locations. Station A transmits a pulse, which starts a counter. This counter is then stopped by the receipt of the time pulse from the distant station B. The information thus obtained at stations A and B is then processed by computer to remove time ambiguity and path length changes.

The clock synchronization experiment was conducted in three modes:

a. A 1-pulse-per-second (pps) time signal was impressed on a standard video modulator and sent as an FM analog video signal via CTS with a nominal RF bandwidth of 20 MHz.

b. A modem developed by NRC, Canada, impressed a 1-MHz signal derived from the 1-pps clock pulse on the FM modulator.

c. COMSAT designed an interface unit for the Harris modem for the time transfer application. This unit received a 1-MHz signal and a 1-pps signal from the cesium beam master clock. These inputs were used to coherently produce a 100-pps data stream, clocked at a 25-kbit/s rate, which was then transmitted via CTS in the form of a 25-kbit/s PPSK signal. Thus, the RF bandwidth used in this mode is compatible with the bandwidth required for a standard 56-kbit/s QPSK data transmission.

Preliminary analyses of the results indicate that the standard deviation

of the measurements obtained from the three modes is as shown in Table 6.

TABLE 6. STANDARD DEVIATION OF MEASUREMENTS FOR THREE MODES

Mode	System	Standard Deviation (ns)	RF Bandwidth (MHz)	C/N <sub>0</sub> (dB·Hz)
1	1-pps TV	10	36	87 dB
2	1-MHz TV	1	36	86 dB
3	100-pps Data on 25-kbit/s BPSK	15	0.030	60 dB

The experiment required about 1.5 hr of operating time per week, with 15 min allocated to reposition the CTS spacecraft antennas for the link between Washington and Ottawa after the Boulder to East Coast link experiments. The link power budgets in Table A-4 apply.

A mode 1 transmission was also made between Boulder and Paris, France, by first linking Boulder and Ottawa via CTS and then Paris and Ottawa via the SYMPHONIE satellite. The results were satisfactory and illustrated the possibility of a multiple-hop satellite circuit for clock synchronization.

#### Experiments using the 4.6-m terminal

##### Project DICE (digitally implemented communications experiment)

The 4.6-m terminal was used in conjunction with NASA's 2.4-m transportable terminal and the 9-m terminal at the Communications Research Centre, Ottawa, Canada, for project DICE. This experiment employed COMSAT Laboratories developed digital video equipment operating at a nominal bit rate of 49 Mbit/s through a 4-phase DPSK modem also developed by COMSAT [5], [6]. The transmission consisted of full-duplex video with an audio channel and simultaneously a full-duplex digital bit stream supporting 60 channels of voice-grade telephone channels, and one data channel. The telephone channels were multiplexed at about 1.5 Mbit/s onto the horizontal synchronization interval of the TV.

The operation of the DICE equipment required a C/N<sub>0</sub> of 94-(dB·Hz), or approximately 19-dB C/N in the 33-MHz RF bandwidth needed for

the 49-Mbit/s 4-phase DPSK signal. A rate 7/8 forward error correction code was used to achieve an error rate of  $10^{-7}$ .

Obtaining the required link performance in both directions necessitated a careful adjustment of the transmit power at each earth terminal. The CTS transponders are such that a signal in transponder 2 will suppress a signal in transponder 1, since both signals pass through the same 20-W TWT in the spacecraft (see Figure 2). The link budget for this experiment is shown in Table A-5 of the appendix.

To obtain the up-link noise performance required in the link, it was necessary to insert both the 4-dB attenuator into transponder 2 and the 5-dB attenuator into transponder 1. Two demonstration transmissions were made for which the calculated link performances were actually obtained with excellent quality TV.

The experiment between COMSAT Laboratories and the NASA terminal located at San Diego, California, enabled two authors (one located in San Diego, the other in Clarksburg, Maryland) to jointly present their paper during a meeting of the AIAA in June 1978. The technical paper was delivered via video conferencing with audiences in attendance at the main meeting in San Diego, and also at COMSAT Laboratories. The 60-voice channel capability of the DICE equipment was demonstrated, but not used, in the teleconference.

A similar teleconference using DICE equipment was held between engineers at COMSAT and at the Communications Research Centre in Ottawa. Echo control equipment, designed by COMSAT, consisted of standard echo suppressors modified to operate in a conference room environment. Both teleconferences were judged quite satisfactory in terms of the equipment performance and their potential as a means for holding technical conferences between distant locations.

#### **Direct broadcast of FM audio via CTS**

At the suggestion of engineers of the Voice of America, a small receive only earth terminal was designed. The terminal has a horn antenna with a 17-cm  $\times$  20-cm aperture (see Figure 24 and Table A-6). Figure 25 is a block schematic of the terminal, in which the small FM portable receiver was used as one of the receivers for the FM audio signal. The transmission format was standard FM broadcast quality with a baseband from 30 Hz to 15 kHz, a modulation index of 5.0, and a bandwidth of 180 kHz.

The terminal used direct conversion from the received frequency of 12.08 GHz to approximately 100 MHz. The output of the receiver is



Figure 24. *Small Horn Receiver Antenna*

connected directly to the antenna of the FM set. Because of the high gain and high noise figure of the front end, the resulting output of the system eliminated most of the commercial stations in the FM band (88–108 MHz), thus facilitating the tuning of the FM set to the desired satellite signal, which was well above the noise. The audio quality of

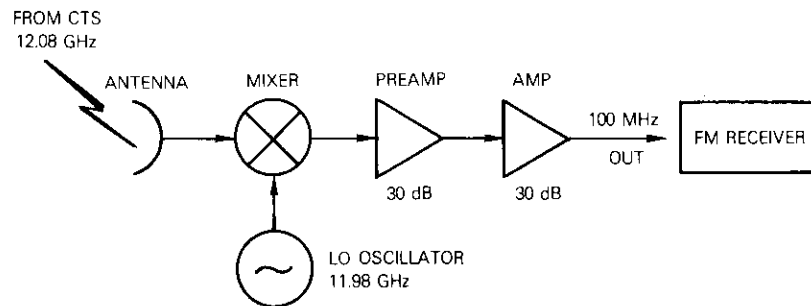


Figure 25. FM Audio Receiver System Schematic

about 59-dB S/N was considered superb. The down-link power budget from the CTS to the small terminal is given in Table A-7 in the appendix. A 3-dB improvement of the terminal's G/T could be obtained with an image rejection mixer, and a further improvement could result from the use of an FET front end.

A demonstration of this receiver in an urban environment showed that the technology exists for using very small inexpensive earth terminals for direct reception of FM via satellite. It was observed that regular window glass of up to 0.6 cm caused no noticeable signal impairment; however, summer foliage on trees and aluminized mylar window film attenuated the signals beyond their usefulness.

### Miscellaneous

During the 3.5 years of experimentation with the CTS spacecraft, valuable experience was gained in the operation of transportable and fixed earth terminals using the 12/14-GHz frequency bands. Locating the CTS from a terminal in a field site was never a problem when the beacon receiver was used. Only a compass and a bubble level were needed, the latter to accurately set the antenna elevation. A search in azimuth always resulted in successful acquisition of the spacecraft.

During the entire experimental period, signal attenuation due to rainfall was a problem on only two occasions. In both instances, the rain rate was high (estimated at over 100 mm/hr) and directly in the beam of the antenna. Severe signal degradations of up to 15 dB were observed.

Equipment reliability was reasonably high except for three failures

of TWT high-voltage power supplies. Two of these occurred in an early version of the power supply for the 20-W TWT; the other was a result of stray capacitance in the long (6-m) cable between the power supply and the 200-W TWT, which was quickly diagnosed and promptly resolved.

There were no failures in the TWTs themselves. The flexible waveguide used in the 1.2-m terminal was damaged from handling in the field. Waveguide and feed components required drying and removal of internal moisture when they enclosed a considerable volume and were exposed to large fluctuations of temperature and humidity.

Local oscillator failures and drift with temperature were a problem. Frequency drift became troublesome only in the digital transmission modes and in the beacon receiver, which for simplicity, used a fixed 30-kHz crystal filter for signal discrimination. Thus, a drift of  $\pm 15$  kHz in the received signal from all causes, including spacecraft beacon frequency drift, would remove the beacon signal from the filter passband.

### Conclusions

The earth terminals designed by COMSAT proved to be well suited to a variety of experiments in satellite communications. These terminals together with the CTS have demonstrated the feasibility of satellite communications from locations in the field and at the user's premises. New methods of communications, such as teleinterpretation and remote translation, have been explored and demonstrated. It was shown that the concept of a scheduled satellite, which assigns definite relatively short periods of its facilities to each user on a prearranged schedule, worked well for a large number of users in two countries [2]. The development of the required 12- and 14-GHz subsystems for the small earth terminals has prompted industry to design components that will be needed when the new generation of communications satellites with 12/14-GHz transponders is placed into service.

### References

- [1] NASA TM-X-71824, *CTS Reference Book*, NASA Lewis Research Center, Cleveland, Ohio, October 15, 1975.
- [2] "HERMES (The Communications Technology Satellite) Its Performance and Applications," *Proceedings of the Twentieth Symposium of the Royal Society of Canada*, 3 Vol., November 29–December 1, 1977.

- [3] O. A. Horna, "Echo Canceller with Adaptive Transversal Filter Utilizing Pseudo-Logarithmic Coding," *COMSAT Technical Review*, Vol. 7, No. 2, Fall 1977, pp. 393-428.
- [4] C. C. Costain, H. Daams, J. S. Boulanger (NRC); D. W. Hanson (NBS); and W. J. Klepczynski (USNO), "Two-Way Time Transfers Between NRC/NBS and NRC/USNO via the HERMES (CTS) Satellite." 10th Annual Precise Time and Time Interval Applications and Planning Meeting, November 1978.
- [5] A. G. Gatfield, H. G. Suyderhoud, and C. J. Wolejsza, Jr., "System Design for the Digitally Implemented Communications Experiment (DICE)," International Conference on Communications, Chicago, Illinois, June 12-15, 1977.
- [6] C. J. Wolejsza, D. Chakraborty, and V. Uzunoglu, "A Universal Modem Design for Digital Satellite Communications," International Conference on Communications, Philadelphia, Pennsylvania, June 14-16, 1976, *Conference Record*, Vol. I, pp. 3-12-3-18.

### Appendix: Link budgets for CTS experiments

The CTS antenna 3-dB contours for three different pointing angles are shown in Figure A-1. The antenna beams were pointed directly toward the experi-

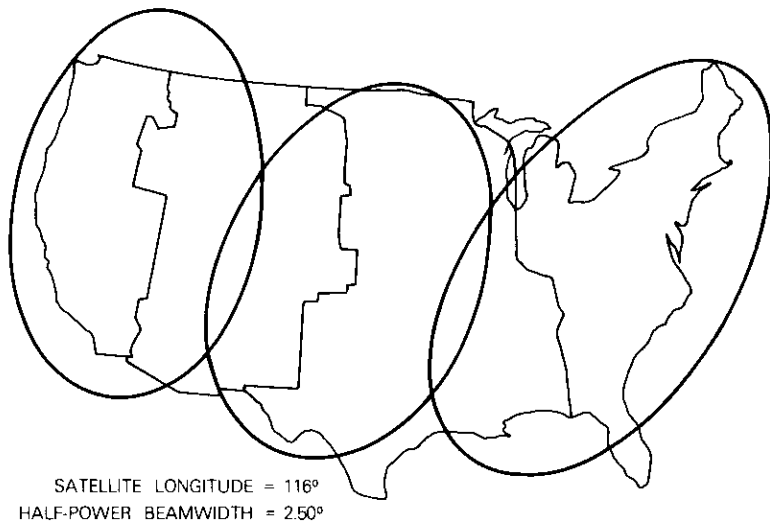


Figure A-1. CTS Antenna Contours

menter's earth terminal location in nearly all cases, so that values of spacecraft antenna gains for beam peak apply for the link budgets calculated in Tables A-1 through A-7.

The relationship of earth terminal e.i.r.p. versus the spacecraft transmitted power shown in Figure A-2 was measured by NASA and verified using the COMSAT terminal. It applies for clear sky conditions and for earth terminal elevation angles of approximately 30°. Since the signals in TB-1 transmitted via the 200-W TWT in CTS also pass through the 20-W TWT, they encounter small signal suppression from signals in TB-2 near saturation of the 20-W TWT. This effect is shown in curve C in Figure A-2. The curves are used to determine the spacecraft e.i.r.p. in the link budgets. Both attenuators, 4-dB in TB-2 and 5-dB in TB-1, were used for DICE; 0, 5 dB were used for the PRELUDE experiments; and 0, 0 dB in the emergency communications experiments using the 1.2-m terminal.

TABLE A-1. LINK POWER BUDGETS FOR 1.2-M TERMINAL EXPERIMENTS

Up-Link from 4.6-m Terminal to CTS in RB-1	
Transmitted Power, 10 W (dBW)	10
Gain (4.6-m antenna) (dB)	54
e.i.r.p. (dBW)	64
Path Loss (dB)	-207.3
Spacecraft $G/T$ (dB/K)	6.4
$C/T_{up}$ (dBW/K)	-136.9
Down-Link from CTS to 1.2-m Terminal in TB-1, Spacecraft Attenuator = 0 dB	
Spacecraft e.i.r.p. (Figure A-2a) (dBW)	58
Path Loss (dB)	-206.3
$G/T$ (1.2-m antenna) (dB/K)	15.5
$C/T_{down}$ (dBW/K)	-132.8
$C/T_{total}$ (dBW/K)	-138.3
$C/N_o$ Available [dB(Hz)]	90
$C/N_o$ Desired* [dB(Hz)]	67
Margin (dB)	23
Up-Link from 1.2-m Terminal to CTS in RB-2	
Transmitted Power, 10 W (dBW)	10
Gain (1.2-m antenna) (dB)	42
e.i.r.p. (dBW)	52
Path Loss (dB)	-207.3
Spacecraft $G/T$ (dB/K)	6.4
$C/T_{up}$ (dBW/K)	-148.9

TABLE A-1. LINK POWER BUDGETS FOR 1.2-M TERMINAL EXPERIMENTS  
(continued)

Down-Link from CTS to 4.6-m Terminal in TB-2, Spacecraft Attenuator = 0 dB	
Spacecraft e.i.r.p. (Figure A-2b) (dBW)	33
Path Loss (dB)	-206.3
$G/T$ (4.6-m antenna) (dB/K)	27
$C/T_{down}$ (dBW/K)	-146.3
$C/T_{total}$ (dBW/K)	-150.8
$C/N_o$ Available (dB.Hz)	78
$C/N_o$ Desired* (dB.Hz)	67
Margin (dB)	11

\* Computation of  $C/N_o$  desired for three voice channels multiplexed on one carrier with 300-kHz RF band:  $S/N = (3/2)[D_p^2/(f_{m_1}^3 - f_{m_2}^3)](C/N_o) \alpha$ , where  $D_p$  = peak deviation = 134 kHz;  $f_{m_1}$  = highest channel frequency;  $f_{m_2}$  = second highest frequency;  $\alpha$  = weighting = 2.5 dB;  $S/N$  desired = 50 dB; and  $C/N_o$  desired =  $S/N + 16.9 = 67$  dB(Hz) for a multiplex system with three channels, e.g., 4-8, 8-12, and 12-16 kHz (0-4 kHz not used).

TABLE A-2. LINK POWER BUDGET FOR 2.0-M TERMINAL EXPERIMENTS  
(color video transmission from Yellowstone National Park, Wyoming, to Cleveland, Ohio)

Up-Link from 2.0-m Terminal to CTS in RB-1	
Transmitted Power, 20 W (dBW)	13
Gain (2.0-m antenna) (dB)	46
e.i.r.p. (dBW)	59
Path Loss (dB)	-207.1
Spacecraft $G/T$ (dB/K)	6.4
$C/T_{up}$ (dBW/K)	-141.7
Down-Link from CTS to 4.6-m Terminal in TB-1, Spacecraft Attenuator = 0 dB	
Spacecraft e.i.r.p. (Figure A-2a) (dBW)	57
Path Loss (dB)	-206.3
$G/T$ (4.6-m antenna) (dB/K)	24
$C/T_{down}$ (dBW/K)	-125.3
$C/T_{total}$ (dBW/K)	-141.8
$C/N_o$ Available (dB.Hz)	86.8
Video $S/N^*$ (dB)	44.2

\* Video  $S/N$  computed from  $S/N = 236.3 + 20 \log d + C/T - 10 \log f_v + Q$  in dB, where  $d$  = deviation index =  $f_d/f_v = 5.2 \text{ MHz}/4.2 \text{ MHz} = 1.4$ ;  $f_d$  = highest peak deviation = 5.2 MHz;  $f_v$  = highest modulation frequency = 4.2 MHz; and  $Q$  = weighting factor = 13 dB.

TABLE A-3. LINK POWER BUDGET FOR 2.0-M TERMINAL EXPERIMENTS  
(color video transmissions from Grandfather Mountain, North Carolina, to 1.2-m terminal in Columbia, South Carolina)

Up-Link from 2.0-m Terminal to CTS in RB-1	
Transmitted Power, 20 W (dBW)	13
Gain (2.0-m antenna) (dB)	46
e.i.r.p. (dBW)	59
Path Loss (dB)	-207.3
Spacecraft $G/T$ (dB/K)	6.4
$C/T_{up}$ (dBW/K)	-141.9
Down-Link from CTS to 1.2-m Terminal in TB-1, Spacecraft Attenuator = 0 dB	
Spacecraft e.i.r.p. (Figure A-2a) (dBW)	57
Path Loss (dB)	-206.3
$G/T$ (1.2-m antenna) (dB/K)	15.5
$C/T_{down}$ (dBW/K)	-133.8
$C/T_{total}$ (dBW/K)	-142.5
$C/N_o$ Available (dB.Hz)	86.1
Video $S/N^*$ (dB)	43.1

\* See footnote to Table A-2.

TABLE A-4. LINK POWER BUDGET FOR PROJECT PRELUDE

Parameter	Video	Digital
Up-Link from 2.4-m Terminal to CTS in RB-2		
Transmitted Power (dBW)	13	10
Gain (2.4-m antenna) (dB)	48.5	48.5
e.i.r.p. (dBW)	61.5	58.5
Path Loss	-207.3	-207.3
Spacecraft $G/T$ (dB/K)	6.4	6.4
$C/T_{up}$ (dBW/K)	-139.4	-142.4
Down-Link from CTS to 2.4-m Terminal in TB-2 Spacecraft Attenuator = 0 dB		
Spacecraft e.i.r.p. (Figure A-2b) (dBW)	43	40
Path Loss (dB)	-206.3	-206.3
$G/T$ (2.4-m antenna) (dB/K)	21.4	21.4
$C/T_{down}$ (dBW/K)	-141.9	-144.9
$C/T_{total}$ (dBW/K)	-143.8	-146.8
$C/N_o$ Available (dB.Hz)	84.8	81.8
$C/N_o$ Required (dB.Hz)		75
Video $S/N^*$ (dB)	41.7	
Margin (dB)		6.8

TABLE A-4. LINK POWER BUDGET FOR PROJECT PRELUDE  
(continued)

Parameter	Video	Digital
Up-Link from 2.4-m Terminal to CTS in RB-1		
Transmitted Power (dBW)	13	10
Gain (2.4-m antenna) (dB)	48.5	48.5
e.i.r.p. (dBW)	61.5	58.5
Path Loss (dB)	-207.3	-207.3
Spacecraft $G/T$ (dB/K)	6.4	6.4
$C/T_{up}$ (dBW/K)	-139.4	-142.4
Down-Link from CTS to 2.4-m Terminal in TB-1, Spacecraft Attenuator = 5 dB		
Spacecraft e.i.r.p. (Figure A-2a) (dBW)	55	52
Path Loss (dB)	-206.3	-206.3
$G/T$ (2.4-m antenna) (dB/K)	21.4	21.4
$C/T_{down}$ (dBW/K)	-129.9	-132.9
$C/T_{total}$ (dBW/K)	-140	-142.8
$C/N_o$ Available (dB.Hz)	88.6	85.7
$C/N_o$ Required (dB.Hz)		75
Video $S/N^*$ (dB)	44.6	
Margin (dB)		10.5

\* See footnote to Table A-2.

TABLE A-5. LINK POWER BUDGET FOR DICE  
(digital color video transmissions)

Up-Link from NASA 2.4-m Terminal to CTS in RB-1	
Transmitted Power, 100 W (dBW)	20
Gain (2.4-m antenna) (dB)	48.5
e.i.r.p. (dBW)	68.5
Path Loss (dB)	-207.3
Spacecraft $G/T$ (dB/K)	6.4
$C/T_{up}$ (dBW/K)	-132.4
Down-Link from CTS to COMSAT 4.6-m Terminal in TB-1, Spacecraft Attenuator = 5 dB	
Spacecraft e.i.r.p.* (Figures A-2a and A-2c) (dBW)	54
Path Loss (dB)	-206.3
$G/T$ (4.6-m antenna) (dBW/K)	28
$C/T_{down}$ (dBW/K)	-124.3
$C/T_{total}$ (dBW/K)	-133
$C/N_o$ Available (dB.Hz)	95.6
$C/N_o$ Required for BER $10^{-7}$ (dB.Hz)	94
Margin (dB)	1.6

\* TB-2 signal suppresses TB-1 signal by 5 dB (Figure A-2c).

TABLE A-5. LINK POWER BUDGET FOR DICE  
(digital color video transmissions)  
(continued)

Up-Link from COMSAT 4.6-m Terminal to CTS in RB-2	
Transmitted Power, 160 W (dBW)	22
Gain (4.6-m antenna) (dB)	54
e.i.r.p. (dBW)	76
Path Loss (dB)	-207.3
Spacecraft $G/T$ (dB/K)	6.4
$C/T_{up}$ (dBW/K)	-124.9
Down-Link from CTS to NASA 2.4-m Terminal in TB-2, Spacecraft Attenuator = 4 dB	
Spacecraft e.i.r.p. (Figure A-2b) (dBW)	48.5
Path Loss (dB)	-206.3
$G/T$ (2.4-m antenna) (dBW/K)	24
$C/T_{down}$ (dBW/K)	-133.8
$C/T_{total}$ (dBW/K)	-134.3
$C/N_o$ Available (dB.Hz)	94.2
$C/N_o$ Required for BER $< 10^{-7}$ (dB.Hz)	94
Margin (dB)	0.2

TABLE A-6. DIRECT BROADCAST OF FM AUDIO VIA CTS

Antenna and Converter	
Rectangular Horn	17-cm $\times$ 20-cm aperture 46-cm long Gain $\approx$ 25 dB at 12 GHz Beamwidth $\sim 10^\circ$
Mixer	Single conversion from 12.08 GHz to 100 MHz Local oscillator = 11.98 GHz Noise figure = 5 dB measured with diode source Operating noise temperature: 1240 K = 31 dB/K

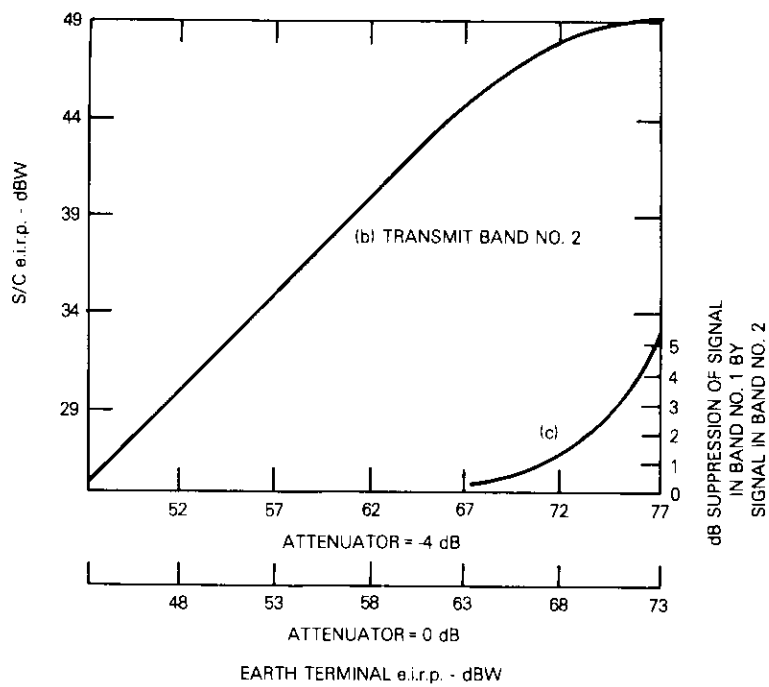
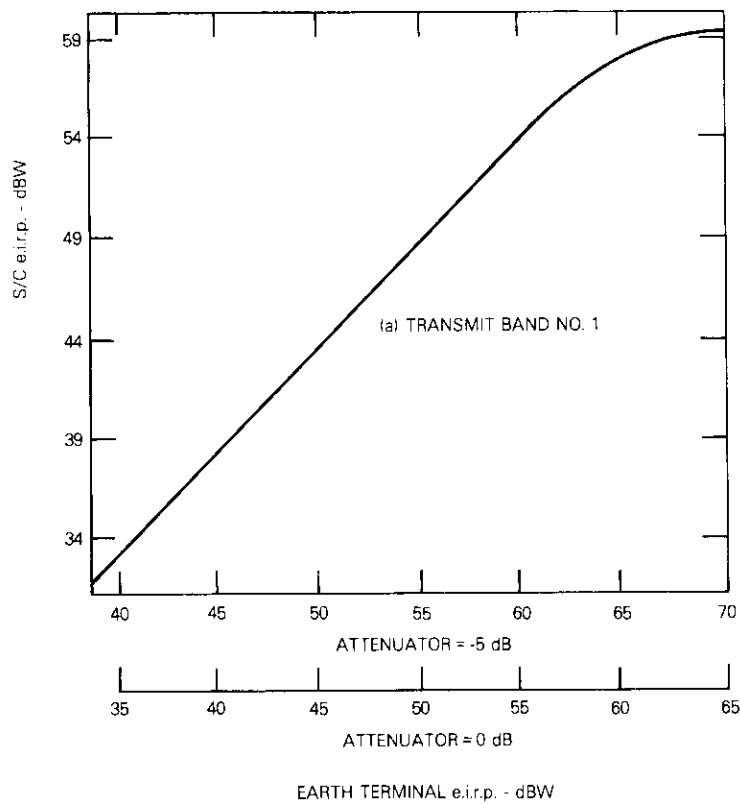
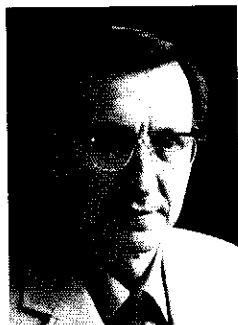


Figure A-2. CTS Spacecraft e.i.r.p. vs Earth Terminal e.i.r.p.

TABLE A-7. LINK POWER BUDGET FOR DIRECT FM AUDIO TRANSMISSION

Up-Link from COMSAT 4.6-m Terminal to CTS in RB-1	
Transmitted Power (dBW)	10
Gain (4.6-m antenna) (dB)	54
e.i.r.p. (dBW)	64
Path Loss (dB)	-207.3
Spacecraft $G/T$ (dB/K)	6.4
$C/T_{up}$ (dBW/K)	-136.9
Down-Link from CTS to Horn Antenna in TB-1, Spacecraft Attenuator = 0 dB	
Spacecraft e.i.r.p. (Figure A-2a) (dBW)	58
Path Loss (dB)	-206.3
$G/T$ (horn antenna 25-dB gain) (dBW/K)	-6
$C/T_{down}$ (dBW/K)	-154.3
$C/T_{total}$ (dBW/K)	-154.5
$C/N_o$ [dB(Hz)]	74.1
$C/N$ in 180 kHz (dB)	21.7
$S/N^*$ (dB)	~60

\*  $S/N$  computed from  $S/N = \frac{3}{2} (\beta)^2 (B_{IF}/f_m) (Q)$ , where  $f_m$  = highest modulating frequency = 15 kHz,  $\beta$  = modulation index = 5,  $B_{IF}$  = 180 kHz, and  $Q$  = weighting factor = 12 dB.



Joachim Kaiser received a B.A. and an M.A. in mathematics in 1943 and 1948, respectively, and completed additional graduate work in communications theory at the University of Michigan in 1967 and 1968. He joined COMSAT Laboratories in 1968 and is Manager of the Small Terminal Development project. He has performed numerous experiments in satellite communications using small earth terminals, was the principal investigator for COMSAT's experiment on the Communications Technology Satellite, and is a senior member of the IEEE.

Lester B. Veenstra received a B.S. in physics and a B.S. in systems science from the University of West Florida, and has pursued graduate work in electrical engineering at Northeastern University. He was with the U.S. Naval Security Group for six years prior to joining COMSAT Laboratories in 1976. Presently, he is a member of the Small Terminal Development group of the Transmission Systems Laboratory. He is a member of IEEE.



Eric Ackermann received an I.E.E. and an M.S.E.E. in engineering in London in 1938 and 1939, respectively. He joined COMSAT in 1975, and is Senior Project Manager for the Electronics Integration Division. For many years, he has been involved in the design and development of small earth terminals operating in the 4/6-, 7/8- and 12/14-GHz frequency bands.

Frederick J. Seidel graduated from the State University of New York with a degree in electrical technology. In 1971, he joined COMSAT Laboratories, where he is a Technical Specialist in the Small Earth Terminals Department, involved in transportable earth terminal experiments. Previously, he was employed by the General Electric Company in the Airborne Electronics Engineering Department.



## ***Periodic bandpass characteristic of microstrip meander line***

Y. S. LEE AND R. C. TRUSHEL

(Manuscript received June 8, 1979)

### ***Abstract***

The periodic comb-type bandpass characteristic of a loosely coupled microstrip meander line was measured up to the 26th frequency band. Group delay response was analyzed in terms of Weiss's meander line dispersion equation using quasi-TEM normal mode parameters which depend upon the phase per unit cell. Experimental measurements of group delay agree with theoretical results when the inherent microstrip dispersion is taken into account. Design considerations for broadband delay of the coupled microstrip meander line are described emphasizing the realization of a very compact, temperature-stable microwave delay circuit. State-of-the-art microwave integrated circuit (MIC) delay components are reviewed for onboard satellite regenerative repeater applications.

### ***Introduction***

Infinite arrays of parallel-coupled microstrip lines have been analyzed [1], [2] using quasi-TEM approximations for the propagation of normal modes. The presence of stop bands has been predicted from the characteristic equation for the microstrip meander line shown in Figure 1. In the nonhomogeneous microstrip medium, the unequal even and odd mode propagation velocities cause the stop band response, and the regu-

larly spaced discontinuities at the bends provide additional effects. Thus, the coupled microstrip meander line has a periodic comb-type bandpass frequency characteristic.

Experimental data on the bandpass characteristic of the microstrip meander line up to less than third-order passband have been published [1]. This paper presents bandpass group delay data up to the 26th passband measured on a loosely coupled, long microstrip meander line photoetched on barium tetratitanate ( $\text{BaTi}_4\text{O}_9$ ), a nondispersive material at least up to 18 GHz [3]. The theoretical group delay has been evaluated. Some of the design considerations are described for the implementation of a compact, broadband, temperature-stable microwave delay element which can be used for a differentially coherent QPSK onboard regenerative repeater [4] directly detecting at the up-link carrier frequency (*i.e.*, 14 GHz).

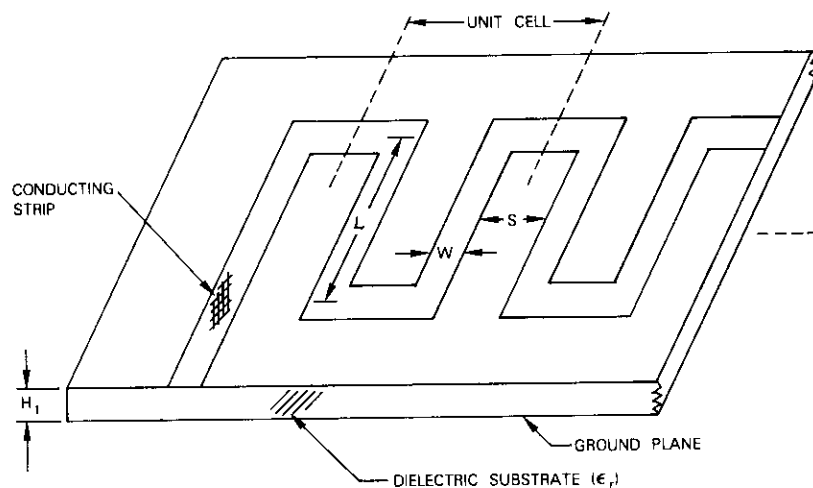


Figure 1. Microstrip Meander Line Configuration

### Experimental

Figure 2 is a photograph of the experimental microstrip meander line, and the design parameters are listed in Table 1.

Figure 3 shows transmission loss versus frequency measured with an automatic network analyzer. The insertion loss at the band center frequencies agrees with the theoretical estimate [3]. The input and output return losses at the band center frequencies are typically  $>10$  dB with

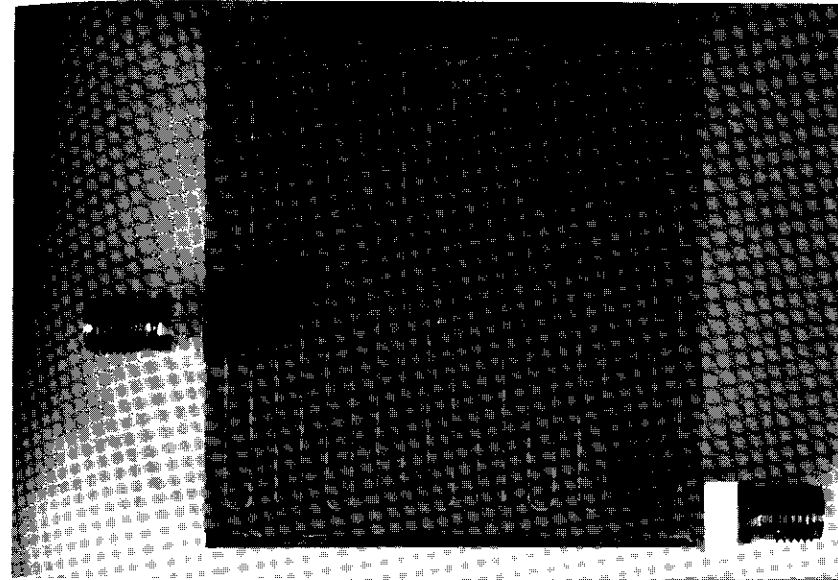


Figure 2. Experimental Meander Line

TABLE I. MICROSTRIP MEANDER LINE PARAMETERS

Substrate	$\text{BaTi}_4\text{O}_9$
$\epsilon_r$	37
$H_1$	$3.81 \times 10^{-4}\text{m}$ (0.015 in.)
$W/H_1$	1.0
$S/H_1$	5.7
$L$	$4.7086 \times 10^{-2}\text{m}$ (1.8538 in.)
No. of unit cells	9

OSM 244-4ASF transitions. Measured group delay up to 16 GHz is presented in Figure 4. The transmission loss and group delay characteristics of Figures 3 and 4 show the well-defined periodic comb-type bandpass characteristics of the coupled microstrip meander line. The frequency separation of adjacent maxima in these characteristics is the reciprocal of the group delay per unit cell.

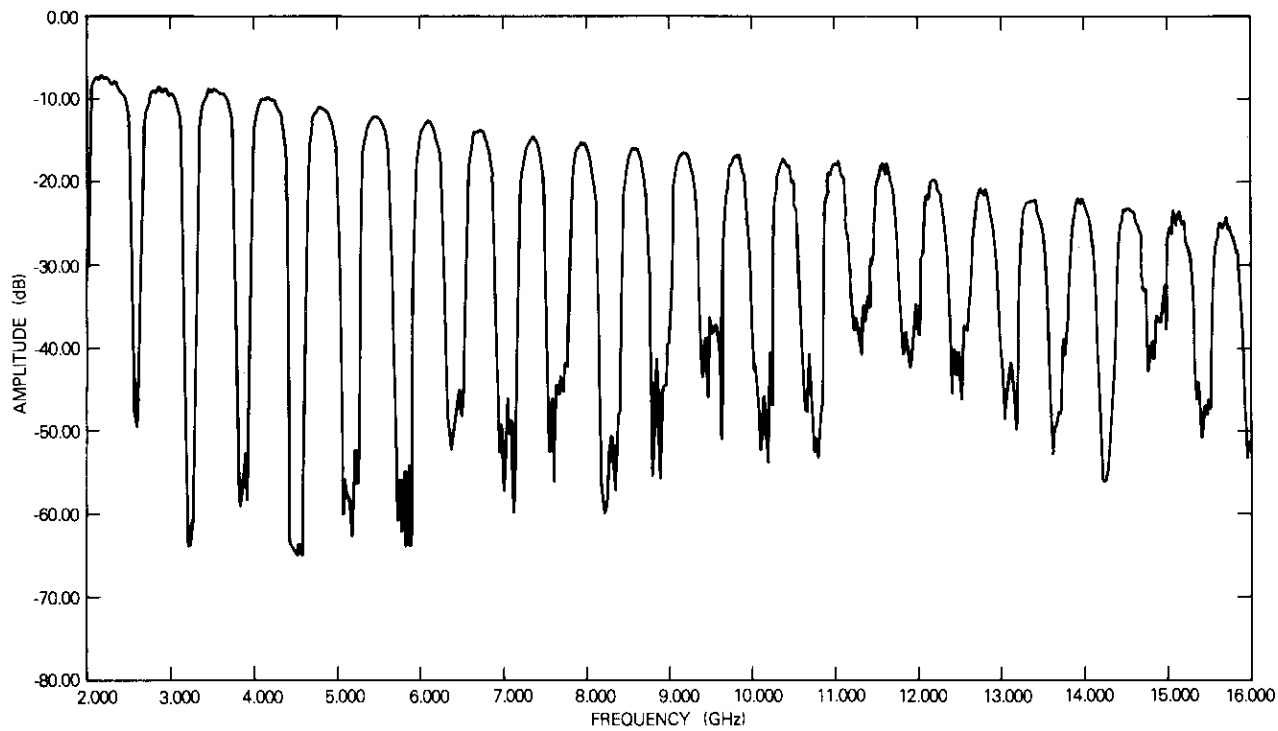


Figure 3. Measured Transmission Loss Characteristic

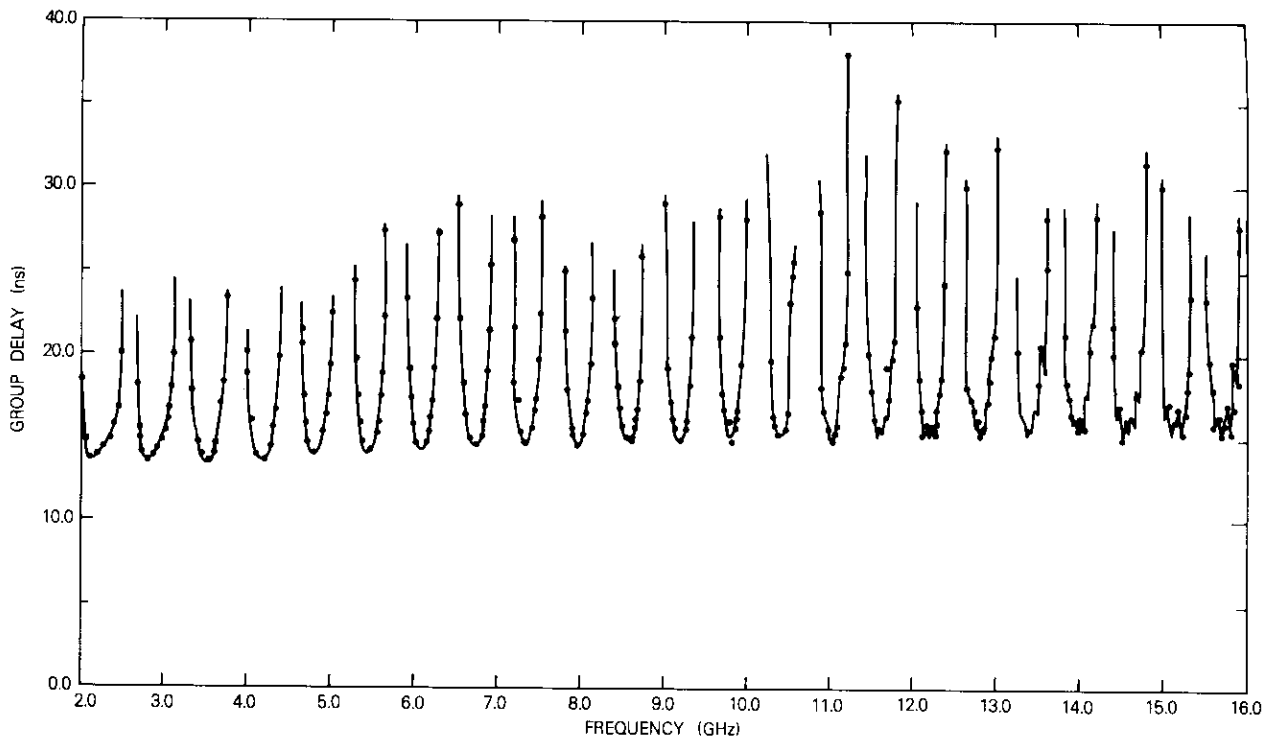


Figure 4. Measured Group Delay vs Frequency

### Theoretical

Theoretical group delay of a coupled microstrip meander line can be computed from the numerical solution of the Weiss dispersion equation [1]:

$$\tan^2 \frac{\phi}{4} = \frac{Z_{oo}(\phi)}{Z_{oe}(\phi)} \begin{cases} \tan \left[ \frac{\pi \sqrt{\epsilon_e(\phi)} L}{c} f \right] \tan \left[ \frac{\pi \sqrt{\epsilon_o(\phi)} L}{c} f \right] \\ \cot \left[ \frac{\pi \sqrt{\epsilon_e(\phi)} L}{c} f \right] \cot \left[ \frac{\pi \sqrt{\epsilon_o(\phi)} L}{c} f \right] \end{cases} \quad (1)$$

where  $Z_{oe}$  and  $\epsilon_e$  = even mode characteristic impedance and dielectric constant

$Z_{oo}$  and  $\epsilon_o$  = odd mode characteristic impedance and dielectric constant

$L$  = unit line length ( $m$ ) as shown in Figure 1

$c$  = velocity of light in vacuum ( $3.0 \times 10^8 m/s$ )

$\phi$  = phase angle increment per unit cell

$f$  = frequency in Hz.

The normal mode parameters are functions of  $\phi$ . The upper and lower terms in equation (1) alternately yield the successive forward and backward wave branches of the dispersion diagram.

Transcendental equation (1) was solved using a numerical relaxation program for  $f$  at all values of  $\phi$  from  $0^\circ$  to  $360^\circ$ , typically in  $5^\circ$  increments. The inputs are  $Z_{oe}(\phi)$ ,  $\epsilon_e(\phi)$ ,  $Z_{oo}(\phi)$ , and  $\epsilon_o(\phi)$  for each  $\phi$ . The normal mode parameters for the design shown in Table 1 are plotted in Figure 5 [5].

Equation (1) gives a multiple-valued solution in  $f$  for a given  $\phi$ . However, each passband is defined by a single-valued  $f$  region for each  $\phi$  from  $0^\circ$  through  $360^\circ$  in phase, and the stop band is defined by the imaginary solution in  $f$ . Transmission group delay,  $\tau_{og}$ , of the overall meander line is then derived using the computed values of  $\phi$  versus  $f$ :

$$\begin{aligned} \tau_{og} &= - \frac{\partial \psi}{\partial \omega} \\ &= - \frac{M \cdot \Delta \phi^\circ}{360^\circ \cdot \Delta f(\text{GHz})} \text{ (ns)} \end{aligned} \quad (2)$$

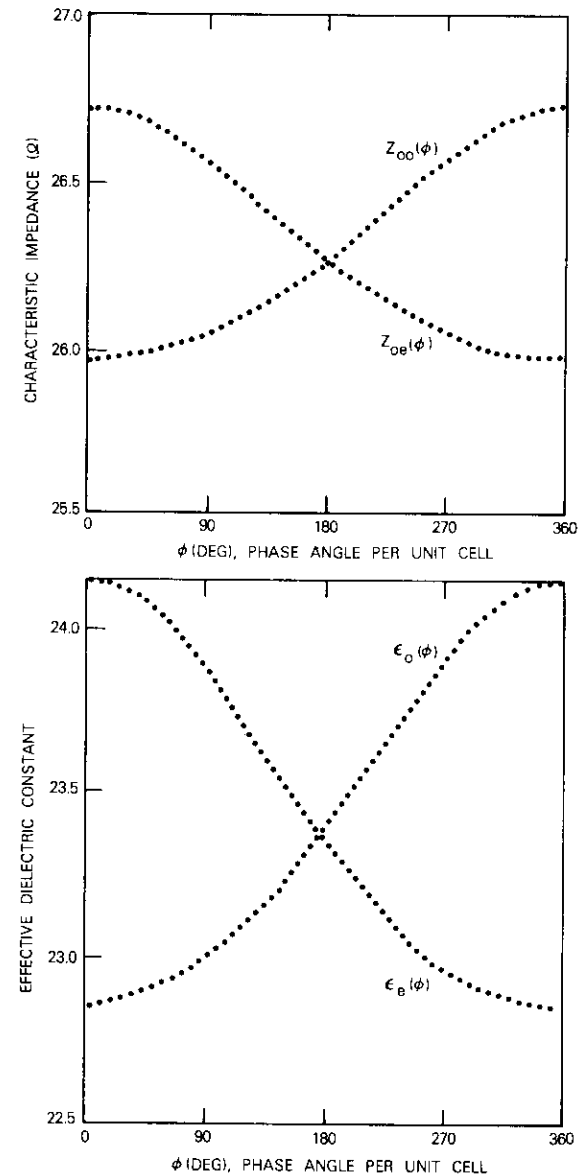


Figure 5. Normal Mode Line Parameters vs Phase per Unit Cell  
a. Even and Odd Mode Characteristic Impedance  
b. Even and Odd Mode Effective Dielectric Constants

where  $M$  is the number of unit cells in the overall meander line structure. Figure 6 shows the computed delay versus frequency for the circuit shown in Figure 2. The small microstrip discontinuities in the bends were neglected in the theoretical analysis.

**Design considerations**

The computed group delay of Figure 5 agrees with the experimental delay of Figure 4 except that the microstrip dispersion effect should also be considered in the quasi-TEM normal mode dielectric constants. The microstrip dispersion effect must be included in the design, particularly for a high order of passband frequencies. The dispersion effect of a single microstrip line on BaTi<sub>4</sub>O<sub>9</sub> is well-known [3], [6], and approximate dispersion formulas are available for a pair of tightly coupled microstrip lines [7]. The experimental meander line of Figure 2 is a loosely coupled ( $S/H_1 = 5.7$ ) microstrip array, and the single microstrip dispersion equation provides a correction to the frequency response, which is particularly useful at band center.

The  $k$ th order passband center frequency,  $f_{ok}$ , is given by

$$f_{ok} = \sqrt{\frac{\epsilon_e(0)}{\epsilon_e(f)}} f'_{ok} \tag{3}$$

where  $f'_{ok}$  is the  $k$ th band center frequency computed from the quasi-TEM normal mode input parameters. The effective dielectric constant of the microstrip line at  $f$  [6] is  $\epsilon_e(f)$ . The corrected group delay,  $\tau_o$ , at band center is

$$\tau_o = \tau_d [1 + \Delta(f)] \tag{4}$$

where  $\tau_o$  is the band center group delay calculated from the quasi-TEM normal mode parameters, and  $\Delta(f)$  is given by Reference 8 as

$$\Delta(f) = \frac{\epsilon_r - \epsilon(0)}{\epsilon_e(f)} \frac{G(f/f_p)^2}{[1 + G(f/f_p)^2]^2} \tag{5}$$

The parameters,  $G$  and  $f_p$ , are defined in References 3 and 6.

A broadband design of meander line delay elements can be realized by decreasing the length,  $L$ , of the unit cell. For a fixed group delay, the number of unit cells must be increased accordingly. Figure 7 is an example of

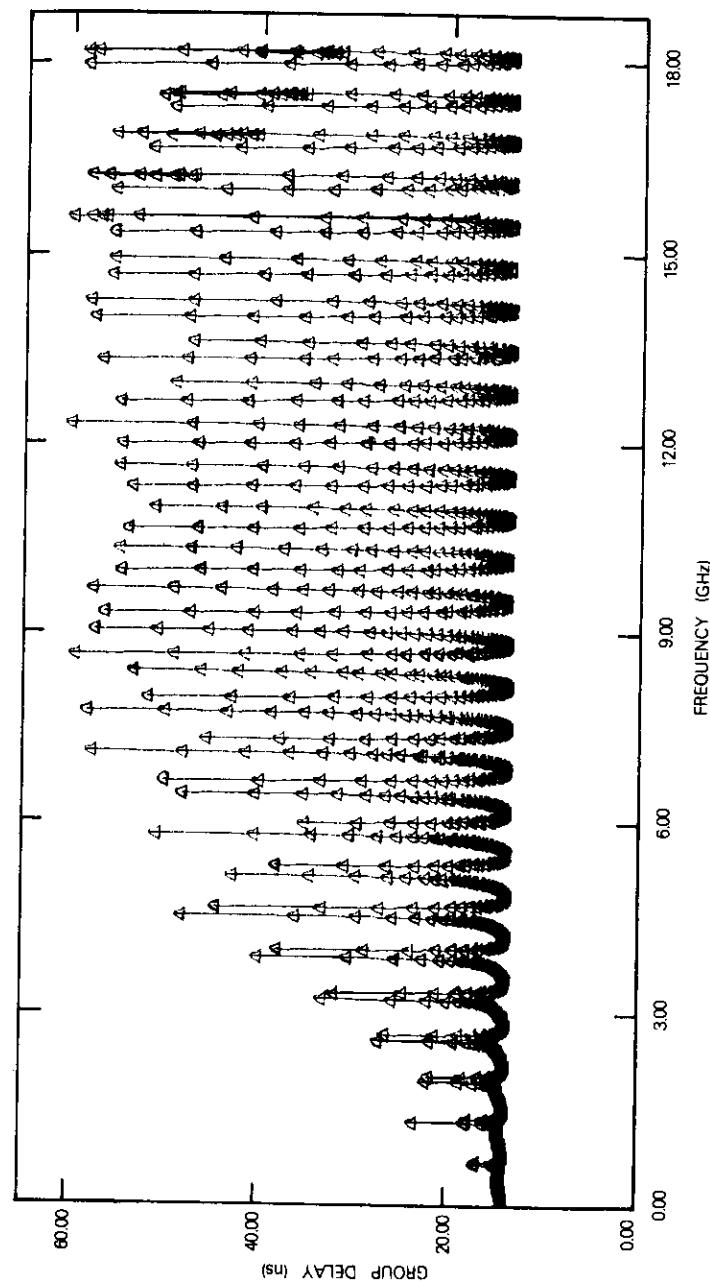


Figure 6. Computed Group Delay vs Frequency Using Quasi-TEM Normal Mode Parameters

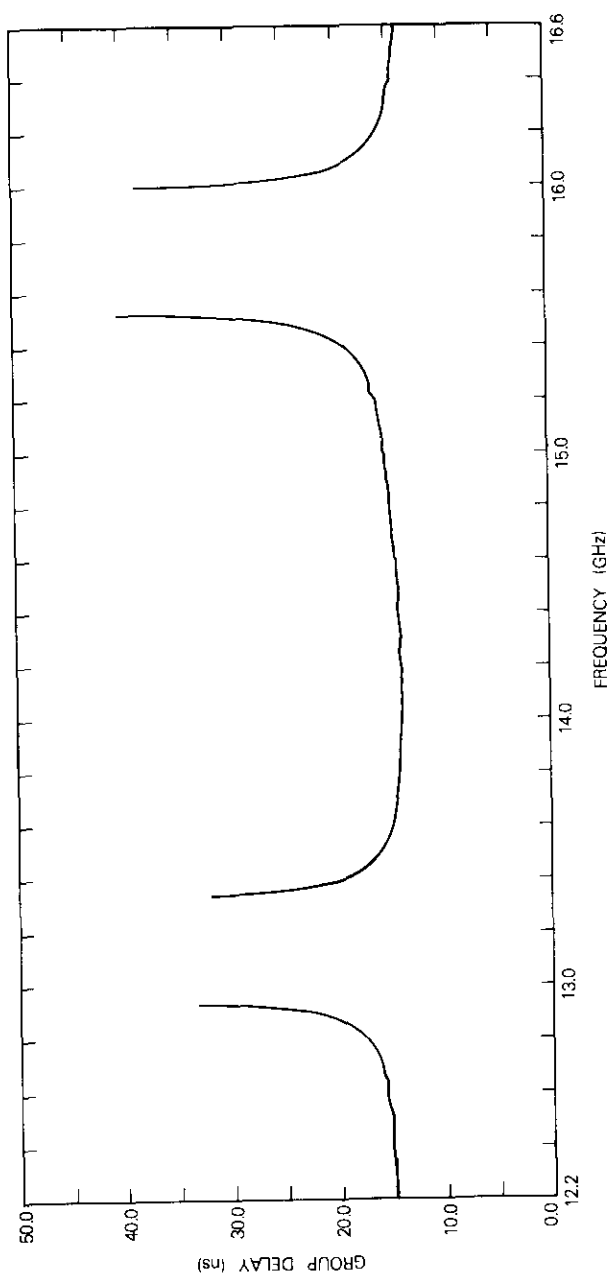


Figure 7. A Theoretical Broadband Delay Response

a theoretical broadband delay design for the 14-GHz band with a loosely coupled ( $S/H_1 = 5.7$ ) microstrip meander line. The length of the unit cell is one-fourth that shown in Figure 2, and the number of unit cells is increased four times. The theoretical response and the experimental correction factors must be used for a broadband design.

When the adjacent line spacing ( $S/H_1$ ) is decreased, the bandwidth decreases rapidly as the number of passbands increases. A theoretical computation on a microstrip meander line with  $S/H_1 = 1.0$  showed that the broadband delay application of the tightly coupled meander line should be limited to low-order passbands.

### Temperature-stable MIC delay elements

A temperature-stable 1-symbol delay element is required for the implementation of a differentially coherent quaternary PSK (DQPSK) onboard regenerative repeater [4]. Recently, a DQPSK demodulator module was designed using MICs to detect 120-Mbit/s data directly at the 14-GHz up-link frequency [9]. A compact 14-GHz MIC parallel-coupled 16-ns delay filter, photo-etched on a fused silica substrate, showed a fractional delay temperature stability of  $-5.3 \times 10^{-6}$  parts/ $^{\circ}\text{C}$  at the band center frequency [10]. The temperature stability in the fused silica MIC filter was mainly determined by the dielectric constant thermal characteristic, and a temperature compensated scheme was devised [11] for the MIC filter design. The usable bandwidth of the delay filter was about 120 MHz.

A rather simple, broadband microstrip  $\text{BaTi}_4\text{O}_9$  delay line was developed using a short sapphire (single crystal  $\text{Al}_2\text{O}_3$ ) microstrip for temperature compensation [8]. The phase temperature coefficient was  $0.6 \times 10^{-6}$  parts/ $^{\circ}\text{C}$  in the temperature range of  $23^{\circ}\text{C} \pm 30^{\circ}\text{C}$ . The bandwidth is essentially unlimited.

The coupled microstrip meander line can be used to design a compact delay element; the temperature compensation technique using a negative dielectric temperature coefficient, such as in  $\text{BaTi}_4\text{O}_9$ , can also be applied to obtain a near zero temperature coefficient. The bandwidth can be adjusted in the design of the unit cell.

### Conclusions

The periodic comb-type bandpass characteristic was investigated up to the 26th order of passband frequency on a loosely coupled microstrip meander line. A theoretical analysis of meander line group delay was

conducted using a numerical relaxation program, and the results were obtained using quasi-TEM normal mode parameters. The experimental data agree with the theoretical results when the inherent microstrip dispersion is considered.

A broadband group delay response can be obtained with shorter unit cell length. The total number of unit cells is determined from the required group delay at the band center frequency. Reduced circuit loss requires wide conductor strips, which should be within the microstrip mode restriction at the design frequency. An ultra-stable temperature characteristic in group delay can be obtained by applying simple passive circuit compensation [8] to BaTi<sub>4</sub>O<sub>9</sub> microstrip.

### Acknowledgment

The authors wish to thank Dr. J. A. Weiss of MIT Lincoln Laboratory for the computed normal mode parameters and Mr. W. J. Getsinger for helpful technical discussions.

### References

- [1] J. A. Weiss, "Dispersion and Field Analysis of a Microstrip Meander-Line Slow-Wave Structure," *IEEE Transactions on Microwave Theory and Techniques*, MTT-22, December 1974, pp. 1194-1201.
- [2] R. Crampagne and M. Ahmadpanah, "Meander and Interdigital Lines as Periodic Slow-Wave Structure, II. Applications to Slow-Wave Structure," *International Journal of Electronics*, 1977, Vol. 43, pp. 33-39.
- [3] Y. S. Lee, W. J. Getsinger, and L. R. Sparrow, "Barium Tetratitanate MIC Technology," *IEEE Transactions on Microwave Theory and Techniques*, MTT-27, July 1979, pp. 655-660.
- [4] Y. S. Lee, "Simulation Analysis for Differentially Coherent Quaternary PSK Regenerative Repeater," *COMSAT Technical Review*, Vol. 7, Fall 1977, pp. 447-474.
- [5] J. A. Weiss, Private Communication, October 12, 1978.
- [6] W. J. Getsinger, "Microstrip Dispersion Model," *IEEE Transactions on Microwave Theory and Techniques*, MTT-21, January 1973, pp. 34-39.
- [7] W. J. Getsinger, "Dispersion of Parallel-Coupled Microstrip," *IEEE Transactions on Microwave Theory and Techniques*, MTT-21, March 1973, pp. 144-145.
- [8] Y. S. Lee and W. H. Childs, "Temperature Compensated BaTi<sub>4</sub>O<sub>9</sub> Microstrip Delay Line," to be presented at the 1979 *IEEE MTT-S International Microwave Symposium Digest*, pp. 419-421.

- [9] C. Mahle, W. H. Childs, and A. Berman, "A DQPSK Satellite Transponder Using 14-GHz MIC Technology," *EASCON 1978 Record*, pp. 411-416.
- [10] Y. S. Lee, "14-GHz MIC 16-ns Delay Filter for Differentially Coherent QPSK Regenerative Repeater," *1978 IEEE MTT-S International Microwave Symposium Digest*, pp. 37-40.
- [11] F. Assal, A. Berman, and C. Mahle, "Temperature-Compensated MIC Filter for On-Board Satellite Regenerators," 8th European Microwave Conference, September 1978, Paris, France, *Conference Proceedings*, pp. 344-350.



Young Soo Lee received a B.S. (1963) and an M.S. (1967) in electronics engineering from Seoul National University and M.S. (E.E.) and Electrical Engineer degrees from M.I.T. (1969). Since September 1969, he has been a member of the technical staff at COMSAT Laboratories where he has specialized in the development of microwave circuits and subsystems for communications satellites. He has contributed to the development of an onboard regenerative repeater for future digital satellite communications systems. His current research interest concerns fiber and integrated optical communications technology. He is a member of IEEE.

Richard C. Trushel received a B.S. from St. Louis University and an M.S. from the University of Iowa. He joined COMSAT Laboratories in 1969 as a member of the technical staff. Since that time, he has performed various types of computer programming. For the past four years, he has worked in the Computer Center for the Engineering Applications Department. He has recently transferred to COMSAT West in Palo Alto, California.



## **12-GHz 10-W amplifier using GaAs IMPATT diodes**

S. M. CHOU

(Manuscript received July 9, 1979)

### **Abstract**

An experimental 10-W 3-stage GaAs IMPATT amplifier has been developed for the 12-GHz communications band. The amplifier uses seven high-efficiency Read-profile IMPATT diodes and employs Wilkinson-type power hybrids to combine the power of two and four individually matched diodes in the last two stages. The overall DC to RF efficiency is 9 percent, and the amplifier can operate over a 500-MHz bandwidth with 10-dB gain.

Gupta's lumped equivalent circuit was used for the computer-aided amplifier design. Both calculated and measured frequency responses for different input power levels are in reasonable agreement. The power combiners and the amplifier bias circuits are constructed in microwave integrated circuit (MIC) form using 0.38-mm-thick fused silica. A small coaxial section with a coaxial transformer connects each IMPATT diode to an MIC and then to a stripline circulator. The amplifier module is mounted on a heat sink which is cooled by free convection.

### **Introduction**

Since the discovery of the avalanche transit-time diode that can provide high-frequency negative resistance, the replacement of traveling wave tubes (TWTs) with IMPATT devices operated as amplifiers has often been considered for communications applications which

require moderate power and solid-state reliability. GaAs Read-profile IMPATT diodes capable of generating several watts of saturated continuous wave (CW) power in the Ku-band are presently available. If the output power of a number of IMPATT amplifiers is combined at the output stage, an amplifier suitable as a satellite transmitter may be feasible.

This paper describes the design and performance of an experimental IMPATT amplifier which delivers 10 W of CW output power in the 11.7- to 12.2-GHz band. The 3-stage amplifier provides 10-dB overall gain with more than 9-percent DC to RF conversion efficiency.

### General description

Two schematics of an amplifier with three stages using seven IMPATT diodes and slightly different power combining techniques are shown in Figure 1. The performances are the same, except that the output power of the type B arrangement is about 0.5 dB better because it has less combining circuit loss. The type A amplifier, which is shown in Figure 2 without the cover, consists of an MIC power combiner and bias circuit on a fused silica substrate connected between a coaxial section containing the IMPATT diode and a stripline circulator.

The coaxial diode module section permitted the rapid interchange of diodes during amplifier development. A comparable all-MIC single-diode amplifier module has been built and tested. The results indicate that the amplifier can be easily converted to an all-MIC model with identical performance and smaller size. The input and output are SMA female connectors. Circulators with one port terminated are used as isolators at the input and output ends because of impedance matching and are used between the amplifier stages to add isolation.

The amplifier is mounted on a 15- × 25-cm heat sink. Seven current-regulated supplies, one to a diode, are packaged and mounted in a heat sink directly beneath the amplifier baseplate for each stage. A 50-V DC source supplies the bias power for all diodes. Power switches and a pilot light for each stage are mounted on a small panel beside the heat sink.

### IMPATT diode

The active devices used in this amplifier are Raytheon MS927A diodes. During operation in the oscillator mode, this Read-profile GaAs

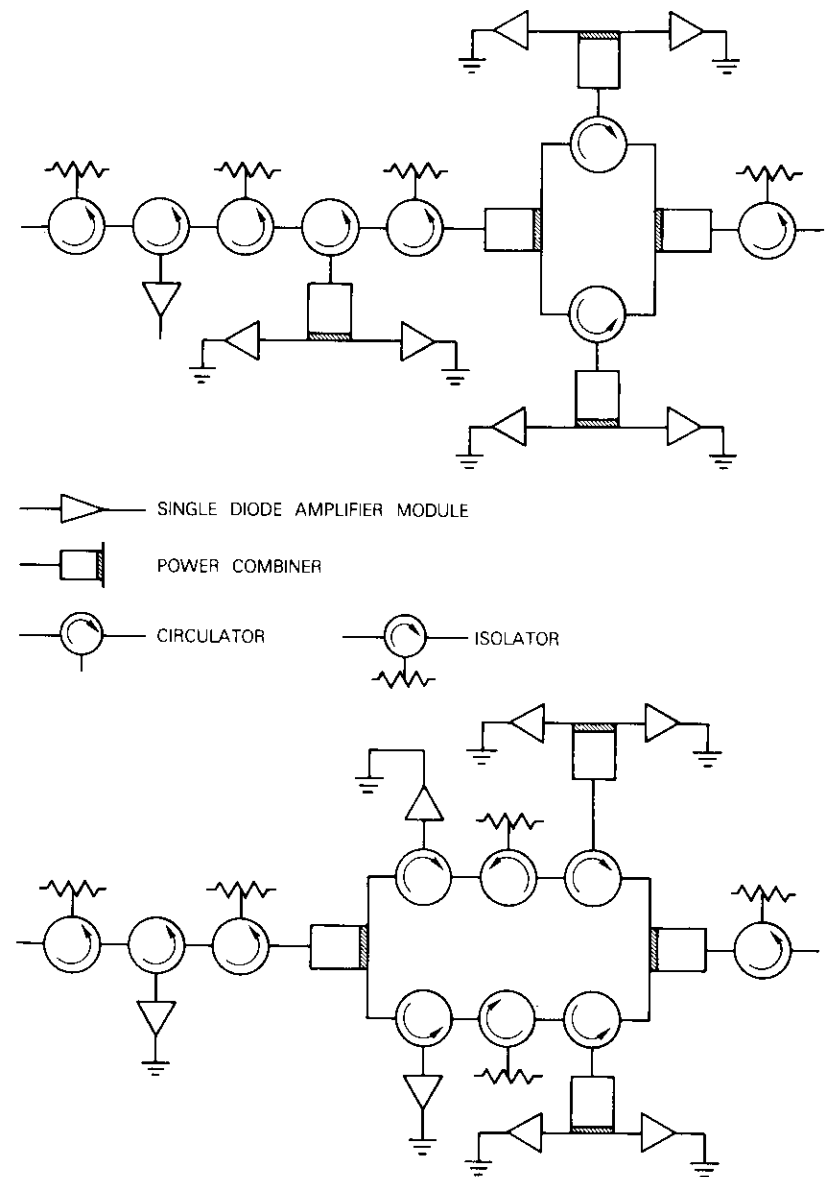


Figure 1. Schematics of 12-GHz IMPATT Amplifier  
a. Type A b. Type B

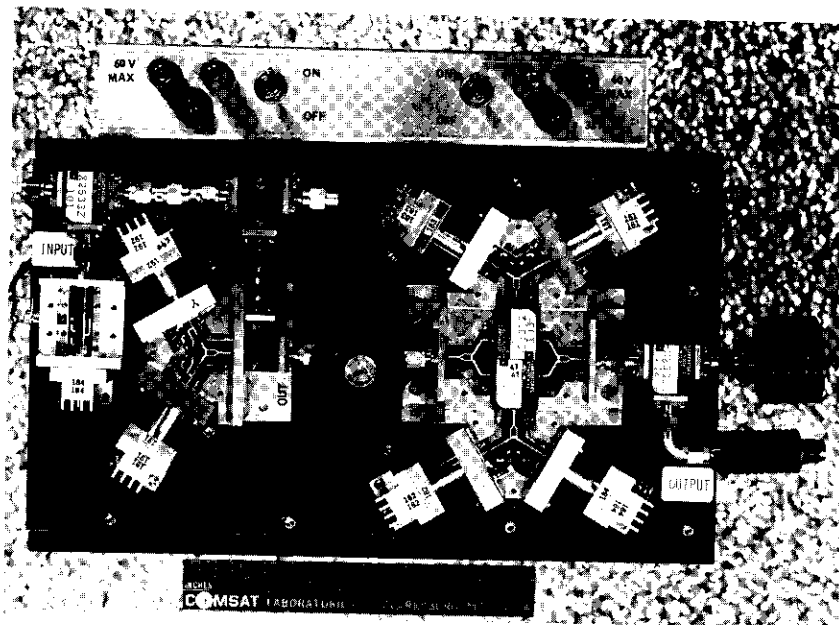


Figure 2. Top View of 12-GHz IMPATT Amplifier

IMPATT diode provides 2.5-W output power at 13 GHz with more than 20-percent DC to RF efficiency. The diode thermal impedance is approximately 18°C/W.

### Amplifier module design

In the design of the single-port, single-diode reflection amplifier module which was the basic building block of this amplifier chain, Gupta's [1], [2] lumped, frequency-independent equivalent circuit was adopted to characterize the large-signal behavior of the IMPATT diode. The equivalent circuit shown in Figure 3 has been used in conjunction with a conventional computer-aided circuit analysis program to generate the circuit element values of the broadbanding network.

The values for the lumped elements constituting the equivalent circuit of the IMPATT diode were determined numerically by fitting the equivalent circuit admittance to the diode admittance obtained experimentally by small-signal measurement. Large-signal behavior is represented by expressing both elements in the inductive branch of the

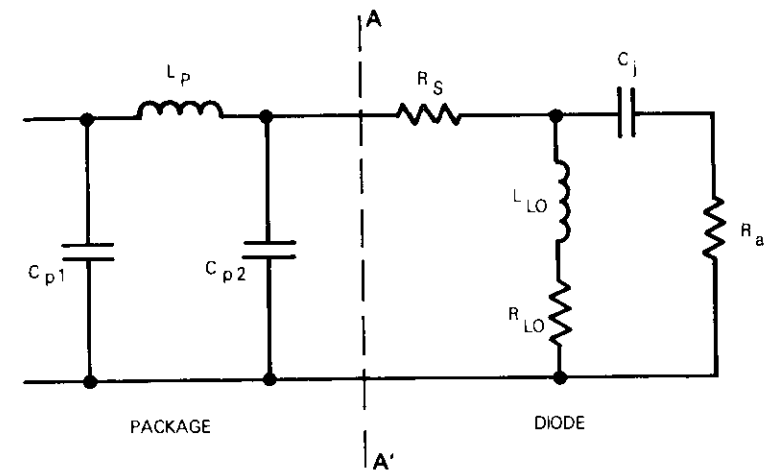


Figure 3. Lumped Equivalent Circuit for Packaged IMPATT Diode

circuit as frequency independent quadratic functions of the peak voltage  $V_1$  across the diode at the reference plane A-A' in Figure 3. Thus,

$$R_{LO} = R_{SO}(1 + \alpha_1 V_1 + \alpha_2 V_1^2)$$

$$L_{LO} = L_{SO}(1 + \beta_1 V_1 + \beta_2 V_1^2)$$

$$V_D(t) = V_1 \sin \omega t$$

where  $R_{SO}$  and  $L_{SO}$  are the small-signal values of the elements and  $\alpha_1$ ,  $\alpha_2$ ,  $\beta_1$ , and  $\beta_2$  are nonlinearity constants of the elements of the inductive branch of equivalent circuit. The values of the four constants given in Reference 1 provide a good fit of the calculated diode equivalent circuit admittance  $Y_{eq}(V_1, \omega)$  to the measured large-signal diode admittance. This admittance was obtained indirectly by measuring single-tuned MS927A diode amplifier gain at various input power levels. Typical parameters of the equivalent circuit of the MS927A GaAs IMPATT diode used for amplifier design are given in Table 1. These parameters are used in a computer program to calculate and plot large-signal admittances of the same diode in an admittance plane (Figure 4) as a function of frequency and peak sinusoidal voltage across the diode.

TABLE 1. TYPICAL PARAMETERS OF THE EQUIVALENT CIRCUIT

Parameter	Value	Parameter	Value
$C_j$	0.2 pF	$\beta_1$	0.003
$R_s$	50 ohms	$\beta_2$	0.00007
$R_{SO}$	32 ohms	$\alpha_1$	0.01
$L_{SO}$	2.5 nH	$\alpha_2$	0.0008
$R_a$	-44 ohms	$C_{p1}$	0.08 pF
$L_p$	0.4 nH	$C_{p2}$	0.22 pF

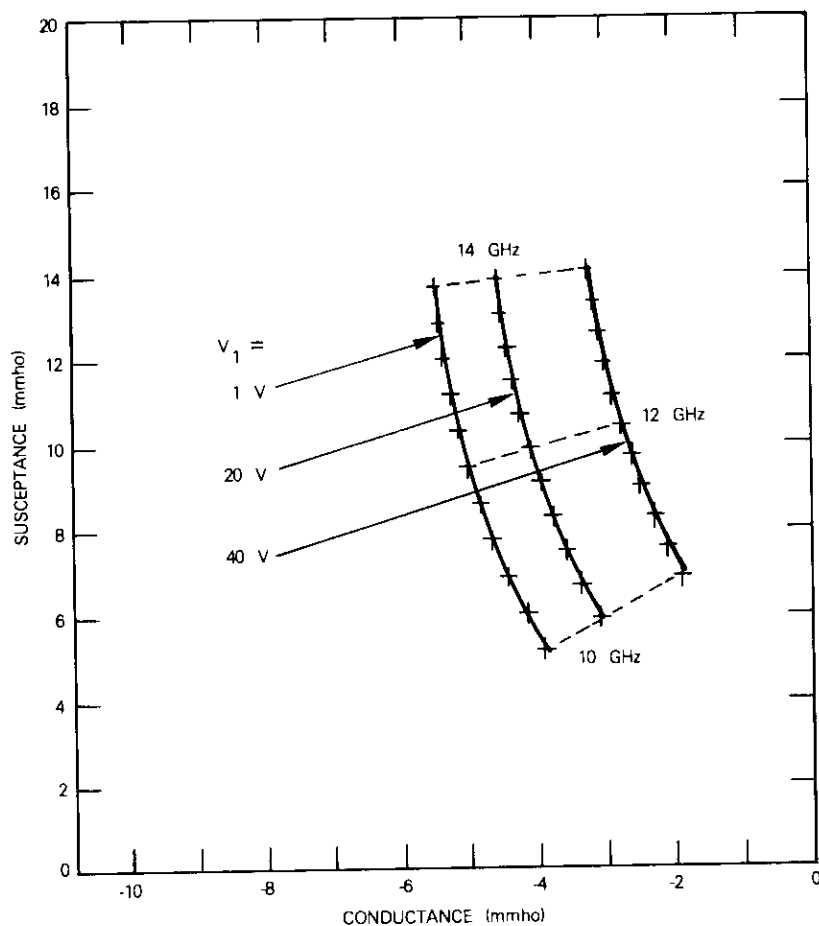


Figure 4. The Admittance of GaAs IMPATT Diode MS927A Calculated from Gupta's Frequency Independent Equivalent Circuit

Based on these equivalent circuit parameters, both single-tuned and double-tuned single-diode amplifier modules have been designed and tested. Figures 5 and 6 illustrate the good correlation between the predicted frequency response of the module to the different input levels and the actual measured values.

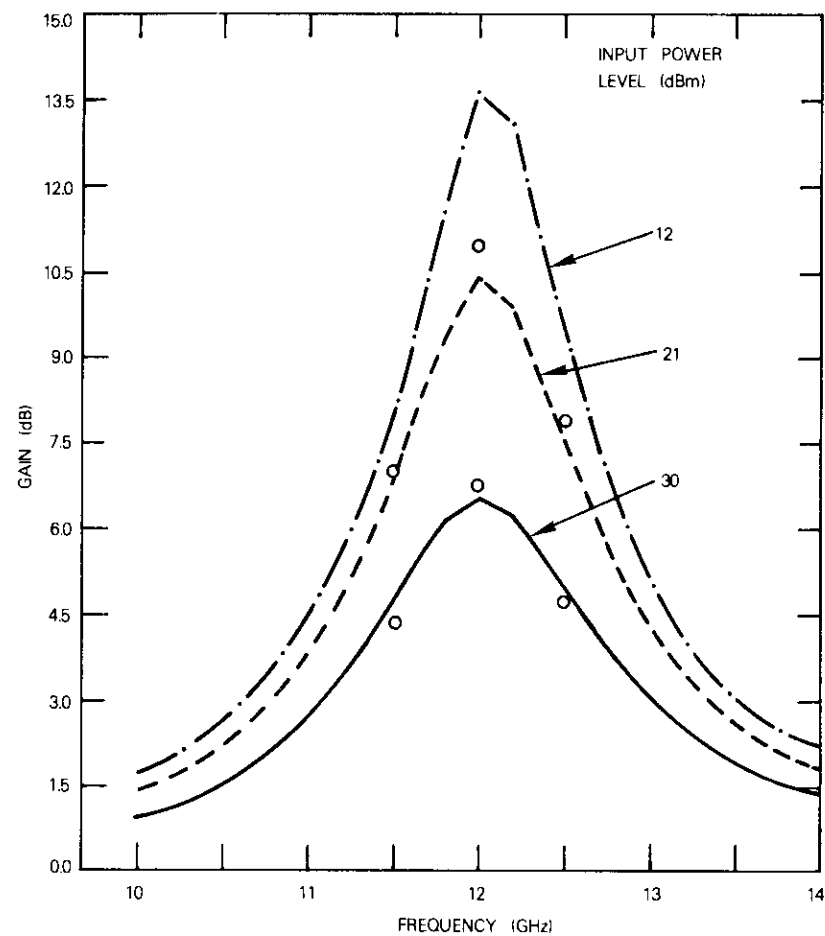


Figure 5. Calculated Frequency Response of Single-Tuned Amplifier Module (small circles indicate measured gain)

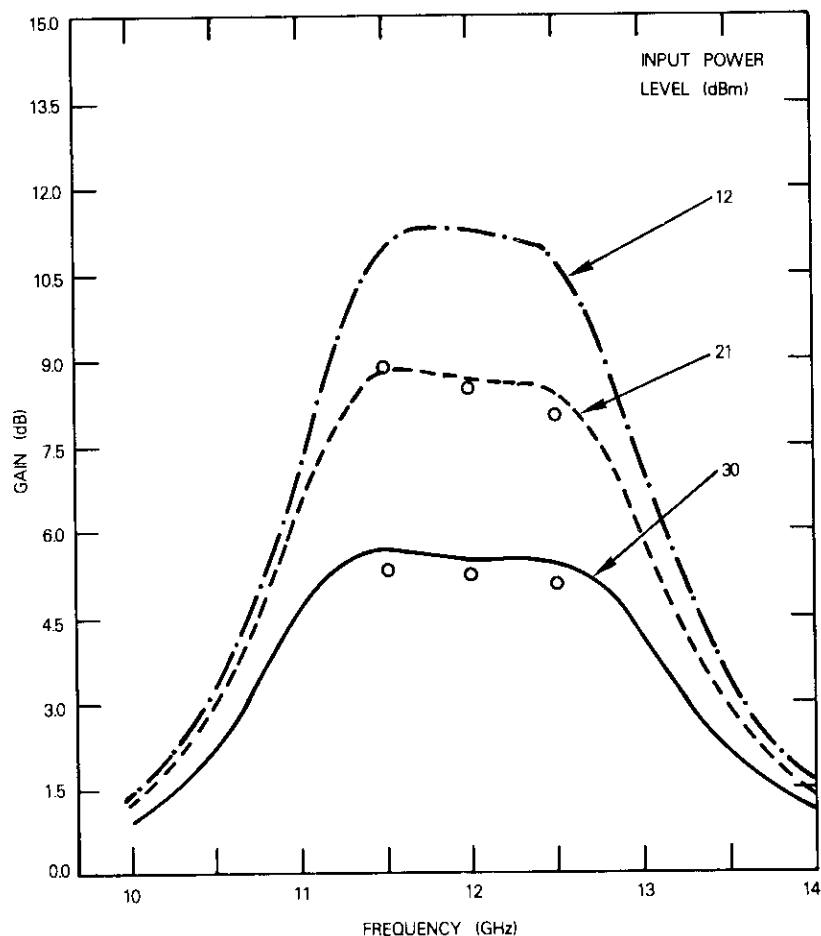


Figure 6. Calculated Frequency Response of Double-Tuned Amplifier Module (small circles indicate measured gain)

### Circuit fabrication

Figure 7 is a cutaway view of the single-diode amplifier module, which consists of an MIC DC block and bias feed circuit, MIC to coaxial transition, a double-tuned transformer, and the diode. The packaged diode is end-mounted in a coaxial line and recessed into the ground

plane to cancel some of its parasitic inductance for operating frequency adjustment. After the operating frequency is centered at the desired level by selecting a holder with the appropriate recess depth, the recessed diode unit can be plugged into any diode module in the amplifier chain and give the same performance without further tuning. This feature especially simplifies the assembly work for the last two power combining stages and reduces the possibility of diode burn-out due to improper RF tuning.

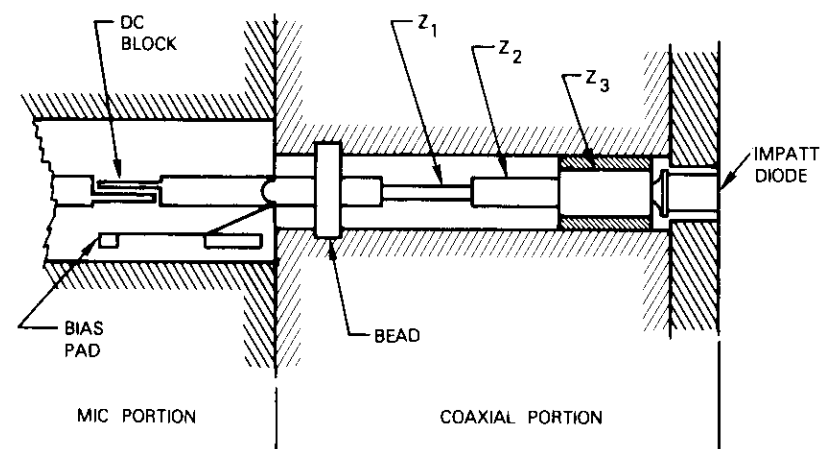


Figure 7. Cutaway View of the Single-Diode Amplifier Module ( $Z_1 = 116\Omega$ ,  $Z_2 = 102\Omega$ , and  $Z_3 = 20\Omega$ )

Three quarter-wavelength coaxial stepped impedance transformer sections are used for broadband impedance matching of the IMPATT diode to the  $50\Omega$  line. A good RF contact between the transformer and diode cap is ensured by a disc spring finger. A  $50\Omega$  transition from coax to MIC occurs at the end where a dielectric bead is located. The MIC is fabricated on a 0.38-mm-thick fused silica substrate. A coupled quarter-wavelength microstrip line with a 0.038-mm gap provides a DC break, which confines the high voltage to the diode circuit; the impedance in the direction of the circulator is  $50\Omega$ . A bandstop filter in the bias line prevents the transition of any in-band signal to the bias circuit. The rejection of this filter from 11 to 13 GHz is greater than 40 dB. The bias circuit continues further in a low-pass feedthrough to provide a low resistance at DC and prevent low-frequency oscillation.

### Power combiner

The power splitting and combining circuit used in the second and third stages are typical 3-port Wilkinson power dividers. The insertion loss of the divider with DC block and a section of 50 $\Omega$  line is 0.2 dB. The isolation between output ports exceeds 20 dB.

### Amplifier performance

The performance of the amplifier is given in Table 2.

Typical swept frequency gain response of a complete amplifier is shown in Figure 8 as line A. Lines B and C represent gain response

TABLE 2. AMPLIFIER PERFORMANCE

Frequency	11.7 to 12.2 GHz
Input Power	30 dBm
Output Power	40 dBm (typical)
Net Gain	10 dB
Gross Gain per Single-Diode Module	5.4 dB
Input/Output VSWR	1.25:1 max
DC to RF Efficiency	9 percent min.
Circulator Insertion Loss	0.3 dB per path

when the third stage and the last two stages are turned off, respectively; clearly, the gain response of each stage is flat. The insertion loss of the complete amplifier in the off condition is about 6 dB. Some of this loss is contributed by connectors and extra transmission lines which are necessary for connecting the stages in this breadboard model. The DC to RF conversion efficiency can be further improved by eliminating connectors and interconnecting all the stages to form a complete MIC design.

The amplifier was designed for optimum efficiency at a normal input power level of 1 W. As the input signal level drops 13 dB below normal, the amplifier tends to be unstable. An input level monitor may be used in a transmitter chain to disable the bias supply in the absence of a sufficient input RF power level to prevent oscillation.

### Conclusion

A 10-W 12-GHz power amplifier which exhibits state-of-the-art performance has been realized using GaAs IMPATT diodes. Computer-

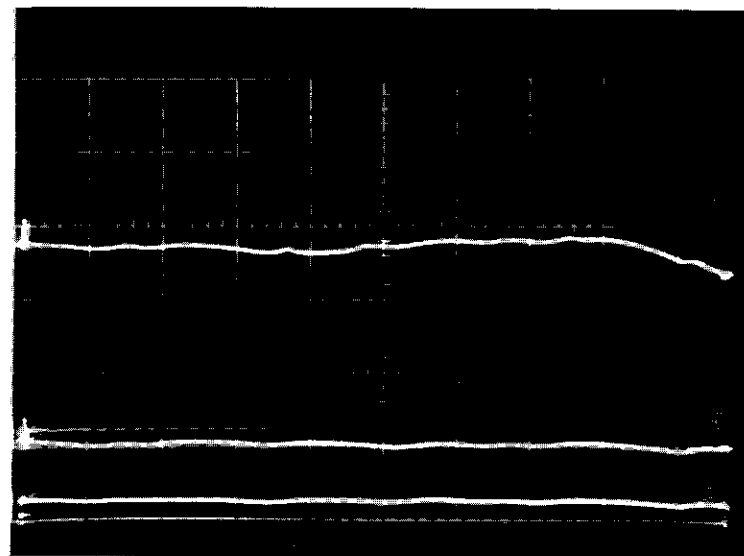


Figure 8. Typical Swept Frequency Gain Response from 11.6 to 12.3 GHz (vertical scale: linear in power 2.5 W/cm, horizontal scale: 70 MHz/cm)

a. All three stages on b. First two stages on c. First stage on

aided design techniques using Gupta's equivalent circuit and test results have been proven effective.

### Acknowledgments

The author is grateful to Messrs. A. Berman, W. Getsinger, and M. Barrett for their technical help and encouragement. The significant help in the fabrication phase from R. Kessler and J. Molz is also highly appreciated.

### References

- [1] Madau-Sudan Gupta, "Large Signal Equivalent Circuit for IMPATT-Diode Characterization and Its Application to Amplifier," *IEEE Transactions on Microwave Theory and Techniques*, MTT-21, No. 11, November 1973, pp. 689-694.

- [2] Madau-Sudan Gupta, "A Small-Signal and Noise Equivalent Circuit for IMPATT Diode," *IEEE Transactions on Microwave Theory and Techniques*, MTT-21, No. 9, September 1973, pp. 591-594.
- [3] M. E. Hines, "Negative-Resistance Diode Power Amplification," *IEEE Transactions on Electronic Devices*, ED-17, January 1979, pp. 1-8.
- [4] I. Tatsuguchi et al., "A 10-W, 6-GHz GaAs IMPATT Amplifier for Microwave Radio Systems," *Bell System Technical Journal*, Vol. 55, No. 2, February 1976, pp. 167-182.
- [5] R. W. Laton et al., "Characteristics of IMPATT-Diode Reflection Amplifiers," *IEEE Transactions on Microwave Theory and Techniques*, MTT-21, No. 11, November 1973, pp. 668-680.



*Su Min Chou received a B.S.E.E. from the Chinese Naval College of Technology in 1954, an M.S. from Chiao Tung University in 1961, and a Ph.D. from the University of Utah in 1967. Prior to joining COMSAT Laboratories in 1968 he was a research assistant at the University of Utah and an engineer in a Chinese shipyard. While he was at COMSAT he developed low-noise amplifiers of various frequency bands and solid-state high-power amplifiers.*

Index: rain depolarization, measurement, attenuation

## **Rain depolarization measurements at 4 GHz**

D. J. KENNEDY

(Manuscript received July 27, 1979)

### **Abstract**

Rain depolarization was measured at the Lario (Italy) INTELSAT earth station for a 15-month period. The cross-polarization discrimination (XPD) was determined for a circularly polarized 4-GHz carrier radiated by a geostationary satellite and received at Lario along a 25° elevation angle slant path. During the same period, 1,412 mm of normalized annual rainfall was measured, and the observed rain rate distribution was found to closely match a Rice-Holmberg distribution for  $M = 1,412$ ,  $\beta = 0.065$ . Continuous radiometric recordings of the 11.6-GHz sky temperature along the same path were used to obtain attenuation values. The radiometrically determined attenuation demonstrated good agreement with a model based on measured rain rates and C.C.I.R. path lengths.

The measured XPD was less than 23.8 dB for 0.01 percent of the time; the lowest sampled value was 19.2 dB. A comparison of the observed depolarization with several semiempirical models based both on measured rain and attenuation distributions and on C.C.I.R. concepts showed reasonable agreement, which improved for occurrence levels below 0.01 percent. As in previous measurement programs, the measured XPD was usually lower (worse) than values obtainable from the models.

### **Introduction**

The increasing implementation of dual-polarization frequency reuse

techniques in the INTELSAT system has made it essential to characterize as accurately as possible the amount of system performance degradation due to rain induced depolarization. This paper reports on the results of depolarization measurements at the Lario, Italy, INTELSAT earth station. A down-link 4-GHz circularly polarized continuous wave (CW) carrier radiated by the INTELSAT Atlantic Major Path satellite (INTELSAT IV-A F-2) was received by a 3.9-m parabolic antenna at an elevation angle of approximately 25°. In addition to depolarization measurements, simultaneous radiometric observations of the 11.6-GHz sky temperature were made along the same path, and rain accumulation data were collected using a colocated tipping bucket gauge. The data collection period extended from March 3, 1977, to June 10, 1978.

The Lario climate may be characterized as continental-subtropical-mountainous with a long-term mean annual rainfall of 1,200 mm; however, over the measurement period, the recorded accumulation was 1,412 mm normalized to one year. This climate differs from that encountered on prior measurement programs at Taipei, Taiwan, and Ibaraki, Japan. Both of these sites experience greater annual rainfall (3,620 mm and 1,680 mm, respectively) and more importantly, a considerably greater fraction of rain with rates exceeding 30 mm/hr. The rainfall at Lario was characterized by low-rate extended duration events occurring over a widespread area, and the 25° elevation angle was intermediate with respect to that of the previous measurement programs (20° and 35°, respectively). Therefore, less depolarization was expected at Lario than at either of the previous sites. In fact, the lowest measured XPD was 19.2 dB, and the cross polarization at the 0.01-percent occurrence level was 23.8 dB; the values at the same occurrence level were 18.3 dB and 22.4 dB for Taipei and Ibaraki, respectively.

In this program the orthogonal linear components and their relative phase angle were directly measured. This approach, which is relatively insensitive to the residual depolarization of both satellite and earth station antennas, is especially suitable for the field environment. It eliminates most of the calibration error and ambiguity that can occur in direct measurement of circular components. In addition, since both linear components are 20 to 30 dB stronger than the circular cross-polarized signal, only small antennas and modest receiving equipment are required at the earth station to provide an adequate signal-to-noise ratio. One objective of the program has been the comparison of actual measurements with empirical and theoretical estimates from available propagation models of depolarization.

## Description of the measurement system

### Measurement method

The principal objective of the program was to determine long-term occurrence statistics of rain induced depolarization at 4 GHz. As the signal was nominally circularly polarized, depolarization was determined in terms of the circular XPD. With reference to Figure 1, this quantity for a transmitted right-hand circularly polarized (RHCP) wave may be defined as

$$XPD_R = 10 \log_{10} \frac{S_{cR}}{S_{xL}} \text{ dB} \quad (1)$$

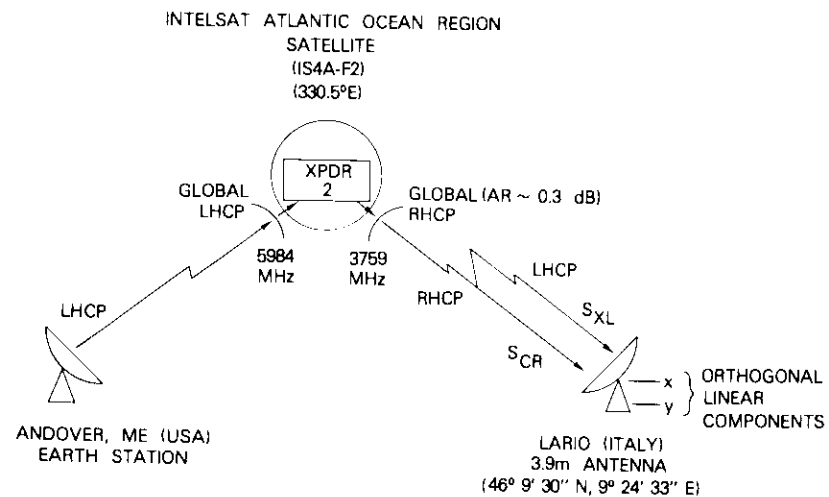


Figure 1. Overview of Depolarization Measurement System

and for a left-hand circularly polarized (LHCP) signal as

$$XPD_L = 10 \log_{10} \frac{S_{cL}}{S_{xR}} \text{ dB} \quad (2)$$

where  $S$  refers to power, subscripts  $c$  and  $x$  indicate the copolarized and cross-polarized components, and  $R$  and  $L$  denote received RHCP and LHCP waves. In system performance studies the parameter of interest is usually the cross-polarization isolation (XPI), which depends

on two transmitted signals of orthogonal polarization. For circular polarization with RHCP and LHCP waves transmitted, the XPI is the (positive) dB difference between the received copolarized signal (*e.g.*, RHCP) and the orthogonally polarized signal (*e.g.*, LHCP) levels received in the copolarized channel. That is,

$$XPI_R = 10 \log_{10} \frac{S_{cR}}{S_{xR}} \text{ dB} \quad (3)$$

and

$$XPI_L = 10 \log_{10} \frac{S_{cL}}{S_{xL}} \text{ dB} \quad (4)$$

For pure circular polarization, it can be shown that

$$XPD_R = XPD_L = XPI_R = XPI_L \quad (5)$$

and even for linear polarization the distinction at 4 GHz between any of the four quantities is not significant.

The XPD given by equation (1) can be determined by directly measuring the received copolarized RHCP signal and simultaneously recording its level as received in a cross-polarized channel. Measurement accuracy is proportional to the calibration precision of these two channels in the receive chains from the dual-polarized feed to the data recorder. In practice this calibration may be difficult, and hence assumptions must be made about gains and losses in the two signal paths. The clear sky isolation between the two signal paths must be of the order of 40 dB to prevent measurement ambiguity. At lower levels of isolation, antenna effects cannot be distinguished from propagation medium effects on the basis of amplitude measurements alone; a measurement of the phase difference can, however, resolve the two contributing components. Although it is not precisely equivalent to obtaining high isolation between orthogonally polarized circular components, sufficient isolation can be achieved in practice by orthogonalizing the earth station receive system to the satellite transmit (slightly elliptical) polarization during clear sky conditions. This is especially important if the satellite axial ratio is about 1 dB (cross-polarization ratio of 24.8 dB) or worse. However, when adequate clear sky isolation is achieved, the cross-polarized component is ordinarily

relatively weak and increases only during rain events. Therefore, large receive antennas and/or low-noise narrow-bandwidth receiving systems are necessary.

For the Lario measurements, circular XPD was determined by using the measured amplitude and phase difference of two orthogonal linear components. Rain depolarization at 4 GHz depends almost entirely on the differential phase shift (*vis-a-vis* differential attenuation) between waves polarized parallel and perpendicular to the effective\* major axis of the oblate spheroidal raindrops. In such a case, the XPD can be expressed as

$$XPD = -20 \log_{10} \left[ \tan \left( \frac{\phi}{2} \right) \right] \text{ dB} \quad (6)$$

where  $\phi$  is the differential phase shift. The phase angle  $\phi$  may be directly measured as the phase difference between two orthogonal linear polarizations aligned with the effective major and minor axes. Since the effective canting angle is generally near  $0^\circ$ , the antenna polarization should be aligned with the local horizontal and vertical directions.

For other antenna tilt angles or effective canting angles  $\neq 0^\circ$ , a differential amplitude will be observed. If it is considered, an exact determination of  $\phi$  is possible. Otherwise, the estimate of  $\phi$  based on the phase-measurement will be lower than the actual; however, the error is relatively small for effective canting angles less than  $10^\circ$ . In the Lario measurements, the differential amplitude was not separately available, but a survey of the individual amplitude channels indicated that it was usually less than 0.5 dB during rain events. Failure to consider a 0.5-dB differential amplitude would indicate a calculated XPD approximately 1.2 dB greater than actual at a true XPD of 25 dB and about 0.3 dB greater at a true XPD of 20 dB.

This second measurement method based on the orthogonal linear components has two important advantages. First, the phase angle can be measured relative to clear sky conditions without the knowledge of either the absolute gain or phase for the two orthogonal channels. Therefore, no ambiguity can result from imprecision in the determi-

\*For an ensemble of drops, a distribution of major axes orientations or canting angles will be represented by one parameter, an average or effective canting angle.

nation of channel gain or absolute phase. In addition, since the linear components are each only 3 dB below the level of the optimally received circular polarization, smaller G/T receive installations become feasible.

### System configuration

Figure 1 shows the depolarization measurement system configuration. The down-link signal was radiated from the Atlantic INTELSAT IV-A F-2 satellite located at 330.5°E longitude at an e.i.r.p. of approximately 15 dBW. Although it is not crucial to the experimental technique, the axial ratio of the satellite transmitting antenna (in the direction of Lario) was better than 0.3 dB, which is quite good.

The Lario receive antenna was a Cassegrain design, 3.9 m in diameter, and fitted with a dual-orthogonal linearly polarized feed. The antenna orientation was fixed; tracking was not required due to the 3-dB beamwidth of about 1.6° and the stationkeeping of INTELSAT IV-A F-2 to within  $\pm 0.1^\circ$  in both longitude and declination. The antenna gain was 40.9 dB, and the cross-polarization ratio was better than 28 dB (over a  $\pm 0.5^\circ$  beamwidth). The elevation angle to the satellite was approximately 24.7°.

Figure 2 shows a block diagram of the equipment at Lario. The RF receiver was a Scientific Atlanta model 1750 phase/amplitude receiver with a phase accuracy of better than  $\pm 0.5^\circ$ . The 11.6-GHz radiometric receive terminal included a 2-m antenna oriented along the path to the satellite. A collocated tipping bucket rain gauge was employed to collect rain accumulation and rate data. The down-conversion occurred in two steps: from 4 GHz to 140 MHz at the antenna site and from 140 to 45 MHz at the electronics rack.

### Analysis of measurement technique

Since the measurement method used to obtain the circular XPD is not direct, the procedure must be analyzed. It is also important to discuss any limitations or errors caused by departure from the ideal in the satellite or earth station antennas. It will be shown that, if both the differential phase and amplitude between the two linear channels are measured, highly accurate circular XPD measurements are possible, regardless of conventional antenna limitations. If only the differential phase is measured, some error will be introduced which is related to a nonzero effective canting angle for the raindrops. However, in most

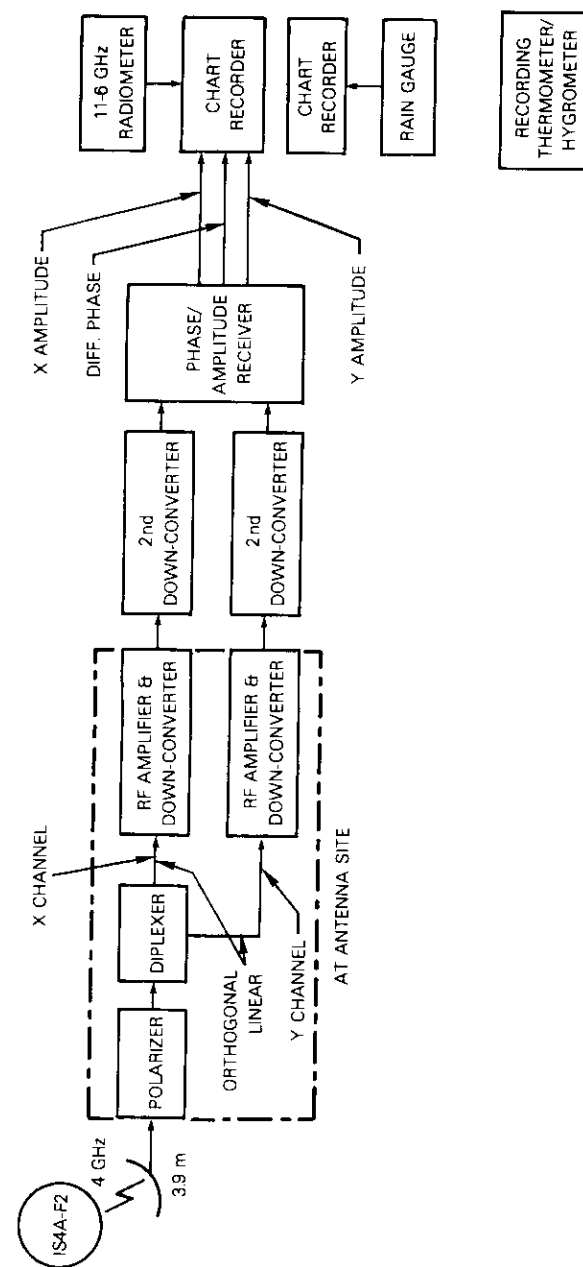


Figure 2. System Block Diagram

of the experimental cases, the canting is  $\leq 10^\circ$ , resulting in small differential amplitudes which introduce only slight inaccuracies.

The underlying theory of the method and the issue of nonideal antennas are addressed initially; for simplicity, potential sources of measurement are examined separately. However, this analysis technique can be easily extended to all factors concurrently operating. The polarization matrix approach is discussed in greater detail in References 1 through 3.

#### Determination of the circular cross-polarization discrimination

The fundamental definition of the circular XPD given by equation (1) may be written in terms of the received voltages as

$$XPD = 20 \log_{10} \frac{|E'_R|}{|E'_L|} \text{ dB} \quad (7)$$

where unnecessary subscripts have been omitted and the primes denote received fields. Received circular components are given by

$$\begin{pmatrix} E'_R \\ E'_L \end{pmatrix} = M_r^{-1} R^{-1} V^{-1} D V R M_t \begin{pmatrix} E_R \\ E_L \end{pmatrix} \quad (8)$$

where  $E_R$  and  $E_L$  are the transmitted circular components. For the Lario measurements,

$$\begin{pmatrix} E_R \\ E_L \end{pmatrix} = \begin{pmatrix} 1 \\ 0 \end{pmatrix} \quad (9)$$

The satellite transmit matrix for circular polarization is

$$M_t = \begin{pmatrix} m_{tR} & n_{tL} \\ n_{tR}^* & -m_{tL}^* \end{pmatrix} \quad (10)$$

with

$$m_t = \sin\left(\mu_t + \frac{\pi}{4}\right) e^{-i\sigma_t}, \quad n_t = \cos\left(\mu_t + \frac{\pi}{4}\right) e^{-i\sigma_t} \quad (11)$$

The axial ratio,  $r_t$ , is related to the angle  $\mu_t$  by

$$\mu_t = \cot^{-1} r_t \quad 1 \leq r_t \leq \infty \quad (12)$$

The tilt angle of the polarization ellipse is  $\sigma_t$ , measured counterclockwise from the horizontal, pointing from the transmitter toward the receiver. In the ideal case of perfect isolation circularly polarized antennas,

$$M_t = \begin{pmatrix} 1 & 0 \\ 0 & -1 \end{pmatrix} \quad (13)$$

Note that the values of  $n_{tL}$  and  $-m_{tL}^*$  are inconsequential when  $E_L = 0$ . Similarly, the receive antenna matrix for circular polarization is

$$M_r^{-1} = \begin{pmatrix} m_{rR}^* & n_{rR} \\ n_{rL}^* & -m_{rL} \end{pmatrix} \quad (14)$$

which for perfect circular polarization becomes

$$M_r^{-1} = \begin{pmatrix} 1 & 0 \\ 0 & -1 \end{pmatrix} \quad (15)$$

Since actual depolarization is most easily studied for linear components, the circular components may be transformed into equivalent linear components and transformed back by the rotation matrices  $R$  and  $R^{-1}$ :

$$R = \frac{1}{\sqrt{2}} \begin{pmatrix} 1 & 1 \\ i & -i \end{pmatrix} \quad (16)$$

$$R^{-1} = \frac{1}{\sqrt{2}} \begin{pmatrix} 1 & -i \\ 1 & i \end{pmatrix} \quad (17)$$

Similarly, the coordinate system may be rotated to axes aligned with the effective raindrop major and minor axes through the effective canting angle,  $\tau$ , via the matrix

$$V = \begin{pmatrix} \cos \tau & \sin \tau \\ -\sin \tau & \cos \tau \end{pmatrix} \quad (18)$$

The inverse is

$$V^{-1} = \begin{pmatrix} \cos \tau & -\sin \tau \\ \sin \tau & \cos \tau \end{pmatrix} \quad (19)$$

Finally, in the coordinate system aligned with the drop major and minor axes, depolarization is given by

$$D = \begin{pmatrix} e^{i(\phi_{sh} - A_{sh})L} & 0 \\ 0 & e^{i(\phi_{sv} - A_{sv})L} \end{pmatrix} \quad (20)$$

where  $L$  is the path length through the medium,  $\phi_s$  is the phase shift in radians/unit length,  $A_{sn}$  is the attenuation in nepers/unit length, and the subscripts refer to the major ( $h$ ) and minor ( $v$ ) axes of the drops.

The differential phase shifts,  $\phi_{sh} - \phi_{sv}$ , and attenuations,  $A_{sh} - A_{sv}$  (dB), are shown in Figure 3 for a carrier frequency of 4 GHz and a 25° elevation angle path (zenith angle  $\psi = 65^\circ$ ). These theoretical results have been obtained from data provided by Oguchi [4]. The differential attenuation at 4 GHz can be neglected in comparison with the differential phase shift. However, the dependence will be retained, at least temporarily, since the resulting forms will be useful in a discussion of the orthogonal linear measurement technique. If a constant multiplicative factor affecting both polarizations is omitted, the depolarization may be written as

$$D = \begin{pmatrix} e^{i\phi - A_n} & 0 \\ 0 & 1 \end{pmatrix} \quad (21)$$

where

$$\phi = (\phi_{sh} - \phi_{sv})L \quad (22)$$

$$A_n = (A_{sh} - A_{sv})L \quad (23)$$

Since  $A_n$  is in nepers,

$$A = e^{A_n} = \frac{e^{A_{sh}L}}{e^{A_{sv}L}} = \frac{A_{sh}}{A_{sv}} \quad (24)$$

so that

$$D = \begin{pmatrix} \frac{e^{i\phi}}{A} & 0 \\ 0 & 1 \end{pmatrix} \quad (25)$$

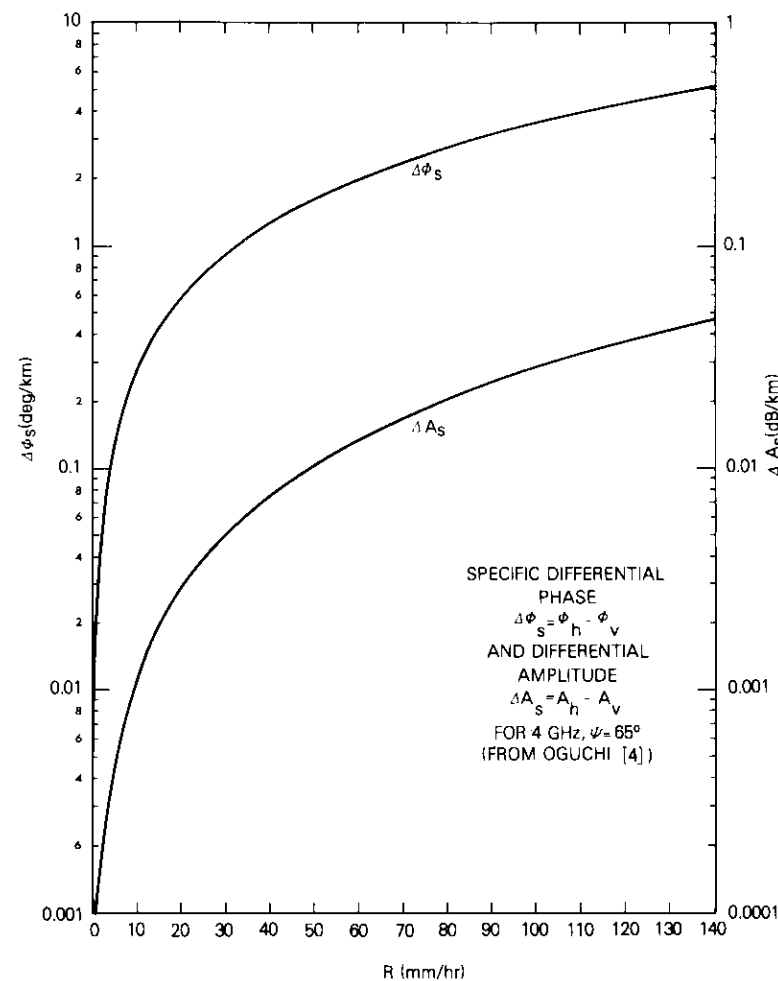


Figure 3. Differential Phase Shift and Attenuation at 4 GHz for Zenith Angle  $\psi = 65^\circ$

where

$$\frac{1}{A} = \frac{A_{sv}}{A_{sh}} \leq 1 \quad (26)$$

If fields along the  $h$  and  $v$  directions,  $E_h$  and  $E_v$ , were measured, then

$$\left| \frac{E_R}{E_V} \right| = \frac{A_{sv}}{A_{sh}} \quad (27)$$

Equation (9) may then be rewritten as

$$\begin{pmatrix} E'_R \\ E'_I \end{pmatrix} = \begin{pmatrix} a_{11} & a_{12} \\ a_{21} & a_{22} \end{pmatrix} \begin{pmatrix} E_R \\ E_I \end{pmatrix} \quad (28)$$

where

$$\begin{aligned} a_{11} &= 1 + \frac{e^{i\phi}}{A} \\ a_{12} &= \cos 2\tau \left( 1 - \frac{e^{i\phi}}{A} \right) - i \sin 2\tau \left( 1 - \frac{e^{i\phi}}{A} \right) \\ a_{21} &= \cos 2\tau \left( 1 - \frac{e^{i\phi}}{A} \right) + i \sin 2\tau \left( 1 - \frac{e^{i\phi}}{A} \right) \\ a_{22} &= 1 + \frac{e^{i\phi}}{A} \end{aligned} \quad (29)$$

For the transmit signal given by equation (9),

$$\begin{pmatrix} E'_R \\ E'_I \end{pmatrix} = \begin{pmatrix} a_{11} \\ a_{21} \end{pmatrix} \quad (30)$$

Thus, from equation (7), the XPD becomes

$$XPD = 20 \log_{10} \left| \frac{a_{11}}{a_{21}} \right| = 20 \log_{10} \left| \frac{1 + (e^{i\phi}/A)}{1 - (e^{i\phi}/A)} \right| \text{ dB} \quad (31)$$

Since  $A$  approaches unity at 4 GHz, the XPD reduces to

$$XPD = 20 \log_{10} \left| \cot \frac{\phi}{2} \right| \quad (32)$$

Hence, the XPD is not a function of the tilt or canting angle. If  $\phi$  can be determined, then equation (32) shows that the circular XPD can be exactly calculated.

#### Basic measurement technique for canting angle of zero

If the transmitted RHCP wave were received by a dual linearly

polarized antenna, the received signals would be

$$\begin{pmatrix} E'_x \\ E'_y \end{pmatrix} = \Lambda_r^{-1} V^{-1} D V R M_t \begin{pmatrix} E_R \\ E_L \end{pmatrix} \quad (33)$$

With the canting angle,  $\tau$ , measured from the horizontal, the linear antenna  $x$  axis will be aligned with the horizontal, and the  $y$  axis perpendicular to both the  $x$  axis and the path. The form for the received signals is identical with equation (8) except that the term  $M_r^{-1} R^{-1}$  is replaced by the linear antenna matrix

$$\Lambda_r^{-1} = \begin{pmatrix} f_{rx} & g_{rx} e^{-i\delta_{rx}} \\ g_{ry} e^{i\delta_{ry}} & -if_{ry} \end{pmatrix} \quad (34)$$

where  $f_{rx}$  = amplitude response of the  $x$  channel in the  $x$  direction  
 $g_{rx}$  = amplitude response of the  $x$  channel in the  $y$  direction  
 $g_{ry}$  = amplitude response of the  $y$  channel in the  $x$  direction  
 $f_{ry}$  = amplitude response of the  $y$  channel in the  $y$  direction  
 $\delta_{rx,y}$  = phase factor related to the antenna ellipticity.

Although this matrix will be discussed in more detail, it suffices at this point to indicate that the normalized response of an ideal antenna linearly polarized in the  $x$  and  $y$  directions is

$$\Lambda_r^{-1} = \begin{pmatrix} 1 & 0 \\ 0 & -i \end{pmatrix} \quad (35)$$

Then multiplication is performed assuming an ideal transmit antenna with  $M_t$  of the form given by equation (13):

$$\begin{pmatrix} E'_x \\ E'_y \end{pmatrix} = \frac{1}{\sqrt{2}} \begin{pmatrix} b_{11} & b_{12} \\ b_{21} & b_{22} \end{pmatrix} \begin{pmatrix} E_R \\ E_L \end{pmatrix} \quad (36)$$

where

$$\begin{aligned} b_{11} &= \left( \cos \tau \frac{e^{i\phi}}{A} - i \sin \tau \right) e^{i\tau} \\ b_{12} &= - \left( \cos \tau \frac{e^{i\phi}}{A} + i \sin \tau \right) e^{-i\tau} \\ b_{21} &= \left( \cos \tau - i \sin \tau \frac{e^{i\phi}}{A} \right) e^{i\tau} \end{aligned} \quad (37)$$

$$b_{22} = \left( \cos \tau + i \sin \tau \frac{e^{i\phi}}{A} \right) e^{-i\tau} .$$

Then, for an RHCP transmitted signal,

$$\begin{pmatrix} E'_x \\ E'_y \end{pmatrix} = \frac{1}{\sqrt{2}} \begin{pmatrix} \cos^2 \tau \frac{e^{i\phi}}{A} + \sin^2 \tau + i \sin \tau \cos \tau \frac{e^{i\phi}}{A} - i \sin \tau \cos \tau \\ \sin^2 \tau \frac{e^{i\phi}}{A} + \cos^2 \tau - i \sin \tau \cos \tau \frac{e^{i\phi}}{A} + i \sin \tau \cos \tau \end{pmatrix} . \quad (38)$$

The effective canting angle is typically small,  $\cong 10^\circ$ . For  $\tau = 0$ ,

$$\begin{pmatrix} E'_x \\ E'_y \end{pmatrix} = \frac{1}{\sqrt{2}} \begin{pmatrix} e^{i\phi} \\ A \\ 1 \end{pmatrix} . \quad (39)$$

Since the differential attenuation at 4 GHz can be neglected, then

$$\begin{pmatrix} E'_x \\ E'_y \end{pmatrix} = \frac{1}{\sqrt{2}} \begin{pmatrix} e^{i\phi} \\ 1 \end{pmatrix} . \quad (40)$$

Thus, if  $E'_x$  and  $E'_y$  are measured directly, the phase angle between the two components is  $\phi$ , and the XPD may be directly calculated using equation (32). The error introduced by assuming  $\tau = 0$  will be evaluated subsequently.

#### The effects of an imperfect satellite antenna

The axial ratio of the nominally RHCP satellite transmit antenna was very good for this series of measurements, better than 0.3 dB.\*

\*The relationship between clear sky isolation or the cross-polarization ratio and the axial ratio is

$$r_{dB} = 20 \log_{10} \left( \frac{10^{CPR_{dB}/20} + 1}{10^{CPR_{dB}/20} - 1} \right)$$

or inversely,

$$CPR_{dB} = 20 \log_{10} \left( \frac{10^{r_{dB}/20} + 1}{10^{r_{dB}/20} - 1} \right)$$

as is illustrated in Figure 4. The relationship between this value and  $r$  is  $r_{dB} = 20 \log_{10} r$ .

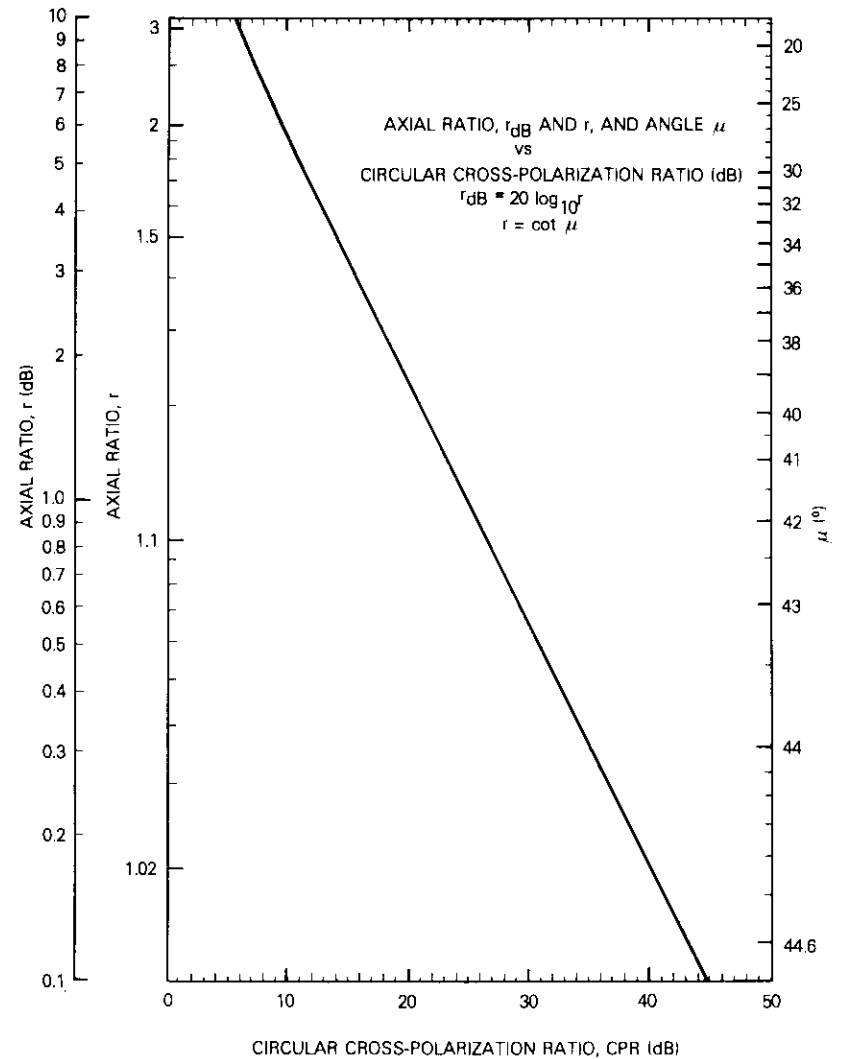


Figure 4. Axial Ratio and Angle  $\mu$  as a Function of the Circular Cross-Polarization Ratio

However, potential inaccuracies introduced by nonideal axial ratios should be evaluated. If the previous approach (including the assumption that  $\tau = 0$ ) is used with the form given by equation (10) for the transmit

antenna matrix rather than that given by equation (13) for an ideal antenna, the received linear fields are

$$\begin{pmatrix} E'_x \\ E'_y \end{pmatrix} = \frac{1}{\sqrt{2}} \begin{pmatrix} e^{i\phi} [m_{tR} + n_{tR}^*] \\ 1 [m_{tR} - n_{tR}^*] \end{pmatrix} = \begin{pmatrix} e^{i\phi} [p_1 e^{-i\gamma_1}] \\ 1 [p_2 e^{-i\gamma_2}] \end{pmatrix} \quad (41)$$

where

$$\begin{aligned} p_1 &= \sqrt{\frac{1 + \cos 2\mu \cos 2\sigma}{2}} \\ \gamma_1 &= \tan^{-1}(\tan^2 \mu \tan \sigma) \\ p_2 &= \sqrt{\frac{1 - \cos 2\mu \cos 2\sigma}{2}} \\ \gamma_2 &= \tan^{-1}(\tan^2 \sigma / \tan \mu) \end{aligned} \quad (42)$$

Thus the received signal may be modified in both amplitude and phase by the presence of a nonideal satellite antenna. This effect is independent and separable from the rain induced differential phase indicated by  $\phi$ . Therefore, if the differential phase attributed to rain (as well as any differential amplitude caused by nonzero canting angles) is referenced to clear sky conditions, the offset caused by a nonideal satellite antenna is eliminated.

As the tilt angle,  $\sigma$ , of the satellite antenna polarization ellipse is varied, it is easy to demonstrate that the observed effect varies between two extremes. In the one case, the nonideal axial ratio produces only a differential phase shift between  $E'_x$  and  $E'_y$  and no differential amplitude, while in the other the total effect is seen as a differential amplitude between  $E'_x$  and  $E'_y$ . These two cases correspond, respectively, to  $\sigma = 45^\circ$  when the polarization ellipse is oriented  $45^\circ$  with respect to both the  $x$  and  $y$  axes, and to  $\sigma = 0^\circ$  or  $90^\circ$  when the major axis of the polarization ellipse is aligned with the  $x$  or the  $y$  axis.

#### The effects of an imperfect earth station antenna

The effects of nonideal isolation between the orthogonal linear ports of the earth station antenna are also of concern. For the 3.9-m antenna used at Lario, this isolation was 28 dB. Potential measurement errors will be investigated by using equation (33) and allowing the receive antenna matrix to depart from the ideal matrix given by equation (35). An alternative (equivalent) approach involves maintaining the framework of circular polarization introduced in equation (8) but permitting

the receive circular antenna to have a very high axial ratio, so that it effectively degenerates into a near linear antenna.

For the linear receive antenna matrix, the normalized elements may be related to the tilt angle,  $\sigma$ , of the antenna polarization axis away from the  $x$  or  $y$  axis, and the axial ratio,  $r$ . The derived dependencies are given by

$$f = \left[ \frac{(1 + \cos 2\mu \cos 2\sigma)}{2} \right]^{\frac{1}{2}} \quad (43)$$

$$g = \left[ \frac{(1 - \cos 2\mu \cos 2\sigma)}{2} \right]^{\frac{1}{2}} \quad (44)$$

$$\delta = \tan^{-1} \left( \frac{\tan 2\mu}{\sin 2\sigma} \right) \quad (45)$$

and the inverses

$$\sigma = \frac{1}{2} \tan^{-1} \left( \frac{2fg \cos \delta}{f^2 - g^2} \right) \quad (46)$$

$$\mu = \frac{1}{2} \tan^{-1} \left[ \frac{2fg \sin \delta}{(f^4 + g^4 + 2f^2g^2 \cos 2\delta)^{\frac{1}{2}}} \right] \quad (47)$$

or

$$r = \frac{(f^2 + g^2) + (f^4 + g^4 + 2f^2g^2 \cos 2\delta)^{\frac{1}{2}}}{2fg \sin \delta} \quad (48)$$

Figure 5 shows the relationship between these parameters. For small  $g/f$ , the polarization approaches linear and exhibits both a high axial ratio and a small tilt angle. As  $g/f$  increases, (i.e., near 0.1) two extremes can occur. The wave may still be linear but tilted with respect to the reference axis. This situation, for which the axial ratio is high, is exemplified by the horizontal portion of the solid curve. Also in this region,  $\delta$  is reasonably small, less than  $10^\circ$ . As  $\delta$  increases, the tilt angle enters a region of abrupt decrease until at  $\sigma = 0^\circ$ , the lowest axial ratio for a given  $g/f$  is reached. At this point  $\delta$  equals  $90^\circ$ , and the polarization state is most elliptical.

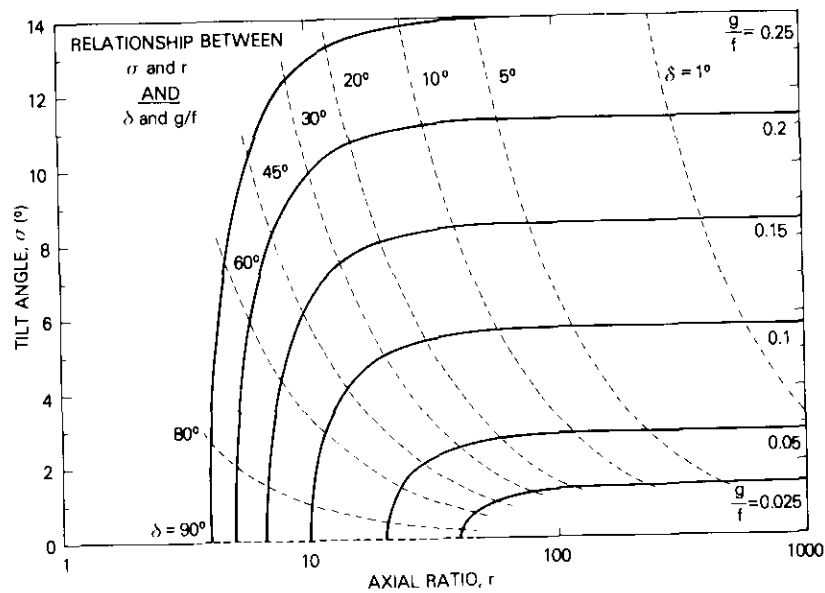


Figure 5. Relationship Between Two Sets of Variables Used to Describe Polarization State

Performing the multiplication indicated by equation (33), for  $\tau = 0$  and a perfect satellite antenna yields

$$\begin{pmatrix} E'_x \\ E'_y \end{pmatrix} = \frac{f}{\sqrt{2}} \begin{pmatrix} e^{i\phi} [1 + i g e^{-i(\delta+\phi)}] \\ 1 [1 + g e^{i(\delta+\phi)}] \end{pmatrix} \quad (49)$$

where, for simplicity, a symmetric antenna has been assumed and  $g$  has been normalized with respect to  $f$ ; i.e.,

$$f = f_{rx} = f_{ry} \quad (50)$$

$$g = \frac{g_{rx}}{f} = \frac{g_{ry}}{f} \quad (51)$$

A comparison of this result with that for the ideal receive antenna given by equation (40) indicates that because of the  $\phi$  dependence in

the modifying multiplicative factors, the effect of an imperfect receive antenna is not separable as it was for an imperfect satellite antenna.

Equation (49) can be rewritten as

$$\begin{pmatrix} E'_x \\ E'_y \end{pmatrix} = \frac{f}{\sqrt{2}} \begin{pmatrix} e^{i\phi} [B e^{i\xi}] \\ 1 [C e^{i\zeta}] \end{pmatrix} \quad (52)$$

where

$$B = 1 + 2g \sin(\delta + \phi) + g^2 \quad (53)$$

$$C = 1 + 2g \cos(\delta + \phi) + g^2 \quad (54)$$

$$\xi = \tan^{-1} \left[ \frac{g \cos(\delta + \phi)}{1 + g \sin(\delta + \phi)} \right] \quad (55)$$

$$\zeta = \tan^{-1} \left[ \frac{g \sin(\delta + \phi)}{1 + g \cos(\delta + \phi)} \right] \quad (56)$$

In general, for small  $g$  ( $\approx 0.1$ ) and for  $\phi$  in the range of interest ( $\approx 20^\circ$ ), equations (55) and (56) demonstrate that the maximum differential phase caused by a nonideal receive antenna is approximately

$$(\xi - \zeta)_{\text{rain}} - (\xi - \zeta)_{\text{clear sky}} \approx -\sqrt{2}g\phi \quad (57)$$

The minimum value of this differential phase is not zero but approximately  $-g\phi$ . Thus, without knowledge of  $\delta$ , reasonable bounds, which differ by only  $\sqrt{2}$ , can be provided. Then for an XPD based only on the measured differential phase [equation (40)], the worst-case differential between the measured and true XPD is approximately

$$XPD_M - XPD_T \approx -20 \log_{10} (1 - \sqrt{2}g) \quad (58)$$

For a 28-dB isolation,  $g$  equals 0.04 and the difference is 0.5 dB, which is sufficiently small to preclude correction in the data analysis. Ideally, such a correction should be based on  $\delta$  rather than the worst-case value. However, this analysis indicates that measurement programs employing the dual-linear technique should consider specifying minimum acceptable isolation.

### Inclusion of differential amplitude and determination of canting angle

The presence of a differential amplitude between the two linear received channels can be related to the existence of a nonzero canting angle. The effect can be analyzed by reexamining previous results without the approximation of the zero canting angle ( $\tau = 0$ ). Since the differential attenuation between polarizations aligned parallel to the raindrop effective major and minor axes is negligible at 4 GHz in comparison with the differential phase, the assumption of  $A = 1$  is acceptable. However, this assumption is not related to the magnitudes of  $E'_x$  and  $E'_y$ , which may be unequal and thus result in an observed differential amplitude between the  $x$  and  $y$  directions. These magnitudes are the same only when the effective canting angle  $\tau = 0$ . *A posteriori* it can be stated that since the observed differential amplitudes are small,  $\tau$  is also small.

A measure of the circular XPD, which is defined at 4 GHz by equation (32), may be obtained from the measured values in equation (38) by first expressing  $E'_x$  and  $E'_y$  as

$$E'_x = P e^{i\omega} \quad (59)$$

$$E'_y = Q e^{i\psi} \quad (60)$$

where

$$P = |E'_x| = \frac{1}{\sqrt{2}} (1 - \sin 2\tau \sin \phi)^{\frac{1}{2}} \quad (61)$$

$$Q = |E'_y| = \frac{1}{\sqrt{2}} (1 + \sin 2\tau \sin \phi)^{\frac{1}{2}} \quad (62)$$

$$\omega = \tan^{-1} \left( \frac{\cos \tau \sin \phi - \sin \tau}{\cos \tau \cos \phi} \right) + \tau \quad (63)$$

$$\psi = \tan^{-1} \left( \frac{-\sin \tau \cos \phi}{\cos \tau + \sin \tau \sin \phi} \right) + \tau \quad (64)$$

Next, a form similar to that given by the argument of the log in equation (31) is evaluated by replacing  $A$  with the differential amplitude ratio  $Q/P$  and replacing  $\phi$  with the differential phase  $\omega - \psi$ . That is,

$$\frac{1 + (P/Q) e^{i(\omega-\psi)}}{1 - (P/Q) e^{i(\omega-\psi)}} = \frac{1 + R e^{i\rho}}{1 - R e^{i\rho}} \quad (65)$$

The differential amplitude and differential phase,  $R$  and  $\rho$ , respectively, are directly measured at the receive terminals. After considerable manipulation, this form reduces to

$$\left| \cot \left( \frac{\phi}{2} \right) \right| \quad (66)$$

Thus, the important result is exactly

$$XPD = 20 \log_{10} \left| \frac{1 + R e^{i\rho}}{1 - R e^{i\rho}} \right| \quad (67)$$

Therefore, although the measured  $\rho$  is unequal to  $\phi$  for nonzero  $\tau$ , the circular XPD can be evaluated exactly if the measured value of  $R$ , the differential attenuation, is used.

This development demonstrates the utility of measuring the differential amplitudes between the received fields in the  $x$  and  $y$  directions. It is instructive to evaluate the degree of error which is introduced when  $R$  is assumed to be unity with  $\rho$  the measure of  $\phi$ . Equation (67) can be used to evaluate the results shown by the solid curves of Figure 6. Basically, circular XPD is plotted as a function of the observed differential phase  $\rho$  with the differential amplitude as a parameter. The case of  $R = 1 = 0$  dB corresponds to a canting angle  $\tau = 0$ , and  $\rho = \phi$ . If a differential amplitude is present, the assumption that  $R = 0$  dB will introduce an error in the calculated XPD; the error is such that the calculated XPD will always exceed that which would be found if the differential amplitude were considered.

The dashed curves in Figure 6 are iso-canting angle contours. They were derived by selecting values of  $\phi$  ( $\tau = 0$ ), determining the corresponding XPD ( $\tau = 0$ ), and then calculating the differential phase which would be observed for this same XPD value for the parametric  $\tau$  values shown. This is useful for characterizing the effect of a nonzero canting angle on the differential amplitude and the XPD, particularly if the differential amplitude is neglected. With measurements of both differential amplitude and phase, the effective canting angle of the raindrops can be specified with limited precision. Since the observed differential attenuation was normally less than 0.5 dB during rain events, it can be inferred that canting angles were also small ( $\cong 15^\circ$ ), at least for the important range of XPD below 25 dB. Limited experimental evidence [4] also suggests that effective canting angles are generally less than  $10^\circ$ .

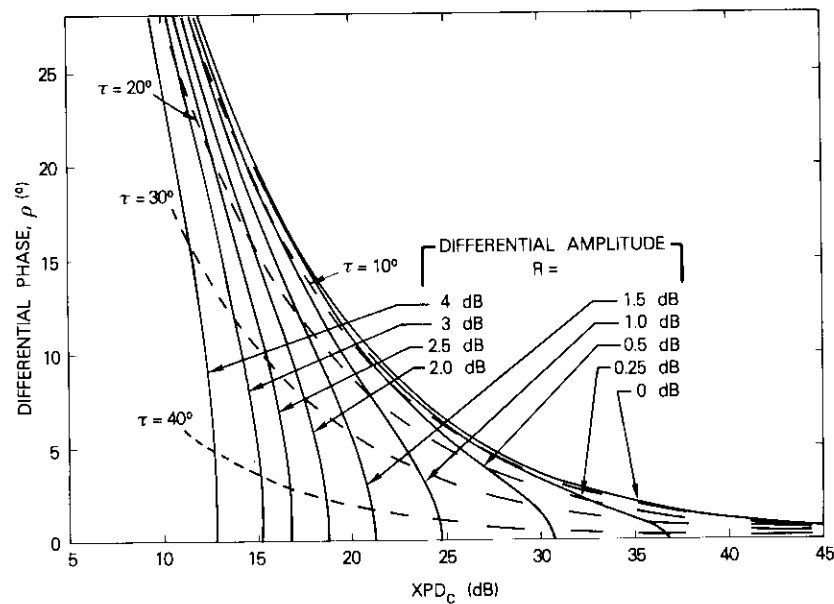


Figure 6. Differential Phase as a Function of the Circular XPD with Differential Amplitude and Tilt Angle as Parameters

### Measurement results

During the measurement program at Lario, rain accumulation, depolarization, and radiometric sky noise data were collected for 464 days.

### Data format and reduction

Figures 7 and 8 are examples of chart recordings during rain events. Figure 7 shows the rain accumulation recording for a strong event on July 25, 1977. For the storm interval of 5 hr and 58 min., the total rainfall accumulation was 42.6 mm, the highest calculated rate exceeded 150 mm/hr, and the minimum XPD was 19.6 dB.

Figure 8 depicts an event which occurred on June 22, 1977. The channels correspond to the two orthogonal linear polarization amplitudes, their differential phase, the 11.6-GHz radiometer sky noise temperature, and the rain tips from a COMSAT-supplied rain gauge. Data samples were read every 5 mm, corresponding to a sampling interval of 72 s. For this event, the maximum sky noise temperature

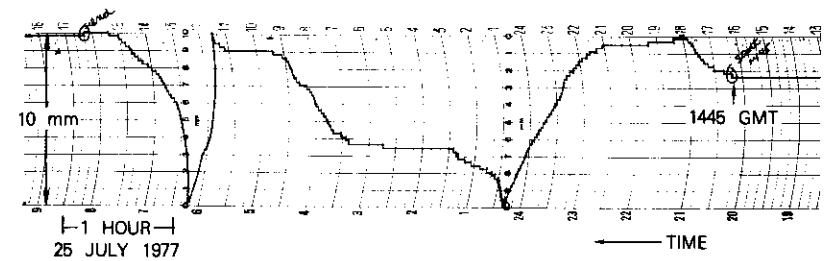


Figure 7. Chart Recording for Rain Accumulation Channel

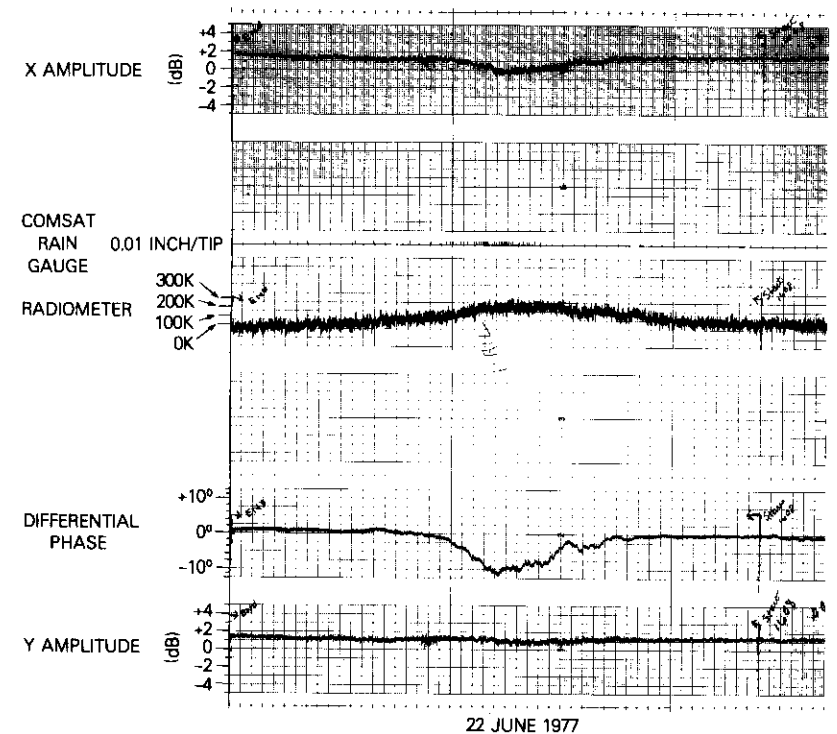


Figure 8. Chart Recording for Depolarization and Radiometric Channels

was 214K, corresponding to an 11.6-GHz attenuation of 6.1 dB. The maximum differential phase, with respect to clear sky, was 12.1°, corresponding to a minimum XPD of 19.5 dB.

### Rainfall measurements

The rain accumulation and rate were determined using a tipping bucket gauge located near the earth station antenna. From 1961 through 1968, the average annual rainfall at Lario was 1,200 mm (with a standard deviation of 256 mm), and there was an average of 105 days per year with measurable precipitation (with a standard deviation of 11 days). The mean worst 3-month period accumulation averaged over the eight years was 419.8 mm, with a standard deviation of 142.7 mm. The mean worst month accumulation was 167.3 mm, with a standard deviation of 96.8 mm.

The measured rain accumulation by month from March 12, 1977, to June 10, 1978, is shown in Figure 9. The total rainfall was 1,764.6 mm, which implies approximately 1,412 mm per year, *i.e.*, 12/15 of 1,764.6 mm. Annual rainfall can also be estimated by averaging together only those calendar months with duplicate measurements (March, April, and May). This procedure indicated an annual amount of 1,458 mm. The difference between the two methods would have negligible effects on modeling; the first value of 1,412 mm will be used. The measured annual amount is thus almost equal to the "mean plus one  $\sigma$ " value of the longer term measurements; therefore, the measurement year

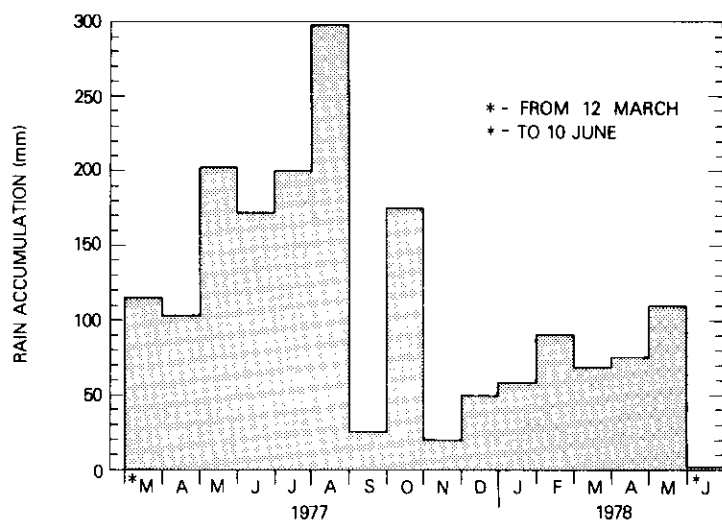


Figure 9. Rain Accumulation by Months

could be characterized briefly as "rainy." Based on accumulation, August was the worst month of rainfall, which with 298.8 mm is more than one standard deviation above the mean worst month. Although rain was scarce in September, 86.8 mm of the August accumulation occurred during the last three days of that month.

The calculated rain rate distribution and the Rice-Holmberg [5] modeled rain rate distribution with parameters  $M = 1,412$  mm and  $\beta = 0.06$  and  $0.07$  are shown in Figure 10. The agreement between the measured and modeled rain rate distributions is good except at the highest rain rates. The value of  $\beta$  providing the best fit, approximately 0.065, is somewhat lower than the 0.1 value found in a world contour map of  $\beta$  [5]. This is the first series of INTELSAT depolarization measurements which exhibited good agreement between the measured and Rice-Holmberg distributions. Previously, at both Taipei and Ibaraki, the Rice-Holmberg distributions significantly overestimated the measured occurrence probabilities at high rain rates ( $>30$  mm/hr). Nonetheless, higher  $\beta$ 's (and  $M$ 's) were in evidence; therefore, on an absolute basis, more high-rate rainfall was observed at these sites than at Lario. The measurements thus suggest a correlation between the shape of the distribution in the high-rain-rate region and  $\beta$  (and perhaps  $M$ ). However, this dependency does not exist in the Rice-Holmberg model.

The calculated rain rate distribution for August 1977, which is shown in Figure 11, closely conforms to the Rice-Holmberg model. At rates above 30 mm/hr, which correspond to the important region for depolarization phenomena, the occurrence probabilities are almost five times the annual ones. A comparison with the ratio of total accumulations indicates that the August total of 298.8 is about 2.5 times the average monthly accumulation. Thus, August exhibits a higher value of  $\beta$  than the year as a whole.

### Rain induced depolarization

The XPD was calculated for each of the sample points using the relationship

$$XPD = -20 \log_{10} \left( \tan \frac{\phi}{2} \right) \text{ dB} \quad (68)$$

where  $\phi$  is the total differential phase. The measurement time base and outage statistics for the differential phase channel are summarized in

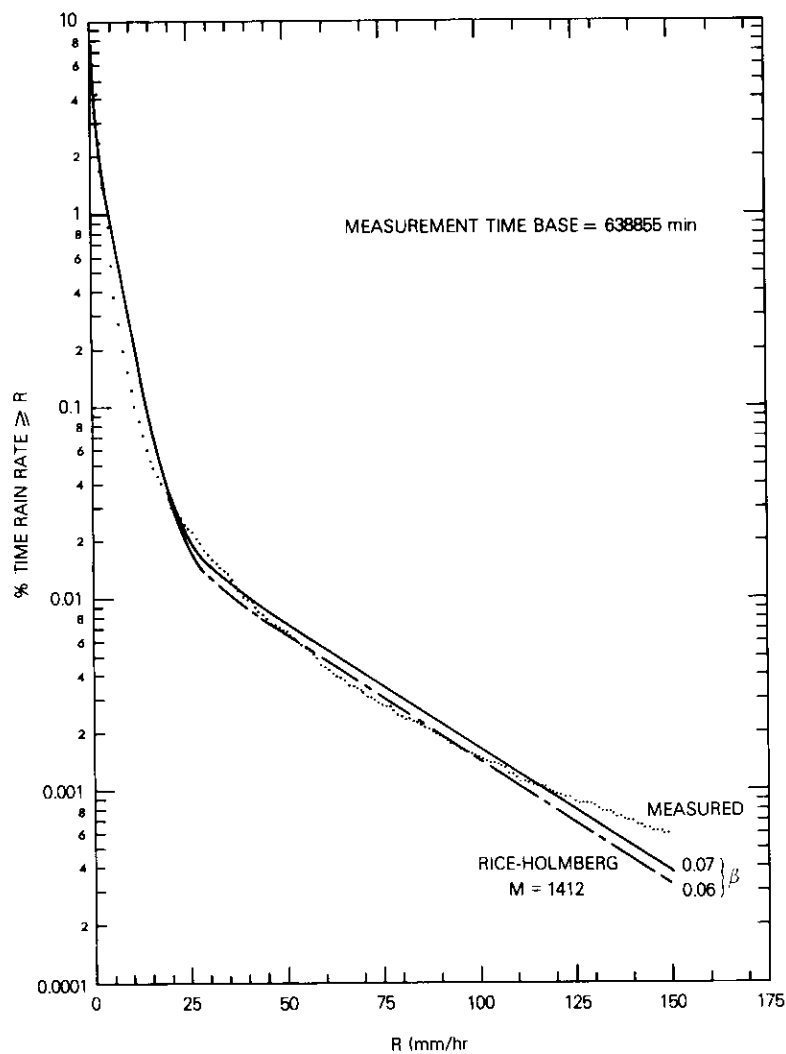


Figure 10. Annual Rain Rate Distribution

Table 1. The Andover carrier was available only on a noninterfering basis with other services using the INTELSAT transponder; preemption of this carrier produced most of the downtime indicated. Event time, which corresponds to the total reduced time, includes time at the

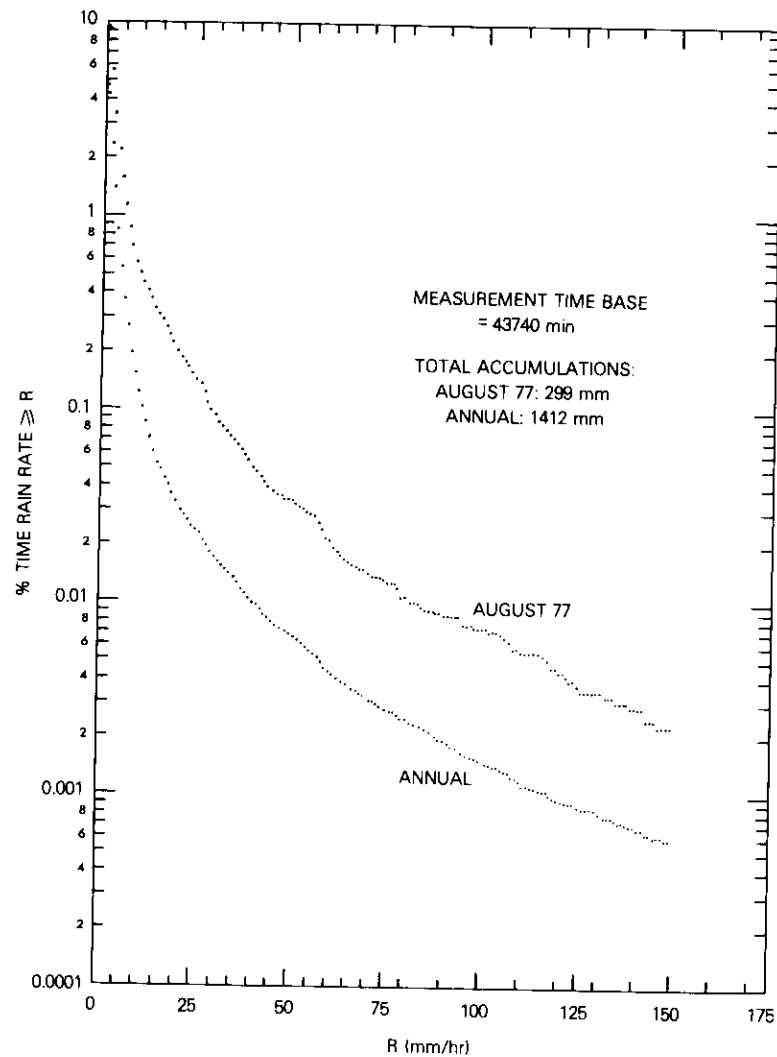


Figure 11. Worst Month Rain Rate Distribution

beginning and end of events for which the  $x_{PD}$  was not appreciably different from the clear sky value. The time that the  $x_{PD}$  was less than 35 dB is smaller than the event time by a factor of approximately seven. Many events contained relatively minor depolarization which,

TABLE 1. DIFFERENTIAL PHASE {DEPOLARIZATION}  
Channel Operating Statistics

Elapsed Time (77062-0700 to 78161-0700)	464 days = 668,160 min.
Time Between Charts	24,747 min. (3.7%) <sup>a</sup>
Down Time	107,223 min. (16.0%) <sup>a</sup>
Operating Time	536,200 min. (80.3%) <sup>a</sup>
Event Time	13,894 min. (2.6%) <sup>b</sup>
Time XPD <35 dB	1,946 min. (0.4%) <sup>b</sup>
Number of Depolarization Events	93

<sup>a</sup>Percent of elapsed time.

<sup>b</sup>Percent of operating time.

although apparently real, did not result in significant XPD values; only 30 of the 93 events contained sampled XPDs below 30 dB.

Figure 12 shows the average number of minutes per year that the XPD falls into each of the 1-dB intervals below 35 dB. These values are normalized to an annual basis for comparison and for system analyses.

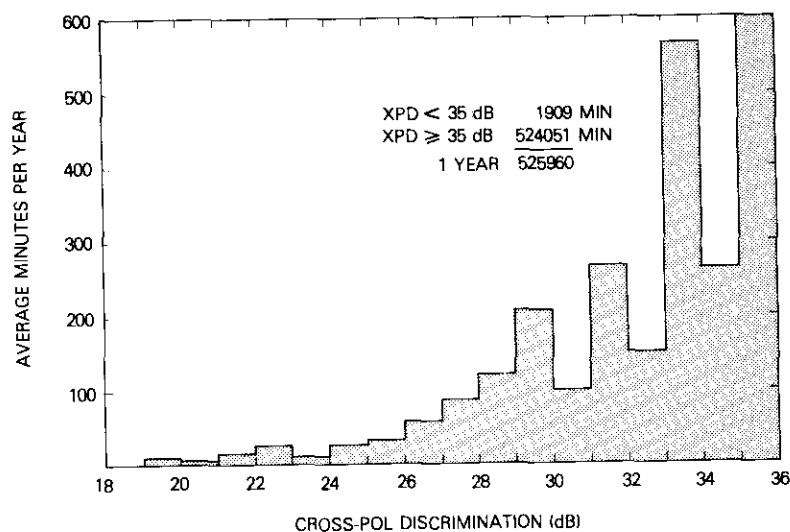


Figure 12. XPD Histogram

The XPD is below 20 dB for only 7.1 min.; and below 25 dB for 82 min. The behavior of XPDs above 29 dB is saw-toothed largely because the data were read from the charts to the nearest millimeter. Thus, since

the sensitivity of the phase channel (in deg/mm) was approximately constant over the measurement period, quantization errors resulting from the data reduction techniques become important for higher XPD values for which only a few millimeters of deflection were recorded. In the long-term cumulative XPD distribution shown in Figure 13, the

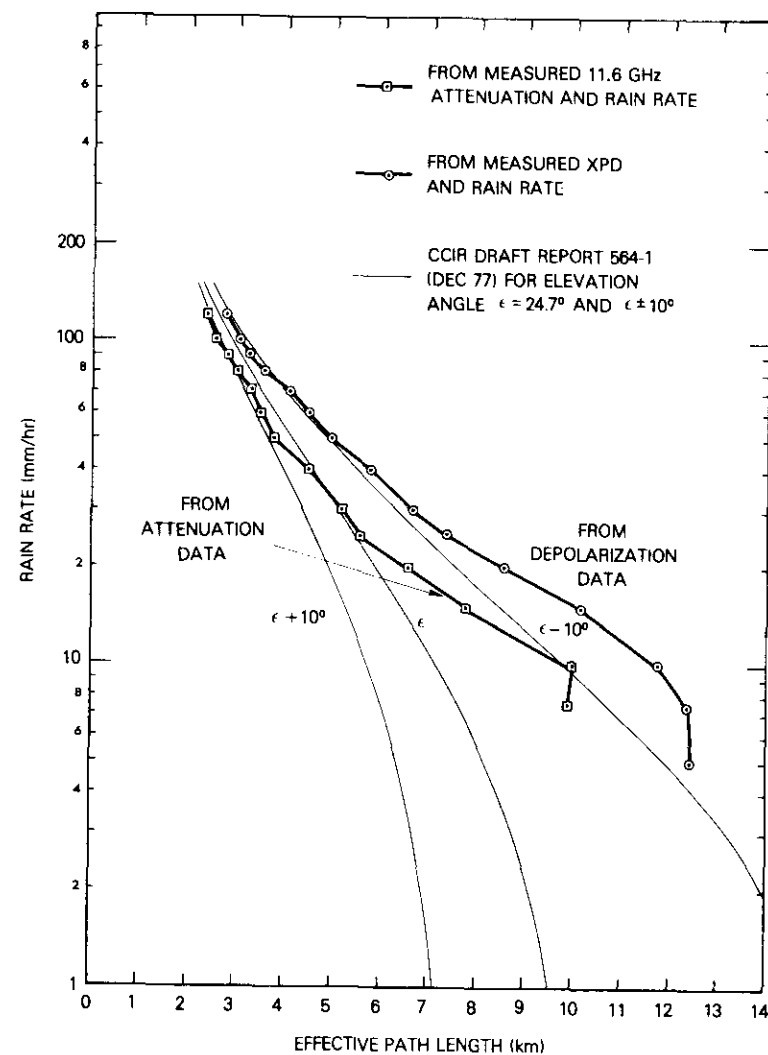


Figure 13. XPD Distribution

XPD is less than 23.8 dB for only 0.01 percent of the time. The minimum recorded value was 19.2 dB.

#### Radiometrically determined attenuation

The 11.6-GHz sky noise temperature was measured by a radiometer located at the site of the 4-GHz receive terminal. The radiometer was calibrated using both a liquid nitrogen ( $T = 80$  K) cold load and an ambient temperature hot load, applied at the feed about once per month. In addition, a reference temperature and a noise diode source were coupled to the radiometer input each hour.

The 11.6-GHz attenuation,  $A$ , was derived from the measured sky temperature,  $T$ , by the relationship

$$A = -10 \log_{10} \left( 1 - \frac{T}{T_0} \right) \text{ dB} \quad (69)$$

where  $T_0$  is the effective temperature of the absorbing medium (assumed to be 283 K). The resulting cumulative distribution of excess attenuation is shown in Figure 14. Also shown is the 11.6-GHz attenuation predicted for the path using the measured rain distribution and C.C.I.R. effective path lengths for a  $24.7^\circ$  elevation angle (Figure 15). The agreement between the two is good over most of the range.

#### Effective path lengths

Discussion and calculation of effective path lengths are useful in the development of depolarization models. The concept originated in connection with attenuation studies and depends on the assumption that, at a given elevation angle, it should be possible to statistically relate the surface point rain rate to the path length over which this uniform rate should occur. Since the total attenuation at a given carrier frequency is then simply the product of the specific attenuation (in dB/km) at that frequency and the path length (in km), attenuation can be related to rain rate and then to a percent time exceedance. Thus, with the effective path length known as a function of the rain rate, the availability of a point rain rate distribution and specific attenuation tables [6] allows the slant path attenuation distribution to be determined for a given location.

The process is reversed when measured attenuation and rain rate data are available; in this case the effective path length can be calculated:

$$L(p) = \frac{A(p)}{A_s[R(p)]} = \frac{A(p)}{a[R(p)]^b} \text{ km} \quad (70)$$

where the attenuation,  $A$ , and the rain rate,  $R$ , are evaluated at the same percentage of time,  $p$ . The value  $A_s$  is the specific attenuation due to rain, which at SHF can be expressed as  $aR^b$ , where  $a$  and  $b$  are constants which vary with carrier frequency and drop size distribution [7]. These values are from the C.C.I.R. [6].

The measured 11.6-GHz attenuation and rain rate data have been used to calculate the effective path lengths shown in Figure 15. Values derived from the C.C.I.R. [8] are also plotted for an elevation angle,  $\epsilon$ , of  $24.7^\circ$  which existed at Lario and for  $\epsilon \pm 10^\circ$ . The calculated effective path lengths are in fairly good agreement with the C.C.I.R. values for rain rates greater than about 20 mm/hr. For rates below this value, the calculated path lengths are in better agreement with those of C.C.I.R. for a lower elevation angle. Although this may be attributed to the mountainous terrain at Lario, the same tendency for relatively longer effective path lengths at lower rain rates was also observed at Ibaraki.

Another approach to defining an effective path length is based on the measured rain rate and XPD distributions. This depolarization effective path length is defined as

$$L(p) = \frac{\phi(p)}{\phi_s[R(p)]} \text{ km} \quad (71)$$

where  $\phi(p)$  is the total differential phase exceeded  $p$  percent of the time, and  $\phi_s[R(p)]$  is the specific differential phase shift (deg/km) for a rain rate  $R$ , which is a function of  $p$  through the measured rain rate distribution. With equation (68), this becomes

$$L(p) = \frac{2 \tan^{-1} [10^{-XPD(p)/20}]}{\phi_s(p)} \text{ km} \quad (72)$$

It is assumed that all of the depolarization is due to the measured differential phase shift.

The calculated depolarization effective path lengths are also shown in Figure 15. In general, although the behavior with rain rate meets expectations, it does not exhibit good agreement with either the

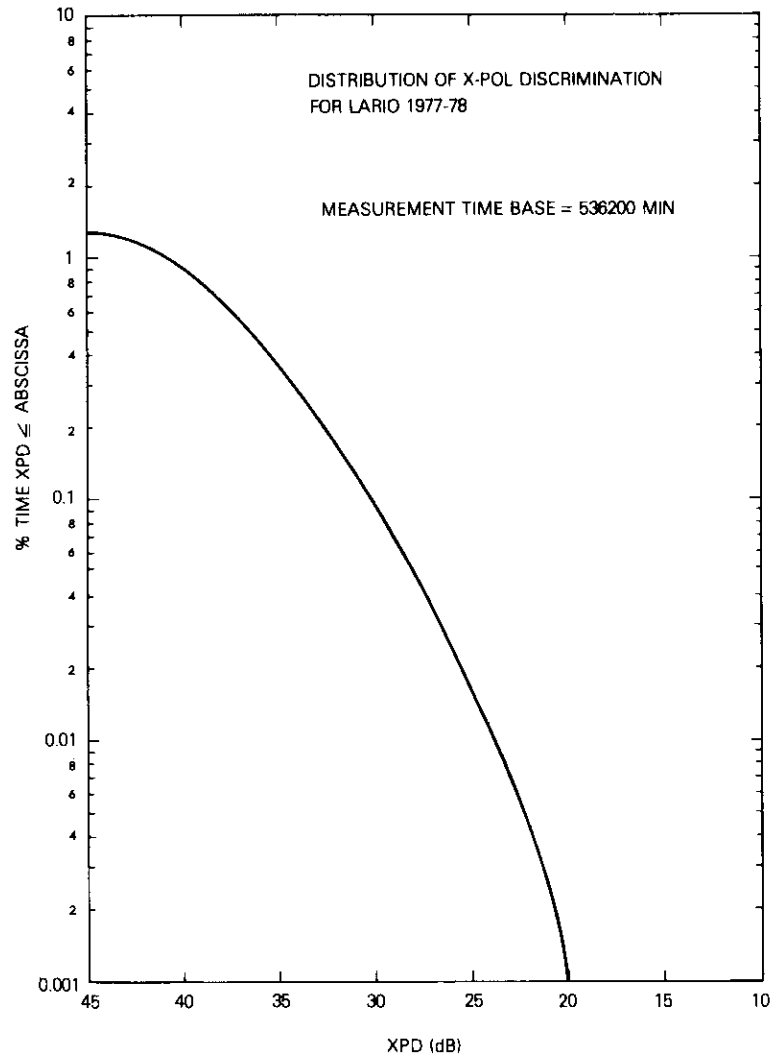


Figure 14. Comparison of Measured Radiometer Attenuation and Measured Rain/C.C.I.R. Path Length Model

C.C.I.R. path lengths or those based on attenuation; the depolarization path lengths are about 20 to 30 percent in excess of those for attenuation. Qualitatively this same behavior was observed at Ibaraki.

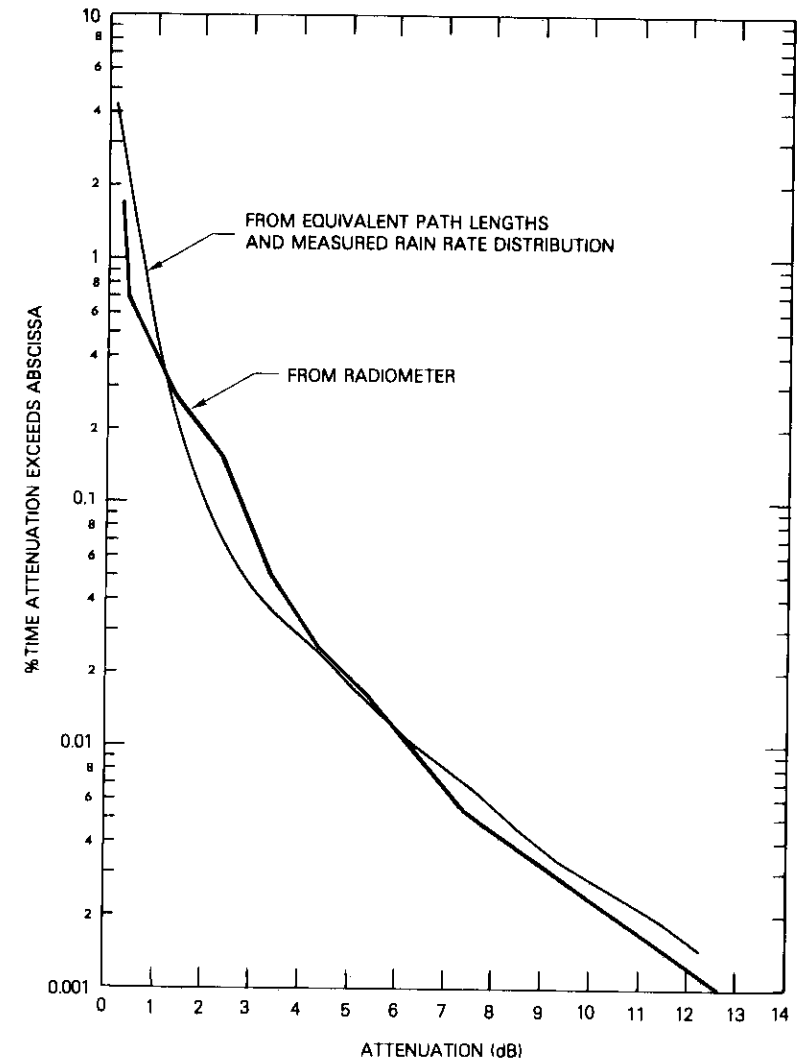


Figure 15. Effective Path Length

Although no physical model adequately explains these observations, a mechanism which produces depolarization but not attenuation (*e.g.*, ice crystals) would result in longer depolarization path lengths. This behavior is related to the observation that modeled depolarization is

somewhat less pronounced than that actually measured.

#### Comparison of measured and modeled depolarization

One of the principal objectives of this measurement program has been the comparison of measured long-term depolarization statistics with various models. Since there is no established C.C.I.R. predictive model or procedure, four different models are developed which depend in varying degrees upon measured attenuation and rain rate results. These four models are based on the differential phase and amplitude coefficients calculated by Oguchi [4] (whose results do not appreciably differ from those of other researchers). The models also assume that measured depolarization is due only to rain, and assumed drop shapes and geometries of orientation are adequate to quantitatively explain the depolarization process. Although ice crystals are known to cause depolarization, it is assumed that such depolarization is rare and does not produce high levels of depolarization at 4 GHz.

The measurement results, which are similar to those from earlier programs, indicated somewhat greater occurrences of mid-level XPD values than the models, but in general, exhibited good agreement at lower XPD levels. The measured depolarization is replotted in Figure 16 with the results from the four models:

*a. Model 1.* The most straightforward depolarization model uses rain and 11.6-GHz attenuation data to determine effective path length as a function of rain rate. Path length is used with the rain rate distribution and the calculated specific differential phases to directly compute an XPD distribution. This method, which is most closely allied with actual measurements of rain rate and attenuation, yields modeled XPDs that exceed the measured values by about 2 dB within the region  $25 < XPD < 35$  dB. Below 25 dB, the difference approaches 1 dB. The shape of the curve is substantially the same as the measured curve.

*b. Model 2.* The only difference between this model and the first is the use of the Rice-Holmberg distribution for  $\beta = 0.065$  and an annual accumulation,  $M$ , equal to the measured 1,412 mm rather than the measured rain rate distribution. For most of the significant XPD range below 30 dB, the differences between the results of the first two models are small (less than 0.5 dB) which is indicative of the excellent agreement between the measured and Rice-Holmberg distributions above 25 mm/hr. Again, at a given occurrence level, the difference between the measured XPD and

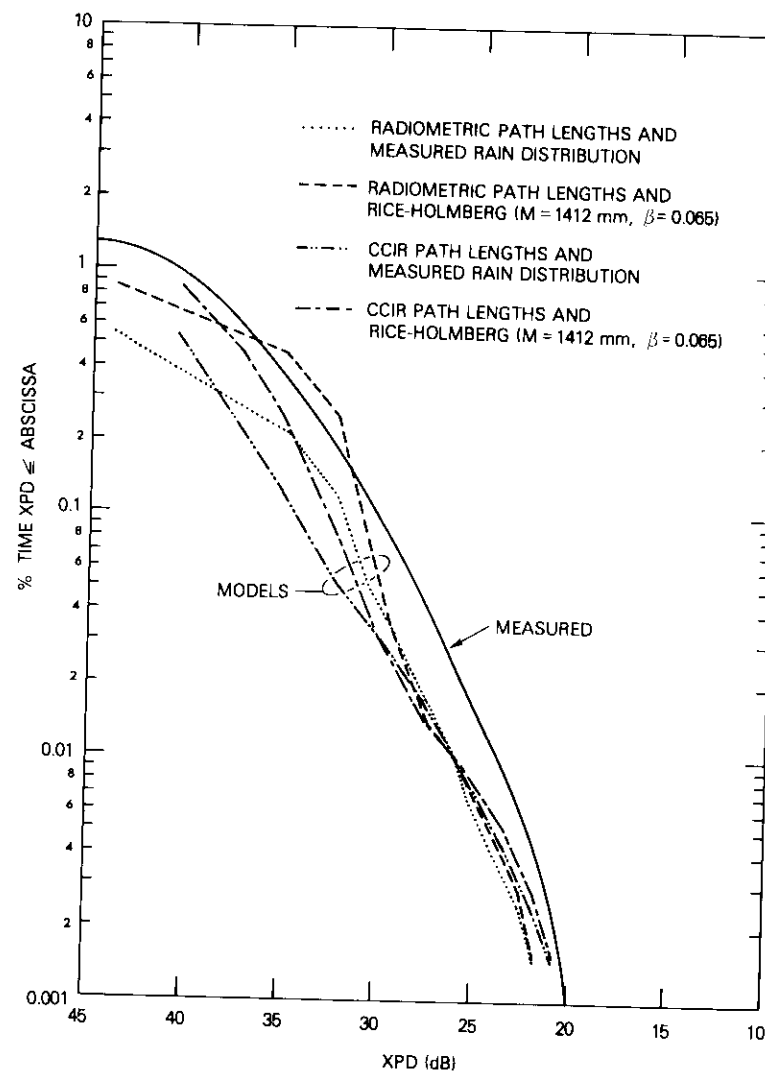


Figure 16. Modeled XPD vs Measured XPD

the model is about 2 dB, which decreases at lower XPDs.

*c. Model 3.* This approach utilizes the measured rain distribution but employs the C.C.I.R. effective path lengths rather than those based on the measured rain/radiometric attenuation. Since the

C.C.I.R. path lengths were shorter than those measured for rates below about 40 mm/hr, the indicated XPDs for the middle and upper XPD range ( $XPD \cong 25$  dB) exceed those of either Model 1 or Model 2. In this range, there is approximately a 4-dB difference from the measured XPDs. For the lower XPD range ( $<25$  dB) the agreement is very good, less than 1 dB.

d. *Model 4.* In this model, the only measured parameters used are  $M$  and  $\beta$  as derived from the measured rain distributions. C.C.I.R. effective path lengths are employed as well as the Rice-Holmberg distribution of rain rates. The agreement is alternately the best of the four models and the worst, depending on the occurrence level. The departure from the measured results is least in the XPD region below 25 dB; this model actually provides the best estimate to the measured values for occurrence levels below 0.01 percent.

The intersection of all the models near the 0.01-percent level is a coincidence based on the following factors: The measured rain and the Rice-Holmberg distributions (for  $\beta = 0.065$ ) intersect near the 0.01-percent level, and the measured 11.6-GHz attenuation matches the C.C.I.R. modeled results for attenuation also near the 0.01-percent level. At this level, measured XPD is 2 dB lower than that of any model; this difference diminishes for occurrence levels below 0.01 percent. Therefore, the models provide a fairly good fit to the measured results for occurrence levels of 0.01 percent and below.

Figure 17 compares the XPD distributions resulting from the three INTELSAT programs which have gathered long-term depolarization statistics. The  $M$  and  $\beta$  of the best fit Rice-Holmberg rain distribution\* and the elevation angle of the slant path are shown. Qualitatively these results meet expectations. Taipei, which has both a low elevation angle and a great amount of rain, displays the most significant depolarization. Ibaraki shows considerably less depolarization than Taipei because of less rain and a higher elevation angle. Lario presents the least overall depolarization, primarily because it has the lowest total rainfall. It also has a low  $\beta$ , indicating a relatively small proportion of rain occurring at high rain rates. However, the elevation angle at Lario is intermediate to the other two; if it had been higher (e.g.,  $35^\circ$  as at Ibaraki), there would be even less depolarization. These comparisons indicate that,

\*It should be noted that, for both Taipei and Ibaraki, the Rice-Holmberg distribution did not give a very good fit to the measured distributions.

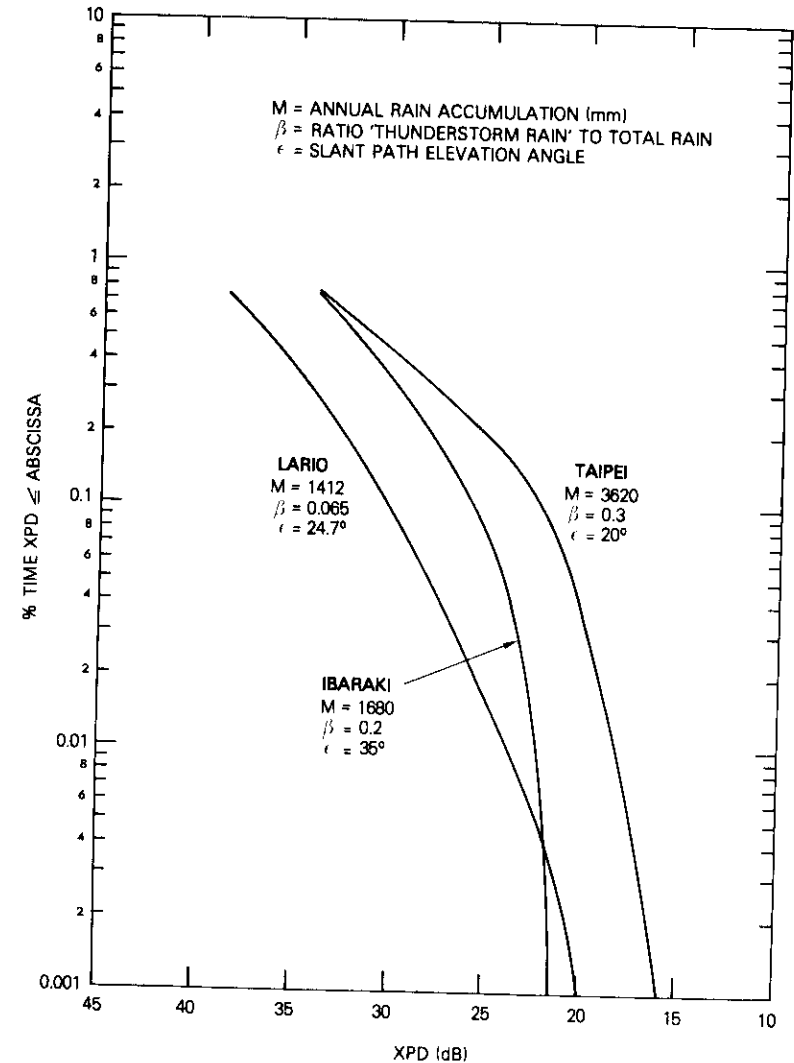


Figure 17. Comparison of Taipei, Ibaraki, and Lario

although further model refinements are necessary, basic trends agree with currently available theory and empirical models.

#### Peak values of significant events

The minimum observed XPD during the measurement period was

19.2 dB. Over the total 536,200 min., only 7.2 min. of sampled data indicated XPD values less than 20 dB, and only 85.2 min. had calculated XPD values below 25 dB. Table 2 lists all events for which the sampled XPD fell below 25 dB.

TABLE 2. PEAK VALUES OF SIGNIFICANT EVENTS

Event No.	Event (Year-Day-Time)	Min XPD (dB)	Total Sample Min. XPD Below					
			20 dB	21 dB	22 dB	23 dB	24 dB	25 dB
1	77173 1608	19.5	1.2	3.6	6.0	7.2	9.6	9.6
2	77189 0130	20.3	—	1.2	2.4	3.6	3.6	3.6
3	77206 1812	19.6	2.4	3.6	13.2	27.6	28.8	30.0
4	77229 2230	25.0	—	—	—	—	—	1.2
5	77230 1212	19.2	3.6	3.6	3.6	7.2	8.4	9.6
6	77230 1757	21.2	—	—	1.2	1.2	1.2	2.4
7	77241 0400	23.8	—	—	—	—	1.2	10.8
8	77241 1500	22.2	—	—	—	2.4	4.8	9.6
9	77242 1425	22.7	—	—	—	1.2	1.2	2.4
10	77243 0830	24.3	—	—	—	—	—	1.2
11	77280 0230	24.3	—	—	—	—	—	2.4
12	77280 0515	24.7	—	—	—	—	—	2.4
	Total Min.		7.2	12.0	26.4	50.4	58.8	85.2

These 12 events listed occurred on only nine calendar days and were concentrated within a limited time span of 108 days or roughly three months (June 22 to October 7). Moreover, the 25 day period of July 25 to August 18 accounted for over 50 percent of the time that the XPD was below 25 dB, and for over 80 percent of the time below 20 dB. Also, the single storm occurring July 25 (77206) accounted for 35 percent of all time below 25 dB and one third of that below 20 dB. Hence, significant XPD events were not uniformly distributed through the year but rather depended on those relatively rare instances when high rain rates were experienced along the path.

### Conclusions

The results of a rain depolarization measurement program conducted at Lario (Italy) for 15 months in 1977–1978 and the theoretical foundation of the measurement technique have been described. The accuracy and potential limitations of the orthogonal linearly polarized approach for determining circular XPD were considered and analyzed. Ancillary data were collected from a colocated rain gauge and 11.6-

GHz radiometer. The rain accumulation was 1,412 mm per year. Calculations of the rain rate indicated a good match with the Rice-Holmberg distribution. The 11.6-GHz attenuation distribution derived from the radiometric data also evidenced good agreement with estimates based on the measured rain rates and C.C.I.R. effective path lengths. The depolarization data agreed reasonably well with several postulated predictive models, particularly at occurrence levels of 0.01 percent or less. In general, the models predicted somewhat less depolarization than was observed, a discrepancy of approximately 2 dB at the 0.01-percent level. The measured XPD at the 0.01-percent level was 23.8 dB, and the minimum recorded value was 19.2 dB.

A comparison of these results with those from two earlier programs at Taipei (Taiwan) and Ibaraki (Japan) revealed that there was less depolarization at Lario. This matched expectations based on annual rain accumulations and incidence of high rain rates. Effective path length was analyzed by using both the rain-radiometric and the rain-depolarization data. The calculated path lengths demonstrate reasonable agreement with C.C.I.R. proposed values for an elevation angle of 25° at medium to high rain rates but were significantly longer at low rain rates. Effective path lengths calculated from the depolarization data were 20 to 30 percent longer than those based on the radiometric data. Finally, each of the 12 depolarization events with an XPD of less than 25 dB were examined to characterize the duration of XPD occurrences at a specified level.

### Acknowledgments

*The author wishes to thank Dr. G. Possenti of Telespazio (Rome) as well as the personnel at the Lario earth station for their assistance and cooperation during the data collection period. At COMSAT Laboratories, this work benefited from useful discussion with Drs. D. Fang, G. Hyde, and D. Rogers.*

### References

- [1] D. F. DiFonzo and W. S. Trachtman, "Antenna Depolarization Measurements Using Satellite Signals," *COMSAT Technical Review*, Vol. 8, No. 1, Spring 1978.
- [2] I. P. Shkarofsky, "Depolarization Due to Precipitation in Satellite Communications," *RCA Review*, Vol. 38, June 1977.

- [3] W. L. Stutzman, "A Depolarization and Attenuation Experiment Using the CTS and COMSTAR Satellites," Supplemental Report 1, NASA Contract NASS-22577, June 1977.
- [4] T. Oguchi, "Rain Depolarization Studies at Centimeter and Millimeter Wavelengths: Theory and Measurement," *Radio Research Laboratories Journal*, Vol. 22, No. 107, pp. 165-211. (Differential phase-shift and amplitude coefficients by private communication.)
- [5] P. L. Rice and N. R. Holmberg, "Cumulative Time Statistics of Surface Point-Rainfall Rates," *IEEE Transactions on Communications*, COM-21, No. 10, October 1973.
- [6] International Radio Consultative Committee (C.C.I.R.), "Propagation in Non-Ionized Media," Study Group 5, Vol. V, Geneva 1974, Report 233-3, p. 78.
- [7] R. L. Olsen, D. V. Rogers, and D. B. Hodge, "The  $aR^b$  Relation in the Calculation of Rain Attenuation," *IEEE Transactions on Antennas and Propagation*, AP-26, No. 2, March 1978.
- [8] International Radio Consultative Committee (C.C.I.R.), XIVth Plenary Assembly, Kyoto, 1978, Doc. 5/1049-E, December 1977.



*David J. Kennedy received a B.S. degree in physics from the University of Notre Dame in 1963, and M.S. and Ph.D. degrees in physics from the University of Florida in 1965 and 1969, respectively. His previous experience in microwave and satellite communications systems was at Martin Marietta Aerospace (1969-1975) and Computer Sciences Corporation (1975-1977). He joined COMSAT Laboratories in September of 1977 as a member of the technical staff in the Propagation Studies Department of the Transmission Systems Laboratory*

*where he was responsible for rain depolarization and tropospheric scintillation measurement programs. He is presently a member of the technical staff at INTELSAT.*

Index: packet switching, ARQ, error, control equipment, satellite transmission

## ***A model for a packet switching node including packet retransmission effects***

A. KAUL

(Manuscript received May 3, 1979)

### ***Abstract***

A model is presented for predicting the performance of a store-and-forward packet switching node transmitting into a single telecommunications channel. This model incorporates the effect of transmission errors and propagation delays assuming a selective repeat ARQ error control mechanism, whereby packets are selectively retransmitted if they encounter transmission errors. The relationships derived are applicable to packet arrivals describable by any general random stationary process and to systems using either satellite or terrestrial telecommunications links. For illustration, a specific example assuming a Poisson packet arrival process and a satellite channel has been used.

### ***Introduction***

The performance of a store-and-forward packet switching node transmitting into a point-to-point communications channel can be predicted by using standard M/G/1 queuing theory models [1]. Chu's analyses of statistical multiplexers with finite buffers [2], [3] and Konheim and Chu's model for an infinite buffer case (yielding a closed-form solution) [4] can also be employed.

Packet switching nodes (e.g., in the ARPANET) automatically selectively

retransmit packets which have encountered transmission errors in the channel. Although the effect of this mechanism, which has not been considered in the aforementioned models, may be negligible at low bit-error rates, it can be significant at higher bit-error rates, especially with long propagation delays, e.g., a communications satellite channel. The effect of high bit-error rates and long propagation delays is twofold. First, a packet may be retransmitted one or more times, which increases overall packet delay. Second, the occurrence of retransmissions over the channel reduces the effective service rate for new packets by producing longer queues and increasing the delays as well as the buffering requirements.

This paper attempts to model a packet switching store-and-forward node transmitting through a single data communications link and incorporating the selective repeat ARQ [5] retransmission mechanism for error control. The results are applicable to both satellite and terrestrial transmission media.

### Mathematical model

Figure 1 is a conceptual representation of a node transmitting into a communications channel. The buffering requirements are assumed to be satisfied by a "queuing buffer," B, and a "waiting buffer," B<sub>w</sub>. The operation of such a system can be described as follows.

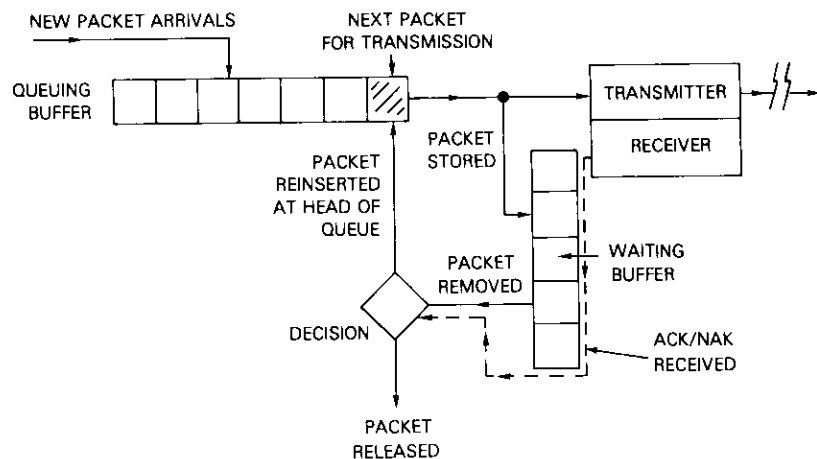


Figure 1. Representation of a Store-and-Forward Packet Switching Node with Selective Repeat ARQ

The packet at the head of B is transmitted into the channel and simultaneously stored in B<sub>w</sub>. The transmitter transmits a packet in a "service interval,"  $\tau$ , as long as B contains at least one packet. It is assumed that transmissions are synchronous, implying that packets are "gated" out of B for transmission at the start of each service interval. Also, if B is empty, an incoming packet can be gated out only at the start of the next service interval. This is equivalent to time slotting, with a basic interval  $\tau$  and transmissions initiated only at the beginning of a slot.

A transmitted packet is retained in the waiting buffer for a period of R slots, corresponding to the effective round-trip delay from completion of the transmission to receipt of the acknowledgment (ACK or NAK). The same packet can be released from the waiting buffer or reinserted at the head of the queuing buffer, B, for retransmission. Thus, if  $\tau_d$  is the effective round-trip delay in seconds, then

$$R = \left[ \frac{\tau_d}{\tau} \right]_+ \quad (1)$$

where  $[n]_+ = n$  if  $n$  is an integer, or the next higher integer if  $n$  is not an integer.

Buffer B is described by a queuing theory model with partial feedback in which the input process consists of new packets (NPs) from one or more sources and retransmission packets (RPs) from the waiting buffer. (RPs receive higher priority.) Since the transmission rate is one packet per slot,  $\tau$ , acknowledgments are also received at that rate. Hence, a maximum of one RP reenters the queue B per service interval. This restriction is not applicable to NP arrivals. The output of this process is provided by the transmission channel operating at a rate of one packet transmitted per slot,  $\tau$ .

In addition, a separate (although not independent) queuing process exists at the waiting buffer. With every transmission, packets are removed according to the arrival of acknowledgments for the stored packets, regardless of whether success or failure is indicated.

The queuing processes at the queuing and waiting buffers, represented by Figure 2, are analyzed based upon the following assumptions:

- a. The number of NP arrivals per slot is a random variable with a stationary independent probability distribution describable by the Z-transform of the probability density function (PDF) as  $P(z)$ . That is, if  $\pi_k$  is the probability that  $k$  NPs arrive per slot, then  $\pi_k$  ( $k = 0, 1, \dots$ ) are identically distributed for all slots and are independent of time.

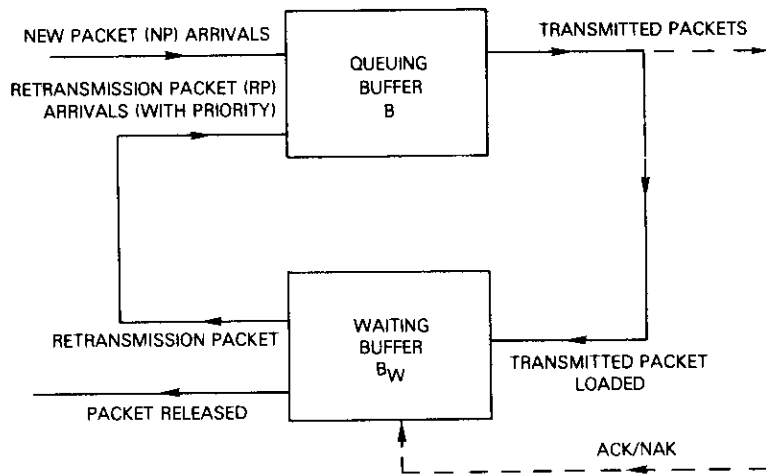


Figure 2. System of Queues with Feedback

The generating function  $P(z)$  is given by

$$P(z) = \sum_{k=0}^{\infty} \pi_k z^k$$

(This is the only assumption concerning the explicit nature of the arrival process.)

b. An infinite buffer is employed. Although only finite buffers can be implemented in a real system, a finite buffer with very low overflow probability can be approximated by an infinite buffer.

c. The system has achieved equilibrium, *i.e.*, the PDFs of various system parameters have time-independent values. (If the system does not have any equilibrium state, a solution cannot be found.)

d. The packets in the queuing buffer are instantaneously “clocked” out at the leading edge of each service interval. This is equivalent to assuming an instantaneous opening and closing of a gate from the buffer to the transmitter.

e. Acknowledgments are sent separately as very short packets so that the probability of losing an acknowledgment is negligibly small. If the channel bit-error rate degrades to a value where the loss of acknowledgment packets becomes significant, the error rate for data packets will be extremely large and the system will have very low

throughput. Thus, for systems with moderate to high throughputs, the short acknowledgment packets can be assumed to be transmitted without errors.

**Model for queuing buffer**

If, under equilibrium conditions,  $N$  represents the number of packets stored in buffer B at the end of a slot, then

$$N = (N - 1)^+ + X + r$$

where  $X$  and  $r$  represent the number of NP arrivals and RP reentries per slot, respectively, and  $(x)^+ = \max(x, 0)$ ;  $(N - 1)^+$  represents the packets remaining in B immediately after a packet has been gated out. It is assumed that both  $N$  and  $r$  have stationary distributions, and that  $r$  can only have values 0 or 1, since only one acknowledgment can be received per slot. When the PDF and the Z-transforms of the process  $X$  are represented by

$$\pi_k = Pr[X = k], \quad k = 0, 1, 2, 3, \dots \tag{2a}$$

$$P(z) = \sum_{k=0}^{\infty} \pi_k z^k \tag{2b}$$

the process  $N$  by

$$q_k = Pr[N = k] \tag{3a}$$

$$Q(z) = \sum_{k=0}^{\infty} q_k z^k \tag{3b}$$

and the process  $r$  by

$$a_k = Pr[r = k], \quad k = 0 \text{ or } 1 \tag{4a}$$

$$A(z) = a_0 + a_1 z \tag{4b}$$

the equilibrium equation can be written as

$$q_k = q_0(a_0 \pi_k + a_1 \pi_{k-1}) + \sum_{l=1}^{\infty} q_l(a_0 \pi_{k-l+1} + a_1 \pi_{k-l}), \quad k = 0, 1, 2, \dots \tag{5}$$

observing that  $\pi_l = q_l = a_l = 0$  for  $l < 0$ . Note that the process  $r$  is not an independent process but depends on past history (as discussed below), and hence the coefficients  $a_0$  and  $a_1$  are not independent.

The PDFs  $a_0$  and  $a_1$  are needed to determine the RP process  $A(z)$  required to obtain the equilibrium  $Q(z)$  for a given NP process  $P(z)$ . Clearly, the RP process in a given slot depends upon whether a packet was transmitted  $R$  slots earlier and whether an error occurred. One transmission per slot occurs each time  $N$  is nonzero at the end of the preceding slot. The transmission error probability is the packet error probability,  $\epsilon$ . Under equilibrium conditions, by definition, the PDFs  $q_k$  for  $N$  are slot independent, and hence  $a_0$  and  $a_1$ , which depend on the value of  $N$ ,  $R$  slots earlier, can be written as

$$a_0 = Pr[N = 0] + Pr[N > 0] Pr[\text{No transmission error}]$$

and  $a_1 = Pr[N > 0] Pr[\text{Transmission error}]$ . The probabilities for  $N$  are slot independent and hence are the same for the current slot. Thus,

$$a_0 = q_0 + (1 - \epsilon)(1 - q_0) = 1 - \epsilon(1 - q_0) \quad (6)$$

and

$$a_1 = \epsilon(1 - q_0) \quad (7)$$

These values depend only on  $\epsilon$  and  $q_0$ . The Z-transform  $A(z)$  is

$$A(z) = 1 + \epsilon(1 - q_0)(z - 1) \quad (8)$$

Since  $A(z)$  is expressed in terms of the specified packet error probability, equation (5) can be multiplied by  $z^k$  and summed over  $k$  from 0 to  $\infty$ . By algebraic manipulation,

$$Q(z) = \frac{a_1 q_0 P(z) z(z - 1) - a_0 P(z)(q_0 + q_1 z) + z H(z)}{z - (a_0 + a_1 z) P(z)} \quad (9)$$

where  $H(z) = q_0 + a_0(q_0 + q_1)[P(z) - \pi_0]$  and  $a_0$  and  $a_1$  are given by equations (6) and (7).  $Q(z)$  is the Z-transform of the equilibrium PDF for the buffer occupancy  $N$ . However, the right-hand side of equation (9) still contains unknowns,  $q_0$  and  $q_1$ . These two unknowns may be eliminated by invoking the conditions for  $Q(z)$  to represent the Z-transform of the  $q_k$ 's; i.e.,  $Q(z)$  must be analytic in the unit disk  $|z| \leq 1$ , and  $Q(1)$  must be unity.

Equation (9) shows a simple pole at  $z = 1$ . Hence, if  $Q(z)$  is to be analytic at  $z = 1$ , the numerator must also vanish at  $z = 1$ . Also, since  $P(1) = 1$ , it can be shown that

$$a_0(q_0 + q_1) = \frac{q_0}{\pi_0} \quad (10)$$

which when substituted into equation (9) yields

$$Q(z) = \frac{q_0(z - 1)(a_0 + a_1 z) P(z)}{z - (a_0 + a_1 z) P(z)} \quad (11)$$

The unknown  $q_0$ , which can be determined by using  $Q(1) = 1$ , becomes

$$q_0 = \frac{1 - \epsilon - \mu}{1 - \epsilon} \quad (12)$$

From equations (6) and (7),

$$a_1 = \mu \epsilon$$

and

$$a_0 = 1 - \mu \epsilon$$

where

$$\mu \epsilon = \frac{\epsilon \cdot \mu}{1 - \epsilon}$$

and  $\mu = E[X] = P'[1]$  is the average NP arrival rate per slot.

Therefore, the Z-transform  $Q(z)$  of the equilibrium PDF for buffer occupancy  $N$  is expressed as

$$Q(z) = (1 - \mu - \mu \epsilon) \frac{(z - 1) F(z)}{z - F(z)} \quad (13)$$

where

$$F(z) = [1 + \mu \epsilon(z - 1)] P(z)$$

It can be shown that, for  $Q(z)$  to represent a generating function,  $q_0$  must be nonzero, and that, for  $q_0$  to represent the probability of an empty buffer,  $1 \geq q_0 \geq 0$ . Thus,  $q_0$  must satisfy  $1 \geq q_0 > 0$  for  $Q(z)$  to represent

an equilibrium generating function for  $N$ ; hence, from equation (12),

$$\mu < 1 - \epsilon \quad (14)$$

must be satisfied.

The mean and variance of the equilibrium buffer occupancy in queuing buffer B can be obtained from the generating function  $Q(z)$ :

$$E\{Q\} = \frac{\sigma^2(1 - \epsilon) + \mu^2\epsilon}{2(1 - \epsilon - \mu)} + \frac{\mu(1 + \epsilon)}{2(1 - \epsilon)} \text{ packets} \quad (15)$$

and

$$\text{var}\{Q\} = \sigma_f^2 + \frac{1}{12} + \frac{\mu_{f_3} - 1}{3(1 - \mu_f)} + \left[ \frac{\sigma_f^2 - (1 - \mu_f^2)}{2(1 - \mu_f)} \right]^2 \text{ packets} \quad (16)$$

where

$$\mu_f = \frac{\mu}{1 - \epsilon} \quad (17)$$

$$\sigma_f^2 = \sigma^2 + \frac{\mu\epsilon(1 - \epsilon - \epsilon\mu)}{(1 - \epsilon)^2} \quad (18)$$

and

$$\mu_{f_3} = \mu_3 + \frac{\epsilon\mu}{1 - \epsilon} [3\sigma^2 + (1 + \mu)(1 + 3\mu) - \mu] \quad (19)$$

with  $\mu$ ,  $\sigma^2$ , and  $\mu_3$  as the mean, the variance, and the third central moment of the NP arrival process  $X$  per slot.

It can be easily verified that, with no transmission errors (*i.e.*,  $\epsilon = 0$ ), equations (13), (15), and (16) correspond to the expressions for a store-and-forward node or multiplexer [4] with no retransmissions.

#### Model for waiting buffer

Under equilibrium conditions, the processes in the waiting buffer occur as follows. In any slot, a packet is input to  $B_w$  with probability  $1 - q_0$ ; no packets are input with probability  $q_0$ . It should be noted that  $q_0$  is the equilibrium probability that queuing buffer B is empty (or the probability that no transmission occurs in a given slot). Each arrival into  $B_w$  is held for

$R$  slots [given by equation (1)] before being discarded or reinserted into the queuing buffer B.

The waiting buffer will contain  $k$  units at the end of a given slot if  $k$  transmissions occurred in the preceding  $R$  slots. Therefore,

$$\text{Pr}[N_w = k] = \binom{R}{k} (1 - q_0)^k q_0^{R-k} \quad (20)$$

The generating function  $Q_w(z)$  for the occupancy in the waiting buffer is

$$Q_w(z) = \sum_{k=0}^{\infty} \text{Pr}[N_w = k] z^k$$

and yields

$$Q_w(z) = [1 + \frac{\mu}{1 - \epsilon} (z - 1)]^R \quad (21)$$

Hence, the mean and variance of the buffer occupancy are given by

$$E[Q_w] = \frac{\mu}{1 - \epsilon} R \quad (22)$$

and

$$\text{var}[Q_w] = \frac{\mu R(1 - \epsilon - \mu)}{(1 - \epsilon)^2} \quad (23)$$

The highest power of  $z$  in equation (21) is  $z^R$ ; hence,

$$\text{Pr}[N_w > R] = 0 \quad (24)$$

indicating that the maximum waiting buffer size needed is  $R$  packets. Average buffer occupancy [equation (22)] is less than  $R$  because of the condition expressed by equation (14) imposed on equation (22).

#### Model for delay

The delay suffered by a packet ("test" packet) randomly arriving within a slot will be examined. Because of retransmissions, the term "delay" is used to imply the time between the arrival of the test packet at

the transmission node and the instant that it is successfully received at the destination node. It is assumed that RP reentries have the highest priority and are always placed at the head of the transmission queue. The total end-to-end delay has the following components:

- a. *Queuing delay* is the delay that the packet experiences between arrival and servicing by the transmitter.
- b. *Service time* for a packet is normally one service interval,  $\tau$ . However, since retransmissions may occur, service time must be defined as the interval between the first transmission initiation and the end of the last required retransmission.
- c. *Propagation delay* occurs between transmitting and receiving nodes for the last (successful) retransmission. The effect of round-trip delay is also included in the service time.

Figure 3 represents the random arrival of a test packet in an arbitrary service interval at time  $\alpha$  ( $0 \leq \alpha \leq 1$ ) within that interval. The queue size  $N$ , prior to the start of a service interval, is given by the generating function  $Q(z)$  under equilibrium conditions. Since transmissions in a slot are

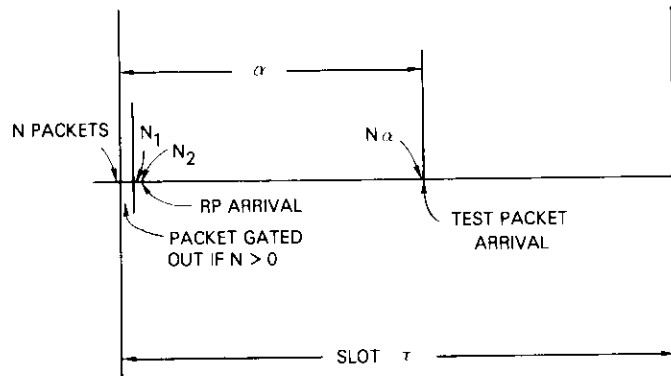


Figure 3. Queue Sizes Prior to Arrival of a Test Packet

gated at the beginning, the queue size immediately following such gating ( $N_1$ ) is given by

$$N_1 = (N - 1)^+ .$$

The random arrival of NPs and RPs over the service interval increases the queue size, which builds up to  $N$  [described by  $Q(z)$ ] at the end of the slot. The priority of an RP reentry (RP reentries can only be 0 or 1)

causes the RP to be placed at the head of the queue regardless of the reentry time. Thus, an RP reentry, if any, occurring at any point within a slot, is equivalent to a reentry that occurs at the instant the gate closes. The queue size after possible RP reentry is given by

$$N_2 = (N - 1)^+ + r .$$

A packet arriving at a random instant  $\alpha$  in the slot encounters a queue formed by  $N_2$  and preceding NP arrivals. The queue size at  $\alpha$  can be represented by

$$N_\alpha = (N - 1)^+ + r + X_\alpha \tag{25}$$

where  $X_\alpha$  represents the number of NP arrivals in fraction  $\alpha$  of the service interval. The generating function  $Q_\alpha(z)$  for  $N_\alpha$  is

$$Q_\alpha(z) = \frac{Q(z)}{P(z)} P_\alpha(z) \tag{26}$$

where  $P_\alpha(z)$  is the generating function for  $X_\alpha$ . In this equation,  $P(z)$ , the input process per slot, is identical to  $P_\alpha(z)$  with  $\alpha = 1$ . Hence, the mean and variance of the queue size at  $\alpha$  are

$$E[Q_\alpha] = E[Q] + E[X_\alpha] - E[X] \tag{27}$$

and

$$\text{var}[Q_\alpha] = \text{var}[Q] + \text{var}[X_\alpha] - \text{var}[X] . \tag{28}$$

Since queue  $N_\alpha$  is distributed according to the generating function  $Q_\alpha(z)$  given by equation (26), the queuing delay ( $D_{Q_\alpha}$ ) consists of the residual time  $(1 - \alpha)$  in the service interval when the test packet arrives and the number of slots,  $d_{N_\alpha}$ , elapsing before service starts, *i.e.*,

$$D_{Q_\alpha} = 1 - \alpha + d_{N_\alpha} . \tag{29}$$

To determine  $d_{N_\alpha}$ , the packets preceding the arrival of the test packet must first enter service. The departure rate is one packet per slot as long as there are no RP reentries. A success occurs when a packet departs from this queue with no RP reentry, and a failure occurs when an RP entry preempts departures from this queue. Therefore, the probability of the

$n$ th success occurring after  $k$  failures has a negative binomial (Pascal) distribution with PDF expressed by

$$f(k; n, \lambda) = \binom{n+k-1}{k} \lambda^n (1-\lambda)^k \quad (30)$$

where  $\lambda$  is the success probability per trial. The generating function of this distribution is given by

$$B_n(z) = \left( \frac{\lambda}{1-z\nu} \right)^n \quad (31)$$

where  $\nu = 1 - \lambda$ .

The queue size  $N_\alpha$  already includes an RP reentry in the test packet arrival slot; hence, the next slot is always a success since one packet from this queue will be transmitted in the next slot. The time for the  $l$ th packet to start service is

$$t_l = 1 + (T_{l-1} - 1) = T_{l-1} \quad (32)$$

where  $T_{l-1}$  is the elapsed time to the  $(l-1)$ th success. The probability that the queuing time for the  $l$ th packet is  $k$  slots has the PDF  $f(k-l+1; l-1, \lambda)$ .

The number of packets,  $L$ , preceding the test packet in the queue is distributed according to  $Q_\alpha(z)$ . Hence, with equation (32),  $f(k-L; L, \lambda)$  is the conditional probability that the queuing time is  $k$  slots when the queue has  $L$  packets preceding the test packet. Therefore,

$$Pr\{d_{N_\alpha} = k\} = \sum_{l=0}^{\infty} f(k-L; L, \lambda) Pr\{N_\alpha = L\}$$

Multiplying by  $z^k$  and summing yields

$$D_\alpha(z) = Q_\alpha[G(z)] \quad (33)$$

with

$$G(z) = \frac{\lambda z}{1-\nu z}$$

Since the success probability,  $\lambda$ , is simply the non-RP reentry probability,

using equations (6), (7), and (12) gives

$$\nu = a_1 = \mu_\epsilon = \frac{\epsilon\mu}{1-\epsilon} \quad (34)$$

and

$$\lambda = a_0 = 1 - \mu_\epsilon \quad (35)$$

The generating function for the queuing delay is

$$D_\alpha(z) = Q_\alpha \left[ \frac{(1-\mu_\epsilon)z}{1-\mu_\epsilon z} \right] \quad (36)$$

With the use of equations (26)–(29), the mean and variance of the queuing delay,  $D_Q$ , averaged over the possible arrival times,  $\alpha$ , of the test packet [assuming uniform probability for arrival in the interval (0, 1)] is

$$\begin{aligned} \overline{E[D_Q]} &= \frac{(1-\epsilon)}{(1-\epsilon-\epsilon\mu)} \left\{ \frac{\sigma^2(1-\epsilon) + \mu^2\epsilon}{2(1-\epsilon-\mu)} + \frac{\mu(1+\epsilon)}{2(1-\epsilon)} - \mu + \overline{\mu_\alpha} \right\} \\ &\quad + \frac{1}{2} \text{ slots} \end{aligned} \quad (37)$$

and

$$\overline{\text{var}[D_Q]} = \frac{(1-\epsilon)^2}{(1-\epsilon-\epsilon\mu)} \left\{ \left( \frac{\epsilon\mu}{1-\epsilon} \right) \overline{E[D_Q]} + \text{var}[Q] - \sigma^2 + \overline{\sigma_\alpha^2} \right\} \quad (38)$$

where the bar indicates averaging over  $\alpha = 0$  to 1,  $\text{var}[Q]$  is given by equation (16), and  $\mu_\alpha$  and  $\sigma_\alpha^2$  are the mean and variance of the number of packets arriving in an interval  $\alpha$ . Thus, for example, if the arrival process is Poisson, then  $\mu_\alpha = \alpha\mu$  and  $\sigma_\alpha^2 = \alpha\sigma^2$ .

The service time can be determined as follows. The probability that a packet requires  $n$  retransmissions ( $n = 0, 1, 2, \dots$ ) is  $\epsilon^n(1-\epsilon)$ , and the total service time required is  $n(1+R) + 1$  slots. Therefore, the mean and variance in service times can be

$$E[S] = \frac{1+\epsilon R}{1-\epsilon} \text{ slots} \quad (39)$$

$$\text{var}[S] = \frac{\epsilon(1+R)^2}{(1-\epsilon)^2} \quad (40)$$

where  $R$  is the round-trip delay in an integer number of slots [equation (1)].

The final factor is one-way propagation delay which can be approximated by  $R/2$  slots. In summary, the mean and variance of the overall delay experienced by a test packet are

$$\begin{aligned} \overline{E}[D] = & \frac{1+R}{2} + \frac{1+\epsilon R}{1-\epsilon} + \frac{(1-\epsilon)}{(1-\epsilon-\epsilon\mu)} \left\{ \frac{\sigma^2(1-\epsilon) + \mu^2\epsilon}{2(1-\epsilon-\mu)} \right. \\ & \left. + \frac{\mu(1+\epsilon)}{2(1-\epsilon)} - \mu + \overline{\mu_\alpha} \right\} \text{ slots} \end{aligned} \quad (41)$$

$$\begin{aligned} \text{var}[D] = & \frac{\epsilon(1+R)^2}{(1-\epsilon)^2} + \frac{(1-\epsilon)^2}{(1-\epsilon-\epsilon\mu)} \left\{ \left( \frac{\epsilon\mu}{1-\epsilon} \right) \overline{E}[D_Q] \right. \\ & \left. + \text{var}[Q] - \sigma^2 + \overline{\sigma_\alpha^2} \right\} \end{aligned} \quad (42)$$

where  $\overline{E}[D_Q]$  is given by equation (37) and  $\text{var}[Q]$  by equation (16).

### Performance

The performance of the system can be measured by efficiency (or throughput), average buffer occupancy, and mean delay:

*a. Efficiency.* Transmission efficiency,  $\eta$ , can be defined by the average information flow rate. Since the average NP arrivals per slot,  $\mu$ , must equal the average information flow rate per slot under equilibrium conditions,

$$\eta = \mu$$

or, if  $\mu_0$  is the average NP arrivals per second,

$$\eta = \mu_0 T \quad (43)$$

The maximum possible utilization is given by equation (14), *i.e.*,

$$\mu < 1 - \epsilon \quad .$$

Hence, the channel efficiency is

$$\eta < \eta_0 (= 1 - \epsilon) \quad .$$

Although efficiency  $\eta_0$  corresponds to the selective repeat ARQ efficiency, it is not achievable with the steady-state operation of a store-and-forward node with random traffic arrival and selective repeat ARQ.

*b. Buffer Occupancy.* The mean and variance for the queuing buffer occupancy are given by equations (15) and (16), and for the waiting buffer occupancy by equations (22) and (23). In a real system, the buffering requirements are satisfied by a common buffer  $B$  for both queuing and waiting. The average and variance of the occupancy in such a buffer can be estimated by using

$$B(z) = Q(z) Q_w(z) \quad . \quad (44)$$

Hence,

$$E\{B\} = E\{Q\} + E\{Q_w\} \quad (45)$$

and

$$\text{var}\{B\} = \text{var}\{Q\} + \text{var}\{Q_w\} \quad . \quad (46)$$

The parameters on the right-hand side of equations (45) and (46) have been defined previously.

*c. Delay.* Equations (41) and (42) give the mean and variance of the expected delay for a test packet.

### Example of model application

The preceding model, which was derived for general random stationary arrival processes, is used in this section for a Poisson packet arrival process and for a communications satellite channel with a 0.54-s round-trip propagation delay. For a Poisson process,

$$\overline{\mu_\alpha} = \overline{\sigma_\alpha^2} = \frac{\sigma^2}{2} = \frac{\mu}{2}$$

and for the random error channel model assumed for these calculations,

$$\epsilon = 1 - (1 - BER)^b$$

where BER is the channel bit-error rate and  $b$  is the packet size in bits. The following is a summary of the results:

*a. Efficiency Limit.* Figure 4 displays the efficiency limit as a function of bit-error rate for any arrival process. These limits, which depend upon packet size (higher for smaller packet sizes), are the efficiencies of selective repeat ARQ for a continuous data stream. For a random packet arrival process, these limits cannot be actually achieved. Actual efficiency is determined by the average arrival rate,  $\mu_0$ , and the ratio of the packet size and channel transmission rate,  $\tau$ , through equation (43).

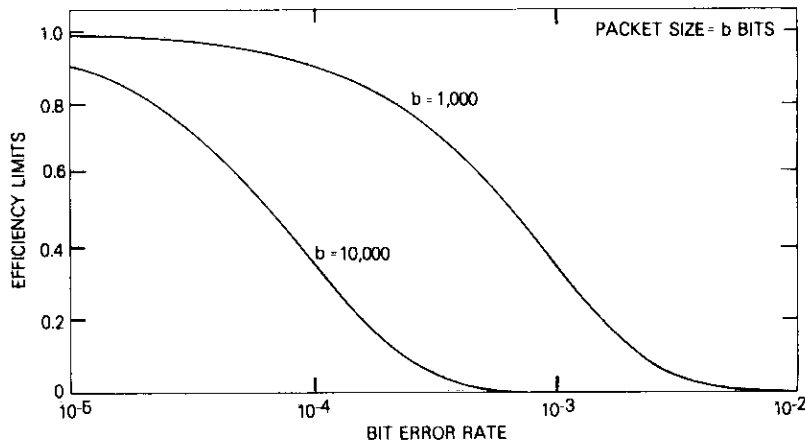


Figure 4. Efficiency Limits Versus Bit-Error Rate for 1- and 10-kbit Packet Sizes

*b. Total Buffer Occupancy.* Figure 5 shows the tradeoff between the average total buffer occupancy and efficiency for bit-error rates of  $10^{-3}$ ,  $10^{-4}$ , and  $10^{-5}$ , and also for an ideal error-free channel with a packet size of 1 kbit over a 56-kbit/s channel. Average buffer occupancy increases sharply as the efficiency limit for each bit-error rate is approached. Also, average buffer occupancy at a specified efficiency is lower at lower bit-error rates.

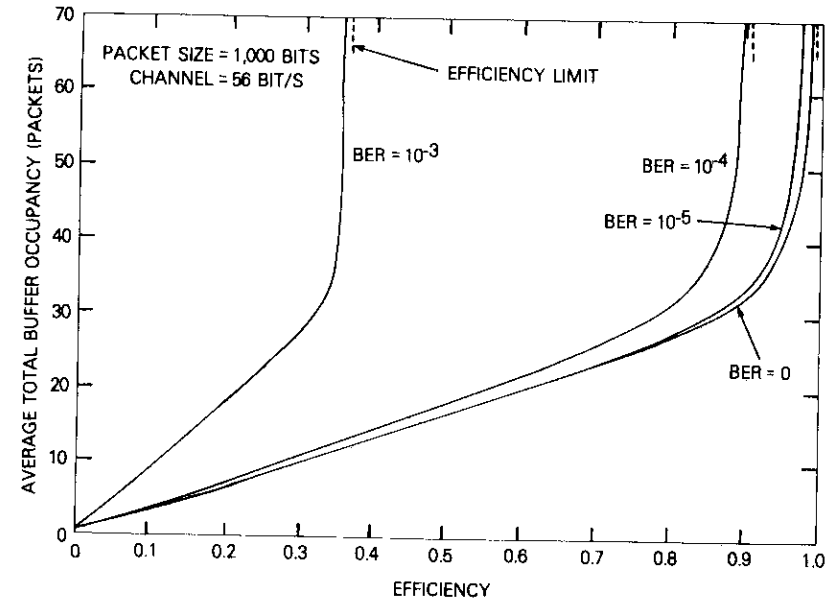


Figure 5. Average Buffer Occupancy Versus Efficiency for a 56-kbit/s Satellite Channel and 1-kbit Packets

*c. Delay/Efficiency Tradeoff.* Figure 6 represents delay/efficiency tradeoffs for the same configuration at the same bit-error rates. Mean delay also increases sharply near the efficiency limits because of the sharp increase in queuing delays. The delays increase with bit-error rate because of increased retransmissions as well as increased queue sizes. Figures 5 and 6 also show that a channel with a bit-error rate of about  $10^{-5}$  can be considered an error-free channel in terms of performance. For other packet sizes or channel transmission rates, similar behavior can be expected in delay/efficiency and buffer/efficiency tradeoffs at various bit-error rates.

Figures 7-9 provide a different view of the delay/efficiency tradeoffs for various packet arrival rates for channels with a specified packet size and bit-error rate. For a given packet arrival rate, the efficiency is varied by changing the channel transmission rate. Systems with high arrival rates perform well over most of the achievable efficiency range; however, the maximum achievable efficiency is limited by the bit-error rate.

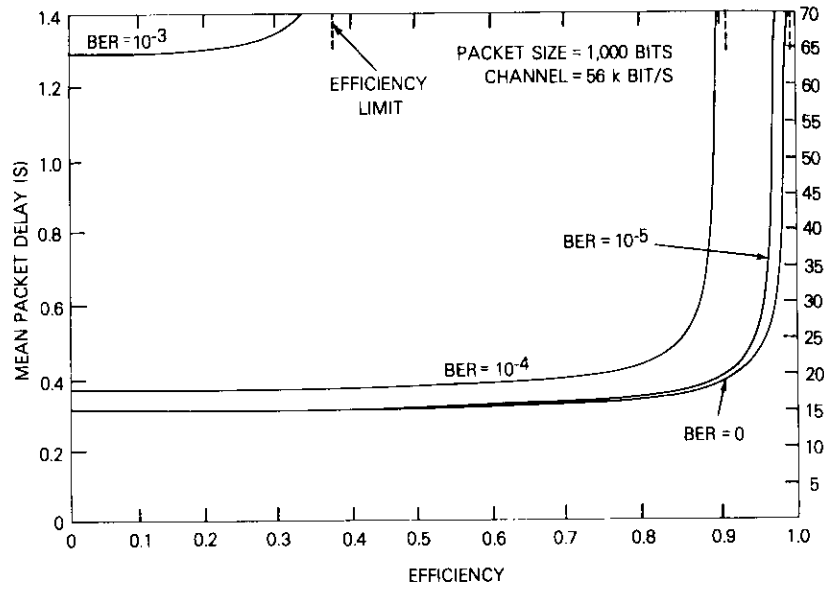


Figure 6. Delay Versus Efficiency Tradeoffs for a 56-kbit Satellite Channel and 1-kbit Packets

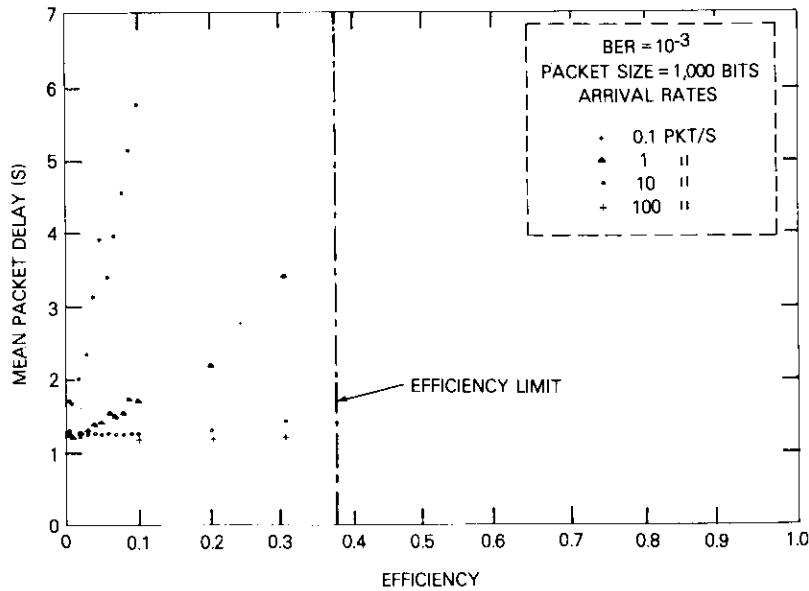


Figure 7. Delay Versus Efficiency Tradeoffs for Different Packet Arrival Rates and  $10^{-3}$  BER

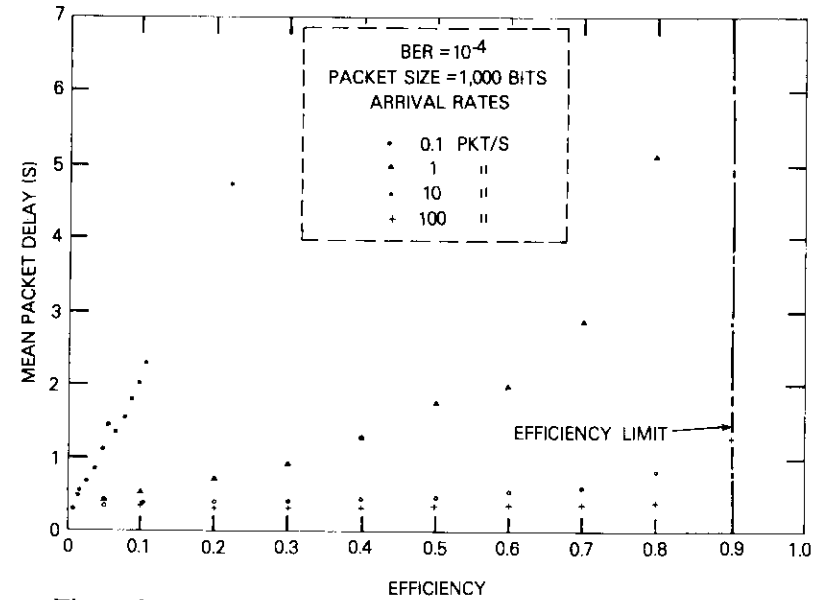


Figure 8. Delay Versus Efficiency Tradeoffs for Different Packet Arrival Rates and  $10^{-4}$  BER

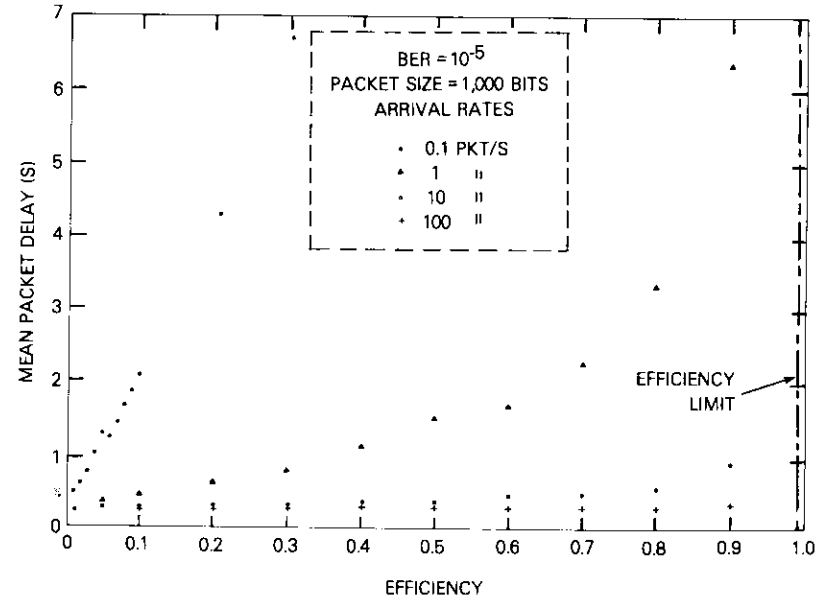


Figure 9. Delay Versus Efficiency Tradeoffs for Different Packet Arrival Rates and  $10^{-5}$  BER

## Conclusions

A model for a store-and-forward packet switching node, including retransmission effects, has been developed. The model displays efficiency limits, buffer occupancy/efficiency, and delay/efficiency tradeoffs which are sensitive to bit-error rates reaching a sufficiently low value, beyond which the system behaves as a conventional store-and-forward node with no retransmissions. The general results are applicable to random stationary packet arrival processes such as Poisson for single packet arrivals and compound Poisson for batch packet arrivals (e.g., multi-packet messages).

## References

- [1] L. Kleinrock, *Queuing Systems*, Vol. I, Chapter 5, New York: J. Wiley & Sons, 1975.
- [2] W. W. Chu, "Buffer Behavior for Poisson Arrivals and Multiple Synchronous Constant Outputs," *IEEE Transactions on Computers*, C-19, No. 6, June 1970, pp. 530-534.
- [3] W. W. Chu, "Buffer Behavior for Batch Poisson Arrivals and Single Constant Output," *IEEE Transactions on Communication Technology*, COM-18, No. 5, October 1970, pp. 613-618.
- [4] W. W. Chu and A. G. Konheim, "On the Analysis and Modeling of a Class of Computer Communications System," *IEEE Transactions on Communications*, COM-20, No. 3, June 1972, pp. 645-660.
- [5] A. Gatfield, "Error Control on Satellite Channels Using ARQ Techniques," *COMSAT Technical Review*, Vol. 6, No. 1, Spring 1976, pp. 179-188.



Ashok K. Kaul received B.Sc. and M.Sc. degrees in physics from the University of Jammu in Kashmir, India, and a Ph.D. in physics from the University of Maryland. In 1973, he joined COMSAT Laboratories, where he is currently Manager of the Computer Communications Department of the Transmission Systems Laboratory, responsible for directing research and experiments in computer communications.

## CTR Notes

### **The effect of buffer access time on HDLC performance**

A. K. KAUL

(Manuscript received Nov. 15, 1978)

#### Introduction

In a previous paper [1] generalized models for high-level data link control (HDLC) throughput efficiencies, using a reject (go-back- $N$ ) error recovery mode, were presented. The models assumed transmission buffering using in-line high-speed core or semiconductor (RAM) memory. In satellite communications, especially at high data transmission rates, the size of the buffer required for high throughput efficiencies is significantly large and expensive. Alternatives to high-speed core or semiconductor memory (e.g., tape or disk storage media) may have to be considered to lower these buffering costs.

The two prime requirements for a storage medium to be usable as a transmission buffer are addressability and sufficiently high read/write speeds. Addressability, which implies the capability to access the stored data at a specific point, is required for retransmission because the transmitter must be able to locate the specific HDLC frame in the storage buffer. The "access" to this location may be sequential, as in tape, or random (i.e., direct), as in disk storage media, and generally involves a finite access time,  $t_a$ , to reach this location. In sequential access media, the access time is generally much longer than that in random-access media. For example, accessing a data record on tape may involve rewinding the tape and/or sequentially stepping through records before the specific

A. K. Kaul is Manager of the Computer Communications Department of the Transmission Systems Laboratory, COMSAT Laboratories.

record can be located. In random-access disk media, the access time is required for address decoding and moving the read/write head to the correct track and location, and hence is much shorter.

The additional requirement of sufficiently high read/write speed is self evident. Clearly, for the buffer to be usable, it should be possible to write and read an entire HDLC frame in a time interval much shorter than the transmission time for such a frame over the communications channel, since otherwise frames would be lost on the receive side, or transmitted with interframe gaps on the transmit side.

If reliability of the storage media is ignored both in terms of electro-mechanical and data integrity during read and write operations, all storage media meeting the requirements of addressability and speed are usable, in principle, as transmission buffers. Therefore, the only significant factor in determining the impact of these alternatives on throughput efficiency is the access time,  $t_a$ , defined as the time interval between the identification of the need to access a specific HDLC frame (e.g., on receipt of an REJ response) and the time that the HDLC frame is read from the buffer and is available for retransmission.

Under the HDLC reject mode, a retransmission of an HDLC frame is followed by a redundant retransmission of all subsequent frames. Thus, the logic identifying the beginning of a retransmission sequence requires an access time,  $t_a$ , to retrieve the first retransmission frame, but all subsequent frames can be automatically retrieved without requiring intervention by the same logic. Appropriate smoothing by two high-speed in-line buffers can prevent gaps in the retransmission sequence, except for the first access, provided that the read speed is sufficiently higher than the data transmission rate.

Consequently, the use of such buffers makes it necessary to include the effect of the access time,  $t_a$ , on the transmission process, and is explained in the next section. The modifications required to the results for throughput efficiency in Reference 1 are also presented. Finally, the modified throughput efficiency equations are used to illustrate the quantitative effect of access time on throughput efficiencies for a 56-kbit/s and a 1.544-Mbit/s satellite channel for HDLC operation in the half duplex (HDX), full duplex normal (FDX-NRM), and asynchronous response (FDX-ARM) modes.

**Modified models**

Figures 1 and 2 illustrate the situation encountered at the transmitter on receipt of a "receive ready" (RR) or "reject" (REJ) response. In Figure 1, no transmission is underway when the acknowledgment is received.

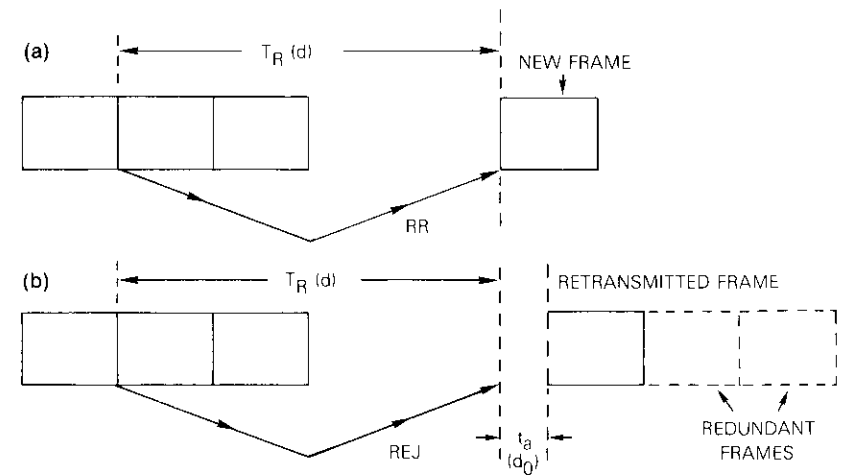


Figure 1. Frame Transmission (a) and Retransmission (b) When an Acknowledgment is Received and no Transmission is in Progress

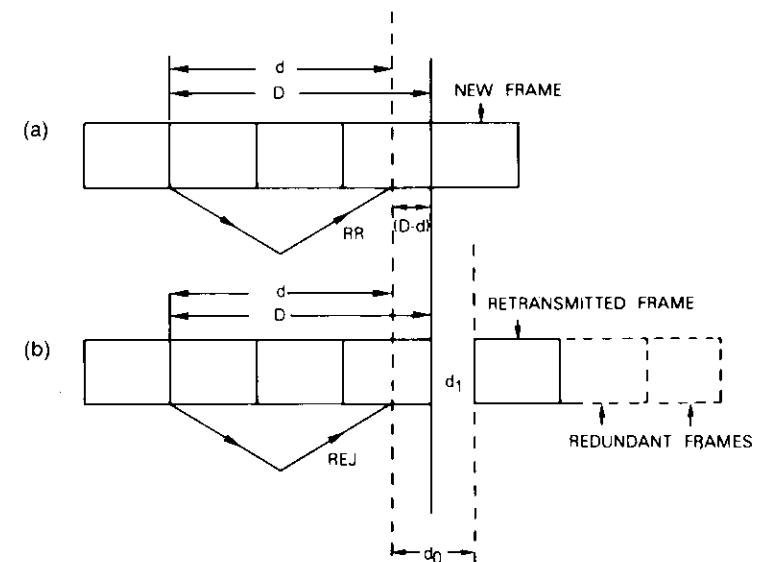


Figure 2. Frame Transmission (a) and Retransmission (b) When an Acknowledgment is Received While a Frame Transmission is in Progress

In the case of an RR response, transmission of the next HDLC frame starts without any delay. However, in the case of a REJ response, the retransmission actually starts  $t_a$  seconds later. This delay in units of frame transmission time can be expressed as

$$d_0 = \frac{Ct_a}{b} \quad (1)$$

where  $C$  is the channel transmission rate in bit/s and  $b$  is the HDLC frame size in bits (including overhead).

Figure 2 illustrates the situation when a transmission is underway at the time that the response is received. If the response is RR, there is no additional delay beyond that required to complete the frame transmission underway. However, for a REJ response, a delay  $d_1$  (in units of frame transmission times) occurs between the end of the current transmission and the start of the retransmission and is given by

$$d_1 = \max[0, (d + d_0 - D)] \quad (2)$$

where 
$$d = \frac{CT_R}{b} \quad (3)$$

and 
$$D = [d]_+ \quad (4)$$

where  $T_R$  is the round-trip propagation delay, and  $[X]_+$  represents  $X$  for integer  $X$  and the next higher integer for non-integer  $X$ .

The net effect of the above is to effectively increase the length of each retransmission cycle which occurs by  $d_0$  or  $d_1$ . In Reference 1, the throughput efficiencies in each case were of the form

$$\eta = \left( \frac{b - A}{b} \right) \frac{\bar{n}}{\bar{i}} \quad (5)$$

where  $b$  = HDLC frame length in bits including overhead  
 $A$  = overhead bits per frame  
 $\bar{n}$  = average frames successfully transmitted per "service cycle"  
 $\bar{i}$  = average duration of a service cycle.

The quantity  $\bar{n}$  remains unchanged in the modified models, and only the quantity  $\bar{i}$  needs to be recomputed; equation (5) then gives the required

throughput efficiencies. The quantities  $\bar{i}$  and  $\eta$  for the three HDLC modes are computed in the appendix.

#### Illustrative cases

The modified models in the preceding section can be used to predict throughput efficiency for any point-to-point HDLC link. For the transmission buffering, any reliable storage medium can be used which satisfies the addressability and speed requirements and has an access time of  $t_a$  seconds to read an HDLC frame from the buffer. Equations (1) and (2) are used to compute  $d_0$  and  $d_1$ , respectively. The throughput efficiencies can then be calculated by using equation (A-3) for the HDX, equations (A-12), (A-22), or (A-29) for the FDX-NRM, or equation (A-41) or (A-45) for the FDX-ARM.

To illustrate the impact of buffer access time,  $t_a$ , on throughput efficiency, the cases of a 56-kbit/s and 1.544-Mbit/s satellite ( $T_R = 0.54$  s) link are presented. A random error channel is assumed so that

$$S = (1 - BER)^b$$

where BER is the bit-error rate. Also only the large buffer cases giving the highest throughputs are considered for the two FDX cases. In the choice of frame sizes for all three modes and the optimal Maxout  $N$  for the HDX mode, near optimal values for  $b$  are chosen for  $t_a = 0$  using the results in Reference 1 to obtain throughput efficiencies near the maximum achievable values. An HDLC frame overhead of 56 bits is used.

Figures 3a-3c show the predicted throughput efficiency of the 56-kbit/s satellite channels in the HDX, FDX-NRM, and FDX-ARM modes, respectively, while Figures 4a-4c show the expected performance for a 1.544-Mbit/s satellite channel in the same three modes. For access times up to about  $T_R$ , there is little decline in throughput efficiency especially at sufficiently low bit-error rates (e.g.,  $10^{-8}$ ). As the bit-error rate is increased and the maximum achievable throughput is reduced, a further reduction occurs at correspondingly lower values of access time. For a large value of  $t_a$ , the percentage reduction in throughput from  $t_a = 0$  values increases as the bit-error rate increases. However, at high bit-error rates the maximum throughput values are so low that the impact of a further reduction caused by increasing  $t_a$  is of academic interest. It is more useful to consider the impact of  $t_a$  on high throughput  $t_a = 0$  cases. For both channels there is a negligible effect on throughput for access times up to about 100 ms, while beyond that some reduction is noticeable especially at the higher bit-

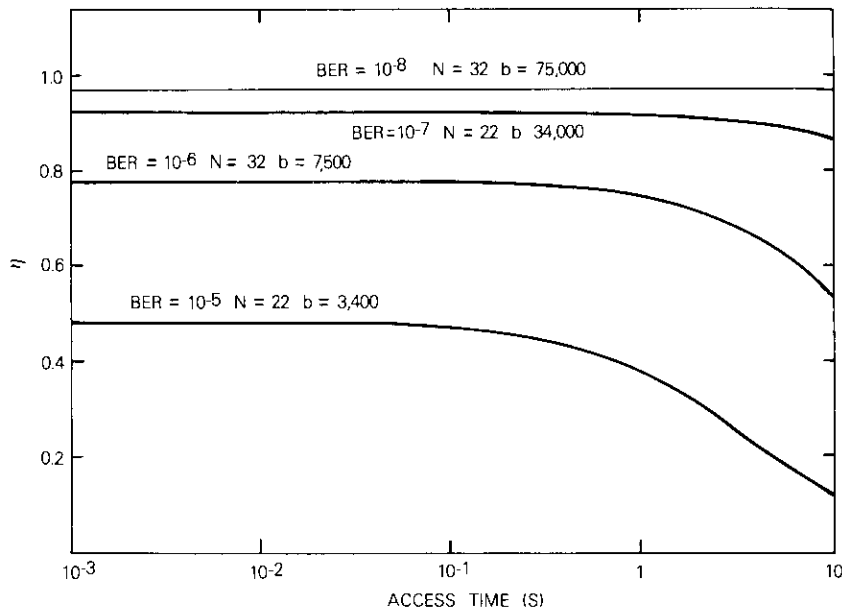


Figure 3a. 56-kbit/s HDX Mode

error rates. Access times up to 1 second are tolerable for bit-error rates of  $10^{-7}$  and lower for the 56-kbit/s channel and  $10^{-8}$  and lower for the 1.544-Mbit/s channel.

Finally, the average access times corresponding to hard disk units are between 10 and 100 ms. For example, the IBM 3330 disk storage unit has an average access time of 55 ms for the maximum number of cylinders. Figures 3 and 4 show that these disk units can be used instead of in-line high-speed buffers for 56-kbit/s and 1.544-Mbit/s satellite channels.

### Conclusions

The models in Reference 1 have been modified for use with HDLC links with transmission buffering provided by storage media other than high-speed in-line buffers. The storage devices must satisfy the requirements of addressability and sufficiently high read/write speed, as well as reliability. If the specific media satisfy these requirements, the models presented in this paper can then be used to predict the impact of access time on throughput efficiency. Specific cases of 56-kbit/s and 1.544-Mbit/s satellite channels, which have been shown as examples, demonstrate that the use

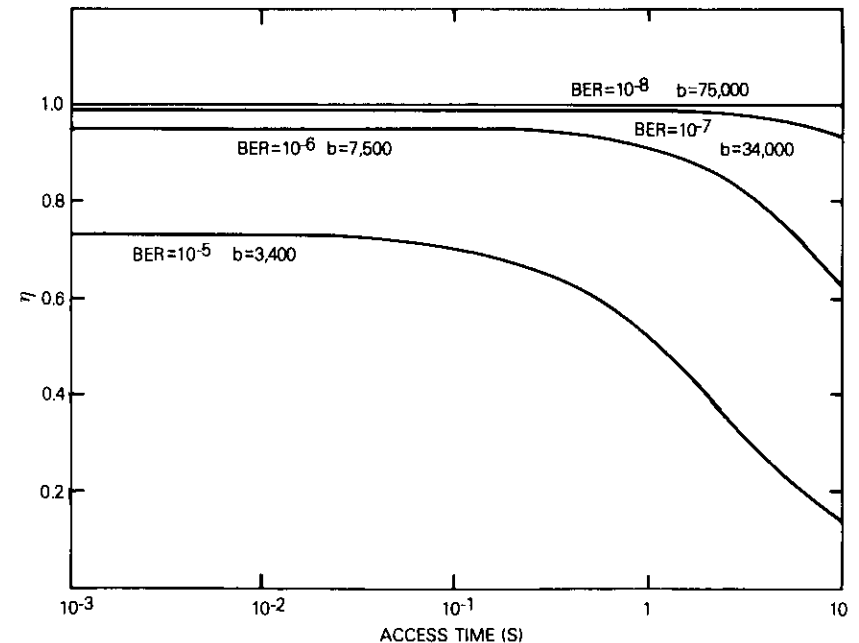


Figure 3b. 56-kbit/s FDX-NRM

of disk storage devices would not cause a noticeable decline in throughput in either of these channels operating in any of the HDLC modes.

### References

- [1] A. K. Kaul, "Performance of High-Level Data Link Control in Satellite Communications," *COMSAT Technical Review*, Vol. 8, No. 1, Spring 1978, pp. 41-87.

### Appendix A. Derivation of modified throughput equations

The modified models presented in this appendix require familiarity with the derivation of the models presented in Reference 1. All equation numbers "R" refer to equation numbers in Reference 1.

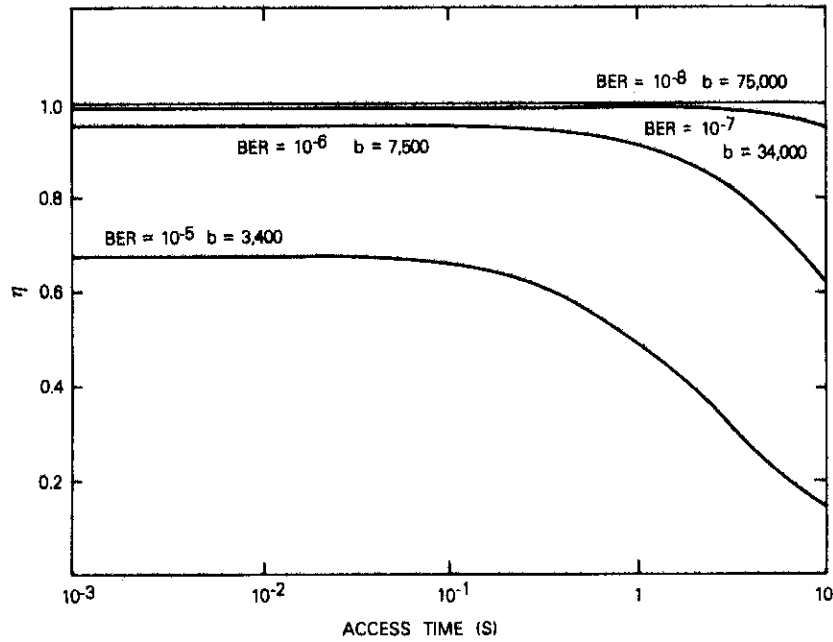


Figure 3c. 56-kbit/s FDX-ARM

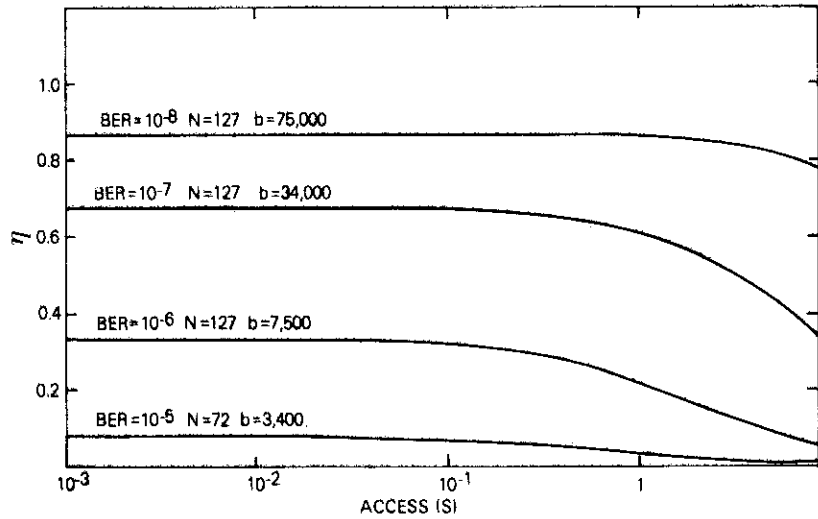


Figure 4a. 1.544-Mbit/s HDX

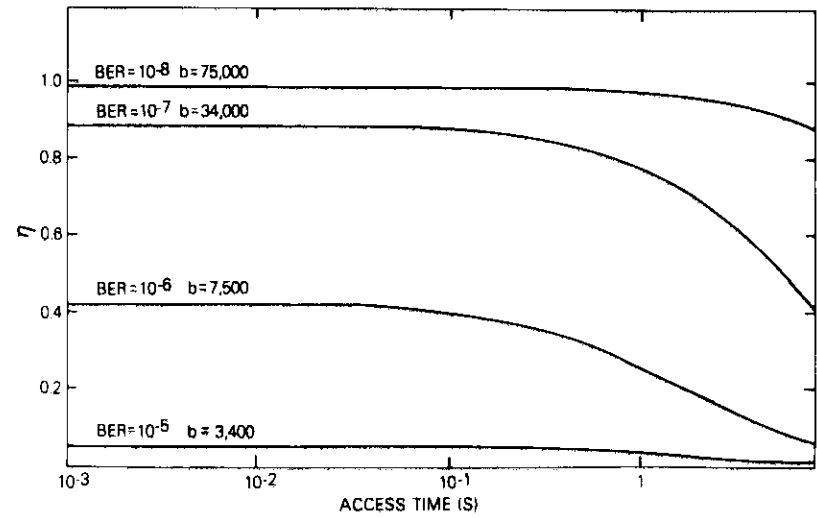


Figure 4b. 1.544-Mbit/s FDX-NRM

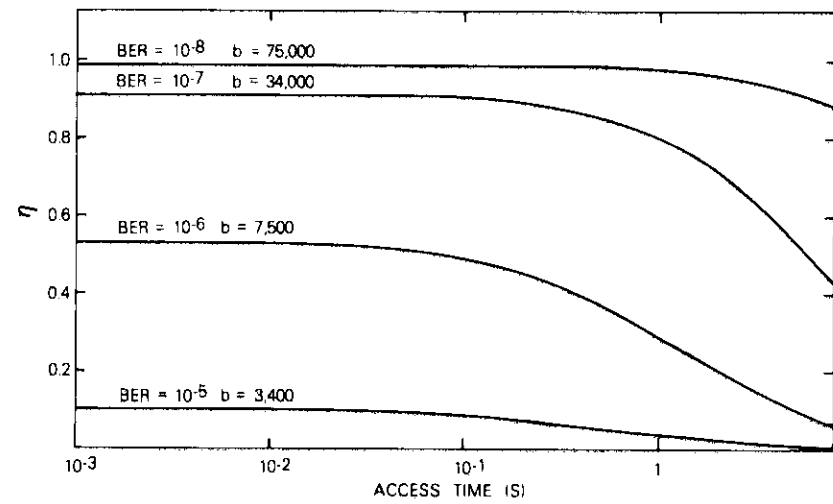


Figure 4c. 1.544-Mbit/s FDX-ARM

**HDX**

In the HDX mode,  $\bar{n}$  is still given by equation (R6):

$$\bar{n} = \frac{S(1 - S^N)}{(1 - S)} \tag{A-1}$$

where  $S$  = HDLC frame transmission success probability  
 $N$  = maxout.

On the other hand,  $t = N + d$  for all new cycles with probability  $S^N$ ; however,  $t = N + d + d_0$  for all retransmission cycles with probability  $(1 - S^N)$ . Hence,

$$\begin{aligned} \bar{t} &= (N + d) S^N + (N + d + d_0)(1 - S^N) \\ \bar{t} &= N + d + d_0(1 - S^N) \end{aligned} \tag{A-2}$$

and with equations (5), (A-1), and (A-2),

$$\eta = \left(\frac{b - A}{b}\right) \frac{S(1 - S^N)}{(1 - S)\{N + d + d_0(1 - S^N)\}} \tag{A-3}$$

where  $d_0$  is given by equation (1).

**FDX-NRM**

Reference 1 presented the FDX NRM as two cases depending on the available buffering (or maxout). In this paper, this mode must be presented as three cases as shown below:

a. *Case A:* When the buffering is such that

$$N < 1 + d$$

there is never a frame under transmission when the response to a poll is received back at the transmitter, and the situation illustrated in Figure 1 is always applicable. Hence, equation (R21) is replaced by

$$\bar{t} = t_m N_m + t_{m_0} N_{m_0} + (t_m + d_0) R_m$$

where  $t_m = t_{m_0} = 1 + d$

and  $N_m$ ,  $N_{m_0}$ , and  $R_m$  are given by equations (R17)–(R20), i.e.,

$$N_{m_0} = \frac{S}{Z} \tag{A-4}$$

$$N_m = \frac{S^{m+1}}{Z} \tag{A-5}$$

$$R_m = \frac{1 - S^{N+1}}{Z} \tag{A-6}$$

where  $Z = 1 + S + S^{m+1} - S^{N+1}$  (A-7)

and  $m = \min[N, 1 + D]$ . (A-8)

For this case,  $m = N$  and hence

$$Z = 1 + S \tag{A-9}$$

Therefore,

$$\bar{t} = \frac{1}{Z} \left[ (1 + d)(1 + S) + d_0(1 - S^{N+1}) \right] \tag{A-10}$$

and with  $\bar{n}$  still given by equation (R26a) as

$$\bar{n} = \frac{S(1 - S^{N+1})}{Z(1 - S)} \tag{A-11}$$

$$\eta = \left(\frac{b - A}{b}\right) \left[ \frac{S(1 - S^{N+1})}{(1 - S)\{(1 + d)(1 + S) + d_0(1 - S^{N+1})\}} \right] \tag{A-12}$$

b. *Case B:* When the buffering is subject to the restriction

$$1 + 2D > N \geq 1 + d \tag{A-13}$$

then  $m = 1 + D$ . Thus, the situation of Figure 1 applies to all retransmission cycles ( $R_m$  cycles) following an  $N_{m_0}$  cycle (a new cycle with  $m_0 = N - m + 1$  frames transmitted), while Figure 2 applies to all other retransmission cycles.

Equation (R21) is replaced by

$$\begin{aligned} \bar{t} &= t_m N_m + t_{m_0} N_{m_0} + (t_m + d_0)[R_m | N_{m_0}] N_{m_0} \\ &+ (t_m + d_1) \{ [R_m | R_m] R_m + [R_m | N_m] N_m \} \end{aligned} \tag{A-14}$$

where  $N_{m_0}$ ,  $N_m$ ,  $R_m$  are given by equations (A-4) through (A-7) and

$$t_m = 1 + D \tag{A-15}$$

$$t_{m_0} = 1 + d \tag{A-16}$$

The transition probabilities [equation (R12)] are given by

$$[R_m | R_m] = 1 - S \quad (\text{A-17})$$

$$[R_m | N_m] = 1 - S^{m_0} \quad (\text{A-18})$$

$$[R_m | N_{m_0}] = 1 - S^m \quad (\text{A-19})$$

where  $m_0 = N - m + 1$  . (A-20)

Substituting in equation (A-14) yields

$$\begin{aligned} \bar{i} = \frac{1}{Z} & \left[ S \{ 1 + d + d_0(1 - S^m) \} \right. \\ & + m \{ 1 + S^{m+1} - S^{N+1} \} \\ & \left. + d_1 \{ 1 - S + S^{m+1} - S^{N+1} \} \right] \end{aligned} \quad (\text{A-21})$$

with  $\bar{n}$  still given by equation (A-11), and hence

$$\eta = \left( \frac{b - A}{b} \right) \cdot \left\{ \frac{S(1 - S^{N+1})}{(1 - S) \{ S \{ 1 + d + d_0(1 - S^m) \} + m \{ 1 + S^{m+1} - S^{N+1} \} + d_1 \{ 1 - S + S^{m+1} - S^{N+1} \} \}} \right\} \quad (\text{A-22})$$

with  $m = 1 + D$ .

*c. Case C:* For large buffers satisfying

$$N \geq 1 + 2D, \quad m = 1 + D \quad (\text{A-23})$$

equation (R31a) for  $t$  is replaced by

$$\bar{i} = mN_m + (m + d_1) R_m \quad (\text{A-24})$$

or

$$\bar{i} = m + d_1 R_m \quad (\text{A-25})$$

where  $R_m$  is given by equation (R30) as

$$R_m = \frac{1 - S^m}{1 + S - S^m} \quad (\text{A-26})$$

and hence

$$\bar{i} = m + \frac{d_1(1 - S^m)}{(1 + S - S^m)} \quad (\text{A-27})$$

With  $\bar{n}$  still given by equation (R34) as

$$\bar{n} = \frac{S(1 - S^m)}{(1 - S)(1 + S - S^m)} \quad (\text{A-28})$$

the throughput efficiency is

$$\eta = \left( \frac{b - A}{b} \right) \left[ \frac{S(1 - S^m)}{(1 - S) \{ m(1 + S - S^m) + d_1(1 - S^m) \}} \right] \quad (\text{A-29})$$

where  $m = 1 + D$ .

### FDX-ARM

As in Reference 1, this mode is presented as two cases determined by available buffering.

*a. Case A:* When the buffering is such that

$$N < 1 + d \quad (\text{A-30})$$

then  $m = N$  and Figure 1 is applicable to retransmission cycles. Although the definition of a service cycle differs, equations (R38)–(R44) remain the same; i.e.,

$$N_m = S^m \quad (\text{A-31})$$

$$F_{N_m} = n_{N_m} = m \quad (\text{A-32})$$

$$T_{N_m} = t = 1 + d \quad (\text{A-33})$$

and

$$R_k = S^{k-1} (1 - S) \quad (\text{A-34})$$

$$F_{R_k} = m + k - 1 \quad (\text{A-35})$$

$$n_{R_k} = k - 1 \quad (\text{A-36})$$

while equation (R45) is replaced by

$$T_{R_i} = t + k + d_o \quad . \quad (\text{A-37})$$

With equations (A-31)–(A-37)  $\bar{n}$  still is the same as equation (R50):

$$\bar{n} = \frac{S(1 - S^m)}{(1 - S)} \quad . \quad (\text{A-38})$$

Equation (R48) is replaced by

$$\bar{T} = tS^m + \sum_{k=1}^m (t + k + d_o)S^{k-1}(1 - S) \quad (\text{A-39})$$

which gives instead of equation (R51)

$$\bar{T} = \left( \frac{1 - S^m}{1 - S} \right) [S + d_o(1 - S)] + t + 1 - (m + 1)S^m \quad (\text{A-40})$$

and hence

$$\eta = \left( \frac{b - A}{b} \right) \left[ \frac{S(1 - S^m)}{(1 - S)[2 + d - (m + 1)S^m] + (1 - S^m)[S + d_o(1 - S)]} \right] \quad (\text{A-41})$$

with  $m = N$ .

*b. Case B.* For large buffers satisfying

$$N \geq 1 + d, \quad m = 1 + D \quad (\text{A-42})$$

it can be shown similarly that equation (R54) is replaced by

$$\bar{T} = mS^m + \sum_{k=1}^m (m + k + d_1)S^{k-1}(1 - S) \quad (\text{A-43})$$

or

$$\bar{T} = \frac{(1 - S^m)}{(1 - S)} \{1 + (m + d_1)(1 - S)\} \quad . \quad (\text{A-44})$$

Therefore,

$$\eta = \left( \frac{b - A}{b} \right) \left[ \frac{S}{1 + (m + d_1)(1 - S)} \right] \quad (\text{A-45})$$

where

$$m = 1 + D \quad .$$

## ***Intelligible crosstalk between large FDM-FM carriers amplified by klystrons***

C. B. COTNER AND A. J. BARNES

(Manuscript received November 21, 1978)

### **Introduction**

The 14-GHz high-power amplifiers (HPAs) being installed at the United States earth terminals intended for use in the INTELSAT V system will handle a relatively small number of large frequency-division-multiplexed frequency-modulated (FDM-FM) carriers [1]. Stringent out-of-band noise specifications (Reference 2, pp. 29, 60) and other considerations led to the conclusion that amplifiers multiplexed on a per-transponder basis, each with two large (432- and 972-channel) carriers, would result in a cost-effective HPA design as opposed to the use of a single HPA. Operation near saturation was envisioned using multiplexing filters to reject inter-modulation products.

Because of the relatively narrow bandwidth of each transponder, klystron HPAs appeared to be attractive candidates for this service. The 14.0- to 14.5-GHz klystrons, as well as completely developed HPAs, were available. The cost of these amplifiers is lower than that of traveling wave tube amplifiers (TWTAs) in the power range from 600 to 2,000 W.

However, it was questionable whether the Standard C (Reference 2, pp. 38, 63) station specification on intelligible crosstalk ( $-58$  dB) could be met using klystrons in the above mode. Earlier work [3] on VA884 C-band klystrons once widely used in the INTELSAT system had indicated that large variations observed in the crosstalk ratio could not be explained in terms of the transmission response of a properly tuned klystron. To resolve this question, tests were conducted on a klystron HPA with carriers representing the intended service. A 2-kW 14-GHz HPA with a VKU7791M klystron was used in the test program.

---

*C. B. Cotner is Assistant Manager of the Special Earth Terminals Department of the Earth Station Engineering Division of COMSAT.*

*A. J. Barnes is a Technician Specialist in the Microwave Systems Department at COMSAT Laboratories.*

### Measurements and results

Measurements performed on the klystron HPA to characterize transmission performance included amplitude, group delay distortion, and phase characteristic versus frequency. A network analyzer was used for the amplitude and phase measurements while amplitude modulation techniques were used to obtain the group delay distortion. The results are shown in Figures 1-3. The group delay distortion and amplitude response curves were purposely offset for clarity and are not attributable to klystron effects. Since the use of amplitude modulation to determine group delay distortion precluded a measurement at saturation, it became necessary to perform a transmission phase measurement to verify the lack of large transmission irregularity.

Phase versus drive level, as well as 1- and 2-carrier transfer characteristics, was also measured. Figures 4, 5, and 6 show these results. The two sets of transfer characteristics were taken with the intermodulation distortion products falling in and out of the klystron passband. The data of Figures 1-6 adequately characterize the klystron transmission performance, and as expected, no gross discontinuities in transmission performance were observed.

The actual crosstalk measurements were performed for two 792-channel 25-MHz carriers representing a severe but not unrealistic test of the anticipated use of the klystron HPA. The crosstalking carrier was noise loaded and pre-emphasized. A CW tone was added in the 3.150-MHz (top) baseband slot at the appropriate per channel test tone level with no noise present.

Simultaneously, an unmodulated carrier represented the interfered carrier. The level of the 3.150-MHz tone at the output of a conventional demodulator was measured first for the crosstalking carrier and then for the interfered carrier (as a function of drive relative to that required for band center saturation of the klystron HPA), the difference yielding the intelligible crosstalk ratio.

Figure 7 gives the frequency arrangements for eight of the sixteen cases measured. A large number of different frequency arrangements were measured to determine the effect of a slight klystron tuning offset on the crosstalk ratio. Cases 2 and 8 are identical in frequency but with data taken 48 hours apart.

Figure 8 plots all crosstalk results as a function of input backoff relative to single-carrier saturation. Finally, Figure 9 presents data taken with two different amplitude slopes inserted into the test setup in the path of the

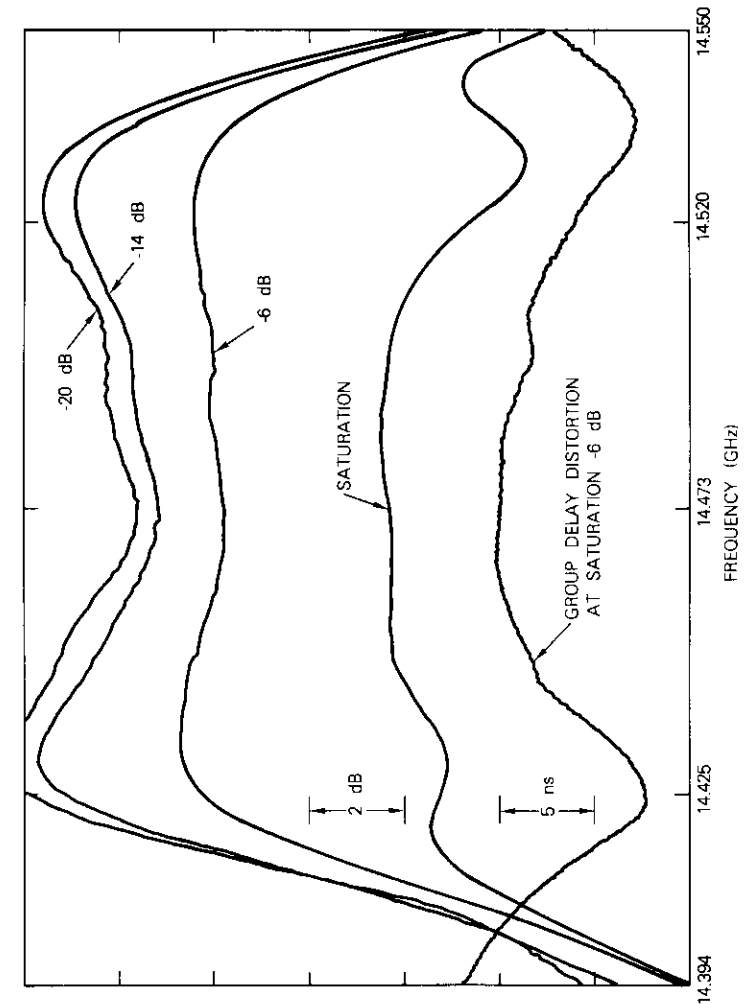


Figure 1. Amplitude (Gain) and Group Delay Distortion

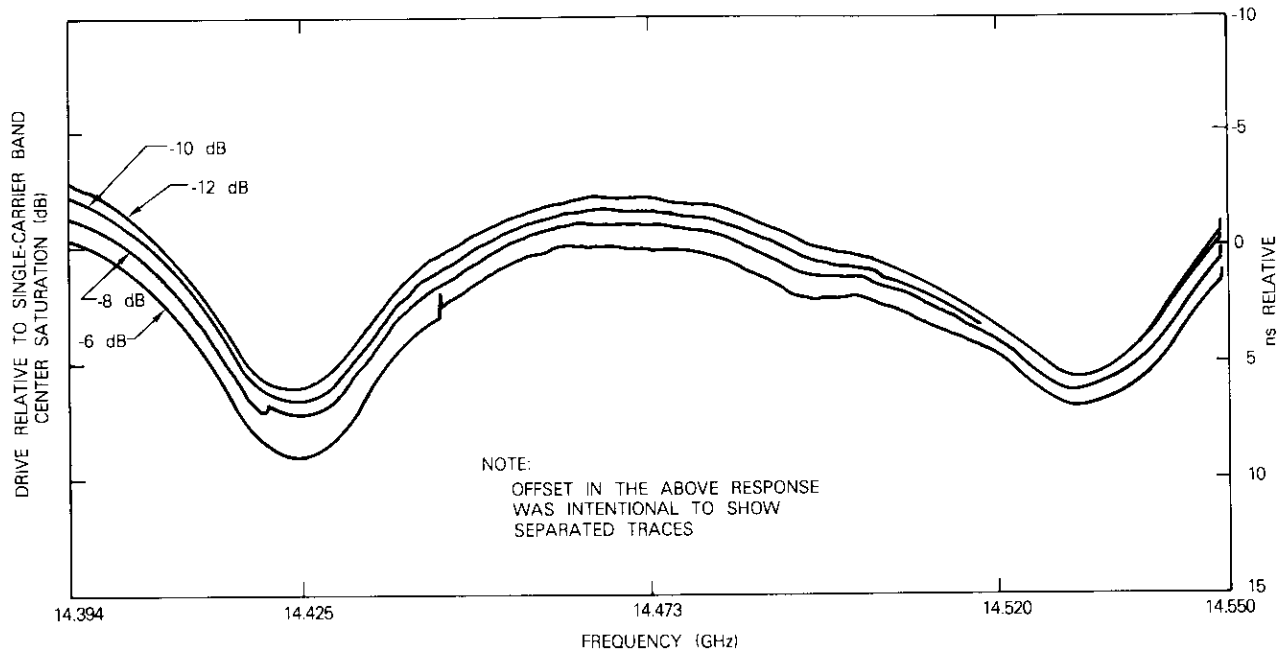


Figure 2. Group Delay Distortion vs Frequency

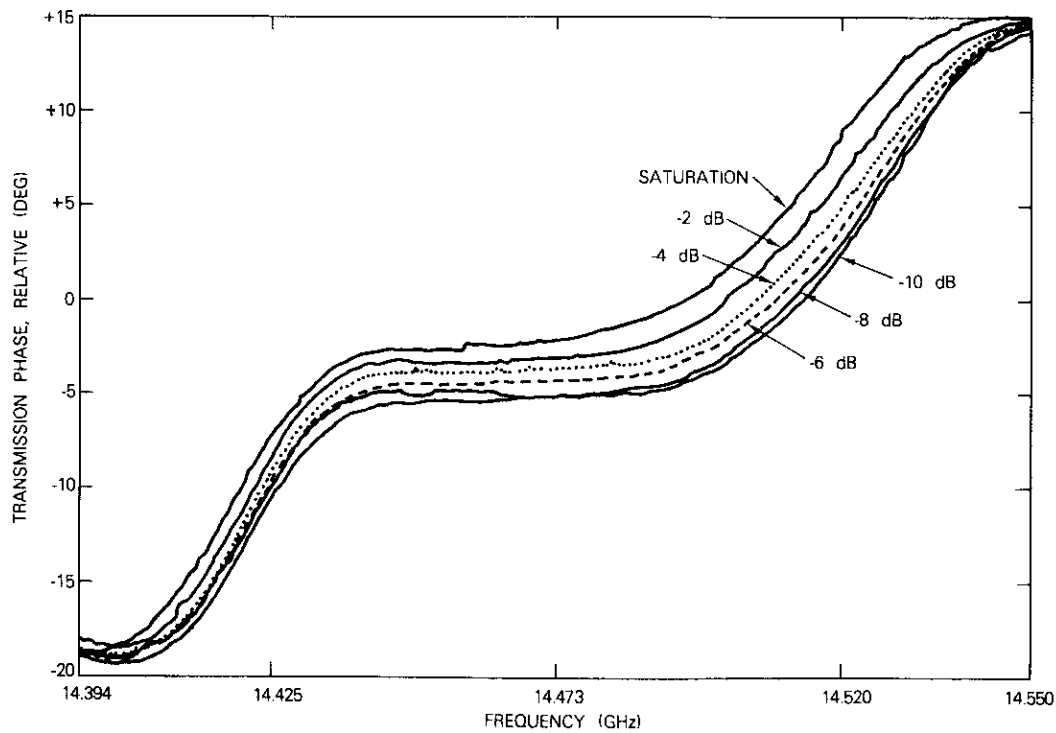


Figure 3. Transmission Phase vs Frequency

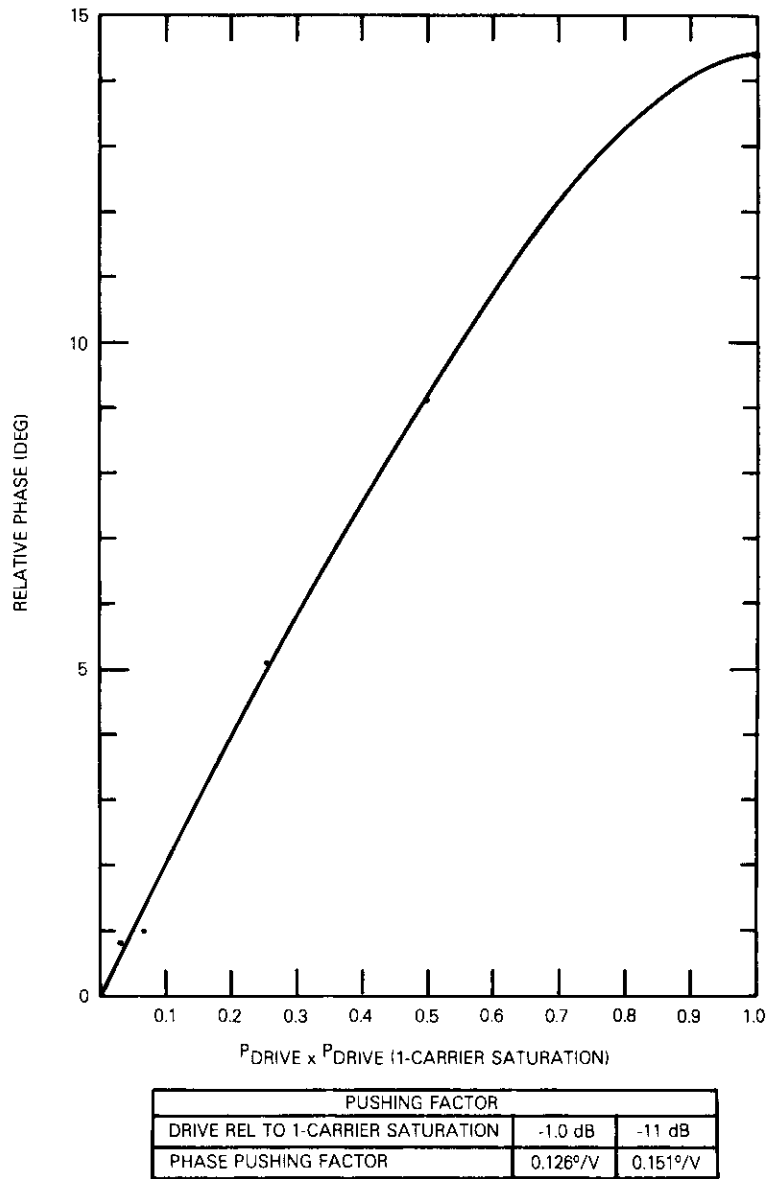


Figure 4. Phase vs Drive Level

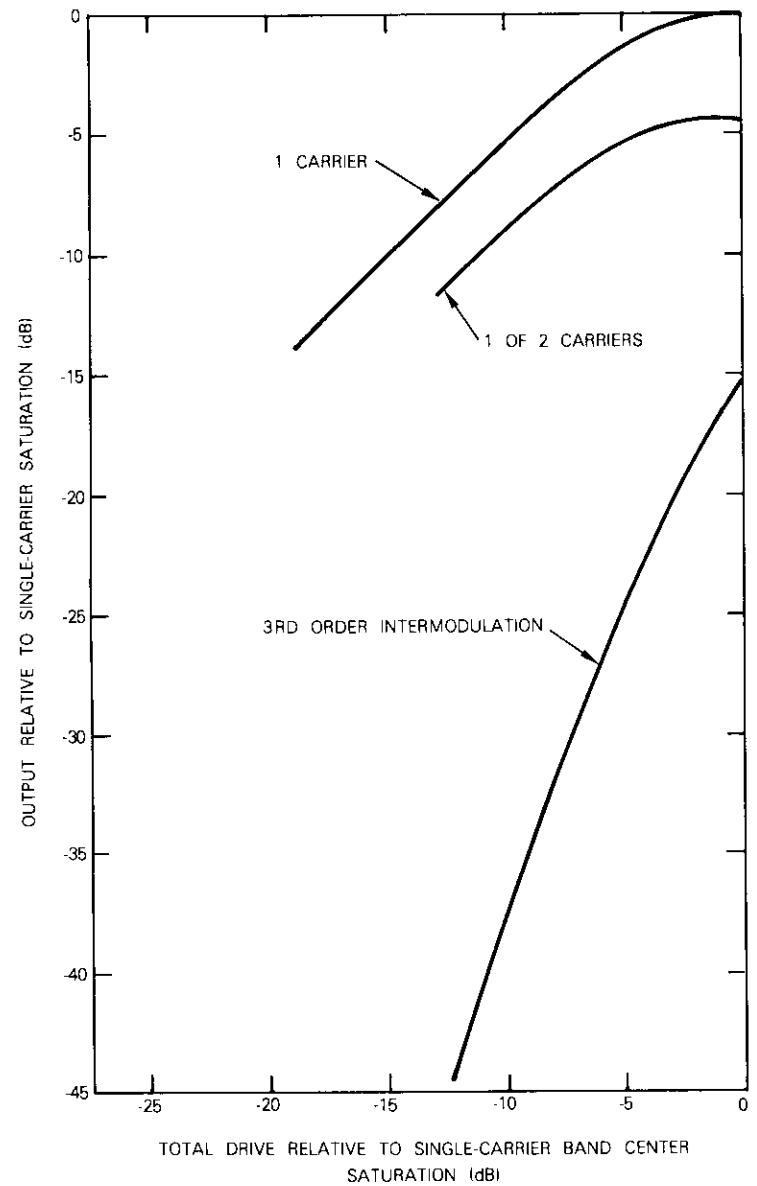


Figure 5. Transfer Characteristic (2 carriers spaced 10 MHz)

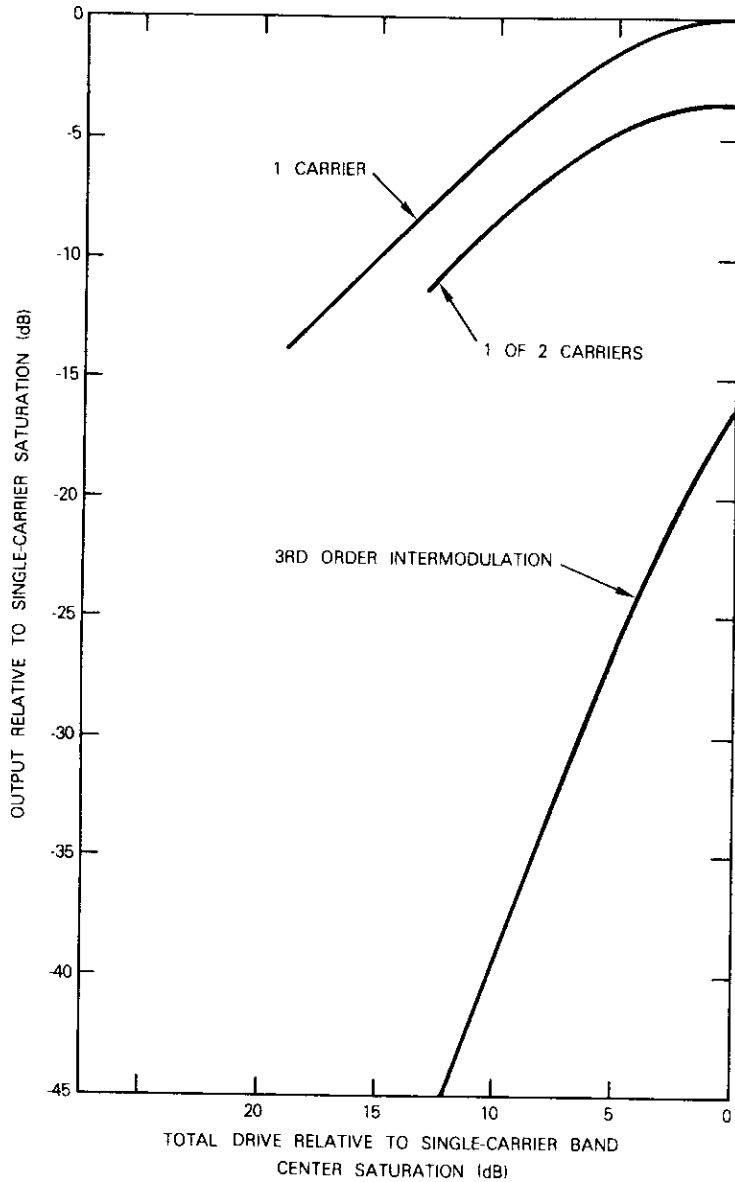


Figure 6. Transfer Characteristic (2 carriers spaced 40 MHz)

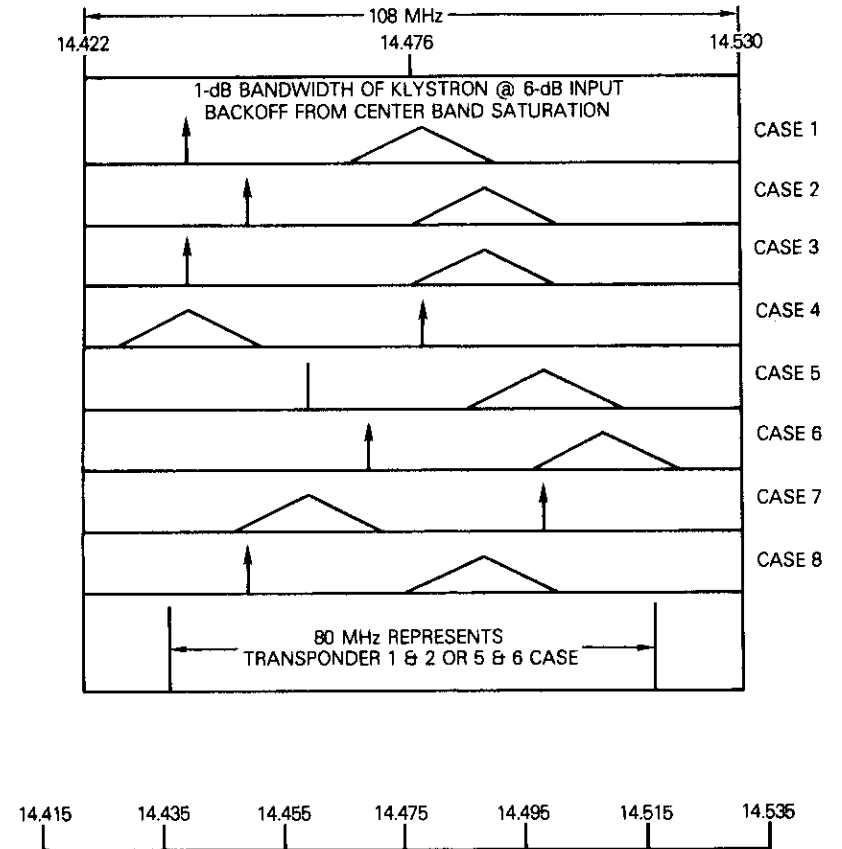


Figure 7. Frequency Arrangements for Crosstalk Measurements for VKU7791M, S/N 133

crosstalking carrier prior to the klystron HPA. This measurement was performed to determine the sensitivity of the crosstalk ratio from the klystron HPA to at least one transmission irregularity occurring elsewhere in the earth terminal.

**Conclusion**

In terms of the measurement results obtained, it appears difficult at best to meet the -58-dB crosstalk specification using klystron amplifiers near saturation for two large FDM-FM carriers.

External characterization of the klystron shows well-behaved passband,

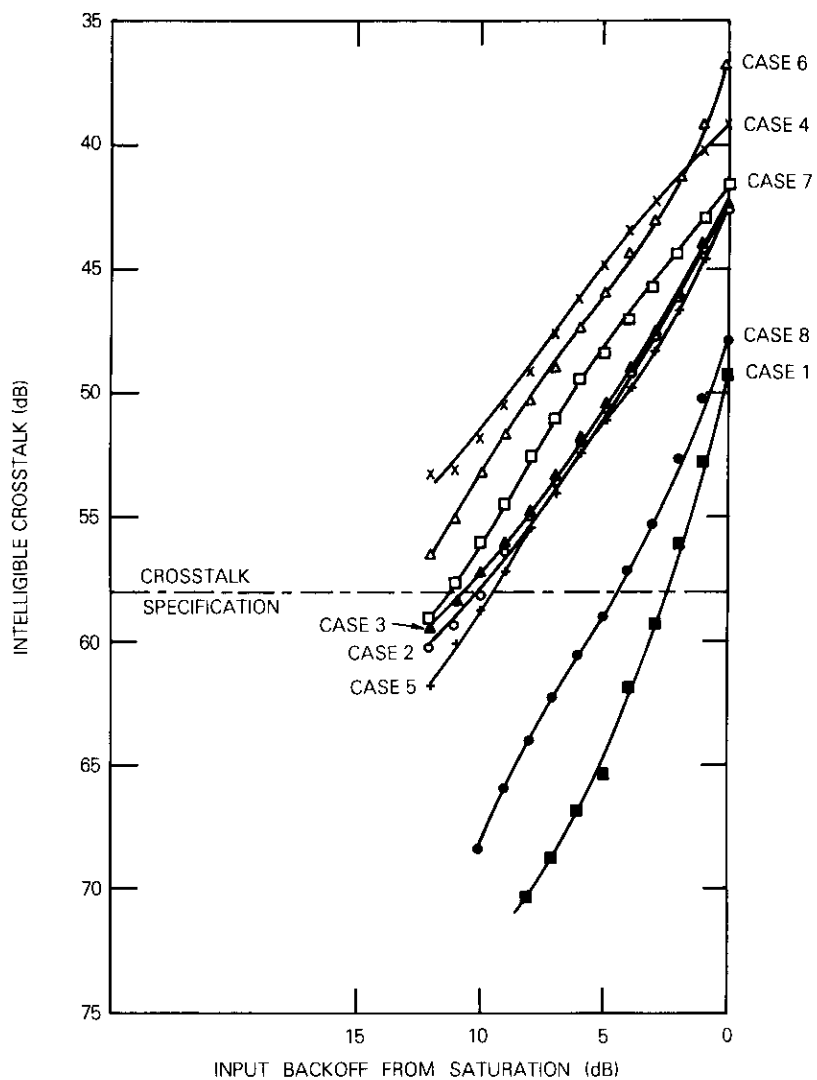


Figure 8. Crosstalk Data for VKU7791M, S/N 133 (3.150-MHz slot; two 792-channel, 25-MHz carriers)

intermodulation, and phase versus drive characteristics. Large variations in intelligible crosstalk are not accounted for by such characterization.

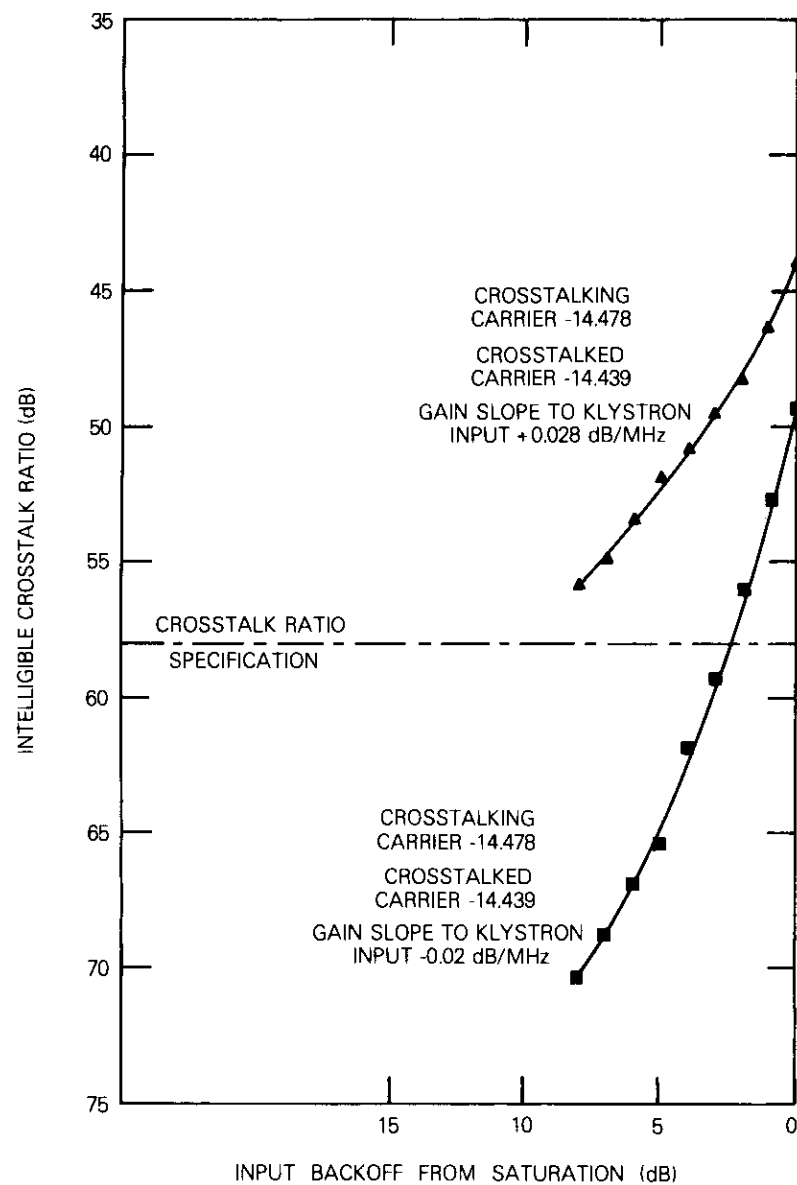


Figure 9. Crosstalk Data for VKU7791M, S/N 133 (3.150-MHz slot; two 792-channel, 25-MHz carriers)

Intelligible crosstalk is produced by two cascaded effects: FM-to-AM conversion generated by a gain slope, followed by AM-to-PM conversion generated by a phase/drive characteristic. In a klystron with several non-synchronously tuned cavities, each followed by a different AM-to-PM characteristic, it is not possible to derive conclusions from external measurements alone. Further work in this area appears desirable.

#### Acknowledgment

*The authors are indebted to L. Pollack, A. Berman, and F. Assal of COMSAT Laboratories for their guidance and encouragement. Discussions with L. Gray and A. Donahoe of the Earth Station Engineering Division of COMSAT were particularly helpful.*

*The tests were performed at Varian Associates in Santa Clara, California, on a Varian 2-kW 14-GHz HPA. Thanks are extended to Varian Associates for making the HPA available.*

#### References

- [1] L. F. Gray and M. P. Brown, Jr., "Transmission Planning for the First U.S. Standard 'C' (14/11-GHz) INTELSAT Earth Station, *COMSAT Technical Review*, Vol. 9, No. 1, Spring 1979, pp. 61-90.
- [2] INTELSAT BG-28-73E, "Standard 'C' Performance Characteristics of Earth Stations in the INTELSAT V System (14 and 11-GHz Frequency Bands)," August 18, 1977.
- [3] L. F. Gray and W. K. Sones, Private Communication.

#### Note on cryptosystems

L. N. LEE

(Manuscript received August 17, 1979)

#### Introduction

A number of comments have been received regarding the security strength of public-key cryptosystems in general, and that of the cryptosystems disclosed in the Spring 1979 issue of *COMSAT Technical Review* [1] in particular. It has been pointed out that Euclid's algorithm can be used to cryptanalyze the public-key cryptosystem described in the above-mentioned reference and that other well-known public-key cryptosystems may also be vulnerable to clever attack.

#### Weakness of the Lu-Lee public-key cryptosystem

The weakness of Lu and Lee's public-key cryptosystem was first observed by L. Adleman and R. Rivest of the Massachusetts Institute of Technology [2], who have developed a systematic approach based on Euclid's algorithm to recover the messages from the cipher text with publicly available information. Since the cipher text is only a linear congruence function of the message, the cryptogram  $X$  can be written explicitly as

$$X = (C_1M_1 + C_2M_2) \bmod r \quad (1)$$

where  $M_1$  and  $M_2$  are two blocks of messages, and  $C_1$ ,  $C_2$ , and  $r$  are enciphering variables available to the public. With  $C_1$  and  $r$  available, it is easy to compute  $C_1^{-1} \bmod r$  by Euclid's algorithm. Multiplying both sides of equation (1) by  $C_1^{-1} \bmod r$  and rearranging terms yields

$$M_1 = (C_1^{-1}X - C_1^{-1}C_2M_2) \bmod r \quad (2)$$

Since  $C_1^{-1}X \bmod r$  and  $C_1^{-1}C_2 \bmod r$  can be computed, the right-hand side of equation (2) is a linear congruence function of  $M_2$ . Depending

---

*L. N. Lee is a Member of the Technical Staff of the Communications Systems Analysis Department, Transmission Systems Laboratory, COMSAT Laboratories.*

on the relative sizes of  $C_1^{-1}C_2 \bmod r$  and  $r$ , the linear congruence function is generally sawtooth shaped as shown in Figures 1a and 1b. Not only the slopes of the sawtooth waves, but also the local maxima and minima, fall in well-defined patterns. Given these well-defined patterns, the value of  $M_2$  at which the linear congruence function

$$f(M_2) = (C_1^{-1}X - C_1^{-1}C_2M_2) \bmod r \quad (3)$$

falls in the legitimate range of  $M_1$  can be found in a straightforward fashion. Adleman observes that the pair  $[f(M_2), M_2]$  at this point is the solution because its uniqueness is guaranteed by the design of the code. In Reference 2, Adleman and Rivest describe an iterative algorithm to find  $M_1$  and  $M_2$  with a table derived from Euclid's algorithm. Since Euclid's algorithm requires about  $\log_2 r$  multiplications, it is an efficient cryptanalytic technique to attack the cryptosystem.

#### Comments on the Lee-Lu multideestinational cryptosystem

Although the multideestinational cryptosystem described in Reference 3 is also based on the Chinese Remainder Theorem and linear congruence relations, cipher text attack as described in Reference 2 is unlikely to succeed because the enciphering key ( $C_i$ ) is kept secret. However, the modified scheme described in Reference 3 is not invulnerable to known plaintext attack as was originally claimed; that is, once a cryptanalyst has at least two plaintext and cryptogram pairs, where both plaintexts are destined to the same location  $i$ , the deciphering key for that location,  $p_i$ , can be computed. For example, if  $X_1, M_1$  and  $X_2, M_2$  are two distinct plaintext and cryptogram pairs, and both  $M_1$  and  $M_2$  are for location  $i$ ,

$$X_j = M_j C_i \bmod p_i, \quad j = 1, 2 \quad (4)$$

or equivalently,

$$X_j = M_j C_i + \ell_j p_i, \quad j = 1, 2 \quad (5)$$

where  $\ell_j$  are generally distinct integers. Cancelling  $C_i$  yields

$$X_1 M_2 - X_2 M_1 = (\ell_1 M_2 - \ell_2 M_1) p_i \quad (6)$$

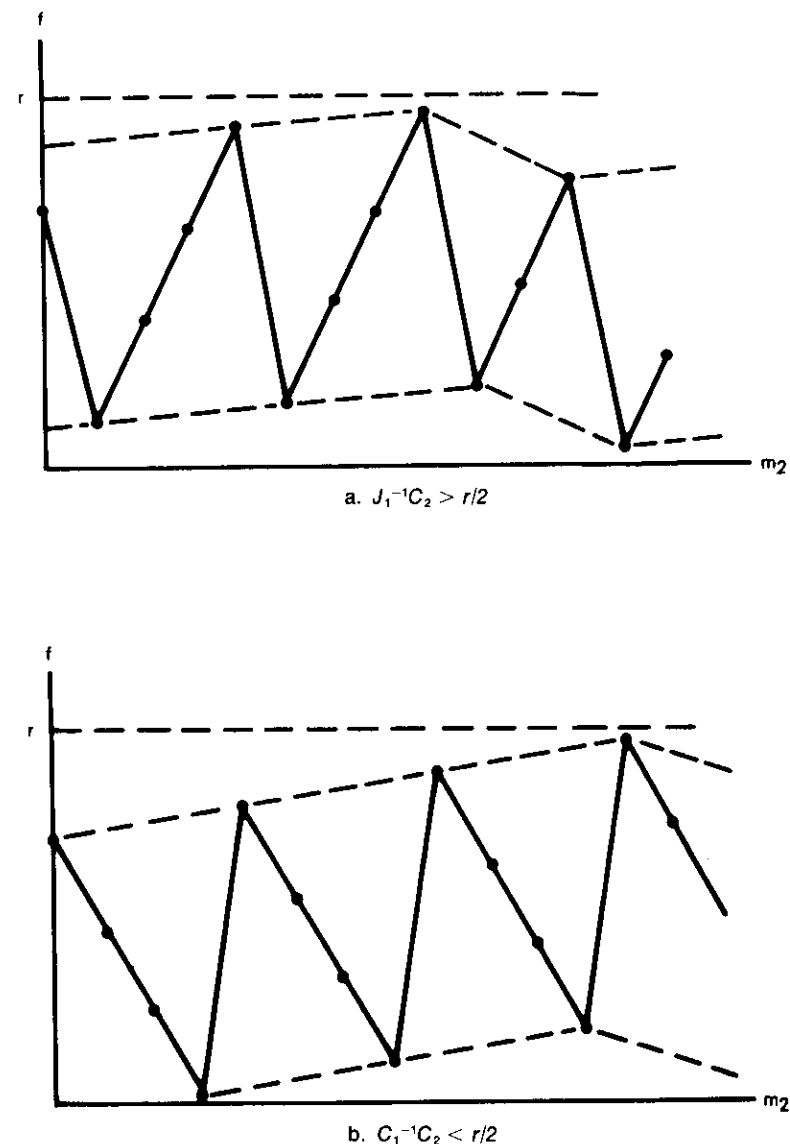


Figure 1. Values of  $f(m_2) = (C_1^{-1}X - C_1^{-1}C_2m_2) \bmod r$  as Functions of  $m_2$

In general,  $\ell_1 M_2 - \ell_2 M_1 \neq 0$ , and is unlikely to be a multiple of any of the deciphering keys,  $p_j$ , in the user community. If  $r = \pi p_j$  is available to the cryptanalyst, he can calculate the greatest common divisor of  $X_1 M_2 - X_2 M_1$  and  $r$  by Euclid's algorithm and determine  $p_i$ . If  $r$  is not available to the cryptanalyst, all he needs is another cryptogram and plaintext pair,  $X_3, M_3$  to form

$$X_2 M_3 - X_3 M_2 = (\ell_2 M_3 - \ell_3 M_2) p_i \quad (7)$$

He can then find the greatest common divisor of  $X_2 M_3 - X_3 M_2$  and  $X_1 M_2 - X_2 M_1$ . Even if  $\ell_1 M_1 - \ell_2 M_2$  and  $\ell_2 M_3 - \ell_3 M_2$  are not relatively prime, the greatest common divisor is generally a small multiple of  $p_i$  and the deciphering key  $p_i$  can easily be derived.

G. Davida of the University of Wisconsin has cited Reference 4, which described a file encryption scheme based on the same principle, but conceived independently. In a revised version, he also described a method to circumvent a known plaintext attack by concatenating a random number of certain length to the messages before enciphering. The procedure is commonly used to enhance the security of this type of systems [5] at the expense of bandwidth expansion. The effort required by the cryptoanalyst is then exponentially dependent upon the length of the random number.

#### Concluding remarks

It is of interest to note that in a recent paper by Herlestam [6] a very ingenious technique was used to successfully attack the Merkle-Hellman public-key cryptosystem. The same paper also demonstrated that a significant portion of the messages enciphered with the Rivest-Shamir-Adleman public-key cryptosystem can be recovered by a modified scheme first suggested in Reference 7 with a practical number of computations. It is clear from the above that public-key cryptography is still under development. Potential users of such cryptosystems must be aware of the risks involved. However, a public-key cryptosystem with acceptable security strength possesses distinct advantages over conventional cryptosystems. Further investigation, including the validation of various proposed public-key cryptographic schemes, should be encouraged.

#### References

- [1] S. Lu and L. Lee, "A Simple and Effective Public-Key Cryptosystem," *COMSAT Technical Review*, Vol. 9, No. 1, Spring 1979, pp. 15-24.
- [2] L. Adleman and R. Rivest, "How to Break the Lu-Lee (COMSAT) Public-Key Cryptosystem," to appear in *Computer Security Journal*.
- [3] L. Lee and S. Lu, "A Multiple-Destinational Cryptosystem for Broadcast Networks," *COMSAT Technical Review*, Vol. 9, No. 1, Spring 1979, pp. 25-36.
- [4] G. Davida, D. Wells, and J. Kam, "A Database Encryption System with Subkeys," TR-CS-78-8, Department of Electrical Engineering and Computer Science, University of Wisconsin-Milwaukee, August 1978.
- [5] B. Arazi, "A Public-Key Cryptosystem Based on Adding Pseudo-Random Values to the Text," 1979 IEEE International Symposium on Information Theory, Trieste, Italy, June 24-29, 1979.
- [6] T. Herlestam, "Critical Remarks on Some Public-Key Cryptosystems," *BIT Nordisk Tidskrift for Informationbehandling*, Copenhagen, Denmark, Vol. 18, 1978, pp. 493-496.
- [7] G. Simmons and M. Norris, "Preliminary Comments on the M.I.T. Public-Key Cryptosystems," *Cryptologia*, October 1977, pp. 406-414.

# Frequency reuse limits for the geostationary orbit

GEORGE R. WELTI

(Manuscript received September 28, 1979)

A given band of the RF spectrum can be used simultaneously in two orthogonal polarizations and on many distinct paths linking earth stations with geostationary satellites. In this note the maximum number of frequency reuses is calculated with certain practical restrictions. In addition, the maximum simultaneous number of co-frequency links (pairs of up- and down-paths with or without an intersatellite path between them) between two earth stations is derived as a function of absolute latitude.

If the use of two orthogonal polarizations is assumed, the maximum number of frequency reuses per satellite is

$$N_R = \frac{2\Omega}{\Phi} \quad (1)$$

where  $N_R$  = number of frequency reuses per satellite  
 $\Omega$  = solid angle subtended by the earth (0.07 steradian)  
 $\Phi$  = solid angle subtended by the coverage area associated with one satellite antenna beam using the full bandwidth.

The beam associated with the solid angle of coverage  $\Phi$  may comprise a number of constituent beams whose beamwidth  $\beta_s$  is equal to or greater than a lower limit determined by the aperture of the satellite antenna. An acceptable level of adjacent beam interference can be guaranteed by spatially separating frequency-sharing earth stations, as viewed from a given satellite, by some minimum number  $K_E$  of constituent beamwidths, whereby these earth stations are separated by the angle  $K_E\beta_s$ . The solid angle  $\Phi$  may be expressed in terms of the angle  $K_E\beta_s$  by assuming some shape for the coverage zone.

The densest satellite beam packing (*i.e.*, smallest  $\Phi$ ) is achieved with a hexagonal tiling of the terrestrial disk as shown in Figure 1.

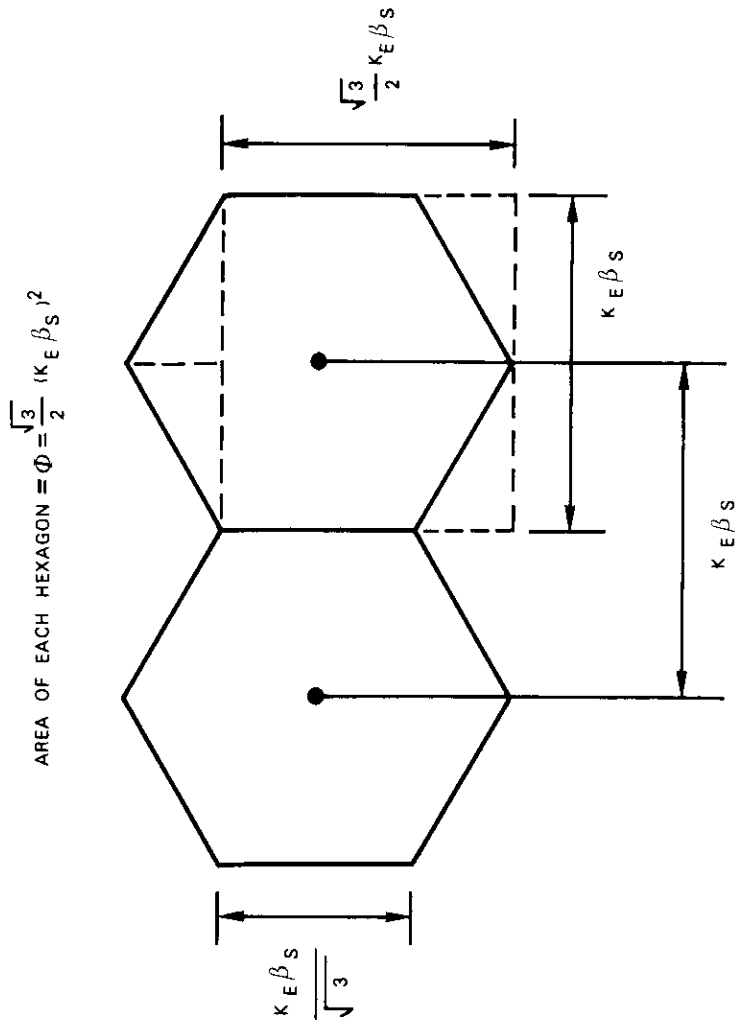


Figure 1. Beam Packing Geometry

In this case

$$\Phi = \frac{\sqrt{3}}{2} (K_E \beta_S)^2 \quad (2)$$

For typical antennas, the beamwidth (in radians) is

$$\beta_S = \frac{1.2\lambda}{D_S} \quad (3)$$

where  $\lambda$  = wavelength  
 $D_S$  = satellite antenna diameter.

Therefore, when equations (1) through (3) are combined and  $K_E$  is assumed to equal 2.2,\* the maximum number of frequency reuses per satellite becomes

$$N_R = \frac{(D_S/\lambda)^2}{43.1} \quad (4)$$

The maximum number of global frequency reuses is

$$N_G = N_R N_S \quad (5)$$

where  $N_S$  = number of satellites. The total area of all satellite antenna apertures in orbit is

$$A = \frac{\pi}{4} D_S^2 N_S \quad (6)$$

Therefore, the maximum number of global frequency reuses becomes

$$N_G = \frac{A}{33.9\lambda^2} \quad (7)$$

This number is independent of the number of satellites in orbit and is plotted in Figure 2. The global capacity achieved for a given value of

\* $K_E = 2.2$  is a reasonable assumption for state-of-the-art satellite antennas.

A is the same for many small satellites as for a few large satellites.

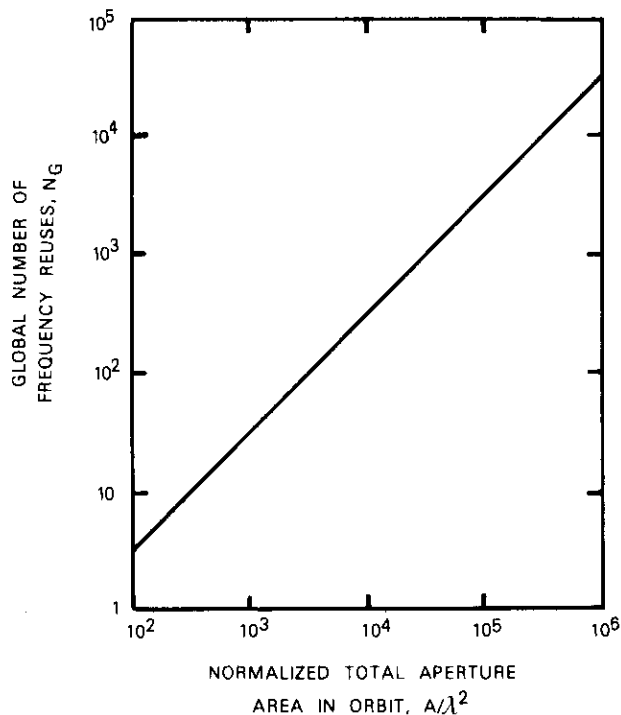


Figure 2. Global Reuses

The maximum capacity of a point-to-point link via satellite is proportional to the number of satellites and does not depend on their individual or combined aperture areas. The maximum number of frequency reuses at a fixed point on earth is

$$N_P = \frac{2\alpha}{\phi} \tag{8}$$

where  $\alpha$  = usable length of geosynchronous arc (rad)  
 $\phi$  = longitude separation of satellites (rad).

The value of  $\alpha$  depends on minimum elevation angle and absolute latitude as shown in Figure 3. A maximum of 2.49 radians is reached

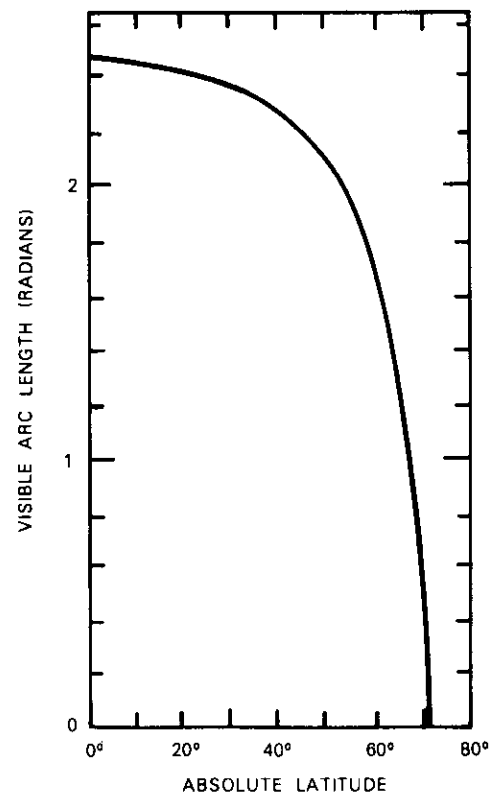


Figure 3. Arc Length Visible Above 10° Elevation Angle

at the equator, for a minimum elevation angle of 10°. The minimum longitude separation  $\phi$  is

$$\phi = K_S \beta_E \tag{9}$$

where  $K_S$  = minimum number of beamwidths between frequency sharing satellites

$\beta_E$  = earth station antenna beamwidth (rad)

and

$$\beta_E = \frac{1.2\lambda}{D_E} \tag{10}$$

where  $D_E$  = earth station antenna diameter. If  $K_S$  is assumed to equal 7\* and equations (8) through (10) are combined, the maximum number of frequency reuses at a fixed point on earth becomes

$$N_P = \frac{\alpha(D_E/\lambda)}{4.20} \leq \frac{D_E/\lambda}{1.69} \quad (11)$$

This relationship is plotted in Figure 4 for several latitudes. High point-to-point capacity requirements are fulfilled by the use of large earth station antennas and by closely spacing the satellites irrespective of their size. If the geosynchronous arcs visible from the two points have little or no overlap, intersatellite links can be used to complete the circuit.

For example, assume that there is a global demand for 1,000 frequency reuses and that the busiest link requires 20 reuses at 50° latitude ( $\alpha = 2.1$  radians). Then, from equation (7),

$$\frac{A}{\lambda^2} = 33,900 \quad (12)$$

If the earth station antenna diameter must be minimized, then, from equation (8), the longitude separation is

$$\phi = \frac{2\alpha}{N_P} = 0.21 \text{ rad} = 12^\circ \quad (13)$$

and the minimum space segment consists of 10 satellites, each with an aperture area equal to

$$\frac{\pi}{4} D_S^2 = \frac{A}{10} \quad (14)$$

Hence, from equation (12) the satellite antenna diameter to wavelength ratio is

$$\frac{D_S}{\lambda} = \sqrt{\frac{4(3,390)}{\pi}} = 65.7 \quad (15)$$

\* $K_S = 7$  corresponds to a satellite spacing of 1° in a system operating with 30-meter earth stations at 4 GHz.

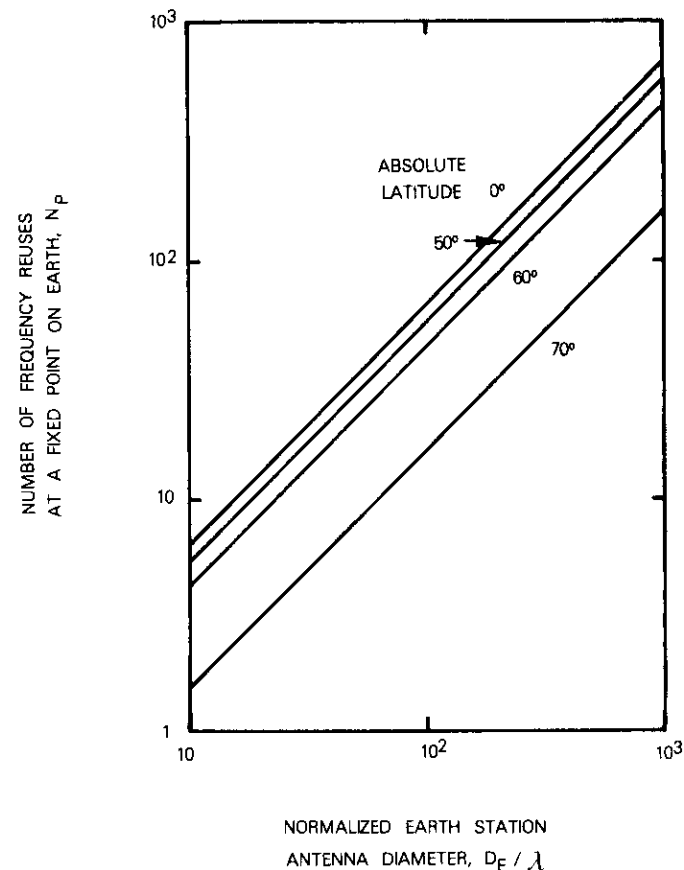


Figure 4. Fixed-Point Reuses

or  $D_S = 4.93$  m at 4 GHz. From equation (3), the satellite antenna constituent beamwidth is

$$\beta_S = \frac{1.2}{65.7} = 0.0183 \text{ rad} = 1.05^\circ \quad (16)$$

Although a single satellite with a 15.6-m antenna can also provide 1,000 global frequency reuses, the number of reuses per link would be only two. Thus, maximum satellite spacing is dictated by busy link requirements rather than global capacity needs. Of course, it is well known

that the minimum spacing is dictated by earth station size, which is evidenced by combining equations (9) and (10).

Although the question of traffic distribution has not been raised so far, it is clear that the global limits established in equation (7) and plotted in Figure 2 can be attained only for traffic that is distributed uniformly over the earth's disk as viewed from orbit. In reality, as traffic tends to be highly concentrated in a few densely populated areas, the attainable number of frequency reuses will be considerably lower. Nevertheless, the conclusions of this analysis remain valid: the total number of reuses is proportional to the total aperture area in orbit, and the number of reuses for a fixed point on earth is twice the number of satellites visible from that point.

## **Translations of Abstracts in this issue**

### **Récepteur de paquets MDF pour systèmes de collecte de données**

K. H. GREENE ET R. F. HEFELE

#### **Sommaire**

L'article décrit un récepteur de paquets de porteuse modulée par déplacement de fréquence (MDF) pour système de collecte de données. Ce récepteur est surtout caractérisé par le fait qu'il doit pouvoir faire l'acquisition de brefs paquets d'information (244 bits) dont l'instabilité de fréquence ( $\pm 10$  kHz) est supérieure d'un ordre de grandeur à la largeur de bande du signal (2 kHz).

Les caractéristiques de fonctionnement du démodulateur et du circuit d'acquisition sont étudiés et les résultats d'expériences sont présentés. L'article s'attarde tout particulièrement sur les méthodes d'analyse de la perte de verrouillage causée par la commutation de la largeur de bande de la boucle d'acquisition. Il présente une méthode analytique qui permet de déterminer le nombre de bits requis pour atteindre un taux donné d'absence d'acquisition en fonction du rapport  $E_b/N_0$  et de la largeur de bande de la boucle d'acquisition.

### **Petits terminaux terriens fonctionnant à 12/14 GHz**

J. KAISER, L. VEENSTRA, E. ACKERMANN ET F. SEIDEL

#### **Sommaire**

Quatre terminaux terriens ont été conçus en vue d'une série d'expériences manées avec le satellite des technologies de télécommunications (CTS), connu également sous l'appellation Hermès. Ces terminaux sont équipés d'antennes de 1,2, 2,0, 2,4 et 4,6 mètres de diamètre. Leur émetteur et leur récepteur, leur système d'excitation d'antenne et leurs filtres, ainsi que la surveillance de l'énergie à l'intérieur du guide d'ondes sont de conception spéciale. Les terminaux de 1,2 et de 2,0 mètres ont été utilisés pour assurer des services de télécommunications d'urgence dans des conditions réelles et simulées; les autres terminaux ont servi à des transmissions expérimentales telles que le fac-similé à grande vitesse, la télévision à balayage lent, les télécommunications entre ordinateurs, la télévision numérique en couleur avec 60 voies télépho-